

**OUTER SPACE AND FOURIER SPACE:  
UNDERSTANDING FOREGROUNDS FOR NEUTRAL HYDROGEN  
EPOCH OF REIONIZATION MEASUREMENTS**

Saul Aryeh Kohn

A DISSERTATION

in

Physics and Astronomy

Presented to the Faculties of the University of Pennsylvania

in Partial Fulfillment of the Requirements for the Degree of Doctor of Philosophy

2018

Supervisor of Dissertation

Graduate Group Chairperson

---

James E. Aguirre  
Associate Professor of Physics and Astronomy

---

Joshua Klein  
Professor of Physics and Astronomy

Dissertation Committee:

Cullen Blake, Assistant Professor of Physics and Astronomy

Adam Lidz, Associate Professor of Physics and Astronomy

Elliot Lipeles, Associate Professor of Physics and Astronomy

Masao Sako, Associate Professor of Physics and Astronomy

*to my grandparents*

**OUTER SPACE AND FOURIER SPACE:  
UNDERSTANDING FOREGROUNDS FOR NEUTRAL HYDROGEN  
EPOCH OF REIONIZATION MEASUREMENTS**

© COPYRIGHT

2018

Saul Aryeh Kohn

This work is licensed under the  
Creative Commons Attribution  
NonCommercial-ShareAlike 3.0  
License

To view a copy of this license, visit

<http://creativecommons.org/licenses/by-nc-sa/3.0/>

# Acknowledgments

While I am the one to have performed the research and compiled it, this thesis is the product of many, of which I must thank a specific few.

It has been a privilege to work alongside the talented and passionate individuals that comprise the PAPER and HERA teams. My co-conspirators of PAPER analysis – Danny Jacobs, Carina Cheng, Matt Kolopanis and Josh Kerrigan – it has been a struggle and a pleasure, and I will sorely miss working with you.

The Department of Physics & Astronomy of the University of Pennsylvania is a fantastic place to work. The cohorts of graduate students it brings together are consistently awesome, engaging and friendly. I have made some of my best friends here, including Ashley Baker, Christian Herwig, Elodie Resseguie, Christina Krawiec, Rachel Wolf and Alyssa Barlis. Outside of Physics & Astronomy, but within the Penn umbrella, I must thank my dear friends Julie Westover, Irteza Binte-Farid and Steve Kocher for their loving support. This is also a good place to thank the School of Arts and Sciences for supporting my final year at Penn with a Dissertation Completion Fellowship.

James, you are *the best* supervisor. I have learned so much from you, and treasure the opportunities you have given me to grow and become the scientist that I am. I know how rare it is to be able to call a PhD supervisor a friend, and I count my luck there daily.

Matt and Debbie, thank you for great conversations, encouraging words and hospitality. I can't want to be your son-in-law. Hannah, Yosef and Ezra, you are always full of loving support and cutting sarcasm, neither of which I ever want to be without. Mom and

Dad, this thesis belongs to you as much as it does me. Your hard work, encouragement and love made me who I am. Thank you. Gabby – you’re the best, and I love you. What more can I say? I’ll save the good stuff for the wedding.

**ABSTRACT**  
**OUTER SPACE AND FOURIER SPACE:**  
**UNDERSTANDING FOREGROUNDS FOR NEUTRAL HYDROGEN**  
**EPOCH OF REIONIZATION MEASUREMENTS**

Saul A. Kohn

James E. Aguirre

Abstracts are written last.

# Contents

<b>Title</b>	<b>i</b>
<b>Dedication</b>	<b>ii</b>
<b>Acknowledgments</b>	<b>iv</b>
<b>Abstract</b>	<b>vi</b>
<b>List of Tables</b>	<b>xii</b>
<b>List of Figures</b>	<b>xiii</b>
<b>I Radiation, Interferometry &amp; Polarimetry</b>	<b>1</b>
<b>1 The Epoch of Reionization</b>	<b>3</b>
1.1 The promise of direct measurements of the EoR . . . . .	3
1.1.1 Statistical detections – power spectra . . . . .	3
1.1.2 Global Signal . . . . .	3
1.1.3 Imaging . . . . .	4
1.1.4 Challenges, briefly . . . . .	4
1.2 Indirect probes . . . . .	4
1.3 This thesis . . . . .	4
<b>2 Astrophysical Radiation</b>	<b>6</b>
<b>3 Interferometry, Calibration &amp; Polarimetry</b>	<b>7</b>
3.1 The Visibility Equation . . . . .	7
3.1.1 The Classical Visibility Equation . . . . .	8
3.1.2 The Measurement Equation . . . . .	11
3.2 Calibration Techniques . . . . .	14
3.2.1 Diagonal and off-diagonal calibration . . . . .	15
3.2.1.1 Ionospheric effects . . . . .	16

3.2.2	Image-based calibration . . . . .	17
3.2.3	CLEAN . . . . .	18
3.2.3.1	Högbom’s algorithm . . . . .	18
3.2.3.2	Delay Transforms and the 1D-CLEAN . . . . .	21
3.2.4	Redundant calibration . . . . .	23
3.3	Instrumental Polarization . . . . .	25
3.3.1	Direction-Dependent Leakage . . . . .	25
3.3.2	Direction-Independent Leakage . . . . .	29
<b>4</b>	<b>Instruments</b>	<b>31</b>
4.1	Instruments used in this work . . . . .	31
4.1.1	The Donald C. Backer Precision Array for Probing the Epoch of Reionization (PAPER) . . . . .	32
4.1.1.1	The PAPER signal chain . . . . .	33
4.1.1.2	PAPER-32 . . . . .	35
4.1.1.3	PAPER-64 . . . . .	36
4.1.1.4	PAPER-128 . . . . .	37
4.1.2	The Hydrogen Epoch of Reionization Array (HERA) . . . . .	38
4.1.2.1	HERA-19 Commissioning Array . . . . .	39
4.1.2.2	Future HERA Build-Outs . . . . .	40
4.2	Other current and future interferometers . . . . .	41
4.2.1	The Low Frequency Array (LOFAR) . . . . .	41
4.2.2	The Murchison Widefield Array (MWA) . . . . .	42
4.2.3	Square Kilometer Array – Low band (SKA-Low) . . . . .	42
<b>II</b>	<b>Structure in Fourier space</b>	<b>44</b>
<b>5</b>	<b>Peering through the EoR Window</b>	<b>46</b>
<b>6</b>	<b>Data Preparation and Processing</b>	<b>47</b>
6.1	Data Compression . . . . .	47
6.1.1	Delay–Delay-Rate Filtering . . . . .	48
6.1.2	Software Implementation . . . . .	50
6.2	Radio Frequency Interference . . . . .	52
6.2.1	PAPER-128 . . . . .	52
6.2.1.1	Average Properties . . . . .	53
6.2.1.2	Individual Properties . . . . .	60
6.2.1.3	Discussion . . . . .	63
6.2.2	HERA-19 and PAPER-19 . . . . .	64
6.2.2.1	HERA Hex RFI . . . . .	65
6.2.2.2	PAPER Hex RFI . . . . .	67
6.2.2.3	Hex-to-Hex Comparisons . . . . .	67

6.2.2.4	Comparison PAPER-128 stacked flags . . . . .	69
6.2.2.5	Discussion . . . . .	70
6.3	Quality Assurance Metrics . . . . .	71
6.3.1	Mean Amplitude Flagging . . . . .	72
6.3.2	Flagging on omnical $\chi^2$ . . . . .	74
<b>7</b>	<b>Polarimetric Calibration</b>	<b>76</b>
7.1	Redundant Calibration . . . . .	77
7.1.1	Mathematical Overview . . . . .	79
7.1.1.1	Redundant calibration with OMNICAL . . . . .	79
7.1.1.2	Including polarization in redundant calibration . . . . .	80
7.1.1.3	Degeneracies . . . . .	81
7.1.1.4	Expectations from simulation . . . . .	82
7.1.2	Data Processing . . . . .	83
7.1.3	Results . . . . .	87
7.1.3.1	Calibration . . . . .	87
7.1.3.2	Pseudo-Stokes Visibilities . . . . .	88
7.1.4	Discussion & Conclusions . . . . .	93
7.2	Imaging Calibration . . . . .	94
7.2.1	Converting historical PAPER data into Measurement Sets . . . . .	94
7.2.2	Imaging PAPER-32 data with CASA . . . . .	95
7.2.3	D-term calibration . . . . .	98
<b>8</b>	<b>The Ionosphere</b>	<b>104</b>
8.1	Historical measurements of TEC and RMs . . . . .	106
8.2	Low frequency observations: discoveries and challenges . . . . .	108
8.3	Relevance for PAPER and HERA EoR measurements . . . . .	109
<b>9</b>	<b>A view of the EoR window from the PAPER-32 imaging array</b>	<b>114</b>
9.1	Observations & Reduction . . . . .	115
9.1.1	Calibration . . . . .	117
9.1.1.1	Initial calibration . . . . .	117
9.1.1.2	Absolute Calibration . . . . .	117
9.1.1.3	Polarimetric factors . . . . .	119
9.1.2	Creating power spectra . . . . .	121
9.2	Results . . . . .	122
9.3	Discussion and Conclusions . . . . .	125
<b>10</b>	<b>A view of the EoR window from the HERA-19 commissioning array</b>	<b>133</b>
10.1	Polarization Leakage Simulations . . . . .	134
10.2	Observations & Reduction . . . . .	135
10.2.1	Calibration . . . . .	136
10.2.2	Forming power spectra . . . . .	142

10.3	Results & Discussion . . . . .	143
10.3.1	General features of the power spectra . . . . .	144
10.3.2	Day-to-day variability . . . . .	145
10.3.3	Polarimetric results . . . . .	145
10.4	Conclusions . . . . .	148
<b>11</b>	<b>Deep integrations on polarization with PAPER-128</b>	<b>153</b>
11.1	Observations & Reduction . . . . .	153
11.1.1	Overview of PAPER-128 observations . . . . .	154
11.1.2	Reduction of Season 1 Epoch 2 data . . . . .	158
11.1.2.1	Redundant calibration . . . . .	158
11.1.2.2	Foreground removal . . . . .	159
11.1.2.3	Binning in LST . . . . .	163
11.1.2.4	Absolute calibration & fringe-rate filtering . . . . .	163
11.1.3	Forming power spectra . . . . .	166
11.2	Results . . . . .	169
11.3	Discussion & Conclusions . . . . .	172
<b>III</b>	<b>Expanding the potential of EoR measurements</b>	<b>174</b>
<b>12</b>	<b>Interferometric sensitivity to the monopole moment</b>	<b>176</b>
<b>13</b>	<b>Higher-order correlation functions between kSZ and 21cm observations</b>	<b>177</b>
13.1	The kSZ-21cm connection . . . . .	178
13.1.1	Foregrounds . . . . .	178
13.1.2	Noises . . . . .	178
13.2	kSZ <sup>2</sup> -21cm squeezed-triangle bispectra . . . . .	178
13.2.1	Semi-analytic approximation . . . . .	178
13.2.2	Counting triangles . . . . .	178
13.2.3	Signal-to-noise estimates . . . . .	178
13.3	kSZ <sup>2</sup> -21cm <sup>2</sup> squeezed-rectangle trispectra . . . . .	178
13.3.1	Semi-analytic approximation . . . . .	178
13.3.2	kSZ <sup>2</sup> -21cm bispectra cross-power spectrum . . . . .	178
<b>14</b>	<b>Deep Learning for 21cm Observations</b>	<b>179</b>
14.1	Neural Networks . . . . .	180
14.2	Classifying reionization models . . . . .	182
14.3	Regressing upon reionization parameters . . . . .	184
14.4	Future directions . . . . .	189
<b>15</b>	<b>Conclusions</b>	<b>191</b>

<b>Appendices</b>	<b>192</b>
<b>A Software</b>	<b>193</b>
A.1 Astronomical Interferometry in Python ( <code>aipy</code> ) . . . . .	193
A.2 Astronomy in Python ( <code>astropy</code> ) . . . . .	194
A.3 Common Astronomy Software Applications (CASA) . . . . .	194
A.4 Deep Learning packages . . . . .	194
A.5 Hierarchical Equal Area isoLatitude Pixelization of the sphere (HEALPix)	194
A.6 <code>pyuvdata</code> . . . . .	195
A.7 The Scientific Python Ecosystem ( <code>scipy</code> ) . . . . .	195
<b>Bibliography</b>	<b>196</b>

# List of Tables

6.1	PAPER-128 RFI frequencies and brief characterization for the averaged flags.	55
6.2	RFI as flagged by HERA	66
6.2	RFI as flagged by HERA	67
6.3	RFI as flagged by the PAPER Hex	68
8.1	Ionospheric Layers	105
11.1	PAPER-128 Observing Seasons & Epochs	154

# List of Figures

3.1	The geometry of a two-element interferometer, with a plane wave incident from direction $\hat{s}$ . . . . .	8
3.2	Four stages of the Högbom CLEAN. . . . .	20
3.3	A graphical representation of the delay transform. . . . .	23
3.4	Simulations of the instrumental direction-dependent Mueller matrix at 120 MHz and 160 MHz. . . . .	28
4.1	An image of a PAPER dipole element with its groundscreen. . . . .	34
4.2	A diagram of the PAPER-128 signal chain. Square-dotted lines indicate RFI-shielding. . . . .	35
4.3	The array layouts of the PAPER-32 element deployment in South Africa.	36
4.4	The array layouts of the PAPER-64 deployment. . . . .	37
4.5	The PAPER-128 array layout. . . . .	38
4.6	Future vision and physical commissioning HERA layout. . . . .	39
4.7	Positions of antennae in the HERA-19 Commissioning Array (including the experimental “subarrays”). . . . .	40
4.8	Array sensitivity as a function of $k$ -mode relative to HERA-19 . . . . .	41
6.1	The schema of the database used to organize and implement PAPER data compression. . . . .	51
6.2	A waterfall plot of RFI flags averaged over 150 days of PAPER-128 data.	56
6.3	The percentage of time that each frequency was flagged over the season. .	57
6.4	Possible FM radio contamination. . . . .	58
6.5	Flights from Cape Town to Johannesburg correspond to RFI in the $120.15 \pm 0.35$ MHz channels. . . . .	59
6.6	The temporal profile of the 5 RFI frequencies with unidentified causes. . .	61
6.7	Waterfalls of RFI flags for nights 2456732, 2456958 and 2457038. . . .	62
6.8	Waterfalls of RFI flags for nights 2456898, 2456924 and 2456965 . . .	63
6.9	Frequency vs. percentage flagging for the HERA Hex and PAPER Hex. .	69
6.10	RFI flag waterfalls of frequency vs. South Africa Standard Time for the HERA Hex and PAPER Hex. . . . .	70
6.11	An example of the mean amplitude flagging metrics on exercised on HERA-47 data. . . . .	73

6.12	Flagging Julian Dates based on the median omnical $\chi^2$ values in the 150–180 MHz band. . . . .	75
7.1	Simulations of pseudo-Stokes visibilities, . . . . .	84
7.2	Arrangement of the PAPER-128 array. . . . .	85
7.3	The phase of the complex gain value for the <i>4pol</i> calibration scheme. . . . .	88
7.4	Histograms of differences in the ‘x’ gain calibrations per antenna between calibration schemes. . . . .	89
7.5	$w^2$ values, summed across the array. . . . .	90
7.6	Pseudo-Stokes visibility amplitudes and phases. . . . .	91
7.7	Delay-transformed pseudo-Stokes visibilities. . . . .	92
7.8	The beam model ( <i>left</i> ) and point spread function ( <i>right</i> ) of the PAPER-32 array, calculated by CASA. . . . .	96
7.9	Full-polarization imaging results from a four-component, Stokes I-only sky model. . . . .	99
7.10	The same field as shown in Figure 7.9, but with the removal of malfunctioning antennas identified by Kohn et al. (2016). . . . .	100
7.11	Imaging results from a file calibrated with gain values derived from the Pictor A transit, which occurred $\sim$ 6 hours after these data were acquired. . . . .	101
7.12	The same field as shown in Figure 7.10, but for pseudo Stokes U and V only, with <i>D</i> -terms partially calibrated. . . . .	103
8.1	Distribution of zenithal ionospheric RMs for 3 LSTs in the PAPER-32 observing season . . . . .	110
8.2	An example of widefield ionospheric RMs calculated by radionoppy. . . . .	112
8.3	The RM of Cas A as viewed from the LOFAR Core site in the Netherlands on April 11th, 2011, according to ionFR and radionoppy. . . . .	113
9.1	The PAPER-32, dual-pol antenna imaging configuration and <i>uv</i> distribution. . . . .	116
9.2	Snapshot images of Stokes parameters before and absolute calibration. . . . .	127
9.3	The values of ionospheric RM for different lines of sight a range of LSTs. . . . .	128
9.4	The absolute value of delay-transformed visibilities over the bandwidth (146–166 MHz) used to create the power spectra shown in this Chapter. . . . .	129
9.5	Log-scaled 2D power spectra from PAPER-32. . . . .	130
9.6	Wedge power spectra from PAPER-32. . . . .	131
9.7	Average power in $0.093 < k_{\perp} < 0.098 \text{ } h\text{Mpc}^{-1}$ as a function of $k_{\parallel}$ for each polarization of PAPER-32 data. . . . .	132
10.1	The perimeter of each dish in the HERA-19 array. . . . .	136
10.2	Fractional RFI flag occupancy per time and frequency over the eight days of observations. . . . .	137
10.3	Multi-frequency synthesis pseudo-Stokes images formed from simulation and data. . . . .	139

10.4	Bandpass solutions for the North-South dipole orientation obtained for the functioning antennae in the array on JD 2457548. . . . .	140
10.5	The effect of calibration on the phases of visibilities from three redundantly-spaced 14.7 m baselines. . . . .	141
10.6	Power spectrum results from the high-band (157–167 MHz). . . . .	149
10.7	Power spectrum results from the low-band (120–130 MHz). . . . .	150
10.8	High band power as a function of baseline length for the center of the pitchfork ( $k_{\parallel} = 0$ h/Mpc) and in the EoR window ( $k_{\parallel} = 0.2$ h/Mpc) for each JD of observation. . . . .	151
10.9	Simulated and observed power as a function of $k_{\parallel}$ for the shortest baseline (14.7 m). . . . .	152
11.1	An annotated photograph of the PAPER-128 array. . . . .	155
11.2	The challenge of Epoch changes. . . . .	157
11.3	Good, bad and rotated antennas in Season 1 Epoch 2. . . . .	158
11.4	Amplitudes of three redundant visibilities before and after OMNICALibration using the <i>4pol+minV</i> scheme. . . . .	160
11.5	The same visibilities as shown in Figure 11.4, but showing their phases instead of their amplitudes. . . . .	161
11.6	Images of Pictor A, used to calibrate the absolute scaling to physical units. . . . .	165
11.7	The point-spread function of an array consisting only of the $\sim$ 30 m power spectrum baselines. . . . .	166
11.8	The average bandpass scaling used for absolute calibration. . . . .	167
11.9	Delay-rate vs. frequency for a 30 m baseline in the ‘xx’ (East-East) polarization. . . . .	167
11.10	Spherically-averaged PAPER-128 power spectra. . . . .	170
11.11	Spherically-averaged noise power spectra. . . . .	173
14.1	21 cm brightness temperature fields for Galaxy-Only and AGN-only models. . . . .	183
14.2	The classification CNN used in this study. Figure taken from Hassan et al. (2018). . . . .	184
14.3	Training data and results of the classifier. . . . .	185
14.4	An input image propagated through the trained kernels of the first layer of the classifier. . . . .	185
14.5	The effect of changing $\zeta$ on the 21 cm brightness temperature field. . . . .	187
14.6	The CNN used for regression. . . . .	188
14.7	The results of training the CNN regressor. . . . .	188
14.8	True vs. predicted values of $\zeta$ from the test set. . . . .	189



# **Part I**

## **Radiation, Interferometry &**

## **Polarimetry**

... His light is like a niche, within which is a lamp, the lamp within glass, the  
glass as if it were a white star... Light upon light.

*Al Quran, Surah An Nur (24:35)*

# **Chapter 1**

## **The Epoch of Reionization**

### **1.1 The promise of direct measurements of the EoR**

#### **1.1.1 Statistical detections – power spectra**

#### **1.1.2 Global Signal**

The 21 cm signal from the Epoch of Reionization (EoR) contains a wealth of information about the Universe at these early times, and can provide key insight inaccessible to other observational techniques (Loeb & Furlanetto, 2012).

In particular, the sky-averaged 21 cm signal, the so-called global signal, directly contains key information about the thermal history of the intergalactic medium (IGM) as a function of redshift (Pritchard & Loeb, 2010). Historically, observational efforts to detect the global signal have been “single dish” experiments, where a single receiving element is characterized to high precision, and then operated in an effort to detect the EoR signal as a function of frequency (and thus redshift). Experiments such as the Experiment to Detect the Global EoR Step (EDGES, Bowman & Rogers 2010), Sonda Cosmológica de las Islas para la Detección de Hidrógeno Neutro (SCI-HI, Voytek et al. 2014), and the Cosmic Twilight Polarimeter (CPT, Nhan et al. 2016), have been proposed or constructed seeking to measure the global signal from the Dark Ages or the EoR, through a deep

understanding of the properties of the instruments. In all cases, the instruments consist of a single-element, and much of the observational effort contributes toward a thorough understanding of systematic uncertainties of the instrument. The signal from the Dark Ages and EoR is thought to be 4–5 orders of magnitude fainter than nearby bright foregrounds, such as galactic synchrotron radiation (McQuinn et al., 2007). As such, an exquisite understanding of the correlated noise in these instruments is of the utmost importance. Largely, these experiments have not yet detected a feature in frequency-space that can clearly be interpreted as a detection of either the Dark Ages or EoR global signal. To date, EDGES has provided a lower-limit on the duration of reionization of  $\Delta z \geq 0.06$  (Bowman & Rogers, 2010).

### 1.1.3 Imaging

### 1.1.4 Challenges, briefly

## 1.2 Indirect probes

## 1.3 This thesis

Everything in this work – algorithmic development, mathematical theory, observations – was carried-out in order to facilitate the detection of the EoR. While these efforts took many forms, they shared that singular motivation of moving the field forward towards a detection of HI at cosmological distances.

This thesis is divided into three parts. Part I is devoted to introducing concepts used throughout this work and building a mathematical formalism around those concepts. Chapter 2 reviews astrophysical mechanisms for producing polarized and unpolarized radiation at low radio frequencies. Chapter 3 builds a formalism around measuring low frequency radio waves with interferometers (and the challenges associated with accurately measuring polarized radiation), and Chapter 4 introduces the instruments used throughout

this work.

In Part II I present the bulk of my efforts: building an understanding of the imprint of the polarized sky, and the instrument itself, in the Fourier space used to set limits on the EoR power spectrum. Chapter 5 reviews the current theory and major results of mapping low frequency interferometric measurements into Fourier space. Chapter 6 details several required quality assurance and compression steps that must be taken to clean and interact with the data. Building from clean data, Chapter 7 presents new algorithms developed to calibrate the measurements. Chapter 8 discusses the impact of Earth’s ionosphere on our measurements. In Chapters 9, 10 and 11 I present successively-deeper integrations on polarized foregrounds in successively-narrower regions of Fourier space.

Part III explores other uses of EoR measurements, beyond detection of the power spectrum. In Chapter 12, I discuss the potential of using long time-averages of interferometric measurements to measure some component of the monopole moment of the sky. In Chapter 13, I present a new formalism for cross-correlating 21 cm emission and CMB anisotropies in Fourier space. Chapter 14 describes my initial investigations into utilizing deep learning techniques for recovering cosmological parameters from simulated EoR measurements. I conclude in Chapter 15.

# **Chapter 2**

## **Astrophysical Radiation**

# **Chapter 3**

## **Interferometry, Calibration & Polarimetry**

In this Chapter I wished to build a formalism around wide-field, polarized interferometric measurements that could be used throughout this work. Many traditional assumptions used in radio interferometry are broken in the case of the wide-field, fully-polarized, drift-scanning measurements native to interferometric EoR observations. In Section 3.1, I derive the equation describing the fundamental observable for an interferometer, called a “visibility”. Section 3.2, I describe calibration techniques relevant to this work and in Section 3.3 I review some of the implications of the previous two sections for polarized measurements.

For a comprehensive review of interferometry from a traditional perspective, see Thompson et al. (2017).

### **3.1 The Visibility Equation**

A radio interferometer (a term used interchangeably with “interferometric array” for radio observations) is an ensemble of receiving elements, where each element’s measurement is correlated with every other element’s. The simplest case is a two-element interferometer,

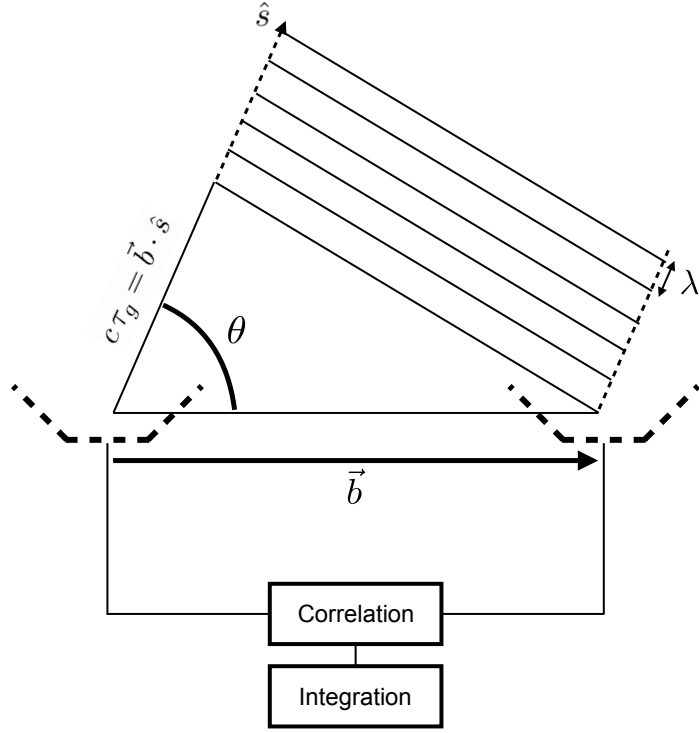


Figure 3.1: The geometry of a two-element interferometer, with a plane wave incident from direction  $\hat{s}$ .

which we will focus on below. We assume that the elements are coplanar and identical.

### 3.1.1 The Classical Visibility Equation

Consider two receiving elements  $i$  and  $j$ , separated by baseline vector  $\vec{b}$ . Suppose a plane wave of wavelength  $\lambda$  is incident upon these elements, with direction of propagation  $-\hat{s}$ . The geometry of this interferometer is illustrated in Figure 3.1.

We can define the electromagnetic wave to have a frequency dependent phase, such that the electric field measured by element  $i$  at time  $t$  is

$$E_i = E_0 e^{-2\pi i v t}. \quad (3.1)$$

The time difference between the arrival at  $i$  and  $j$  is called the “geometrical delay”,

$\tau_g$ :

$$\tau_g = \frac{\vec{b} \cdot \hat{s}}{c}, \quad (3.2)$$

and the electric field measured by element  $j$  is

$$E_j = E_0 e^{-2\pi i v(t+\tau_g)}. \quad (3.3)$$

An interferometer is an instrument which measured voltages induced by these electric fields, and correlates them together, integrating their product over some coherent time-scale. This correlation grants:

$$\langle E_i E_j^* \rangle = \lim_{T \rightarrow \infty} \frac{1}{2T} \int_{-T}^T E_i(t) E_j(t) dt = |E_0|^2 e^{-2\pi i v \tau_g} \quad (3.4)$$

where  $e^{-2\pi i v \tau_g} = e^{-2\pi i v \vec{b}_{ij} \cdot \hat{s}/c}$  is known as the “fringe” term, due to its sinusoidal nature. We can generalize this relationship to include more than a single plane wave from direction  $\hat{s}$ . Many plane waves, from all directions, can be incident upon the interferometer at a given time and frequency. We can represent the power distribution on the sky as  $S(\Omega)$ , where  $S(\Omega)$ . However, no instrument is equally sensitive to radiation from every direction  $\hat{s} \in \Omega$ . Instead, an instrument has some sensitivity pattern – a *beam pattern* – that tapers the power distribution on the sky into an “observed sky”,  $S'(\Omega) = A(\Omega)S(\Omega)$ .

These generalizations lead to the classical visibility equation:

$$V_{ij}(v) = \int A(\Omega, v) S(\Omega, v) e^{-2\pi i v \vec{b}_{ij} \cdot \hat{s}/c} d\Omega \quad (3.5)$$

for a “visibility” – the fundamental interferometric observable –  $V_{ij}$  as a function of frequency.

If we choose to represent the source direction in terms of directional cosines  $\ell$  and  $m$ , and represent the baseline vector in units of wavelengths,  $\vec{b}_{ij}/\lambda = (u, v, w)$ , we can perform a change of variables in Equation 3.5 to give

$$V_{ij}(u, v) = \int \int A(\ell, m) S(\ell, m) e^{-2\pi i(u\ell + vm + w\sqrt{1-\ell^2-m^2})} \frac{d\ell dm}{\sqrt{1-\ell^2-m^2}}. \quad (3.6)$$

This relationship is often simplified by assuming only a small area of the sky is under observation – that is, that  $A(\ell, m)$  falls-off steeply from zenith – and therefore  $\ell^2$  and  $m^2$  are small. This grants

$$V_{ij}(u, v) \approx e^{-2\pi iw} \int \int A(\ell, m) S(\ell, m) e^{-2\pi i(u\ell + vm)} d\ell dm, \quad (3.7)$$

which plainly casts  $V(u, v)$  as the Fourier transform of the observed sky if  $w$  is small: that is, the array is co-planar and no appreciable curvature of the sky is probed. Modern low frequency interferometers used in this work greatly violate this approximation, the consequences of which I will discuss in the proceeding sections.

Even though it is often violated, the Fourier relationship shown in Equation 3.7 is an extremely useful one to work with when translating between visibilities and images. Images can be created by inverse Fourier transforming all of the visibilities measured by an array. Following Equation 3.6, a reconstructed image  $\tilde{S}(\ell, m)$  is given by

$$\frac{A(\ell, m)\tilde{S}(\ell, m)}{\sqrt{1-\ell^2-m^2}} = \int \int \Xi(u, v)V(u, v)e^{2\pi iv(u\ell + vm)} du dv. \quad (3.8)$$

In Equation 3.8, we see that the reconstructed image  $\tilde{S}(\ell, m)$  is attenuated by the beam response  $A(\ell, m)/\sqrt{1-\ell^2-m^2}$ . The function  $\Xi(u, v)$  defines the sampling of the  $u, v$  - plane. It is equal to 1 at the points sampled by the interferometer (baselines of length and direction defined by the vector  $\vec{b} = (u, v)$  exist in the array) and 0 elsewhere. As an example, the “array” shown in Figure 3.1 would be described by a  $\Xi(u, v)$  function that was zero at all points except for a single  $(u, v)$  coordinate described by baseline vector  $\vec{b}$ .

The effect of the sampling function  $\Xi(u, v)$  is that the true sky  $S(\ell, m)$  can never be completely reconstructed, since it is impossible to build an interferometer that samples every  $u, v$  mode. The true sky is convolved with the Fourier transform of  $\Xi(u, v)$ , which astronomers refer to as the “dirty beam”.  $\Xi(u, v)$  contains zeros, so a complete deconvolution of  $\tilde{S}(\ell, m)$  is impossible.

We now note that an important aspect of light has been absent throughout the derivations above: the polarization state of the radio wave that induces the electric field in Equation 3.1. Interferometers are typically constructed with two feeds, sensitive to polarization states of an incident radio wave along two separate axes. In the case of all of the instruments used in this work (see Chapter 4), an antenna  $i$  had two dipole feeds perpendicular to one another. These were along the North-South direction ('n') and the East-West direction ('e'). We can attempt to generalize Equation 3.5 to include polarization, setting antenna  $i$  to have orientation  $p$  and antenna  $j$  to have orientation  $q$ ,  $p, q \in (e, n)$ :

$$V_{ij}^{pq} = \int A_{pq}(\Omega, v) S_{pq}(\Omega, v) e^{-2\pi i v \vec{b}_{ij} \cdot \hat{s}/c} d\Omega. \quad (3.9)$$

However, two aspects of this equation are unsatisfactory. As explored in Chapter 2, the polarized sky is defined with the four Stokes parameters; an " $S_{pq}$ " polarized sky does not exist. Likewise, a dipole is not purely sensitive to a single vector orientation from the sky, but probes a wide range of angles<sup>1</sup>. Therefore a  $A_{pq}$  polarized beam is ill-defined. These shortcomings lead us to rewrite the visibility equation, cohesively including polarization from the outset.

### 3.1.2 The Measurement Equation

The Radio Interferometric Measurement Equation (RIME) provides an extremely useful framework for describing wide-field polarized observations. Formulated by Hamaker et al. (1996), it was re-introduced to the radio astronomy community through a series of papers by O. M. Smirnov (Smirnov, 2011a,b,c,d). In this section I review the portions of his work most relevant to this thesis, and defer the reader to the series for a useful and thorough walk-through of wide-field radio interferometry and high dynamic-range calibration.

---

<sup>1</sup>In the case of the PAPER instrument, described in the next Chapter, the dipole feeds probed the entire hemisphere of the sky.

Returning to Equation 3.1, a radio wave incident on an antenna induces a voltage in along feed arm

$$\vec{E} = (e_p, e_q); \vec{v} = (v_p, v_q) = \mathbf{J}\vec{E} \quad (3.10)$$

where  $\mathbf{J}$  is a  $2 \times 2$  complex matrix termed the “Jones matrix” (Jones, 1941). Jones matrices represent linear transformations along the signal path, from the emission of the radio wave onwards. Multiple stages along the signal propagation can be represented by multiplying different Jones matrices together as a “Jones chain”, which may be expanded or collapsed as convenient.

Interferometric visibilities are pairwise correlations of the components of  $\vec{v}$  between antennas  $i$  and  $j$ , integrated over some small time span (Equation 3.4), which we can represent hold in matrix form (the layout of which will become clear in a moment):

$$\mathbf{V}_{ij} = \begin{pmatrix} \langle v_i^p v_j^{p*} \rangle & \langle v_i^p v_j^{q*} \rangle \\ \langle v_i^q v_j^{p*} \rangle & \langle v_i^q v_j^{q*} \rangle \end{pmatrix} = \langle \vec{v}_i \vec{v}_j^H \rangle. \quad (3.11)$$

Above,  $H$  represents the Hermitian transpose operation.

Using this formalism allows us to map the emitted electric field to the observed visibilities,

$$\mathbf{V}_{ij} = \mathbf{J}_i \begin{pmatrix} \langle e_i^p e_j^{p*} \rangle & \langle e_i^p e_j^{q*} \rangle \\ \langle e_i^q e_j^{p*} \rangle & \langle e_i^q e_j^{q*} \rangle \end{pmatrix} \mathbf{J}_j^H = \mathbf{J}_i \mathbf{C}_{ij} \mathbf{J}_j^H \quad (3.12)$$

where  $\mathbf{J}_{i,j}$  may be Jones chains of arbitrary length. We have assumed instrument stability to move them out of the time averages in the central matrix. We refer to  $\mathbf{C}_{ij}$  as the “coherency matrix”.

In Chapter 2 the Stokes parameters we introduced. Hamaker & Bregman (1996) showed that the components of the coherency matrix are closely related to the Stokes parameters:

$$\begin{pmatrix} \langle e_i^p e_j^{p*} \rangle & \langle e_i^p e_j^{q*} \rangle \\ \langle e_i^q e_j^{p*} \rangle & \langle e_i^q e_j^{q*} \rangle \end{pmatrix} = \begin{pmatrix} I+Q & U+iV \\ U-iV & I-Q \end{pmatrix}. \quad (3.13)$$

The Jones formalism allows for a construction of the visibility equation that does not make explicit assumptions regarding polarization or field-of-view, in which we can map the Stokes parameters into the instrumental basis that visibilities are computed in:

$$\mathbf{V}_{ij} = \int \mathbf{J}_i(\hat{s}) \mathbf{C}_{ij}(\hat{s}) \mathbf{J}_j^H(\hat{s}) e^{-2\pi i v \vec{b}_{ij} \cdot \hat{s}/c} d\Omega, \quad (3.14)$$

which Smirnov (2011a) refers to as the “Full Sky Radio Interferometric Measurement Equation”<sup>2</sup>. Note that all of these quantities are functions of frequency as well, in general.

So far, the formalism shown has used the  $2 \times 2$  “Jones basis”. It is sometimes more useful to work in the  $4 \times 4$  “Mueller basis” (Mueller, 1948), which acts on visibilities in  $4 \times 1$  vector form:

$$\begin{pmatrix} V^I \\ V^Q \\ V^U \\ V^V \end{pmatrix} = \mathbf{S} \vec{\mathbf{V}}_{ij} = \begin{pmatrix} 1 & 0 & 0 & 1 \\ -1 & 0 & 0 & 1 \\ 0 & 1 & 1 & 0 \\ 0 & -i & i & 0 \end{pmatrix} \begin{pmatrix} V^{pp} \\ V^{pq} \\ V^{qp} \\ V^{qq} \end{pmatrix}. \quad (3.15)$$

It is important to note that Equation 3.15 lists a vector of “Stokes-polarized visibilities” on the left-hand side, whereas Equation 3.13 shows that the coherency matrix contains linear combinations the Stokes parameters. This is not an inconsistency. While visibilities are quantities that are integrated over the sky, the Stokes parameters are only defined *on* the sky. One must transform the visibilities from the *uv*-plane onto the image-plane and deconvolve the beam in order to measure the Stokes parameters. Instead, linear combinations of visibilities measure a proxy for each the Stokes parameters. To make the inequality between visibilities and Stokes parameters explicit, I will refer to the “Stokes-polarized visibilities” as “pseudo-Stokes visibilities” from now on.

One can translate between these two formalisms using the definition of  $\vec{\mathbf{V}}_{ij}$  (c.f. Equation 3.10),

---

<sup>2</sup>We choose to explicitly show the exponent in this formulation for ease of comparison with Equation 3.5. Smirnov (2011a) shows that this term can written as a “phase delay Jones matrix” and absorbed into the Jones chain.

$$\vec{V}_{ij} = (\mathbf{J}_i \otimes \mathbf{J}_j^H) (\vec{E} \otimes \vec{E}^H). \quad (3.16)$$

Comparison of Equation 3.5 and 3.14 shows that the Jones chain must, at the very least, encapsulate the beam pattern of the instrument. We can build such a Jones matrix by considering the response of feed  $p$  on antenna  $i$  to an electric field from infinity in the direction  $(\theta, \phi)$ :

$$\vec{A}_i^p(\hat{s}) = A_{i,\theta}^p(\hat{s})\hat{\theta} + A_{i,\phi}^p(\hat{s})\hat{\phi}, \quad (3.17)$$

where we have suppressed the frequency dependence. The antenna patterns may be written as components of a “Beam Jones matrix” for an antenna,

$$\mathbf{J}_i^B(\hat{s}) = \begin{pmatrix} A_{i,\theta}^p(\hat{s}) & A_{i,\phi}^p(\hat{s}) \\ A_{i,\theta}^q(\hat{s}) & A_{i,\phi}^q(\hat{s}) \end{pmatrix}. \quad (3.18)$$

These are the essential components for understanding the fundamental measurement performed by an interferometer. However, there are several effects one must take into account for the equations to truly reflect an interferometric measurement; effects such as instrumental gains, reflections between antennas, Faraday rotation in the ionosphere, etc. Most importantly, we must consider how these factors affect the measurement of polarization.

## 3.2 Calibration Techniques

The purpose of calibration is to remove effects of the instrument and the atmosphere from the data. Visibilities are measured in “data units”. That is, a given feed on an antenna will record some measurement of power, but some scalar conversion factor is required to calibrate that power to units of flux density. As visibilities measure the pairwise correlations of antenna powers, the estimation of the calibration factors can quickly become difficult as the number of antennas increases. In this Section we explain different approaches to such a challenge.

### 3.2.1 Diagonal and off-diagonal calibration

The calibration term that converts the power measured by an antenna to physical units is referred to as the “antenna gain”. This may be summarized per feed as a direction-independent “Gain Jones matrix”,

$$\mathbf{J}_i^G = \begin{pmatrix} g_i^p & 0 \\ 0 & g_i^q \end{pmatrix}, \quad (3.19)$$

where we have suppressed the frequency dependence. The components of  $\mathbf{J}_i^G$  are complex numbers, the argument of which represents instrumental phase, and the modulus represents instrumental amplitude. Note that this formulation of  $\mathbf{J}_i^G$  is only appropriate for linear antenna feeds. Circular feeds, which we will not comment on for the rest of this work, require an additional rotation matrix applied to move from a linear to a circular polarization frame.

Unfortunately, a direction-independent scaling is not the only term that requires estimation. As Equation 3.18 makes clear, a given feed is not receptive to a single plane of polarization. In general, we expect some fraction of power measured by feed  $p$  to be transferred into feed  $q$  via imperfect electronics (clever feed designs can attempt to minimize this effect, e.g. Parashare & Bradley, 2006; Parsons et al., 2010). This kind of power leakage is described by an off-diagonal matrix, and the components are known as “ $D$ -terms”,

$$\mathbf{J}_i^D = \begin{pmatrix} 1 & D_i^p \\ D_i^q & 1 \end{pmatrix}. \quad (3.20)$$

$D$ -terms are often left un-calibrated, as they are generally a few percent of the gain term for a given feed. However, a  $\sim 5\%$  error in calibration could represent an error large enough to inhibit an EoR detection. Unless an EoR instrument is shown to have very low  $D$ -terms, they must be taken in to account.

### 3.2.1.1 Ionospheric effects

Chapter 8 details the importance of the ionosphere for EoR measurements. Briefly put, the ionosphere is an upper layer of the Earth's atmosphere; an ionized plasma formed from solar radiation. Coupled with the Earth's magnetic field, it becomes a time- and position-variable Faraday screen (see Chapter 2) capable of rotating the polarization axis of an incident electromagnetic wave. This adds an additional term to the Jones chain in Equation 3.14. Representing the ionospheric Faraday screen as  $\Phi(\hat{s}, t)$ , this term is

$$\mathbf{J}_i^I = \begin{pmatrix} \cos(2\Phi(\hat{s}, t)c^2/v^2) & \sin(2\Phi(\hat{s}, t)c^2/v^2) \\ -\sin(2\Phi(\hat{s}, t)c^2/v^2) & \cos(2\Phi(\hat{s}, t)c^2/v^2) \end{pmatrix}. \quad (3.21)$$

The ionosphere's effect on polarized radiation is the most important one to consider for this work. However, the more commonly worried-about effect of the ionosphere (among radio astronomers) is its diffractive property. Neglecting the Earth's magnetic field, the refractive index  $\eta$  of a cold, collisionless plasma is (Thompson et al., 2017)

$$\eta = \sqrt{1 - \frac{v^2}{v_P^2}}, \quad (3.22)$$

for an electromagnetic wave of frequency  $v$  and plasma frequency  $v_P$ , given by

$$v_P = \frac{1}{2\pi} \sqrt{\frac{n_e e^2}{m_e \epsilon_0}} \quad (3.23)$$

where  $n_e$  is the number density of electrons,  $e$  and  $m_e$  are the electron charge and mass and  $\epsilon_0$  is the permittivity of free space. This term is typically of the order of a few MHz (Vedantham & Koopmans, 2015). This causes a direction- and time-dependent phase shift in the propagating wave. This shift is

$$\gamma(\hat{s}, v) = \int dl \frac{2\pi v}{c} \eta(\hat{s}) \approx \int dl \frac{2\pi v}{c} - \frac{1}{2} \int dl \frac{2\pi v_P^2}{cv} \quad (3.24)$$

where  $l$  is the distance through the ionosphere, and we have Taylor-expanded Equation 3.22 for the approximation. This effect can be represented as a diagonal, direction-dependent Jones matrix,

$$\mathbf{J}_i^{\Gamma}(\hat{s}, v) = \begin{pmatrix} \exp(i\gamma(\hat{s}, v)) & 0 \\ 0 & \exp(i\gamma(\hat{s}, v)) \end{pmatrix}, \quad (3.25)$$

where we have made the frequency dependence explicit.

Due to the turbulent nature of the ionosphere, both of these terms are extremely difficult to calibrate (Intema et al., 2009; Vedantham & Koopmans, 2015). In Chapter 8, we present the effects *not* calibrating the polarized component when averaging together large numbers of polarized visibilities.

### 3.2.2 Image-based calibration

Traditionally, the approach taken for estimating the components of all of the above was to observe a calibration source. A calibrator source would be unresolved, such that its position and phase is a direct measure of ionospheric diffraction and instrumental phase. Deviation from its catalogued position can be subtracted off, calibrating the phase (the argument of the components of  $\mathbf{J}_i^G$ ; Equation 3.19). For an interferometer that cannot point in a given direction, but instead “drift-scans”, observing the sky as the Earth rotates, calibration takes place when the calibrator source is at zenith (for a telescope that can point, the calibrator source would be observed in the center of the field-of-view). With a well-catalogued flux density and minimal beam attenuation, the amplitude of the visibility can be scaled appropriately to estimate the moduli of instrumental gains.

If the polarization state of the calibration source was known (and non-zero), forming Stokes parameters in the image plane can provide a measure of instrumental polarization, as gain errors and  $D$ -terms move power between the Stokes parameters (see Section 3.3 and Chapter 7). If the calibration source is known to be unpolarized, then the same method can be used to place a limit on the  $D$ -term magnitudes by maximizing Stokes I while minimizing Stokes Q, U and V.

The approach described above is only as good as the sky and instrument models used, as one must “simulate” the expected visibilities for a given sky model passing over a simulated instrument. For the wide field-of-view observations that are native to low-

frequency instruments, obtaining a sky model that accurately describes the point sources and diffuse structure on the sky is a daunting task. Barry et al. (2016) included the 4,000 brightest catalog sources in their sky (unpolarized) model of the one of the Murchinson Widefield Array’s (MWA; see Chapter 4) EoR observation fields, but this granted insufficient dynamic range to allow for an EoR measurement. They found too much contamination from a large population of faint, unmodelled point sources.

### 3.2.3 CLEAN

An uncalibrated array is one where the power in the  $uv$ -plane is incorrectly distributed. Transforming an uncalibrated  $uv$  distribution to the image plane will result in power scattered throughout the image plane; this is referred to as a “dirty image”. By precisely calibrating visibility complex gains (etc.), one is in effect rearranging the power distribution on the sky into the distribution astrophysical sources. An accurate calibration is one that does so and reproduces the flux density measured by other studies.

To perform an image-based calibration, one must be able to move easily between the  $uv$  and image planes. There are two major challenges in doing so: the limited distribution of spatial scales probed by an interferometer, as encapsulated by the  $\Xi(u,v)$  sampling function, and errors in instrumental calibration. The former challenge can be faced by using deconvolution techniques that estimate the missing information, known under the umbrella term of “CLEANing algorithms”. The latter can be faced by precise calibration – in which an image can be of great utility to iterate upon.

#### 3.2.3.1 Högbom’s algorithm

Högbom (1974) devised the first deconvolution algorithms to become widely used by the radio astronomy community, known as CLEAN. It is an iterative numerical deconvolution process applied in the image plane, based on the assumption that the sky is composed of a distribution of point sources<sup>3</sup>.

---

<sup>3</sup>In the era of wide field-of-view instruments, many more accurate and precise deconvolution algorithms

The Högbom algorithm proceeds as follows:

1. Compute the amplitude and position of the point of greatest intensity (the ‘peak’) in the dirty image.
2. Subtract from the dirty image, at the position of the peak, the peak strength multiplied by the dirty beam pattern (recall that the dirty beam is the Fourier transform of  $\Xi(u, v)$ ) and a factor  $\gamma \leq 1$  (the ‘loop gain’). Record the position and amplitude of the subtracted component, as this will form the model that will become the CLEANed image.
3. Repeat Steps 1 & 2 iteratively until all significant structure has been removed from the image (where the value of ‘significance’ is set by the astronomer). This may be constrained to ‘CLEAN-windows’ within a larger image.
4. Convolve the accumulated point model with a ‘CLEAN beam’, usually a Gaussian with Full-Width Half-Max equal to the central lobe of the dirty beam. This is the ‘CLEAN image’
5. Add the residuals of the dirty image to the CLEAN image.

An example of different CLEANing stages is shown in Figure 3.2.

A major shortcoming of the Högbom algorithm is its proliferation of small-scale structures around the locations of point sources. This is because the subtraction in Step 2, above, leaves new, local maxima around the perimeter of subtracted region. Later deconvolution algorithms, such as the one devised by Cornwell (1983), avoid this by padding the surrounding region according to an additional smoothness parameter.

Imaging with extremely wide field-of-view instruments is explored in Chapter 7.

---

have been developed that are able to calibrate images of diffuse structures, rather than point sources. There are also many other algorithms besides Högbom’s that focus on point sources, such as Clark or Cotton-Schwab. However, for the purposes of this descriptive chapter, we focus on the Högbom CLEAN.

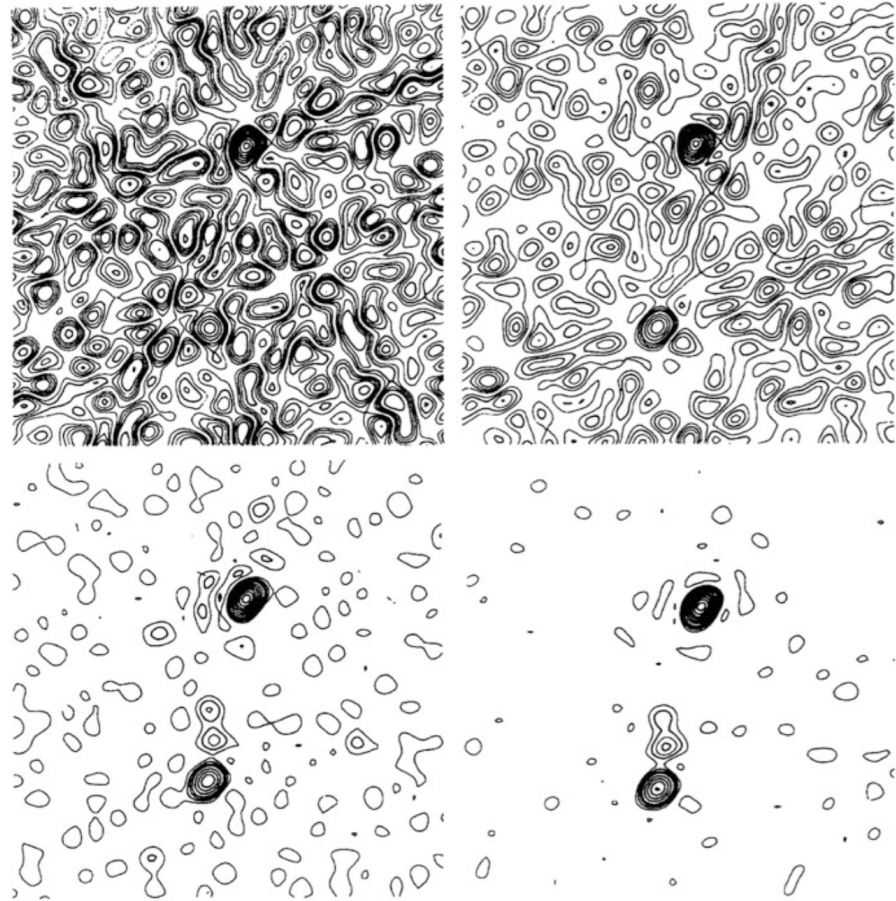


Figure 3.2: Four stages of the Högbom CLEAN, as implemented on data from the Green Bank Interferometer. The top left panel shows the dirty image, with power scattered throughout the image plane. The top right panel shows the image after a single iteration with  $\gamma = 1$ . The bottom left and bottom right panels show the image after two and six iterations, respectively. Contours are steps of 5% from the maximum in each image. Figure taken from Högbom (1974); Thompson et al. (2017).

### 3.2.3.2 Delay Transforms and the 1D-CLEAN

There are a variety of CLEANing techniques that are central to this thesis, but do not operate on images at all. Parsons & Backer (2009) and Parsons et al. (2012b) introduced the 1D-CLEAN, a deconvolution algorithm that operates on visibilities Fourier-transformed along the frequency axis, never gridding them on the  $uv$ -plane. Much more about Fourier-transformed visibilities will be spoken of throughout this work, and we discuss the basic points here.

A Fourier transform along the frequency axis of a visibility is called a ‘delay transform’. This nomenclature comes from the fact that Fourier conjugate of frequency is a quantity in units of time – and the correct interpretation of this value is the time delay between a wavefront incident upon antenna  $i$  and  $j$ . The delay  $\tau_g$  of a source at (R.A.,Dec.)=( $\alpha, \delta$ ) is

$$\tau_g = \frac{\vec{b}}{c} \cdot \begin{pmatrix} \cos \delta \cos(h - \alpha) \\ -\cos \delta \sin(h - \alpha) \\ \sin \delta \end{pmatrix}, \quad (3.26)$$

for local sidereal time  $h$ . This value can be isolated in “delay space” via a delay transform (where it is convenient to use the classical visibility equation for clarity, but all steps can be folded into the Jones formalism),

$$\begin{aligned} \tilde{V}_{ij}(\tau, t) &= \int d\nu g_i^*(\nu, t) g_j(\nu, t) V_{ij}(\nu, t) e^{2\pi i \nu \tau} \\ &= \int \tilde{g}_i(\tau, t)^* \tilde{g}_j(\tau, t) * \sum_n^N [\tilde{A}(\tau, \hat{s}_n(t)) * \tilde{S}_n(\tau) * \delta_D(\tau_g + \tau_{e,i,j} - \tau)] \end{aligned} \quad (3.27)$$

which is true for any polarization, so we have dropped our polarization indexing. Like the Högbom algorithm, this explicitly assumes the sky can be expressed by  $N$  point sources at positions  $\hat{s}_n$ . Instrumental absolute gains and phases are expressed as  $g_i, g_j$  and  $\tau_{e,i,j} = \tau_j - \tau_i$ . Clearly, this procedure isolates a source  $n$  as a delta function with amplitude  $\tilde{S}_n$  at a given delay (assuming a smooth spectrum; see below), convolved by a kernel that describes the chromaticity of the instrument. If the instrument is designed to have a

smooth frequency response, the  $\tilde{g}_{i,j}(\tau)$  and  $\tilde{A}(\tau)$  terms will be narrow functions in delay space and the value of  $\tau_g + \tau_{e,i,j}$  will be well-constrained. If the instrument has an unsmooth spectral response, many more  $\tau$ -modes will be required to describe it, resulting in a spread of power in delay space.

Figure 3.3 shows a graphical representation of a two-source sky model mapping from celestial coordinates to delay space. Note that the delay transform is not a one-to-one mapping – sources in a plane perpendicular to the baseline vector share the same  $\tau_g$ . Dotted lines in the delay-space plot demarcate an extremely important value of  $\tau$ . A given baseline will have a *maximum delay value*,  $\tau_{\max} = |b|/c$ , the light travel time between the antennas. With sufficient bandwidth and frequency resolution, this boundary can be clearly resolved, and all sources with smooth spectra (as is the case for unpolarized synchrotron radiation, but not for Faraday rotated polarized radiation or HI; see Chapter 2 and almost all of Part II) will have their maximum power values within the  $-\tau_{\max} \leq \tau \leq \tau_{\max}$  region.

By delay-transforming simulated visibilities with a simple sky model of the brightest sources and comparing to an observed sky with those sources close to zenith, one can estimate the instrumental delays and gains and obtain a delay-based calibration for  $\mathbf{J}_i^G$ . However, Fourier-transforming along an axis with discontinuities – such as spikes or divets caused by Radio Frequency Interference (RFI) and its subsequent flagging – will result in sinc-like side lobes throughout delay space. Some interpolation is required to bridge these gaps, presented in Parsons & Backer (2009) as the complex 1D-CLEAN. The algorithm proceeds as follows:

1. Delay-transform the visibility containing nulled frequency channels – this is the “dirty image”.
2. As in the Högbom algorithm, iteratively propagate the largest magnitude feature, by  $\tau$  bin, to a model after convolving it with the Fourier transform of the flags themselves – this is the “dirty beam”.

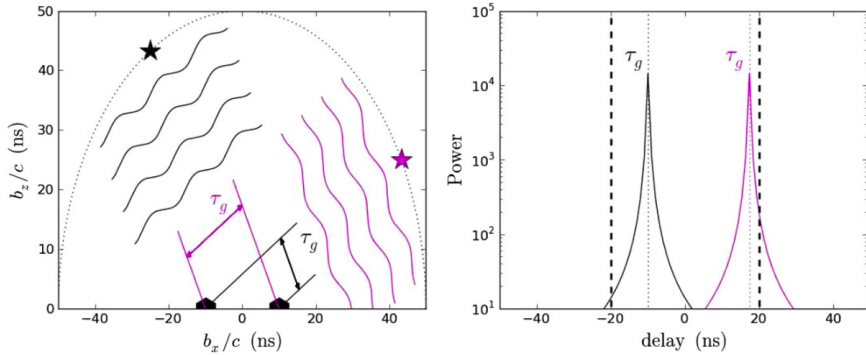


Figure 3.3: A graphical representation of the delay transform. The left panel shows the relationship between celestial position and geometrical delay relative to a 60 m baseline (which has a  $\sim 20$  ns light-travel-time between antennas). The right panel shows an example delay transform of the visibilities recorded by this model interferometer. With perfect phase calibration, power from the sources is isolated to their geometrical delay, with some spread in delay space due to the chromaticity of the instrument. Figure taken from Parsons et al. (2012b).

3. Stop when the residual power in delay space is beneath some defined threshold.  
Add this residual power to the model.

The importance of the delay transform for EoR studies is discussed in Chapter 5, and a variant of it is presented in Chapter 11.

### 3.2.4 Redundant calibration

Thus far we have discussed calibration techniques that require some model of the sky to begin with. For an interferometer without any repeated baseline vectors, these methods are sufficient. However, some EoR studies, such as those discussed in this thesis, have opted to construct highly redundant arrays, with many repeated baselines. Such interferometers sample comparatively few modes of the  $uv$ -plane, leading to poor images – but their visibilities can be averaged together in order to reduce noise for EoR measurements on specific spatial scales.

We defer detailed discussion of redundant calibration to Chapter 7, but provide a brief overview here (studies that explore this technique in depth include Wieringa (1992); Liu et al. (2010); Zheng et al. (2014) and Dillon et al. (2017)). In a redundant array, there are several examples of a given “visibility type”. Assuming the antennas have identical beams (understanding non-redundant beams is a contemporary effort), the only difference between the visibilities should be due to their complex gains. For a visibility type  $V_{|i-j|}^{pq}(\nu, t)$ , all baselines with baseline vector  $\vec{b}_{|i-j|}$  may be described as

$$V_{ij}(\nu, t) = g_i^p(\nu, t)g_j^q(\nu, t)V_{|i-j|}^{pq}(\nu, t) + n_{ij}(\nu, t), \quad (3.28)$$

where the  $n_{ij}$  term represents noise on that visibility. For a redundant array, this system of equations is highly overdetermined to solve for  $g_i^p$  and  $g_j^q$ , as long as  $V_{|i-j|}^{pq}$  can be formed (this can simply be the median of all of the visibilities of that type in the data). Again, for a fuller mathematical overview we defer to Chapter 7.

We have made the frequency and time dependence explicit in order to emphasize that the complex gains can be solved-for each every frequency, time sample. This is unlike the delay transform (which requires a frequency bandwidth to transform over) or imaging calibration (which can in principle be implemented per-time and frequency, but is difficult due to the resultant very noisy dirty images).

Using redundant calibration, when available, can reduce the number of diagonal gains to solve for from  $\frac{1}{2}N_{\text{ants}}(N_{\text{ants}} - 1)$  to just a few unknowns. These unknowns are degeneracies of the system of equations defined in Equation 3.28, and arise from the fact that no information from the sky is required to obtain diagonal gains that are self-consistent between antennas. For the simplest implementation of such a system, as presented in Zheng et al. (2014), there are four degeneracies per feed arm (so eight overall). These are:

- Overall amplitude scaling (to obtain the correct flux density of the sky),
- Overall phasing (an arbitrary additional phase ramp),

- Phasing along the  $\hat{\theta}$  direction (correct positions on the sky),
- Phasing along the  $\hat{\phi}$  direction (correct positions on the sky).

These additional parameters can be obtained by making an image of a calibration field – no CLEANing should be required, since power should be self-consistently distributed in the  $uv$ -plane – where the sky will likely be incorrectly centered and of incorrect amplitude.

### 3.3 Instrumental Polarization

An interferometer is capable of measuring pseudo-Stokes visibilities, which contain components of Stokes power, somehow convolved by the instrumental response. Understanding this instrumental response is crucial for performing polarimetry at low frequencies. As we will see, the instrument will inherently ‘leak’ power between polarizations in direction dependent (effects that occur inside the visibility integral) and independent (outside of the visibility integral) ways. These leakage modes must be well-understood in order to make any statements about the nature of the polarized sky.

Synthesizing the Jones formalism introduced in Section 3.1 and the calibration terms in Section 3.2, we seek to understand how the Jones chain,

$$\mathbf{J}_i = \mathbf{J}_i^D(v) \mathbf{J}_i^G(v) \mathbf{J}_i^I(\hat{s}, v) \mathbf{J}_i^\Gamma(\hat{s}, v) \mathbf{J}_i^B(\hat{s}, v), \quad (3.29)$$

influences the power in pseudo-Stokes visibilities.

#### 3.3.1 Direction-Dependent Leakage

The direction-dependent terms in the Jones chain concern the beam, and ionospheric effects. In this section, we will concentrate on the beam Jones matrix – the ionospheric effects are discussed in detail elsewhere (e.g. Intema et al., 2009; Vedantham & Koopmans, 2015, 2016, [Martinot et al. \(in prep.\)](#)).

Unless  $\mathbf{J}_i^B(\hat{s}, v)$  is both diagonal and, at any given point on the sphere, the diagonal elements are equal, there will be mixing or “leaking” of different Stokes parameters together into each element of  $\mathbf{V}_{ij}$  in a direction dependent way (e.g. Geil et al., 2011; Smirnov, 2011a,b; Nunhokee et al., 2017). Focusing on pseudo-Stokes I and neglecting other Jones terms for a moment,

$$\begin{aligned} V_{ij}^I(v) &= \text{Tr}(\mathbf{V}_{ij}) = \int \text{Tr}(\mathbf{J}_i^B \mathbf{C}_{ij} \mathbf{J}_j^{BH}) \exp(-2\pi i v \vec{b} \cdot \hat{s}/c) d\Omega \\ &= \int \mathbf{M}_{00} I + \mathbf{M}_{01} Q + \mathbf{M}_{02} U + \mathbf{M}_{03} V \exp(-2\pi i v \vec{b} \cdot \hat{s}/c) d\Omega \end{aligned} \quad (3.30)$$

where I, Q, U and V are the true Stokes sky and are functions of direction and frequency, and the  $\mathbf{M}_{ab}$  terms are components of the direction dependent instrumental Mueller matrix, also functions of direction and frequency:

$$\mathbf{M}_{ab}(\hat{s}, v) = \text{Tr}(\sigma_a \mathbf{J}_i^B \sigma_b \mathbf{J}_j^{BH}) \quad (3.31)$$

and  $\sigma_k$  are the Pauli matrices, where the indices are reordered from the quantum mechanical convention such that

$$\sigma_0 = \begin{pmatrix} 1 & 0 \\ 0 & 1 \end{pmatrix}, \sigma_1 = \begin{pmatrix} 1 & 0 \\ 0 & -1 \end{pmatrix}, \sigma_2 = \begin{pmatrix} 0 & 1 \\ 1 & 0 \end{pmatrix}, \sigma_3 = \begin{pmatrix} 0 & -i \\ i & 0 \end{pmatrix} \quad (3.32)$$

$$V^I = \text{Tr}(\sigma_0 \mathbf{V}), V^Q = \text{Tr}(\sigma_1 \mathbf{V}), V^U = \text{Tr}(\sigma_2 \mathbf{V}), V^V = \text{Tr}(\sigma_3 \mathbf{V}).$$

Equation 3.30 explicitly shows that the pseudo-Stokes I visibility is inherently composed of the weighted sum of all of the Stokes parameters, where the weighting is direction- and frequency-dependent, given by the Mueller terms  $\mathbf{M}_{ab}(\hat{s}, v)$  in Equation 3.31. In turn, the  $\mathbf{M}_{ab}(\hat{s}, v)$  terms are completely determined by the beam Jones matrix; a collection of complex voltage beam patterns. With a simulated instrument, one can obtain the  $4 \times 4$   $\mathbf{M}(\hat{s}, v)$  matrix and model the contribution of each Stokes parameter to each pseudo-Stokes visibility. The key to such a Mueller matrix is

$$\mathcal{M}_{ab}(\hat{s}, v) = \begin{pmatrix} I \rightarrow V^I & I \rightarrow V^Q & I \rightarrow V^U & I \rightarrow V^V \\ Q \rightarrow V^I & Q \rightarrow V^Q & Q \rightarrow V^U & Q \rightarrow V^V \\ U \rightarrow V^I & U \rightarrow V^Q & U \rightarrow V^U & U \rightarrow V^V \\ V \rightarrow V^I & V \rightarrow V^Q & V \rightarrow V^U & V \rightarrow V^V \end{pmatrix} \quad (3.33)$$

Fagnoni & de Lera Acedo (2016) simulated the feed, faceted parabolic dish and analog signal chain for the Hydrogen Epoch of Reionization Array (HERA) instrument using the CST<sup>4</sup> package. They generated the  $\vec{E}$ -field receptivity patterns that could be used to form  $\mathbf{J}_i^B$  and  $\mathbf{M}(\hat{s}, v)$ . Examples of  $\mathbf{M}(\hat{s}, v)$  at 120 MHz and 160 MHz are shown in Figure 3.4, projected in the R.A., Dec. basis. Note that this basis has a singularity at the South Pole, leading to wide-field asymmetries in components to do with Stokes Q and U. Due to the large spread in dynamic ranges between  $\mathbf{M}_{00}$ , other diagonal terms, and off-diagonal terms, we use separate color maps for each. All of the dynamic ranges are normalized to the peak of  $\mathbf{M}_{00}$ , which is 1 at zenith. The off-diagonal terms are 2- to 8-orders of magnitude less than the diagonal terms.

As discussed in Chapter 2, at the low frequencies and large scales relevant to EoR experiments, the Stokes I sky is extremely bright compared to the other Stokes parameters, and few polarized point sources have been found. This makes the first column of  $\mathbf{M}(\hat{s}, v)$ , representing  $I \rightarrow V^I V^Q V^U V^V$  the most interesting for characterizing the polarized response of an instrument observationally. It can be reasonably expected that even a small amount of leakage from Stokes I into the other Stokes parameters will dominate over Stokes Q, U and V power alone.

Deconvolution of  $\mathbf{M}(\hat{s}, v)$  for wide field-of-view instruments is not at all a solved problem, with contemporary studies “learning to live with it”. Hypothetically, with accurate polarized sky and instrument models, one could use the linear nature of the Jones formalism to compute each “visibility component”,

$$\hat{V}_{ij}^{ab} = \int \mathbf{M}_{ab}(\hat{s}, v) S_P(\hat{s}, v) \exp(-2\pi i v \vec{b} \cdot \hat{s}/c) d\Omega, \quad (3.34)$$

---

<sup>4</sup>[www.cst.com](http://www.cst.com)

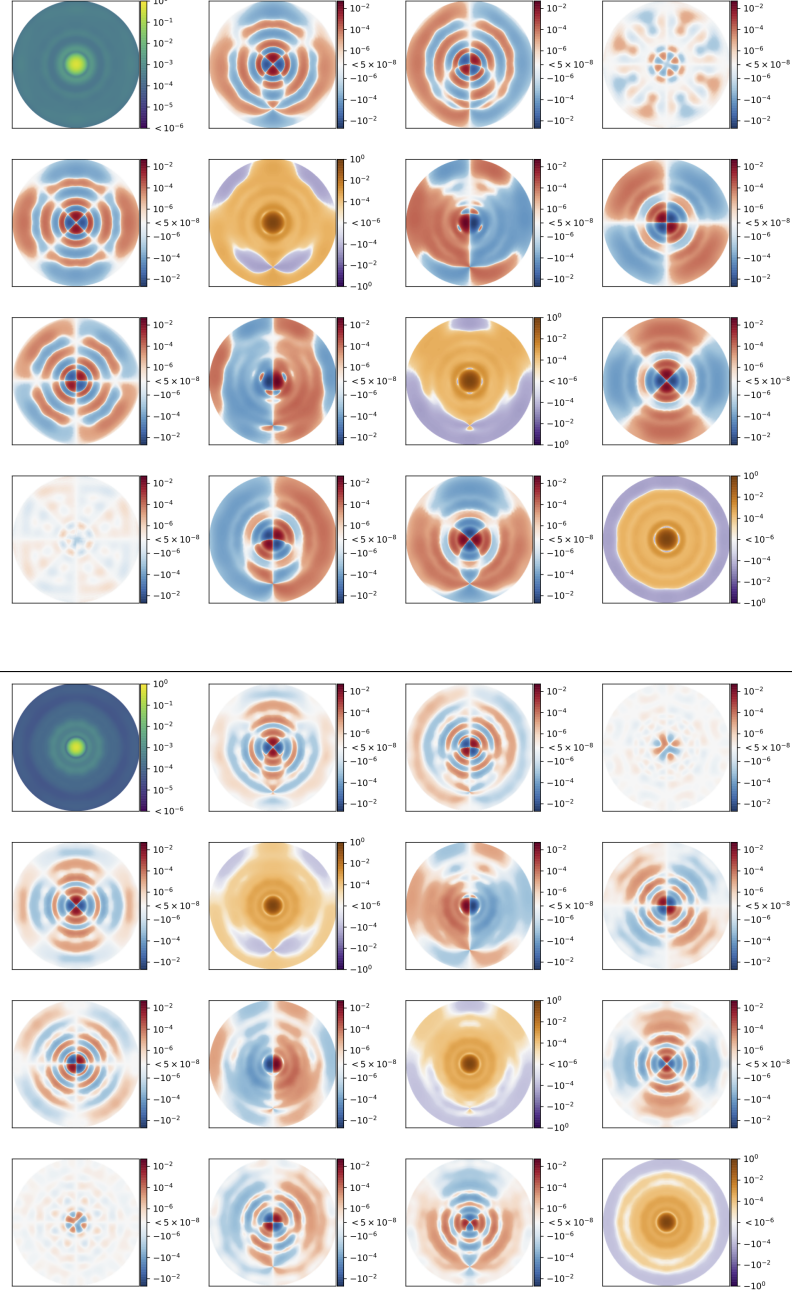


Figure 3.4: Simulations of the instrumental direction dependent Mueller matrix at 120 MHz and 160 MHz (*above* and *below*, respectively) projected into the RA, Dec basis. Color scales for frequencies are relative to the peak of  $\mathbf{M}_{00}$  (which itself is normalized to 1 at zenith). To account for the wide variety of dynamic ranges required to show detail, we use separate color maps for  $\mathbf{M}_{00}$ , diagonal, and off-diagonal terms. The off-diagonal terms are 2- to 8-orders of magnitude less than the diagonal terms. For a key to these matrices, see Equation 3.33.

where  $S_P \in (I, Q, U, V)$ . Subtracting the additional components from a given pseudo-Stokes visibility could isolate that Stokes parameter. While accurate instrument models are presently becoming available (see Chapter 10 for verification of the simulations shown in Figure 3.4, at least for pseudo-Stokes I), verifying the accuracy of such a method would require precise expectations of the nature of the low frequency polarized sky. At the time of writing, this is only beginning to become clear through polarized sky surveys from the Low Frequency Array (LOFAR; e.g. Van Eck et al. (2018)) and the MWA (e.g. Lenc et al., 2016, 2017).

### 3.3.2 Direction-Independent Leakage

In addition to the mixing of Stokes parameters due to the primary beam, it is possible to mix them in a direction independent way. Calibration errors – errors in the estimation of the components of  $\mathbf{J}_i^D(v)$  and  $\mathbf{J}_i^G(v)$  – are capable of leaking signal between pseudo-Stokes visibilities independent of the sky. Writing the gains as  $g_i^p(v) + \delta g_i^p(v)$ , and  $\mathbf{J}_i(v) = \mathbf{J}_i^D(v)\mathbf{J}_i^G(v)$ , a direction-independent Mueller matrix may be composed (Thompson et al., 2017):

$$\mathbf{M}'(v) = \mathbf{J}_i(v) \otimes \mathbf{J}_j^H(v) \quad (3.35)$$

such that

$$\begin{pmatrix} V'_I \\ V'_Q \\ V'_U \\ V'_V \end{pmatrix} = (\mathbf{I} - \frac{1}{2}\delta\mathbf{M}') \begin{pmatrix} V_I \\ V_Q \\ V_U \\ V_V \end{pmatrix} \quad (3.36)$$

where

$$\delta\mathbf{M}' = \begin{pmatrix} \delta g_i^p + \delta g_i^q + \delta g_j^{p*} + \delta g_j^{q*} & \delta g_i^p - \delta g_i^q + \delta g_j^{p*} - \delta g_j^{q*} & D_i^p - D_i^q + D_j^{p*} - D_j^{q*} & -\mathbf{i}(D_i^p + D_i^q - D_j^{p*} - D_j^{q*}) \\ \delta g_i^p - \delta g_i^q + \delta g_j^{p*} - \delta g_j^{q*} & \delta g_i^p + \delta g_i^q + \delta g_j^{p*} + \delta g_j^{q*} & D_i^p + D_i^q + D_j^{p*} + D_j^{q*} & -\mathbf{i}(D_i^p - D_i^q - D_j^{p*} + D_j^{q*}) \\ D_i^p - D_i^q + D_j^{p*} - D_j^{q*} & -(D_i^p + D_i^q + D_j^{p*} + D_j^{q*}) & \delta g_i^p + \delta g_i^q + \delta g_j^{p*} + \delta g_j^{q*} & \mathbf{i}(\delta g_i^p - \delta g_i^q - \delta g_j^{p*} + \delta g_j^{q*}) \\ -\mathbf{i}(D_i^p + D_i^q - D_j^{p*} - D_j^{q*}) & -\mathbf{i}(D_i^p - D_i^q - D_j^{p*} + D_j^{q*}) & \mathbf{i}(\delta g_i^p - \delta g_i^q - \delta g_j^{p*} + \delta g_j^{q*}) & \delta g_i^p + \delta g_i^q + \delta g_j^{p*} + \delta g_j^{q*} \end{pmatrix}$$

where we have approximated the components to first order in  $\delta g$  and  $D$ , dropped the frequency dependence of each term, and  $\mathbf{i}$  indicates the imaginary unit.  $V'_I$  denotes the observed value of the pseudo-Stokes I visibility. In the regime of leaked pseudo-Stokes I power dominating over pseudo-Stokes Q, U and V, this shows that pseudo-Stokes I appears in pseudo-Stokes Q through errors in diagonal gain calibration, and pseudo-Stokes U and V through uncalibrated  $D$ -terms.

A fraction of the  $D$ -term leakage from pseudo-Stokes I into U and V may approximated by a delay between the  $p$  and  $q$  feeds,  $\tau_{pq}$ . This is a valid approximation, as a time delay between a wavefront incident upon two feed arms is exactly what circular polarization is, so signal appearing in Stokes V should be able to be described in this form. In Chapter 9 we present a fit for this parameter across the array, and find that through such a fit pseudo-Stokes V signal can be transferred to pseudo-Stokes U. In Chapter 7, we present a method that combines such a fit with redundant calibration, allowing us to minimize leaked power into pseudo-Stokes V on a per-time and -frequency sample basis.

This Chapter has reviewed the fundamentals of radio interferometry, providing a formalism generalized to wide field-of-view observations, and polarization. The importance of understanding the polarized response of the instrument has been emphasized many times. In the Part II, this emphasis will be justified from several data- and theory-based approaches.

# Chapter 4

## Instruments

In the following chapters I present data and results from a variety of configurations of two massively redundant low frequency interferometers, PAPER and HERA. In this Chapter I describe these instruments (Section 4.1), along with other current and future low frequency interferometers contributing to EoR science (Section 4.2).

### 4.1 Instruments used in this work

The vision of Hydrogen Epoch of Reionization Arrays was first laid out in the Backer et al. (2010) White Paper. That work proposed three consecutive efforts, improving upon their predecessors, to construct low frequency interferometers capable of detecting the EoR. While the physical feeds and elements of low frequency interferometers were relatively simple to construct, signal processing, calibration and imaging required new hardware and software to be invented. A research community of observational cosmologists interested in cosmological HI had to be nurtured.

The first of the three stages of Reionization Arrays was a parallel effort. The Precision Array for Probing the Epoch of Reionization (PAPER; Section 4.1.1) and the Murchinson Widefield Array (MWA; Section 4.2.2) investigated separate approaches to<sup>1</sup> antenna

---

<sup>1</sup>Among other things; see Section III B of Backer et al. (2010) for an enumerated list.

design, array layout and calibration techniques, with the objective of setting upper limits on and perhaps detecting the power spectrum of the EoR.

The second stage of the Reionization Arrays brought together the teams from the first stage to design and construct a new interferometer based on the lessons learned from PAPER and the MWA. This new instrument, named *the* Hydrogen Epoch of Reionization Array (HERA; Section 4.1.2) is currently under construction with a build-out schedule that brings new antennas online as they are commissioned. HERA’s objective is not only the detection of the EoR power spectrum, but its characterization at very high signal-to-noise. Attempts at low-fidelity imaging of ionized bubbles will be made.

The nature of the third stage is, at the time of writing, somewhat undetermined and contingent on the next decade of funding for low frequency radio astronomy. In the vision of Backer et al. (2010), its objective will be to image structure evolution throughout the EoR.

#### **4.1.1 The Donald C. Backer Precision Array for Probing the Epoch of Reionization (PAPER)**

Much of this thesis presents data from PAPER. PAPER was planned, like HERA, as a staged build-out to larger and larger arrays. In each build-out the correlator was replaced, and (nominally) identical antennae and signal chains were added to the existing array. The first iterations of PAPER consisted of 8 dipole antennae in Green Bank, West Virginia and 4 in Western Australia (Parsons et al., 2010). While the Australian site had a far better observing environment in terms of human-generated radio interference, the site in the USA was easier for the team to design and test on. Green Bank was intended as a test site – brighter foregrounds in the Northern Hemisphere and an unprotected low frequency band inhibited the science goals of the experiment. Nonetheless, the array in Green Bank was build-up to 32 antennae and reconfigured from a more traditional “imaging” configuration to a redundant grid, in order to experiment with redundant calibration and increased sensitivity to discrete Fourier modes (Parsons et al., 2012a; Pober et al.,

2012). Simultaneously, the PAPER-32 array and correlator were constructed in the Karoo Radio Quiet Zone (KRQZ) in South Africa.

#### 4.1.1.1 The PAPER signal chain

The PAPER signal chain changed little throughout the PAPER build-outs in South Africa, and it remained in operation for the HERA-19 Commissioning Array out to HERA-127. HERA elements are actually PAPER feeds, turned upside-down and suspended over a 14 m dish. This heritage was important to understand when interpreting PAPER or HERA data. We briefly describe the PAPER signal chain below. For a more thorough description, refer to Parsons et al. (2010).

Radio waves were incident upon, and induced a voltage in, a dual-polarization PAPER feed. The feed was a sleeved copper dipole protected by a wire-mesh groundscreen. The sleeve broadened the frequency response of the dipole element, and the groundscreen was used to increase sensitivity to emission from zenith (see Figure 4.1 for a photograph).

Electronics next to the dipole element amplified the voltage by a factor of  $10^6$ , which then propagated down a 150 foot  $75\ \Omega$  coaxial cable. All cables were of the same length to minimize the amount of extra calibration required per feed, and were above-ground. These cables ran to 8 “receiverators”; RFI-shielded mini-fridges which contained amplifiers which re-amplified the voltage signals by a factor of  $10^4$  (to correct for signal loss along the 150 ft coaxial cables) and applied an analog bandpass filter. The filter was designed to have a smooth frequency response which was relatively flat between 120 and 180 MHz (e.g. Moore, 2014).

More 50 foot,  $75\ \Omega$  foot coaxial cables ran from these to an RFI-shielded enclosure for further processing. For PAPER and the HERA-19 commissioning array, this enclosure was a specialized shipping container next to the array. For future HERA build-outs, processing will occur in the Karro Array Processing Building (KAPB) and the receiverator architecture will be replaced with underground “nodes” (see DeBoer et al. (2017) for more detail).



Figure 4.1: An image of a PAPER dipole element with its groundscren.

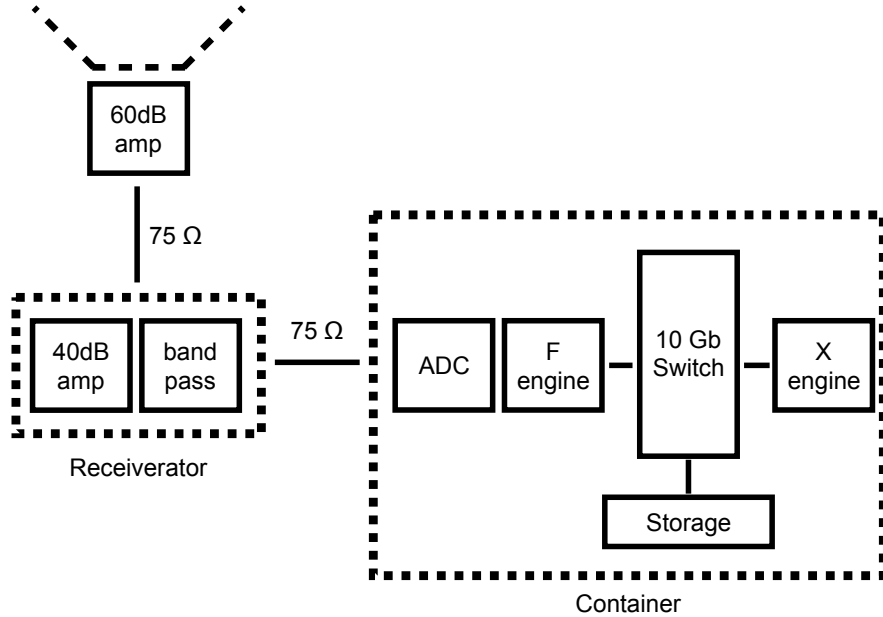


Figure 4.2: A diagram of the PAPER-128 signal chain. Square-dotted lines indicate RFI-shielding.

The filtered analog signal was then digitized with a sampling rate of 100 MHz and passed through an F-engine which Fourier transforms the signal using a 4-tap polyphase filter bank (which allowed for a smooth frequency and Fourier-space response; Price (2016b)). The integration time of each Fourier transform was 10 s. The Fourier transformed signals were distributed over a 10 Gigabit Ethernet switch to the X-engine (Parsons et al., 2008), which cross-multiplied all signals with each other to form visibilities, storing them in MIRIAD files.

A summary of the system described above is shown in Figure 4.2.

#### 4.1.1.2 PAPER-32

The PAPER-32 array in South Africa used a highly redundant configuration in order to take the measurements resulting in, at the time, the strongest upper limits on the EoR

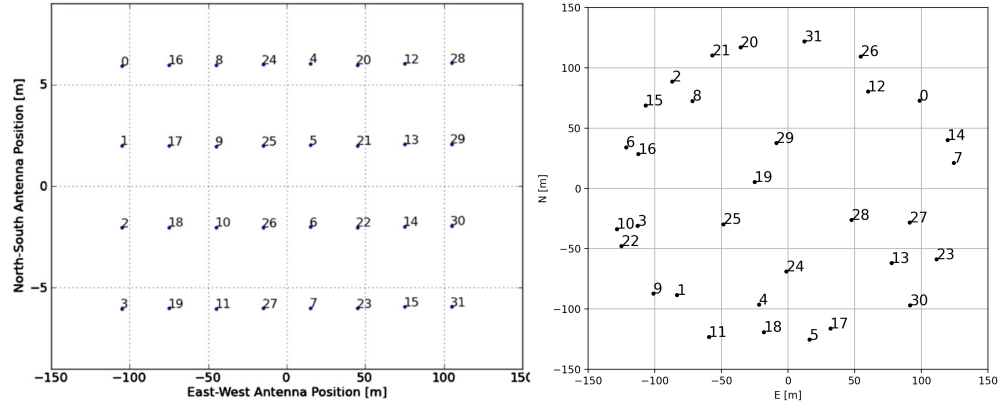


Figure 4.3: The array layouts of the PAPER-32 element deployment in South Africa. *Left:* The redundant grid. Four rows, with each element 30 m from the next in the East-West direction, and closely-packed ( $\sim 4$  m) in the North-South direction. Figure taken from Parsons et al. (2014). *Right:* The polarized imaging array. Elements were arranged in a pseudo-random scatter.

power spectrum (Parsons et al., 2014; Jacobs et al., 2015; Moore et al., 2017, sections of Moore et al. 2017 are presented in Chapter 8). The array was in redundant configuration from December 2011 to February 2012. For three nights in September 2011, the 32 elements were reconfigured into an polarized imaging configuration. The results from this deployment were used to make the first 2D power spectra of polarization, presented in Kohn et al. (2016) and in Chapter 9. For images and a brief description, see Figure 4.3.

#### 4.1.1.3 PAPER-64

During the PAPER-32 EoR integration, there were actually 64 antennas present in the Karoo, South Africa. However, the correlator at that time could only process 64 voltage streams – enough for 32 dual-polarization antennae. This is why 64 element single-instrument-polarization imaging results were published prior to any PAPER-32 studies (Jacobs et al., 2013; Stefan et al., 2013). EoR integrations in the 64 element redundant

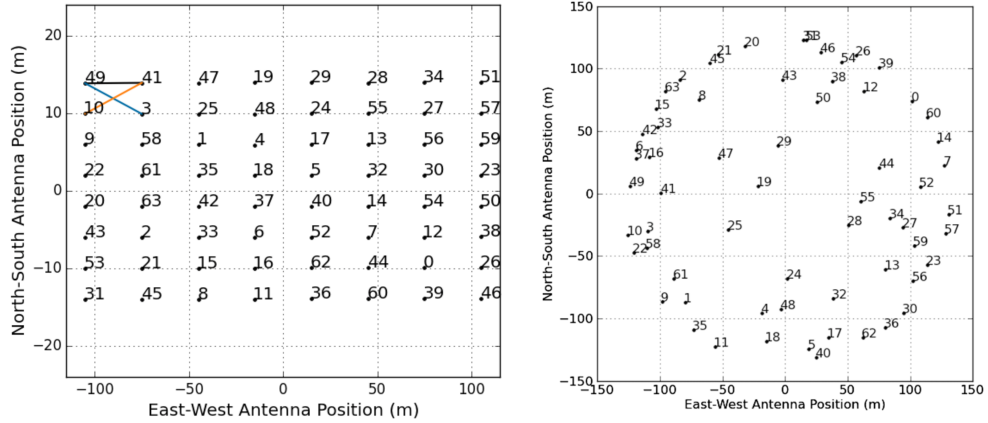


Figure 4.4: The array layouts of the PAPER-64 deployment. *Left:* The redundant grid, built-out from the PAPER-32 grid. Figure taken from Ali et al. (2015), which highlights the baseline-types used for power spectrum measurements. *Right:* the imaging array, used by Jacobs et al. (2013) to set an absolute flux scale for PAPER experiments. Figure taken from Jacobs et al. (2013).

configuration were only possible after a new correlator was produced in 2012. Results from this array were published in (Ali et al., 2015; Pober et al., 2015, Cheng et al. *in prep.*, Kolopanis et al. *in prep.*). Diagnostic results from the PAPER-64 redundant configuration that informed studies of time-averaged visibilities are presented in Chapter 12. The array layouts are shown in Figure 4.4.

#### 4.1.1.4 PAPER-128

The culmination of the PAPER experiment was the 128 element deployment. There were two observing seasons recorded: November 2013 to March 2014, and July 2014 to January 2015. In this configuration, 112 antennas were laid-out in a redundant grid with 15 m East-West spacings and 4 m North-South spacings. The remaining 16 antennas were arranged in ‘out-rigger’ and ‘in-rigger’ positions to increase *uv*-coverage and enable some

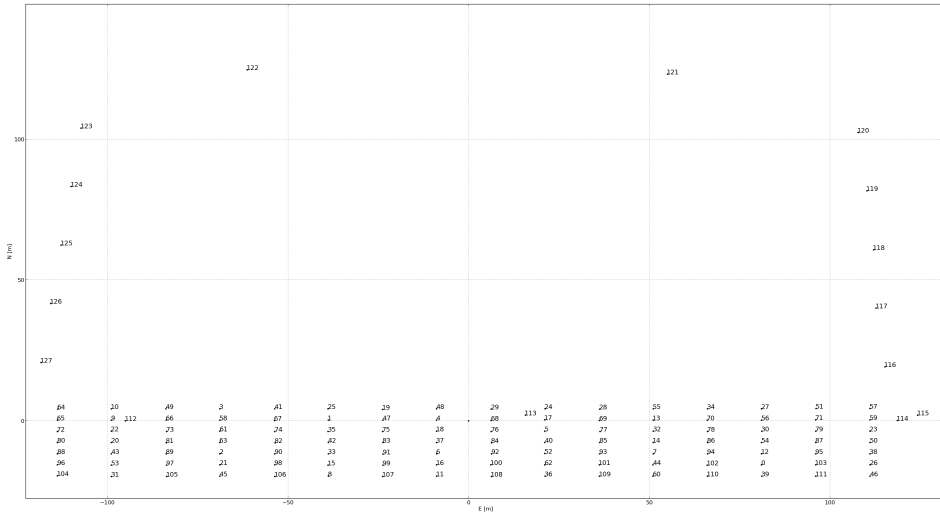


Figure 4.5: The PAPER-128 array layout. 112 antennas were laid-out in a redundant grid with 15 m East-West spacings and 4 m North-South spacings, and the remaining 16 antennas were arranged in ‘out-rigger’ and ‘in-rigger’ positions to increase *uv*-coverage.

level of imaging. Results from the first observing season of this array are presented in Chapters 6, 7 and 11. The array layout is shown in Figure 4.5.

#### 4.1.2 The Hydrogen Epoch of Reionization Array (HERA)

HERA was ranked as the “top priority in the Radio, Millimeter, and Sub-millimeter category of recommended new facilities for mid-scale funding” by the National Research Council Decadal Survey in astronomy and astrophysics (NRC, 2010). It brought together the largely US-based experts working on PAPER and the MWA to construct a new low-frequency array on the PAPER site in South Africa. The array, comprised of 14 m diameter dishes, was designed to be build-out in stages of close-packed hexagons of increasing size. For a full description of the instrument, refer to DeBoer et al. (2017).

The design of the HERA dish, feed, antenna layout and signal chain are intimately related to lessons learned by the PAPER and MWA EoR teams about the nature of EoR measurements (e.g. Thyagarajan et al., 2015b). One of the major considerations was



Figure 4.6: *Left:* a rendering of the 320 element HERA core. *Right:* the 19 element commissioning array (with the construction team). Leftover PAPER dipoles can also be seen in the background, forming three experimental arrays (described in Section 4.1.2.1). Figure taken from DeBoer et al. (2017).

how the instrument couples to the bright foregrounds, and how to control that coupling – the paradigm of the “wedge” and the “EoR Window”, which are discussed in detail in Chapter 5. Measurements based on prototype feeds were presented in (Ewall-Wice et al., 2016a; Neben et al., 2016, Patra et al. *submitted*).

HERA is a staged experiment, building-out in close-packed hexagons from a 19 element commissioning array, to 37, 127, 240 and finally 350 elements (320 in a dense, fractured core and 30 out-riggers, see Dillon & Parsons 2016 for more detail). Figure 4.6 shows a rendering of the core alongside an image of the HERA-19 commissioning array.

#### 4.1.2.1 HERA-19 Commissioning Array

In October 2015 a HERA commissioning array was completed, connected to the PAPER-128 256-input correlator. This array comprised of four separate components: the first 19 HERA dishes in a close-packed hexagon (HERA-19), 19 PAPER dipoles at the central locations of a hexagon of future HERA dishes (the “PAPER-Hex”), 40 PAPER dipoles in a redundant grid where every-other dipole was rotated 45° (to experiment with different polarization bases; “PAPER Pol”), and the remaining inputs filled with PAPER dipoles arranged in a pseudo-random scatter for imaging (“PAPER-Img”). Studies with this array are presented in Chapter 6 and 10. A diagram of the commissioning setup is shown in

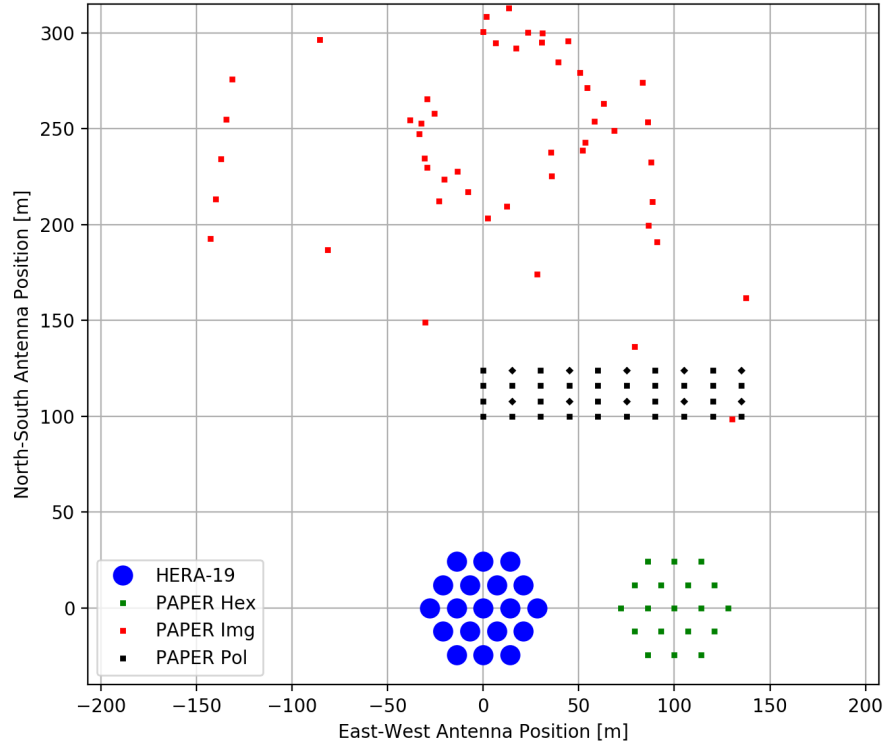


Figure 4.7: Positions of antennae in the HERA-19 Commissioning Array (including the experimental “subarrays”).

Figure 4.7.

#### 4.1.2.2 Future HERA Build-Outs

Each HERA element is much more sensitive than a PAPER element, based purely on collecting area. Figure 4.8 illustrates the varying sensitivities and collecting areas of different arrays and their elements, respectively. PAPER-128 was forecast to make marginal detections of the EoR power spectrum after  $\sim 1000$  hours of integration – HERA-127 should be capable of characterizing the EoR power spectrum at high significance, and the full HERA-350 array will be an extremely powerful survey instrument (e.g. Pober, 2015).

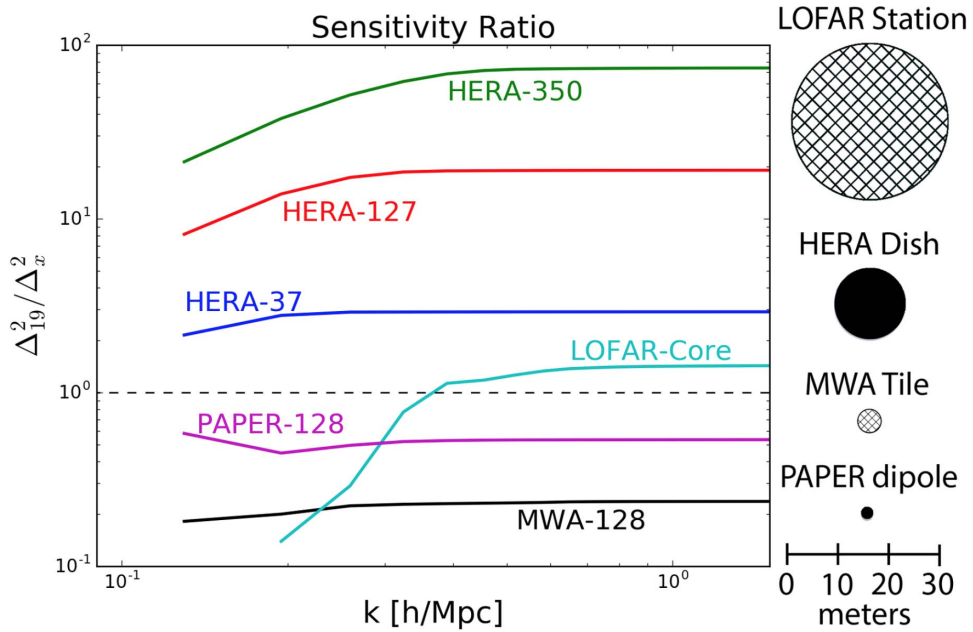


Figure 4.8: Instantaneous array Sensitivities as a function of  $k$ -mode (e.g. Chapter 5) relative to HERA-19. Differing element collecting areas are shown on the right. Taken from DeBoer et al. (2017).

We present forecasts for this future instrument in Chapter 13.

## 4.2 Other current and future interferometers

PAPER and HERA were not the only instruments researching the EoR and how to detect it. Several low-frequency interferometers around the world are contributing to the understanding of the EoR and the difficulties of observing it. Below I briefly describe a few of the leaders of the field – but it is not an exhaustive list.

### 4.2.1 The Low Frequency Array (LOFAR)

The Low Frequency ARray (LOFAR) is an interferometer made-up of “stations”, the core of which are arranged in a random scatter near Exloo in the Netherlands (van Haarlem

et al., 2013). LOFAR baselines extend across Europe with stations in Ireland, Sweden, Germany, Poland and other locations. These extremely long baselines can provide LOFAR with exquisite imaging capabilities.

LOFAR has detected diffuse, linear polarization structures that may be related to the Milky Way’s magnetic field and interstellar medium (Jelić et al., 2015). Patil et al. (2017) presented deep limits on the EoR power spectrum from one night of LOFAR data (also see Yatawatta et al. (2013)). A series of publications has investigated polarization in Fourier space (Jelić et al., 2014; Asad et al., 2015, 2016, 2017) – results that we build upon and verify throughout this work.

### 4.2.2 The Murchinson Widefield Array (MWA)

The Murchinson Widefield Array (MWA), based in Murchison Radio-astronomy Observatory in Western Australia, is composed of 256 “tiles” of 16 feeds each. At the time of writing, 72 tiles are arranged in compact hexagonal configurations in an effort to increase EoR sensitivity while retaining imaging capabilities with the rest of the array. The most complete low-frequency catalog of the southern sky, GLEAM, was presented by Hurley-Walker et al. (2017).

The MWA uses separate analysis pipelines for its EoR measurements (Sullivan et al., 2012a; Jacobs et al., 2016; Trott et al., 2016), a concept that will be implemented on future HERA measurements. The MWA has detected polarized signal from diffuse Galactic emission (Lenc et al., 2016, 2017) and set deep limits on the EoR power spectrum (e.g. Dillon et al., 2014, 2015). Pioneering work on the ionosphere was accomplished using MWA data (e.g. Loi et al., 2015), which we discuss in Chapter 8.

### 4.2.3 Square Kilometer Array – Low band (SKA-Low)

The Square Kilometer Array (SKA) will be built on two sites: the Karoo Radio Quiet Zone, currently occupied by HERA, will be the central location of the “high–mid band”

(350 MHz – 14 GHz; “SKA-Mid”) observatory and the Murchison Radio-astronomy Observatory, currently occupied by the MWA, will be the central location of the “low band” observatory (50 – 350 MHz; “SKA-Low”).

SKA-Low will consist of over 100,000 receiving elements in an imaging configuration. It will be the most powerful low-frequency radio telescope ever created, and be used not only for EoR science but a host of low-frequency science objectives (e.g. Carilli & Rawlings, 2004; Schilizzi et al., 2007; Dewdney et al., 2009). Learning from the work of EoR teams working on PAPER, HERA, MWA, LOFAR and other instruments will be crucial to the success of SKA-Low’s EoR science goals.

## **Part II**

### **Structure in Fourier space**

The Gemara asks: Do we not see that comets pass Orion? The Gemara rejects this: The aura of the comet passes Orion and it appears as though the comet itself passes. Rav Huna, son of Rav Yehoshua, said a different answer: It is merely that veil, one of the firmaments, rips and furls and the light of the next firmament is seen, and this appears like a comet. Rav Ashi said another explanation: It is not a comet that passes Orion, but a star that is uprooted from one side of Orion, and another star, from the other side of Orion, sees it and gets startled and shudders, and appears as if it is passing.

*Talmud Berakhot (58b:11)*

# **Chapter 5**

## **Peering through the EoR Window**

# Chapter 6

## Data Preparation and Processing

The data volume of interferometric measurements inherently scale as the square of the number of antennas in the array ( $N_{\text{ant}}$ ). Not only does the sheer volume of data from large- $N_{\text{ant}}$  arrays pose a problem for data storage, but also it requires precise and efficient efforts to quality assure (QA) the data.

In this chapter, I will outline some of the efforts involved in data preparation, pre-processing and QA that are required for an EoR power spectrum estimate.

### 6.1 Data Compression

The PAPER-128 correlator produced 288 MIRIAD files per night. Each of these contained 8126 baselines, and each baseline contained visibilities over 1024 98 kHz frequency channels and 56 10 s time integrations. The four instrumental polarizations were in separate files. In sum, each file was 4.2 GB which meant that each night 1.2 TB of data were recorded.

In order to efficiently transport the data over Gigabit Ethernet from the Karoo Radio Quiet Zone (KRQZ) to Cape Town, and from Cape Town under transatlantic cables to Philadelphia, some compression was required. It was also required that such a compression, while lossy, did not effect the targeted cosmological signal.

### 6.1.1 Delay–Delay-Rate Filtering

The compression algorithm implemented for PAPER observations, Delay–Delay-Rate (DDR) filtering, was introduced in Parsons & Backer (2009) described in Parsons et al. (2014), and we briefly review it below.

The geometric delay of a celestial signal, originating from direction  $\hat{s}$ , incident on an interferometric baseline described by vector  $\vec{b}$ , is

$$\tau_g = |\vec{b} \cdot \hat{s}|/c \quad (6.1)$$

where  $c$  is the speed of light. This relationship implies that  $\tau_g$  is bounded for a given baseline

$$-|\vec{b}|/c \leq \tau_g \leq |\vec{b}|/c \quad (6.2)$$

Equation 6.2 therefore gives the maximum value of  $|\tau_g|$  physically meaningful for a given array – the maximum baseline length in that array, divided by  $c$ . For PAPER, the maximum baseline length is 300 m, corresponding to  $\max(|\tau_g|) = 1\mu\text{s}$ . As reviewed in Chapter 5, the delay axis may be accessed by Fourier transforming a visibility along the frequency axis. Once in delay space, power at delays larger in magnitude than  $1\mu\text{s}$  could be removed. With a sufficiently large frequency bandwidth, this would not produce aliased signal, according to the critical Nyquist rate. By using the  $1\mu\text{s}$  as a delay bound for all visibilities, the frequency axes of all compressed visibilities remained the same (reduced in number from 1024 to 203), which while sub-optimal from a compression point of view, allowed for ease of programming at later stages.

A similar geometric bound can be obtained by Fourier transforming the time axis of visibilities, provided that they were obtained in drift-scan mode (see Chapter 3). Parsons & Backer (2009) showed that the rate at which the geometric delay on an interferometric baseline changes is governed only by the position of the array on Earth, and the Earth’s rotation:

$$\dot{\tau}_g = -\frac{\omega_{\oplus} \cos \delta}{c} (b_x \sin \alpha + b_y \cos \alpha) \quad (6.3)$$

where  $\omega_{\oplus}$  is the angular frequency of the Earth's rotation,  $\alpha$  and  $\delta$  are the hour-angle and declination of a point on the celestial sphere, respectively, and  $\vec{b} = (b_x, b_y, b_z)$  is the baseline vector expressed in equatorial coordinates.

For arrays not close to the geographic poles,  $|b_y| \gg |b_x|$ , there is a maximum rate of change (corresponding to  $(\alpha, \delta) = (0, 0)$ ), producing a bound on  $\dot{\tau}_g$ :

$$-\omega_{\oplus} |b_y|/c \leq \dot{\tau}_g \leq \omega_{\oplus} |b_y|/c \quad (6.4)$$

for a 300 m East-West baseline, the maximum delay-rate is approximately  $\max(|\dot{\tau}_g|) = 0.07 \text{ ns s}^{-1}$ . This delay-rate was not Nyquist sampled by a single PAPER file: requiring the previous and next files generated for that polarization to be appended on either side of each visibility's time axis to prevent aliasing from the decimation. For the large scale processing of months of data, this required a software pipeline described in Section 6.1.2.

There are also other issues with DDR compression, largely associated with instrument systematics. Delay transforms rely on the fact that the bright foregrounds that dominate the measured signal are spectrally smooth, and that the frequency response of the instrument is also spectrally smooth: this of course is the basis for the EoR window paradigm reviewed in Chapter 5. Likewise, delay-rate filtering assumes temporal smoothness. Radio Frequency Interference (RFI) signals created by human communications violate both models of smoothness, since they are typically confined to narrow bandwidths (creating sharp spikes along the frequency axis) and may be transient (creating sharp spikes along the time axis). This requires steadfast identification and flagging algorithms for RFI (see Section 6.2), and some variety of interpolation, fitting, or CLEANing across the flagged regions prior to compression.

By DDR filtering of PAPER-128 data using a 300 m baseline to set the width of the filters we were able to reduce the volume of the data by an approximate factor of 70.

### 6.1.2 Software Implementation

The first season of PAPER-128 data, due to a variety of circumstances, required compression on the computing cluster at the University of Pennsylvania. The raw data were stored on a high-volume drive that was able to connect with the cluster via a low-speed switch. The hardware capable of performing any sort of high-performance processing (i.e. holding the data in RAM) were ten “compute nodes” connected to the cluster via a high-speed switch, and mounted in an NFS architecture. The compute nodes could only hold  $\sim 10$  PAPER-128 files in storage.

The processing stages for compression of a night of PAPER data, described below, required knowledge of the location and compression state of not only individual files, but also the neighbors-in-time of the file in question, in order to implement the DDR filter described above. To supervise the compression we created a MySQL database, which we interacted with via Shell and Python scripts. The database contained a table for the data files under processing and their compression state, a table of neighbor-relations, a table of file details, and a table of the processing nodes available. The schema of this database is shown in Figure 6.1.

To implement the compression, per file, the following steps were required:

1. Copying the file from the storage volume to the cluster. For a single night of data, this required roughly 8 hours.
2. Copying the file from the cluster to the compute node. This required roughly 5 minutes.
3. Generate copy of the file, with metadata corrections. This required roughly 1 minute.
4. Delete the raw file.
5. RFI-flag the high frequency-resolution data. This required roughly 2 minutes.
6. Delete the metadata-corrected file.

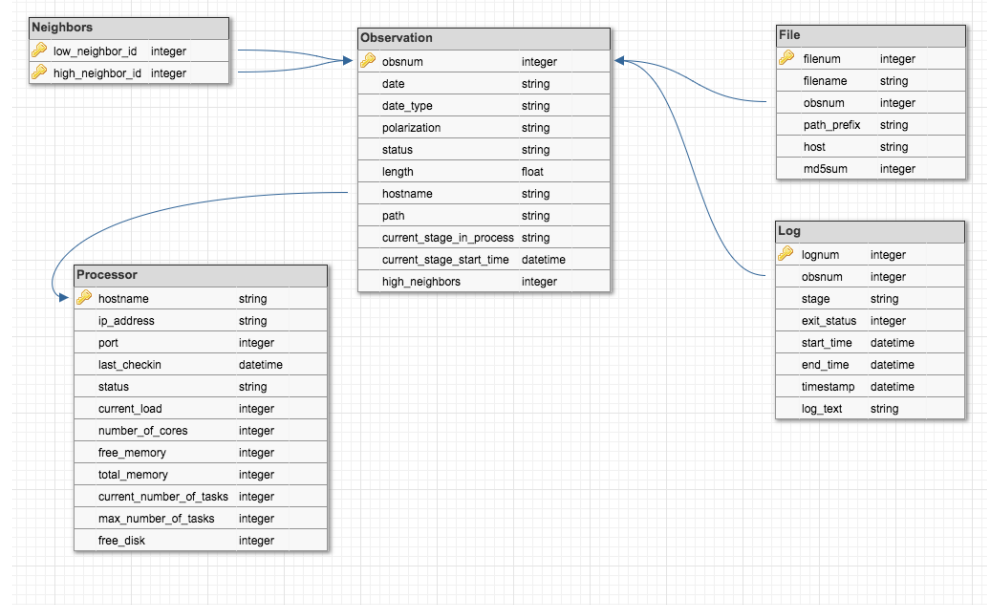


Figure 6.1: The schema of the database used to organize and implement PAPER data compression.

7. Acquire time-neighbors to the file in question, and bring them to the RFI-flagged stage. The time required for this stage varied with cluster activity, but usually required roughly 20 minutes.
8. DDR filter the RFI-flagged data, using an high-tolerance iterative CLEAN. This required roughly 20 minutes.
9. RFI flag the compressed data (coarse flagging), saving the flags to a separate file. This required roughly 1 minute.
10. Apply the coarse RFI flags to the *uncompressed*, RFI-flagged data. This required roughly one minute.
11. DDR filter the now twice-RFI-flagged data, using a low-tolerance iterative CLEAN. This required roughly 120 minutes.
12. Copy compressed data to the cluster.

13. Delete the twice-RFI-flagged data.
14. If the once-RFI-flagged data are not required as neighbors, delete them.
15. Delete the compressed data from the compute node.
16. If neighbors have already been compressed, delete them, otherwise begin their compression.
17. After all files are compressed, delete the uncompressed files from the cluster.

In total, this meant that across ten compute nodes, and efficient use of the fact that the neighbors could progress through the processing stages while the central file was being compressed, meant that it took roughly 20 to 24 hours to compress a night of observations.

## 6.2 Radio Frequency Interference

As noted above, RFI was able to introduce spectral and temporal structure that would cause ringing in the data during compression if it was not flagged. This meant that both identification and characterization of RFI was crucial to the scientific goals of the PAPER and HERA experiments. In Section 6.2.1, I present characterization of RFI in the second season of PAPER-128 data. By averaging flags in local time I was able to investigate “repeat offender” frequency bands and identify outlying “quiet” and “loud” days. In Section 6.2.2 I analyze RFI flags from the first Internal Data Release (IDR1) of HERA commissioning data, which contained 19 HERA feeds suspended above 5 m dishes in a close-packed hexagon, and 19 PAPER feeds in the same positions as the central dishes, allowing us to investigate the difference in flagging between feeds at different altitudes.

### 6.2.1 PAPER-128

The PAPER-128 2014 observation season ran from 18th June 2014 through the 30th April 2015. During this run, some 150 nights of data were recorded. A “night”, which I will

refer to using the JD at the start of observations, consists of twelve hours of observation from 6pm to 6am South African Standard Time (SAST). Observations as processed by the PAPER correlator are recorded in MIRIAD uv files. These files contain visibilities for each antenna pair in the array. Each integration is 20 seconds long over 1024 frequency bins from 100 to 200 MHz. Each uv file contains 56 integrations per antenna pair, and 72 uv files are recorded per linear polarization (xx, xy, yx, yy) per night.

Early in the PAPER data compression process, visibilities are flagged for RFI. This is accomplished by the aipy script *xrfi\_simple.py*, which takes the derivative of the frequency axis of all baselines associated with a single antenna, and flags any frequencies with a derivative  $\geq 6\sigma$  above the mean. We always flag the band-edges ( $\sim 7$  MHz on each side), since these frequencies are not useful to us, and always flag the  $137 \pm 0.6$  MHz band associated with ORBCOMM satellite network transmissions. This process is repeated per integration within each uv file and stored in a Python numpy zip (npz) file. This means that any baseline associated with antenna 1 can contribute a flag to the resultant npz file, which in turn is applied to the data.

The result is 280 files of high-time and -frequency resolution files per night per linear polarization containing information about the RFI environment of the HERA site. I report on the properties of these flags in time- and frequency-space over the 2014 observation season. This section is organized it as follows: in Section 6.2.1.1, I analyse the average properties of RFI over the season by stacking flags in local time and normalizing appropriately. In Section 6.2.1.2 I address nights with particularly strange RFI properties. I discuss the implications of my findings in Section 6.2.1.3.

### 6.2.1.1 Average Properties

In order to assess the average properties of the RFI environment, I calculated a weighted average of flags over the season. Over 150 nights, one-time occurrences are washed-out beneath the 1% level, allowing me to assess persistent issues.

Nominally, each night should grant 3920 integrations-worth of flags over 1024 fre-

quency bins, per linear polarization. In reality, most of the time this holds true, but occasionally not all files are compressible (hence failing to generate flags) or observations fail to start at the correct time (so there are no data to flag). Also, in the event of an X-engine failure within the correlator, contiguous chunks of the band (in eighths, i.e. 25 MHz across) are flagged-out, usually for the rest of the night.

For this reason, I calculated a weighted average of the flags across the season, but neglected nights with correlator failures or late starts. Weights were simply the number of nights that contained that integration-bin in SAST. The resultant “flag density waterfall” is shown in Figure 6.2. The color scale is indicative of flagging frequency across the season, and line plots above and to the right of the the waterfall showing the percentage of times and frequencies that were flagged, respectively.

A summary of the persistent (flagged  $\geq 1\%$  of the time per channel) RFI frequencies can be found in Table 6.2.1.1. I have investigated each frequency and tried to find the most likely source for each. In most cases, this required looking at the properties in time as well as frequency. Others were more obvious from frequency alone, e.g. the 149.8 MHz transmission frequency from the International Space Station (ISS). Still others I could not track down a convincing explanation for, and these are listed with a ‘?’ . A ‘?’ next to a possible cause indicates that the listed cause is the most prevalent at that frequency, but that the temporal properties of that cause do not necessarily make sense. Many of the characterizations arise from the South African Table of Frequency Allocations (SATFA; Staatskoerant (2008)).

Figure 6.3 shows the detail of the top panel of Figure 6.2. This figure highlights the broad swath of the band from roughly 150 to 180 MHz that was, on average, clear of RFI. This roughly corresponds to 21 cm redshifts  $z = 6.9$  to  $8.5$ . This is one of the reasons that the Parsons et al. (2014) and Ali et al. (2015) limits on the 21 cm power spectrum concentrated on this redshift range – there were simply more unflagged data to average-down with. Furlanetto et al. (2006) show that the  $z \sim 8$  universe can be considered roughly coeval over an  $\sim 8$  MHz bandwidth. As such, the 30 MHz chunk could be used to

Table 6.1. PAPER-128 RFI frequencies and brief characterization for the averaged flags.

$\nu$ MHz	Flagged %	Cause (Possible)	Notes or Time (SAST) Characterization
103 ± 3	100	BAND EDGE	Built-in to flagger.
107.25 ± 0.25	2.6	FM radio	Constant background at 2% level
107.55 ± 0.05	1.9	FM radio	Constant background at 2% level
108.1 ± 0.4	9	FM radio?	Rises with time, peaking at midnight and 4am
109 ± 0.4	11.5	FM radio?	Rises with time, peaking around 4am
112.8 ± 0.1	1.4	Aircraft?	Constant background at 1% level
114.05 ± 0.85	3.7	?1	Decreases till midnight; peak at 4am
116.55 ± 0.35	2.2	?2	Peak at midnight
120.15 ± 0.35	3.2	Aircraft	Roughly follows CPT↔JNB flight times
124.95 ± 0.35	5.5	Aircraft	Roughly follows CPT↔JNB flight times
130.25 ± 0.55	4.3	?3	Falls (7pm) and rises (3am) steeply
131.75 ± 0.35	10.3	Aircraft?	Peaks at 6:30, 7:30, 8:30, 9:30, 10 and then a steep falloff
136.05 ± 0.45	33.1	Radar?	Decreases over night
137.35 ± 0.85	100	ORBCOMM	
141.45 ± 0.35	2.1	Mobile phones?	High until 9pm, then at background 1% level
145.85 ± 0.45	10.7	Amateur radio	Strong 9pm-1am – this is the official downlink for ISS-HAM
149.75 ± 0.55	90.7	ISS	"Beeps", but in stacked data peaks 2am
175.15 ± 0.35	20.5	VHF TV (video)	Channel 4. Peaks at 8:30pm, then falls to background 7%
181.15 ± 0.15	1.6	VHF TV (audio)	Channel 4. 2% level turns-off at 10pm
182.15 ± 0.35	75	?4	Decreases until 10pm (to 15%), when it begins a slow rise again
183.2 ± 0.5	89.7	VHF TV (video)	Channel 5. Rises throughout night.
186.25 ± 0.35	4.6	?5	Extreme turn-off at 9:45
189.15 ± 0.35	41.4	VHF TV (audio)	Channel 5. Rises throughout night.
189.9 ± 0.4	100	VHF TV	Channel 6. Built-in to flagger.
191.1 ± 0.3	100	VHF TV	Channel 7. Built-in to flagger.
196 ± 4	100	BAND EDGE	

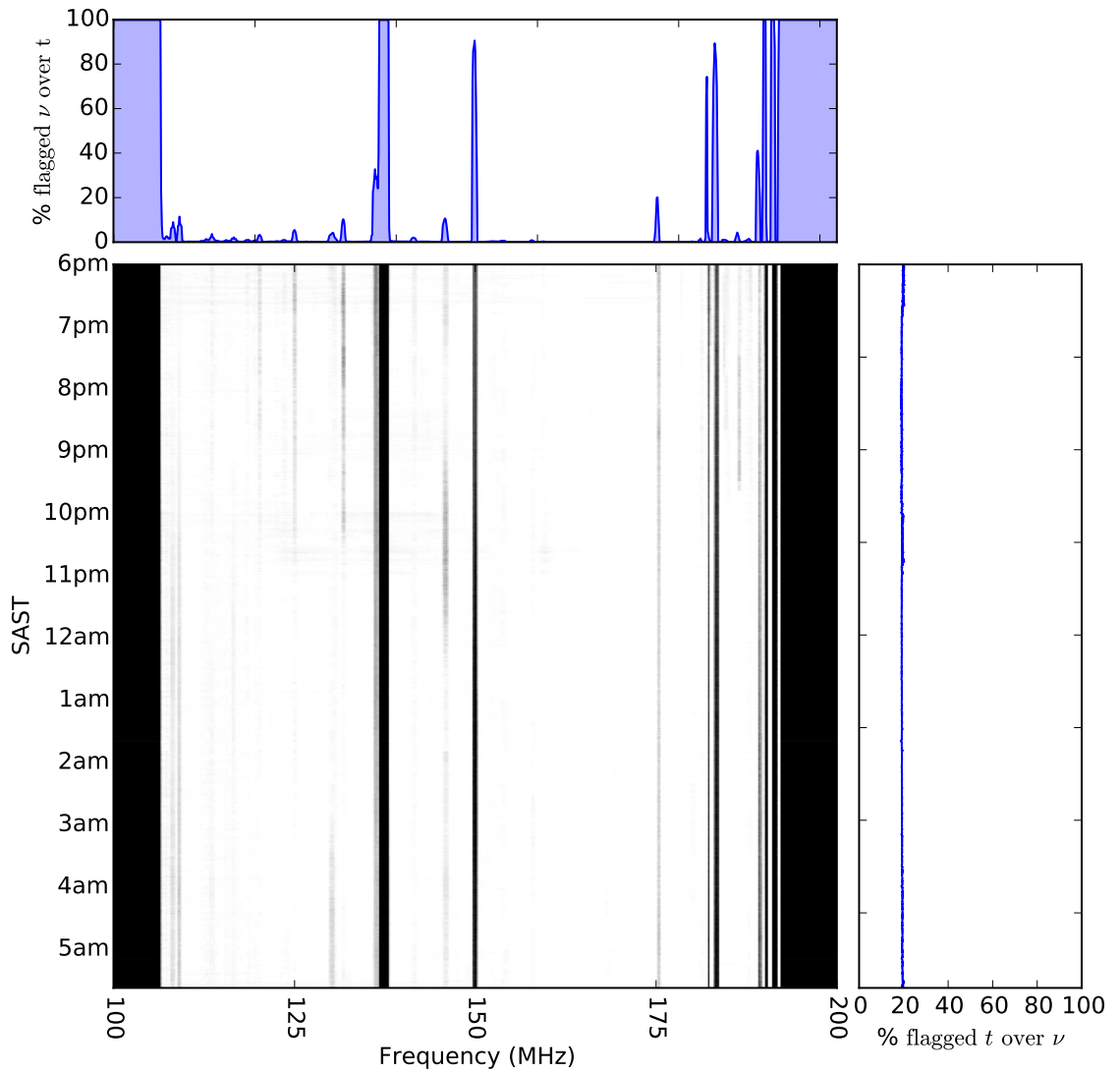


Figure 6.2: A waterfall plot of RFI flags averaged over 150 days of data. The gridding process is described in the text. Above the waterfall I show the percentage of the season each frequency is flagged, and to the right I show the percentage of frequencies that are flagged per integration.

create  $\sim 3$  power spectra, as demonstrated in Jacobs et al. (2015). As we show below, the deactivation of VHF TV broadcasts could enable measurements up to the band edge.

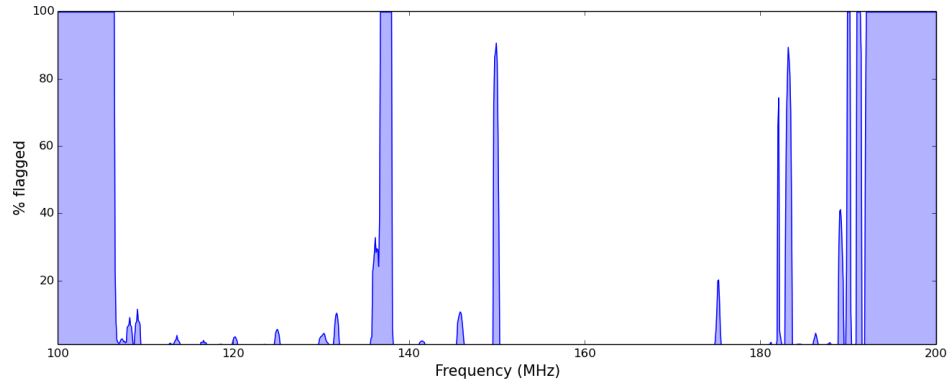


Figure 6.3: The percentage of time that each frequency was flagged over the season.

## FM Radio

SATFA lists the frequency band 87.5–108 MHz as available for FM radio broadcasts, leading me to postulate that the low-level RFI we observed in the  $107.25 \pm 0.25$  and  $107.55 \pm 0.05$  MHz bands had FM radio as the leading cause. The  $108.1 \pm 0.4$  and  $109 \pm 0.4$  MHz bands were outside of the official range, and exhibit odd temporal properties for human activity – two peaks at midnight and 4am – with a increasing number of flags throughout the average night (see Figure 6.4).

## Aircraft communications

It was difficult to argue that the  $112.1 \pm 0.1$  MHz signal is caused by aircraft communications since it maintained a constant background level. However, SATFA listed this frequency as reserved for aircraft communications and it has been used in the past as a calibration frequency for aircraft instruments South African Civil Aviation Authority (2008).

The other aircraft frequencies were obvious, because they closely traced the 2-hour

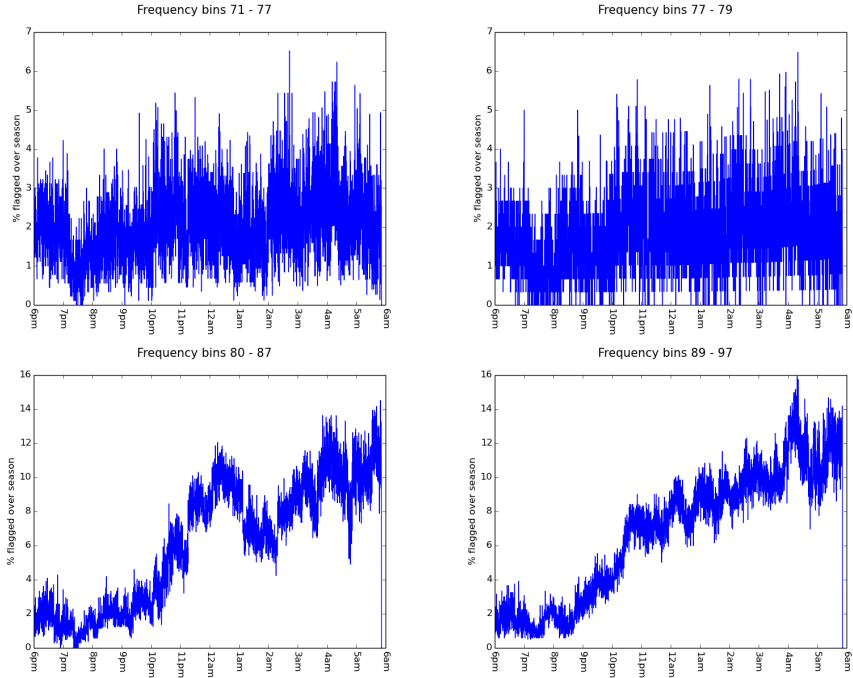


Figure 6.4: Possible FM radio contamination in the *Top, left to right*:  $107.25 \pm 0.25$  and  $107.55 \pm 0.05$  MHz bands, and *Bottom, left to right*:  $108.1 \pm 0.4$  and  $109 \pm 0.4$  MHz bands.

flight from Cape Town to Johannesburg<sup>1</sup>. An example ( $120.15 \pm 0.35$  MHz) is shown in Figure 6.5. SATFA reserved frequencies 108–117.975 MHz for aeronautical radionavigation and 117.975–137 MHz for aeronautical mobile. In Table 6.2.1.1 I listed  $131.75 \pm 0.35$  MHz as caused by aircraft since it falls in the aeronautical mobile band, but it does not follow the flight patterns as closely as the other bands.

## Orbital communications

ORBCOMM Inc.’s constellation of 29 LEO communication satellites is a well-known contaminant of the low-frequency sky, dominating over any astronomical signal at 137–138 MHz (although each satellite emits within a 20 kHz band). For this reason there was

---

<sup>1</sup>Credit to Danny Jacobs for first spotting this and noting it in an internal PAPER circular in December 2009.

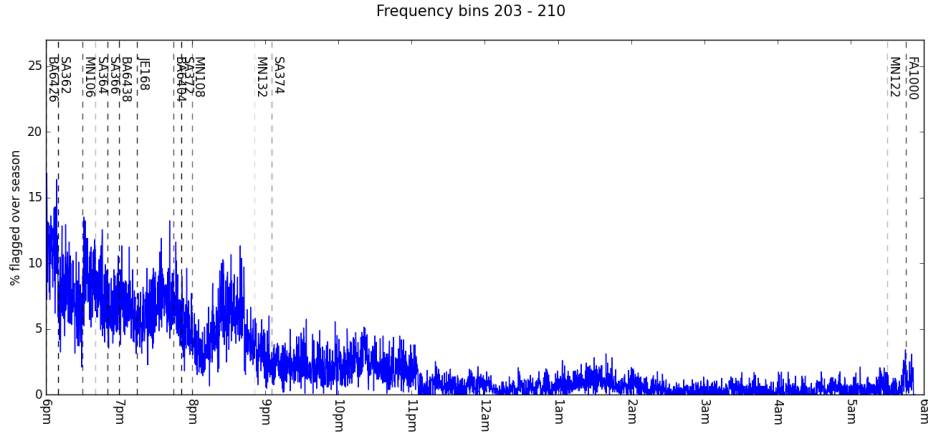


Figure 6.5: Flights from Cape Town to Johannesburg correspond to RFI in the  $120.15 \pm 0.35$  MHz channels. Vertical dashed lines indicate a flight leaving Cape Town (flights from Johannesburg are roughly concurrent) and the flight code is listed. The transparency of a line is inversely proportional to how many days a week that flight is scheduled for. The flight is 2 to 2.5 hours long – and about 2 hours after the last flight of the day, the flags fall to background level (but notably, not always to zero).

built-in flagging at  $137.35 \pm 0.85$  MHz within the compression pipeline.

The largest contaminant without built-in flags in the pipeline were communications from the ISS. The  $149.75 \pm 0.55$  MHz transmissions were semi-regular in time; they ‘beep’.

Onboard the ISS are HAM radio devices. Some countries have also launched satellites with these onboard, one of the purposes of which is to provide HAM radio operators something in space to communicate with. These devices are licensed to operate at 145.2 and 145.8 MHz, and SATFA listed the 144-146 MHz band as reserved for ‘Amateur–Satellite’ communications. We detected RFI at  $145.85 \pm 0.45$  MHz, although strong signal across  $\sim 10\%$  of the season that occurs 9pm-1am argues against human operation.

## Mobile phones and VHF TV

A weak RFI signal at  $141.45 \pm 0.35$  MHz was within the ‘mobile 1 BTX’ and aeronautical mobile band in SATFA, but other than this single listing I did not build a strong case for

the signal's cause.

VHF TV is broadcast over specifically-spaced video and audio frequencies. The strong signals at  $183.2 \pm 0.5$  MHz and  $189.15 \pm 0.35$  MHz had almost identical gradients for the percentage of flagging as a function of time of night. These frequencies corresponded exactly to Channel 5 of South African System I 625-line VHF TV signals for video and audio transmission, respectively. Similarly, the weaker signals at  $175.15 \pm 0.35$  and  $181.15 \pm 0.15$  MHz corresponded to Channel 4's video and audio transmission, respectively, but they did not share the same temporal properties.

### Unidentified sources

There were 5 RFI frequencies in the averaged data that I could not identify the sources of: weak emissions (flagged < 5% of the season) at  $114.05 \pm 0.85$ ,  $116.55 \pm 0.35$ ,  $130.25 \pm 0.55$  and  $186.25 \pm 0.35$  MHz, and one strong emission at  $182.15 \pm 0.35$  MHz. The variation of each source with time is shown in Figure 6.6. The  $186.25 \pm 0.35$  MHz had a sharp turn-off around 9:45pm each night, suggesting that it originated from some kind of automated device.

#### 6.2.1.2 Individual Properties

Using the flags per night, I was able to assess the total number of flags as a percentage of the waterfall (i.e.  $N_{\text{flags}} / (3920 \times 1024)$ ). The average flagging per night was  $19.2 \pm 0.5\%$ , which was dominated by the permanent flagging of ORBCOMM and band edges. Four nights deviated from the average by a  $\geq 2\sigma$  excess: JDs 2456965, 2456732, 2456958 and 2457038. Their flag waterfalls are shown in Figure 6.7 (2456732, 2456958 and 2457038) and Figure 6.8 (2456965). While the strange nature of night 2456965 is discussed below, the three others followed the pattern of having strong contamination from FM and aircraft communication bands, but also had broadband 'pulses' up to about 20 minutes in length. The source of these broadband pulses is not well understood, although it was clear that

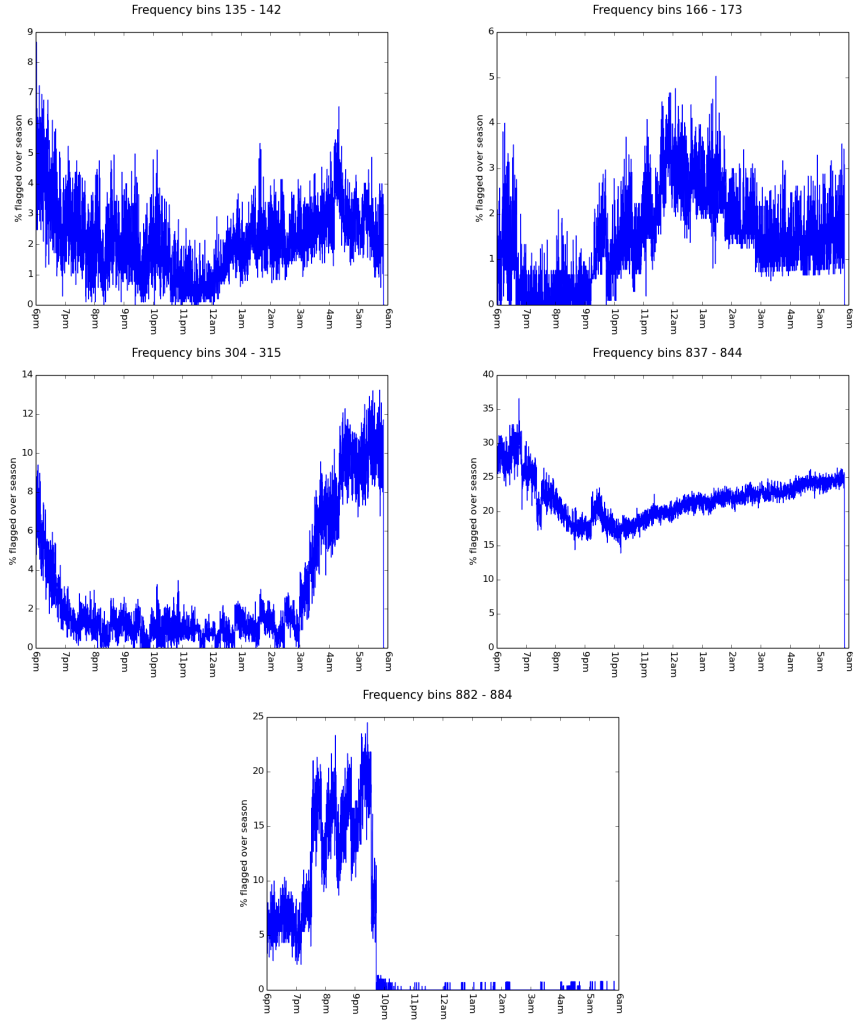


Figure 6.6: The temporal profile of the 5 RFI frequencies with unidentified causes. *Top, left to right:*  $114.05 \pm 0.85$  and  $116.55 \pm 0.35$  MHz. *Middle, left to right:*  $130.25 \pm 0.55$  and  $182.15 \pm 0.35$  MHz. *Bottom:*  $186.25 \pm 0.35$  MHz. The  $182.15 \pm 0.35$  MHz frequency is flagged a large amount of the time, making it our most-offending unidentified source.

ORBCOMM tends to spill outside of its allocated band on occasion.

JD 2456965 was easily the worst offender, and it exhibited a strange signal that wanders in frequency and time close to the ISS band. An event of note on this date (23rd November 2014) was a Soyuz FG launch that docked with the ISS – this may have been

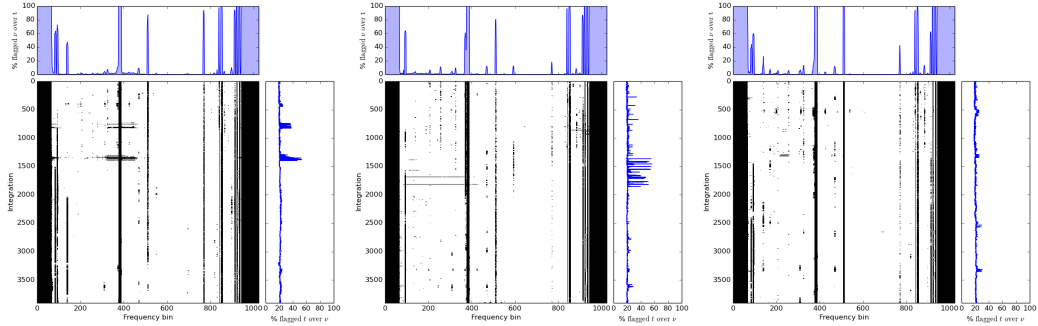


Figure 6.7: *Left to right:* waterfalls of flags for nights 2456732, 2456958 and 2457038. These three nights, along with 2456965, are  $>20.2\%$  flagged;  $>2\sigma$  above the average flagging amount per night.

a signature of their transmissions<sup>2</sup>. Similar signals were seen on 2456898 (28th August 2014; although only at the beginning of the night) and 2456924 (23rd September 2014). There was no listed orbital or suborbital activity for 2456898. There was an US ICBM test off of the coast of Virginia on 2456924, but this was probably not the cause of the RFI. The flag waterfalls for these nights are shown in Figure 6.8.

Another property that the flag waterfalls in Figures 6.7 and 6.8 highlight is the presence of broadband RFI signals, typically present at frequencies lower than the ORB-COMM band. However, while we flagged at the low-end of the band (which had higher noise levels to begin with), it is likely that such broadband pulses dominated the band at those times, and that we failed to flag all of the integrations. Our flagging routine `xrfi_simple.py` does contain a thresholding option for flagging the entire integration given some arbitrary number of frequencies flagged during that integration: some experimentation will be required to decide if that threshold should change.

---

<sup>2</sup>The internet also suggests... less plausible explanations: <https://www.youtube.com/watch?t=11&v=VtZx8iP04zs>.

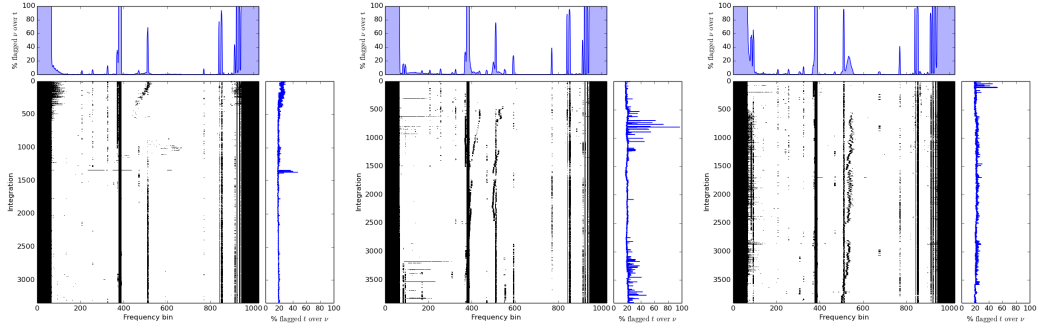


Figure 6.8: *Left to right:* waterfalls of flags for nights 2456898, 2456924 and 2456965. These three nights exhibit a strange behaviour of RFI that changes in frequency and time. JD 2456965 is by far the worst, and during this night as well as 2456898, we see a broadband ‘comb’ of flagged frequencies near the band edges

### 6.2.1.3 Discussion

Based on my findings, I was able to recommend some actions that could be taken in the KRQZ to enable better measurements:

- Steps to reduce and ideally eliminate the VHF TV transmissions in the area would be very helpful, since these were clearly interfering with our measurements in the high-end of the band.
- The ISS  $149.75 \pm 0.55$  MHz band should be permanently flagged within the compression pipeline.
- Pursuing re-routing of flight paths will not do much to help: we see aircraft signals for the duration of their flight, not just when they’re over the Karoo.
- A lower threshold for identifying broadband RFI should be investigated.

A new, lower-frequency feed is currently under development by the HERA analog group. This would nominally allow measurements to be taken in the range 50–250 MHz, allowing science observations of the Dark Ages and the post-reionization Universe. It should be noted that at the lowest frequencies FM radio will be a constant harassment to

these measurements. At the higher frequencies, VHF TV will be the primary contaminant, but should be much easier to remove as it is both narrow-band and within the KRQZ’s power to shut off.

### 6.2.2 HERA-19 and PAPER-19

The HERA-19 IDR1 consisted of four subarrays: the HERA-19 hexagon of dishes (the ‘HERA Hex’), a hexagon of 19 PAPER dipoles in the exact positions of not-yet-constructed HERA dishes (the ‘PAPER Hex’), an imaging array and an experimental array for polarization measurements. I will concentrate on the two Hexes in this Section. I analyzed RFI as flagged in the linear  $xx$ -polarization only. Asymmetric beams can in principle receive different RFI events for different linear polarizations, but analysis of that was outside the scope of this diagnostic study.

IDR1 consisted of one ‘golden day’, JD 2457458. This ran from 6pm on March 10th 2016 to 6am the following day. This gave, per baseline, roughly 4000 integrations of 10 seconds each over 1024, 100 kHz frequency channels from 100 to 200 MHz.

In order to flag RFI I used the aipy script *xrfi\_simple.py*. I took the union of all baseline flags as data to analyze. Unlike in Section 6.2.1, these data did not have a-priori flagging of band edges, which allowed me to make a more complete study of RFI in the HERA band. I did have to implement custom flags in order to get more than a zeroth-order view of the RFI (since these would dominate the flagging routine unless they are flagged already), but my results from Section 6.2.1 gave a better idea of what was flagged to get there.

Below I present measurements of high-power, mostly narrow-band RFI channels as flagged in HERA Hex data and PAPER Hex data separately. In both cases, I was able to list any channels that are flagged for  $\geq 1\%$  of the night. I could then compare the flagging Hex-to-Hex, and to PAPER-128.

### 6.2.2.1 HERA Hex RFI

Table 6.2.2.1 shows all narrowband frequency ranges flagged in HERA-19 visibilities, with columns of the frequency range in MHz, % flagging over time, plausible identification, whether or not it was identified in PAPER-128 data, and other notes (often details of the possible identification). Frequencies with 100% flagging indicate manual flags required for `xrfi_simple` to work on the rest of the channels.

Clearly, the low-end of the band was swamped by FM radio broadcasts. One notable frequency was the  $109.2 \pm 0.3$  MHz band, which was heavily flagged in HERA visibilities, but was only flagged a few percent in PAPER-128 data.

As seen before, ORBCOMM satellite emissions spilled out of their allocated 137–138 MHz band down to 136.3 MHz.

There were many narrowband RFI channels, across the band, that PAPER-128 did not pick-up. Most of these were flagged only at low levels, with two exceptions:  $111.3 \pm 0.2$  MHz and  $113.5 \pm 0.1$  MHz. Both of these were in the aircraft navigation band. There is some evidence (Civil Aviation Authority, 2016) that 111.3 MHz band is for air force communications. The 113.5 MHz band is a known band for radionavigation beacons ('VOR navaids' World Aero Data, 2016).

A particularly annoying ‘new’ emitter was in the  $153.8 \pm 0.2$  MHz region, which is close to the center of our nominal EoR band. It could correspond to mobile phones being used close to site.

Table 6.2. RFI as flagged by HERA

$\nu$ MHz	Flagged %	Cause (Possible)	Seen by PAPER-128	Notes
100.7 ± 0.2	50	FM Radio	n/a	RSG "Dis Die Een" Prieska
101.5 ± 0.3	36	FM Radio	n/a	RSG "Dis Die Een" Calvinia
102.4 ± 0.1	100	FM Radio	n/a	RSG "Dis Die Een" Carnarvon
102.8 ± 0.3	57	FM Radio	n/a	RSG "Dis Die Een" Pofadder
104.2 ± 0.1	100	FM Radio	n/a	SAfm Prieska
105.1 ± 0.2	100	FM Radio	n/a	SAfm Calvinia
106.2 ± 0.3	100	FM Radio	n/a	SAfm Carnarvon
106.9 ± 0.1	15	FM Radio	n/a	Sentech
107.2 ± 0.1	18	FM Radio	Yes	
107.8 ± 0.2	15	FM Radio	Yes	
108.3 ± 0.1	31	FM Radio?	Yes	
109.2 ± 0.3	93	FM Radio?	Yes...	...but not to this degree
111.3 ± 0.2	25	Air force?	No	
112.5 ± 0.1	5	Aircraft?	No	
113.5 ± 0.1	21	Aircraft	No	VOR navaids
115.5 ± 0.1	3	Navaids?	No	
115.9 ± 0.1	3	Navaids?	No	
116.6 ± 0.2	9	Aircraft?	Yes	VOR-DME navaids
120.1 ± 0.2	5	Aircraft	Yes	CPT< – >JNB
125.0 ± 0.2	6	Aircraft	Yes	CPT< – >JNB
130.0 ± 0.2	4	Aircraft	No	Communication
131.6 ± 0.2	15	Aircraft	Yes	KLM OPS
136.4 ± 0.1	9	ORBCOMM	Yes	
136.7 ± 0.1	10	ORBCOMM	Yes	
137.4 ± 0.4	100	ORBCOMM	Yes	
145.7 ± 0.4	18	ISS/Amateur Radio band	Yes	
149.9 ± 0.1	100	ISS	Yes	
153.8 ± 0.2	7	Mobile phones?	No	
175.0 ± 0.1	100	VHF TV	Yes	Channel 4 Video
178.3 ± 0.2	8	VHF TV	No	Channel 7?
181.2 ± 0.1	100	VHF TV	Yes	Channel 4 Audio
182.2 ± 0.2	9		Yes	
183.5 ± 0.6	100	VHF TV	Yes	Channel 5 Video
184.1 ± 0.1	2	VHF TV?	Yes	Channel 5?
184.7 ± 0.1	6	Broadcasting	No	
187.8 ± 0.1	4		No	
189.1 ± 0.1	52	VHF TV	Yes	Channel 5 Audio
190.1 ± 0.3	13		n/a	

Table 6.2—Continued

$\nu$ MHz	Flagged %	Cause (Possible)	Seen by PAPER-128	Notes
$191.1 \pm 0.1$	100	VHF TV	n/a	Channel 7
$197.2 \pm 0.2$	18		n/a	
$199.4 \pm 0.5$	100	BAND EDGE	n/a	

### 6.2.2.2 PAPER Hex RFI

Table 6.2.2.2 has the same description as Table 6.2.2.1, but for the PAPER Hex. There were far fewer RFI frequencies flagged in PAPER visibilities, almost all of which were seen by HERA. The only RFI seen by the PAPER Hex and not the HERA Hex was the  $123.5 \pm 0.1$  MHz emission, which I could find a plausible identification for.

### 6.2.2.3 Hex-to-Hex Comparisons

As mentioned above, the PAPER Hex saw far fewer narrowband RFI channels than HERA does. This highlighted an interesting trade-off between dipoles and dishes: at first glance, one might have expected PAPER dipoles to be more susceptible to RFI given their broader effective beams. However, HERA dipoles are lifted several meters above the ground, and this change in height may have been the source of the greater susceptibility to RFI. RFI comes from the horizon, which would be more easily received in the far sidelobes of the beam.

Even for the RFI channels they did share, HERA flagged them more often. Taking the difference in percentage-flagging for the common RFI channels (think of the left panel subtracted from the right panel for common channels in Figure 6.9), those channels had an average of 8% more flagging in HERA visibilities. The difference was particularly high in the aeronautical radionavigation bands, where HERA had on average 38% more flagging than the PAPER Hex.

Figure 6.10 shows the flags on a per-sample basis (these were averaged over time to

Table 6.3. RFI as flagged by the PAPER Hex

$\nu$ MHz	Flagged %	Cause (Possible)	Seen by PAPER-128	Notes
100.0 ± 0.1	100	BAND EDGE	n/a	
100.7 ± 0.1	11	FM Radio	n/a	RSG "Dis Die Een" Calvinia
101.6 ± 0.2	6	FM Radio	n/a	RSG "Dis Die Een" Calvinia
102.4 ± 0.1	100	FM Radio	n/a	RSG "Dis Die Een" Carnarvon
102.7 ± 0.1	100	FM Radio	n/a	RSG "Dis Die Een" Pofadder
104.2 ± 0.2	100	FM Radio	n/a	SAfm Prieska
105.1 ± 0.2	100	FM Radio	n/a	SAfm Calvinia
106.2 ± 0.3	100	FM Radio	n/a	SAfm Carnarvon
108.2 ± 0.1	3	FM Radio?	Yes	
109.1 ± 0.1	26	FM Radio?	Yes	
113.6 ± 0.1	2	Airplane Communications	No	VOR navaid
120.2 ± 0.3	3	Aircraft	Yes	CPT< - >JNB
123.5 ± 0.1	1		No	Not seen by HERA
125.0 ± 0.2	6	Aircraft	Yes	CPT< - >JNB
130.0 ± 0.3	3		No	
131.7 ± 0.2	14	Aircraft	Yes	
136.4 ± 0.2	6	ORBCOMM	Yes	
136.7 ± 0.2	6	ORBCOMM	Yes	
137.4 ± 0.4	100	ORBCOMM	Yes	
145.8 ± 0.3	14	ISS/Amateur Radio band	Yes	
149.9 ± 0.1	100	ISS	Yes	
153.8 ± 0.2	3	Single frequency mobile phones?	No	
175.1 ± 0.2	100	VHF TV	Yes	Channel 4 Video
178.3 ± 0.2	100	VHF TV	No	Channel 7?
181.2 ± 0.1	100	VHF TV	Yes	Channel 4 Audio
183.2 ± 0.2	100	VHF TV	Yes	Channel 5 Video
189.2 ± 0.1	100	VHF TV	Yes	Channel 5 Audio
191.2 ± 0.1	100	VHF TV	n/a	Channel 7
199.8 ± 0.2	100	BAND EDGE	n/a	

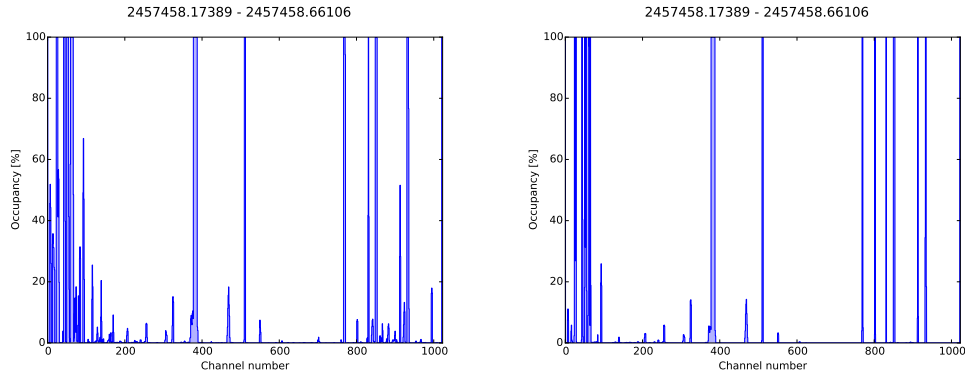


Figure 6.9: Frequency vs. percentage flagging for the HERA Hex (*left*) and PAPER Hex (*right*). Any band with greater than 1% flagging is reported in Tables 6.2.2.1 and 6.2.2.2.

create Figure 6.9). Most apparent was the occupancy of the HERA plot compared to the PAPER Hex one. An important component of this plot is the averages over frequency in the right-hand panels. We saw that the average flagging for a given time sample was about 5% higher for HERA than for the PAPER Hex, mostly due to the higher occupancy of the FM band. But we also saw something new; HERA appeared to be much more sensitive to broadband bursts of RFI. The PAPER Hex caught one of these events (around 1.30am SAST) at high significance, but most of them hardly rose above average flagging. HERA saw five to seven bursts across the night.

#### 6.2.2.4 Comparison PAPER-128 stacked flags

Section 6.2.1 presented RFI flags stacked over 150 days of observations. This method washed-out single events that effect analysis on a single-night basis, but was sensitive to repeatedly offending frequencies. Due to the PAPER-128 analysis pipeline, many channels were automatically flagged (particularly large portions of the band edges), which artificially boosted the average flagging per time and did not allow for closer inspection of the ends of the band. There was some evidence of broadband emission (see Figure 6.2) but the band was largely free of RFI in the middle of the night. Obviously, the data presented in this section shows a less-clean band, but it also only concentrated on a single

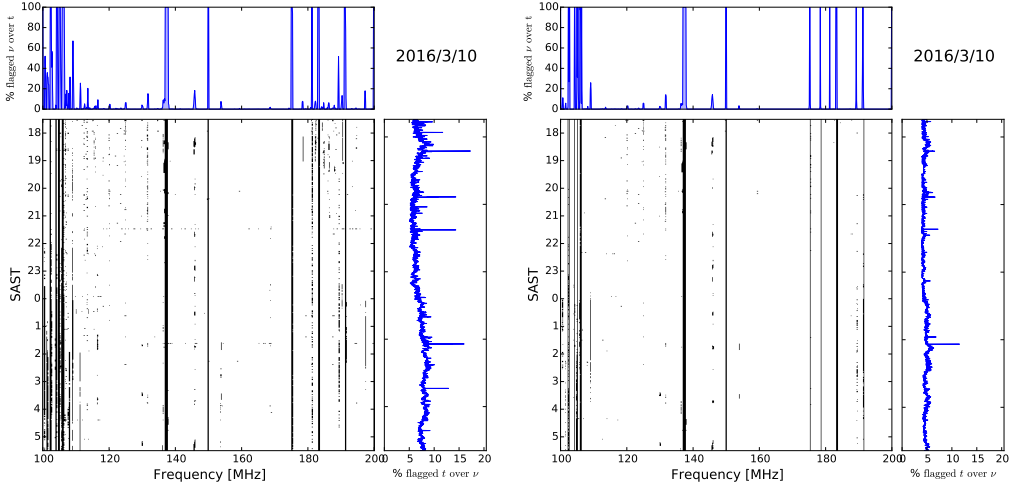


Figure 6.10: RFI flag waterfalls of frequency vs. South Africa Standard Time for the HERA Hex (*left*) and PAPER Hex (*right*). The top panels show the average over time (identical to Figure 6.9), while the right panels show the average over frequency.

night's data, so it may be that IDR1 was conspicuous compared to an 'average' night of observations.

Traits shared between the two analyses were:

- Aircraft communications disrupting data until around local midnight.
- ORBCOMM spilling out of its band.
- VHF TV frequencies emitting throughout the night in the high end of the band.

Table 6.2.2.1 highlighted many frequencies seen by HERA and not by PAPER-128. Again, given the fact that flags were stacked and averaged in Section 6.2.1, these may not have been 'new', but they could have been. Particularly conspicuous were the emissions in the aeronautical radionavigation band.

### 6.2.2.5 Discussion

I have presented a first look at RFI in HERA-19 Commissioning data. Probably due to the height of the receiving element on HERA versus PAPER dipoles, much more RFI

was apparent, especially on the low and high ends of the band. Luckily, the EoR band was largely clean of RFI, except for an emitter at about 154 MHz, which could have corresponded to single-frequency mobile phone communications. Such communications are officially banned in the SKA Radio Quiet Zone (SKA Panel, 2012), which HERA is in the center of.

Only looking at a single night of RFI flags limited the predictive power of this study. More data will be required to establish whether or not this level of RFI was ‘normal’. Broadband RFI bursts require closer investigation.

Efforts to extend the HERA band to lower and possibly higher frequencies are currently under way. The FM radio band extends to around 65 MHz, while the VHF TV band extends to around 230 MHz, so the RFI environment should be a consideration for these efforts.

Meanwhile, I note that the RFI flagging routine used here, `xrfi_simple`, is indeed ‘simple’. More advanced RFI flagging algorithms such as AOFlagger (Offringa et al., 2012) should be tested in later studies.

## 6.3 Quality Assurance Metrics

Throughout reduction of PAPER-128 data, we found a number of ways for data to become corrupted, including failure of analog or digital components, incorrect cable connections, or improper feed installation. Many of these can cause failure of redundant calibration algorithms that are sensitive to non-redundancies within an array. In the case of a real-time calibration pipeline, such as the one implemented for HERA, it is essential to have quickly-generated metrics to assess the overall health of the array. Much of the heritage of PAPER-128 data processing is present in the HERA Real Time Calibration Pipeline (RTC; [Ali et al. \(in prep.\)](#)).

### 6.3.1 Mean Amplitude Flagging

The most critical and likely failure that an antenna could have was malfunctioning electronics losing power and temporarily “killing” it. This failure mode was characterized with unusually low signal coming from the antennas, causing the visibilities associated with that antenna to have much lower than average amplitude. This leads to the definition of the mean visibility metric for antenna  $i$ :

$$M_i = \frac{\sum_{j,v,t} |V_{ij}|}{N - 1} \quad (6.5)$$

where  $V_{ij}$  is the visibility for the baseline involving antennas  $i$  and  $j$ ,  $N$  is the number of antennas in the array, and the sum is taken over all antennas  $j$  ( $i \neq j$ ), times, and frequencies. When  $M_i$  is compared across the array, it can reveal antennas with anomalously low signal to noise.

Erroneously cross-polarized antennas were ones where the feed was rotated 90 degrees, or the cables were swapped for the two polarizations along the signal path (such a failure mode could be expected for a large array under active construction). This caused the linear polarization visibilities ( $EE$  or  $NN$ ) to have a lower amplitude or correlation relative to the cross-polarizations ( $EN$  and  $NE$ ). While these could appear to be dead antennas, the cross-polarization visibilities would show that one of the antennas in a given visibility is cross-polarized.

We defined the mean visibility cross-polarization metric as

$$P_i = \frac{M_i^{NE} + M_i^{EN}}{M_i^{NN} + M_i^{EE}}, \quad (6.6)$$

where  $M_i$  is defined in Equation 6.5 and are calculated for all the polarization pairs. If  $P_i$  is larger than some threshold, then antenna  $i$  may be cross-polarized. This method is effective when applied to long baselines, but for the shortest baselines in HERA, large-scale astrophysical polarization (e.g. Lenc et al., 2016) is observed by in all the instrumental visibilities (since, for example, the  $NN$  visibility is equal to the sum of the Stokes I and Q

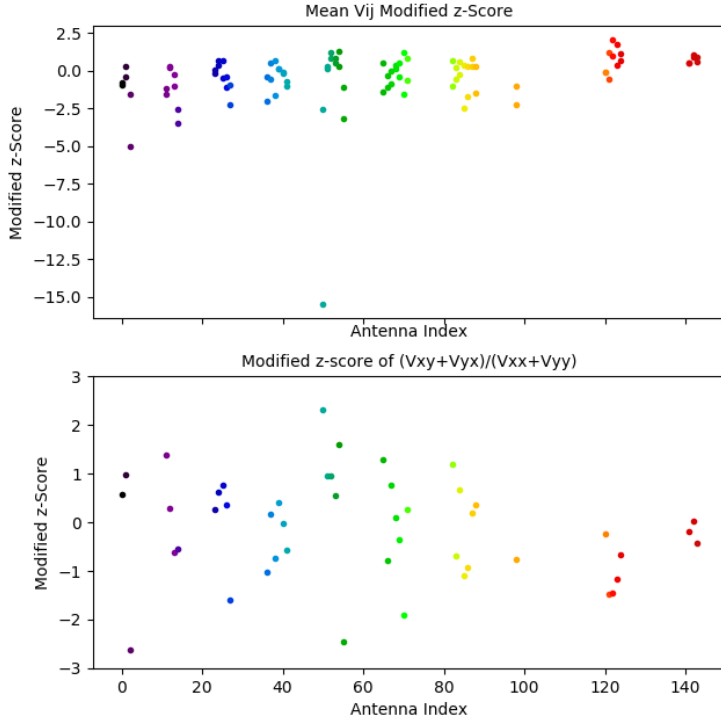


Figure 6.11: An example of the mean amplitude flagging metrics on exercised on HERA-47 data. The top panel shows the mean amplitude flagging metric  $M_i$ , and the lower panel shows the cross-polarization metric  $P_i$ . The  $E$  feed of antenna 50 shows at  $\sim 15\sigma$  deviation, causing it to be flagged from further processing.

visibilities). This brings  $P_i$  closer to unity for any antenna  $i$ .

Figure 6.11 shows the application of the metrics described above to raw HERA-47 data in the RTC system. Note that we plotted the modified  $z$ -score and not the raw metric. Traditionally the  $z$ -score is defined as the deviation from the mean divided by the standard deviation, and is a method to detect outliers. However, since our metrics were not necessarily normally-distributed, we use the modified  $z$ -score defined as

$$MZ_i = 0.6745 \frac{|x_i - \tilde{x}|}{MAD}, \quad (6.7)$$

where  $x_i$  is some data point (in our case this was a metric),  $\tilde{x}$  is the median of  $\{x_i\}$ , and MAD is the median absolute deviation. Iglewicz & Hoaglin (2010) recommend that modified  $z$ -scores with an absolute value greater than 3.5 should be flagged as outliers. In the analyses shown in Figure 6.11, we took the cut-off to be 5, to account for greater acceptable variation in our metrics.

The top panel of figure 6.11 shows the modified  $z$ -score for the mean visibility metric as a function of antenna number. Antenna 50E (East-West polarization) was a  $\sim 15\sigma$  outlier, indicating a problem with amplification along the signal chain. Upon further inspection, antenna 50E was shown to exhibit strange behavior, dropping in and out of the signal chain. Further investigation is needed to know the root cause of this misbehavior.

The bottom row of figure 6.11 shows the modified  $z$ -score for the cross polarization metric as a function of antenna number. There were no modified  $z$ -scores outside of the [-5,5] range, indicating that there were no cross polarized antennas. Further inspection of the raw visibility data validated this finding.

### 6.3.2 Flagging on omnical $\chi^2$

We developed a metric that identified days of PAPER-128 observations with poor overall omnical  $\chi^2$  values. Using the median of the  $\chi^2$  values in the EoR band (channels 100–160; 150–180 MHz), over all days of observation, we flagged days that exceeded the average of the median by one standard deviation from the mean. Figure 6.12 shows an example of this flagging method used on the latter half of the first PAPER-128 observing season. Clearly, there were just a few JDs that had exceptionally high  $\chi^2$  values. Our metric captures almost all of these outliers – the possible exceptions being JDs 2456717 and 2456718.

The omnical software also provides  $\chi_a^2$  values for each antenna  $a$  – that is, how much each antenna contributed to the overall non-redundancy of the array. The above sigma-clipping metric was applied to  $\chi_a^2$ , and was able to identify the same bad antennae using the mean amplitude flagging metric described in Equation 6.5.

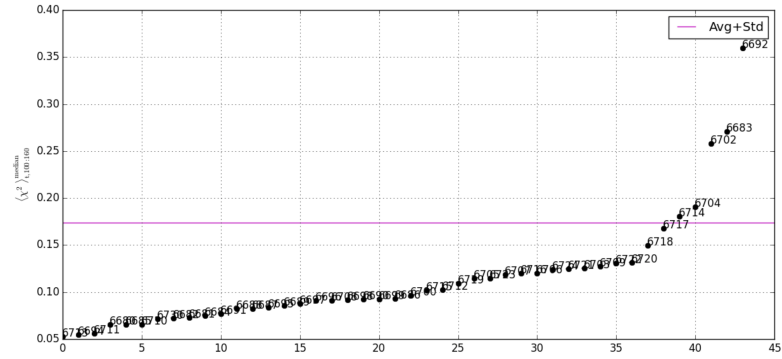


Figure 6.12: Flagging Julian Dates (JDs) based on the median omnical  $\chi^2$  values in the 150–180 MHz band. Shown in pink is the flagging boundary. The JD labels have been abbreviated to drop the ‘245’ prefix that they all share. Clearly, there are just a few JDs that have exceptionally high  $\chi^2$  values.

# Chapter 7

## Polarimetric Calibration

Hypothetically, integrating over long observing seasons should average-down the noise in the EoR window, allowing for the study of the EoR without the risk of foreground contamination. However, the wedge-window paradigm arises due to the chromaticity of the interferometer as well as the signal. Spectral structure can be imparted to interferometric visibilities by the frequency evolution of the antenna beam and by calibration. Spectral structure can also be induced on otherwise-smooth foregrounds via Faraday rotation of polarized foregrounds. In of itself Faraday rotation is not a problem, since HI emission should be largely unpolarized, but errors in calibration and beam deconvolution can leak polarized signal into unpolarized visibilities (e.g. Thompson et al., 2017, ; Chapter 3).

Interferometers with  $N$  antennae that are sensitive to  $N_{\text{pol}}$  polarizations will generate  $N_{\text{pol}}N(N - 1)/2$  visibilities per time-frequency sample, defined as:

$$V_{ij,pq}(\nu, t) = g_{p,i}^*(\nu, t)g_{q,j}(\nu, t)\exp(-2\pi\nu\tau_{pq}) \times \int d\Omega A_{pq}(\nu, \hat{s})S_P(\nu, \hat{s})\exp(i\vec{b}_{ij} \cdot \hat{s}\nu/c) \quad (7.1)$$

where  $p, q \in x, y$  denote instrumental polarizations, i.e. the response to signal projected into the North-South direction or the East-West direction, or whichever direction the dipole arms of the instrument are oriented;  $i, j$  refers to two antennae with baseline

vector  $\vec{b}_{ij}$ ,  $S_P(v, \hat{s})$  is the sky temperature for Stokes parameter  $P$ , and  $A_{pq}(nu, \hat{s})$  is the spatial sensitivity of the instrument to  $S_P$  (projected into the instrumental basis). Outside the integral are three direction-independent variables that must be calibrated: the complex gain of each dipole arm  $g_{p,i}(v, t)$  and the phase between dipole arm  $p$  and  $q$ ,  $\tau_{pq}$ . For  $p = q$ ,  $\tau_{pq} = 0$ .

All the above presents a data processing challenge: these visibilities must be precisely calibrated over long observing seasons to ensure that the cosmological signal is not averaged away by calibration errors and not contaminated by spectral structure. One way of overcoming part of this challenge is to construct large arrays of redundantly-spaced elements. The redundancy of the visibilities of such an interferometer allows the gain terms to be solved-for precisely by least-squares minimization algorithms (Liu et al., 2010). In Section 7.1, I explore the implications of implementing full-polarization redundant calibration on PAPER-128 data. However, redundant calibration is not the only tool radio astronomers posses that can be used to obtain precise calibration solutions. In Section 7.2, I present a basic implementation of full-polarization image-based calibration on data from the PAPER-32 polarized imaging array.

## 7.1 Redundant Calibration

Unpolarized redundant calibration has been pursued by the Donald C. Backer Precision Array for Probing the Epoch of Reionization (PAPER; Parsons et al. (2010)), the Hydrogen Epoch of Reionization Array (HERA; DeBoer et al. (2017)) and part of the Murchison Widefield Array (MWA; Tingay et al. (2013)). For EoR studies this has the advantage of being able to average-down noise in the EoR window once all redundant visibilities are calibrated, for potentially very high signal-to-noise measurements of narrow regions of  $k$ -space. However, it sacrifices  $uv$ -coverage, leading to poor imaging capabilities.

Redundant calibration of low-frequency interferometers has been demonstrated by Zheng et al. (2014) with the MIT EoR experiment, Parsons et al. (2014); Jacobs et al.

(2015); Ali et al. (2015) and Kolopanis et al. (2018) with PAPER and Li et al. 2017 with part of the MWA. All of these studies calibrated linearly-polarized instrumental visibilities.

Moore et al. (2017) used the same calibration parameters as Parsons et al. (2014) and Jacobs et al. (2015), but also solved for a single value of  $\tau_{pq}$  for the observing season, since their analysis was for cross-polarized visibilities also. These PAPER studies took linear combinations of instrumental visibilities to form ‘pseudo-Stokes’ visibilities (e.g. Thompson et al. (2017), Moore et al. (2013)). In this Chapter, we use the notation and convention

$$\begin{pmatrix} V_I \\ V_Q \\ V_U \\ V_V \end{pmatrix} = \frac{1}{2} \begin{pmatrix} 1 & 0 & 0 & 1 \\ 1 & 0 & 0 & -1 \\ 0 & 1 & 1 & 0 \\ 0 & -i & i & 0 \end{pmatrix} \begin{pmatrix} V_{xx} \\ V_{xy} \\ V_{yx} \\ V_{yy} \end{pmatrix} \quad (7.2)$$

for these quantities.

As noted above, the spectrally-structured HI emission from the EoR should only be detected in  $V_I$ , but fractions of Faraday-rotated (spectrally structured)  $V_Q$  and  $V_U$  are capable of leaking into  $V_I$  via calibration errors and intrinsic properties of the complex beam. Short of detecting the polarized power spectrum of  $V_Q$  and  $V_U$ , which may be at levels beneath the EoR signal, we require confidence that we are accurately calibrating our data to prevent as much leakage as possible into  $V_I$ .

At these low frequencies and inherently large scales probed by modern instruments, the Stokes V sky appears to be empty. Indeed, Patil et al. (2017) used the spherical power spectra of their Stokes V images as a proxy for the thermal noise power spectrum. In wedge-space, one test of polarimetric calibration is therefore to see how close to thermal noise  $V_V$  is. Kohn et al. (2016) observed a direction-independent bias in  $V_V$ , but that study implemented a Moore et al. (2017)-style polarimetric calibration of  $\tau_{pq}$ , solving for a single value across the array, which could indeed lead to a direction-independent bias (but was more powerful than not calibrating it at all; see their Figure 5).

In Section, we explore different schemes of redundant calibration which include polar-

ization. We present three different calibration schemes, all based around the OMNICAL<sup>1</sup> package (Zheng et al., 2014), and compare their uses and shortcomings. We structure the discussion as follows: in Section 7.1.1 we give a mathematical overview of the least-squares minimization algorithms implemented for the different calibration schemes and show basic simulations of each algorithm in action. We describe the real data used to test the calibration schemes, and the results of those tests, in Sections 7.1.2 and 7.1.3, respectively. We discuss our findings and conclude in Section 7.1.4.

### 7.1.1 Mathematical Overview

In this section we briefly describe the fundamental steps of the redundant calibration scheme implemented in OMNICAL. For a more thorough discussion of the algorithm, see Wieringa (1992), Liu et al. (2010), Zheng et al. (2014) and Dillon et al. (2017).

#### 7.1.1.1 Redundant calibration with OMNICAL

We can express visibilities for baseline separation  $|i - j|$ , polarization  $pq$  as a system of equations, of form

$$V_{ij,pq} = g_{p,i}^* g_{q,j} V_{|i-j|,pq} + n_{ij} \quad (7.3)$$

where we have dropped the frequency and time dependence; this is true for every time-frequency sample. This system is overdetermined for a highly redundant array configuration. We assume that all polarizations have the same noise statistics for noise  $n_{ij}$ . An initial estimate for the least-squares fit can be obtained by solving the linearized equation in logarithmic space (termed *logcal*)

$$\log V_{ij,pq} = \log g_{p,i}^* + \log g_{q,j} + \log V_{|i-j|,pq} \quad (7.4)$$

which can constrain the parameter space, but produces biased results since noise is

---

<sup>1</sup><https://github.com/HERA-Team/omnical>

additive in linear space. Taylor expanding Equation 7.3 around the estimated values (denoted with bars) for each parameter as found by 7.4 grants a system of linearized equations (termed *lncal*)

$$V_{ij,pq} = \bar{g}_{p,i}^* \bar{g}_{q,j} \bar{V}_{|i-j|} + g_{p,i}^* \bar{g}_{q,j} \bar{V}_{|i-j|} + \bar{g}_{p,i}^* g_{q,j} \bar{V}_{|i-j|} + \bar{g} *_{p,i} \bar{g}_{q,j} V_{|i-j|} \quad (7.5)$$

which can be solved iteratively, minimizing the least-squares statistic  $w$

$$w^2 = \sum_{\text{all } i \neq j} \sum_{p,q \in x,y} \frac{|V_{ij,pq} - g_{p,i}^* g_{q,j} V_{|i-j|,pq}|^2}{\sigma_{ij}}. \quad (7.6)$$

### 7.1.1.2 Including polarization in redundant calibration

We test three different calibration schemes for polarization.

- Use OMNICAL separately on the two linearly polarized visibilities  $V_{xx}$  and  $V_{yy}$  to obtain independent estimates for all gain terms, and apply those gains to all four instrumental polarizations of visibilities. We will refer to this scheme as *2pol* calibration.
- Include all four instrumental polarizations in the least-squares statistic. This means that, for example, information on the  $g_{x,i}$  term will come from  $V_{xx}$  and  $V_{xy}$ . This will be referred to as *4pol* calibration.
- Use a scheme in which the cross-polarized visibilities  $V_{xy}$  and  $V_{yx}$  share values of the model visibility  $V_{|i-j|,pq}$ . This means that we are minimizing the value of  $V_{yx} - V_{xy}$  during calibration; effectively minimizing the pseudo-Stokes V visibility. There is validity to assuming the pseudo-Stokes V visibility to be noise-like, as discussed above. We refer to this calibration scheme as *4pol+minV* calibration.

### 7.1.1.3 Degeneracies

One virtue of OMNICAL is that it can calibrate all antennas relative to one another without reference to an explicit sky model. However, this results in known degeneracies in the minimization of  $w^2$  that cannot be resolved with OMNICAL and must be fixed afterwards with absolute calibration of the whole array using external information. The number of degeneracies is equal to the number of zero eigenvalues that arise in the linearized  $w^2$  minimization algorithm. For a single polarization, there are 4 degenerate modes, which can be interpreted physically as overall amplitude, overall phase, phase tilt, and phase tip. Phase tilt and tip can be interpreted as a two-dimensional phase slope across the array. It is clear that these factors do not affect the product  $g_{p,i}^*(\nu, t)g_{q,j}(\nu, t)V_{ij,pq}(\nu, t)$  (and we again refer the reader to Dillon et al. (2017) for a comprehensive description):

- Overall amplitude:  $g_{p,i} \rightarrow Ag_{p,i}$  and  $V_{ij,pq} \rightarrow V_{ij,pq}/A^2$ .
- Overall phase:  $g_{p,i} \rightarrow g_{p,i}e^{i\phi}$
- Two-dimensional phase slope: for a co-planar array, define a phase vector  $\vec{\Upsilon} = (\Upsilon_X, \Upsilon_Y)$  where  $\Upsilon_X, \Upsilon_Y$  refer to Cartesian directions as opposed to polarizations. For an antenna at position  $\vec{v}_i$ , and defining  $\vec{d}_{ij} = \vec{v}_i - \vec{v}_j$ , then  $g_{p,i} \rightarrow g_{p,i}e^{i\vec{\Upsilon} \cdot \vec{v}_i}$  and  $V_{ij,pq} \rightarrow V_{ij,pq}e^{i\vec{\Upsilon} \cdot \vec{d}_{ij}}$ . This is allowed because  $\vec{d}_{ij}$  is the same for all redundant visibilities.

OMNICAL ‘fixes’ the amount that the amplitude degeneracy is able to drift between samples by imposing that the average of the absolute of the gains over the array average to unity. Similar tricks can be played with the other degeneracies to project them into a space that does not adversely effect calibration.

The phenomenon of ‘degeneracy fixing’ in polarized redundant calibration was explored in depth by Dillon et al. (2017). In that work, they showed how the number of degeneracies changes with polarized calibration scheme, focussing on what we refer to as the *2pol* and *4pol* schemes in this work. We briefly review their results here.

In the *2pol* scheme, there are the 8 expected redundancies as expected for two independent calibrations; it is as if there are two co-located arrays for  $xx$  and  $yy$ , each with the four degeneracies listed above. However, in the *4pol* scheme, the number of degeneracies is reduced to 6. Introducing  $V_{xy}$  and  $V_{yx}$  breaks the phase tilt and tip degeneracies per polarization, and leaving a polarization-independent phase tilt and tip. Extending this formalism to the *4pol+minV* scheme<sup>2</sup>, the number of degeneracies is further reduced to 5. By imposing equality between  $V_{xy}$  and  $V_{yx}$ , the ‘overall phase’ degeneracies per polarization are broken and there remains only a single overall phase for the array.

Dillon et al. (2017) emphasized the importance of understanding how fixing degeneracies can effect the amplitude of noise in redundant calibration solutions. They found that although the number of degeneracies decreased in the *4pol* scheme,  $V_{xy}$  and  $V_{yx}$  had low enough signal to noise that their inclusion in calibration greatly increased the noise in the gain solutions. Fixing only the 6 degeneracies of that scheme introduced much greater noise amplitude in the calibration solutions. However, fixing the 8 degeneracies from the *2pol* scheme *while still calibrating* with the *4pol* scheme gave almost identical gain solutions. Learning from this, we fix the 8 degeneracies from the *2pol* scheme throughout the rest of this work, independent of the calibration scheme used.

#### 7.1.1.4 Expectations from simulation

Using the formalism of Nunhokee et al. (2017) and Chapter 3, and the HFSS<sup>3</sup> complex voltage simulations of the PAPER beam described therein, we simulated the polarized response of the instrument to an unpolarized sky. That is, we passed a Stokes I - only sky model (de Oliveira-Costa et al., 2008) over a 30 m East-West baseline – the baseline vector of interest for the PAPER experiment (Parsons et al., 2014; Jacobs et al., 2015; Ali et al., 2015; Moore et al., 2017). This meant that whatever was observed in the pseudo-Stokes Q, U and V visibilities could be interpreted as direction-dependent leakage from

---

<sup>2</sup>As explored in the public HERA Memo #30.

<sup>3</sup><http://www.ansys.com/Products/Electronics/ANSYS-HFSS>

Stokes I (the expected regime for a single night of observations with PAPER; Kohn et al. (2016)). The 2008 Global Sky Model used for the simulation was primarily diffuse in nature, with the ‘A-Team’ of bright low-frequency sources (Fornax A, Pictor A, etc.) also included. The diffuse nature was appropriate for the fringe profile of a 30 m baseline. The output of the simulation is shown in Figure 7.1 with and without the inclusion of an instrumental noise model, with the system noise drawn from Moore et al. (2017).

### 7.1.2 Data Processing

We tested these different calibration schemes on one night (JD 2456680.20 – .65; January 22nd-23rd 2014; 6pm – 6am South African Standard Time; Local Siderial Time 2 – 13.5 hours) of PAPER 128-element observations. The PAPER-128 signal chain and full observation season results will be discussed in forthcoming publications, but we will provide a brief overview here.

PAPER-128 consisted of 128 dual-polarization dipole receivers, 112 of which are arranged in a highly-redundant configuration, and the rest placed as in- and outriggers to the array in order to improve *uv*-coverage; see Figure 7.2. Since all dipole arms were oriented North-South (‘x’) and East-West (‘y’), *xy* and *yx* correlations have very low signal-to-noise compared to *xx* and *yy*.

All visibilities were RFI flagged using PYTHON scripts from the AIPY<sup>4</sup> library. These took the derivative of the frequency axis of all baselines associated with a given antenna and flagged any frequencies with a derivative  $6\sigma$  above the mean, per integration. We took the union of all baseline flags and applied them to the data. The 5 MHz on both band-edges were always flagged. Compression proceeded as described in Appendix A of Parsons et al. (2014), filtering to critical Nyquist sampling rates for the longest (300 m) baseline of 493 kHz along the frequency axis (203 channels) and 42.9 s along the time axis.

After RFI flagging and compression, *xx* and *yy* visibilities were checked for erroneous

---

<sup>4</sup><https://github.com/HERA-Team/aipy>

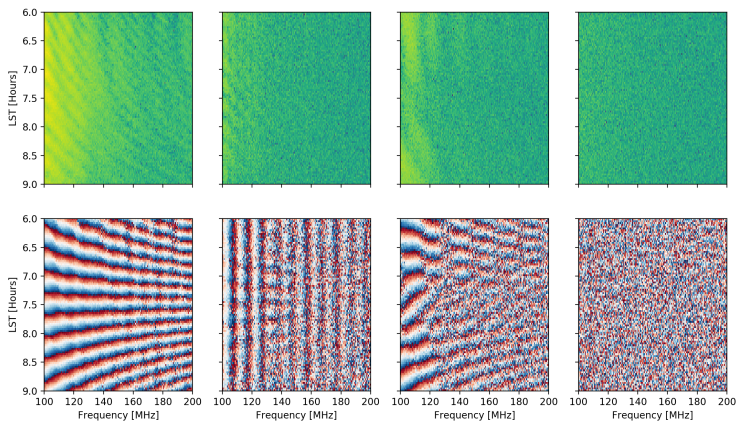
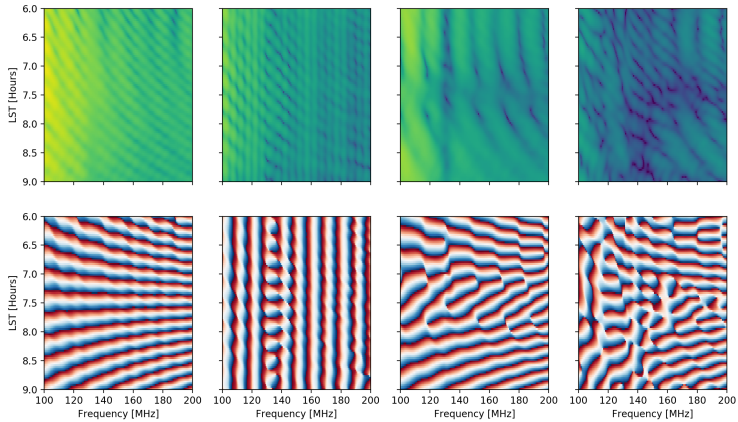


Figure 7.1: Simulations of absolute value (*upper panels*) and phase (*lower panels*) of pseudo-Stokes visibilities (left to right: pseudo-Stokes I, Q, U and V), as measured by a 30 m East-West PAPER baseline. The upper group shows the noiseless simulation, and the lower shows the same simulation with the addition of a realistic PAPER noise model (Moore et al., 2017). Only a Stokes I sky was used – all of the structure seen in  $V_Q$ ,  $V_U$  and  $V_V$  can be attributed to direction-dependent leakage.<sup>84</sup>

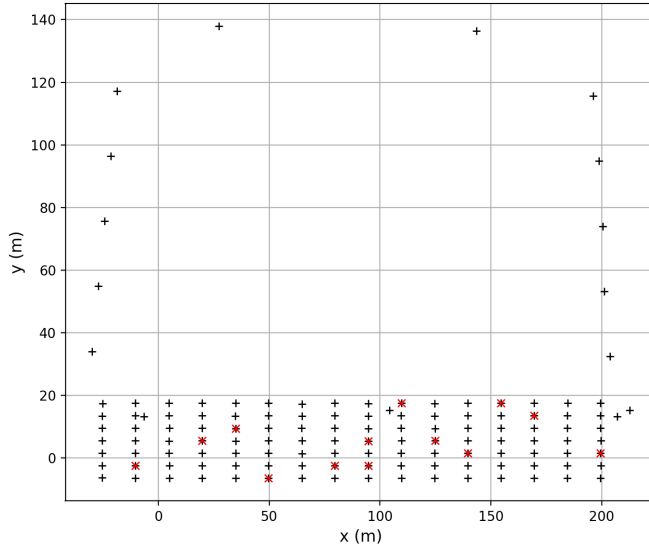


Figure 7.2: Arrangement of the PAPER-128 array. Antennae determined to be malfunctioning are shown with red crosses and were excluded from analysis.

behavior including  $2\sigma$  deviations from the median in number of RFI flags and mean visibility amplitude. Antennae exhibiting these behavior were excluded from further analysis (and are shown with red crosses in Figure 7.2). If an antenna qualified as ‘bad’ in one polarization, it was excluded in all of them. Also note that we could only calibrate the 112 antennae in the redundant grid using OMNICAL.

For the least-squares fit to converge at the *logcal* stage of calibration, visibilities cannot exhibit phase-wraps, since the system of equations solved at this stage are insensitive to additive offsets of  $2\pi$  in their imaginary parts (*lincal* will be able to re-insert these as required; Liu et al. 2010). Therefore we had to flatten the phases on all visibilities prior to any implementation of OMNICAL. We were able to do this redundantly without reference to the sky; taking the ratio of redundant (uncalibrated) visibilities together and averaging over time, defined as:

$$\mathcal{V}(\nu) = \langle V_{ij,pq}(\nu, t) V_{kl,pq}^*(\nu, t) \rangle_t. \quad (7.7)$$

Because this is the ratio of two nominally-redundant visibilities (i.e. baselines  $ij$  and  $kl$  belong to the same redundant group with model visibility  $V_{|i-j|,pq}$ ), and the measurements are not yet calibrated, we can expand Equation 7.7 as

$$\mathcal{V}(\nu) = \langle g_{p,i}^* g_{q,j} g_{p,k} g_{q,l}^* |V_{|i-j|,pq}|^2 \rangle_t. \quad (7.8)$$

Writing the complex gains as  $g_{p,a} = G_{p,a} e^{-i\nu\tau_{p,a}}$  for antenna  $a$ , we can reduce the product of gain-amplitudes and the squared visibility into some frequency-dependent function, and an exponential product of gain phase terms

$$\mathcal{V}(\nu) = K(\nu) \exp(i\nu(\tau_i - \tau_j - \tau_k + \tau_l)). \quad (7.9)$$

A Fourier transform along the frequency axis (which we term a *delay transform*; Parsons et al. 2012b) of  $\mathcal{V}(\nu)$  gave a function that was sharply-peaked at a given delay

$$\tilde{\mathcal{V}}(\tau) = \tilde{K}(\tau) * \delta_D(\nu(\tau_i - \tau_j - \tau_k + \tau_l)). \quad (7.10)$$

We can define a variable as the maximum of the above function:

$$\mathcal{T}_{ijkl}(\tau) = \max |\tilde{\mathcal{V}}(\tau)|, \quad (7.11)$$

which will occur at value

$$\tau = \tau_{\max} = \nu(\tau_i - \tau_j - \tau_k + \tau_l). \quad (7.12)$$

With enough redundant baselines involving antennae  $i, j, k \& l$  this is a linearly-solvable set of equations for each value of  $\tau$ . Multiplying  $V_{ij}$  by  $e^{-2\pi i\nu(\tau_i - \tau_j)}$  by definition flattened the phase across the band. This method was very sensitive to signal-to-noise, so these initial phase estimates were created with  $p = q$ ; that is  $xx$  and  $yy$  visibilities only. The estimates were then applied to all visibilities appropriately. We could then run OMNICAL according to each of the schemes described in Section 7.1.1.2.

### 7.1.3 Results

We ran OMNICAL using the *2pol*, *4pol* and *4pol+minV* schemes, which granted complex gain values for each antenna feed in the redundant grid. In this Section we chose to concentrate our analysis on the 30 m East-West spacings used for PAPER power spectrum studies.

#### 7.1.3.1 Calibration

The complex-gains dataset alone was highly multidimensional. We chose to analyze short time- and frequency- averages for these data. For example, the  $\langle |g_{x,a}^{2\text{pol}}| \rangle_{t,v}$  notation indicates the average of the absolute value of the gain value for antenna  $a$ , polarization ‘x’ in the *2pol* calibration scheme. The average was over 10 minutes (the length of a single MIRIAD file produced by the PAPER correlator) and a 10 MHz band running from 145 to 155 MHz (the center of the PAPER band, generally clear of RFI and used for power spectrum analyses).

Figure 7.3 shows  $\langle \arg(g_a^{2\text{pol}}) \rangle_{t,v}$ , the average phase of the gain calibration for ‘x’ and ‘y’ polarizations. It very clearly shows the phase-slope degeneracy present for both dipole orientations, sloping in opposite directions.

Figure 7.4 shows the differences in ‘x’ gain solutions between calibration schemes. The difference between *4pol* and *4pol+minV* was consistently smaller than the difference of either of these with the *2pol* scheme.

As noted in Section 7.1.1.3, OMNICAL tried to fix the average gain amplitude over the array to unity to avoid drifts in the amplitude degeneracy from sample to sample, so we were able compare amplitude calibrations in terms of percentage deviation. The average difference in gain amplitude per antenna between *2pol* and *4pol* was 3.5%, between *2pol* and *4pol+minV* was 2.9%, and was 0.7% between *4pol* and *4pol+minV*. The  $\sim 30$  degree spread in the differenced phases between the *2pol* scheme and the other two was likely due to different realizations of phase degeneracies between these calibration schemes.

Figure 7.5 shows the sum of  $w^2$  values (see Equation 7.6) over all antennas in the

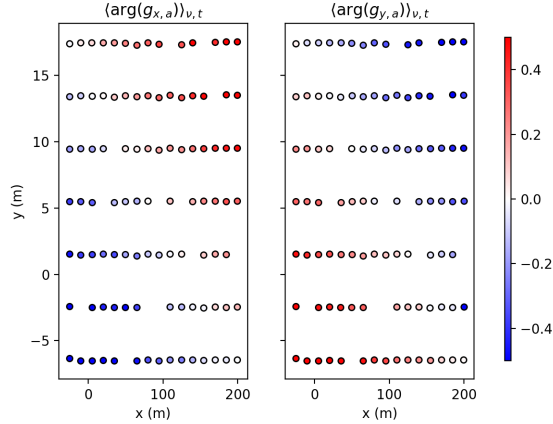


Figure 7.3: The phase of the complex gain value for the *4pol* calibration scheme is shown on the color axis (radians) for the redundant grid. The phase of the ‘x’ gains is shown on the left, and the ‘y’ gains on the right. The phase-slope degeneracy is clear in both panels, as is the fact that the slope is in opposite directions for the two dipole orientations.

array for each feed polarization in each of the three calibration schemes. The color scale is logarithmic. Clearly, the *2pol* scheme achieves a much greater level of redundancy in each feed polarization throughout the band. Towards the end of the night, the Galaxy was in the far side-lobes of the PAPER beam and introduces higher sky temperatures, which accounted for the trend in all calibration schemes performing worse towards the end of the night. However, the reason for rapid transitions in  $w^2$  at Local Sidereal Time  $\sim 10.5$  in the *4pol* and *4pol+minV* schemes is not well understood. In general,  $w^2$  was an order of magnitude higher for the *4pol* and *4pol+minV* schemes.

#### 7.1.3.2 Pseudo-Stokes Visibilities

Applying the complex gains to the visibilities, we constructed pseudo-Stokes visibilities. These data are shown in Figure 7.6. Figure 7.7 shows the delay-transformed pseudo-Stokes visibilities. The “stripe” of power across the frequency axis within the first 100 integrations was a thermal effect due to the sun not yet being fully below the horizon.

The upper panels in Figure 7.6 – the absolute-valued visibilities – show that Stokes

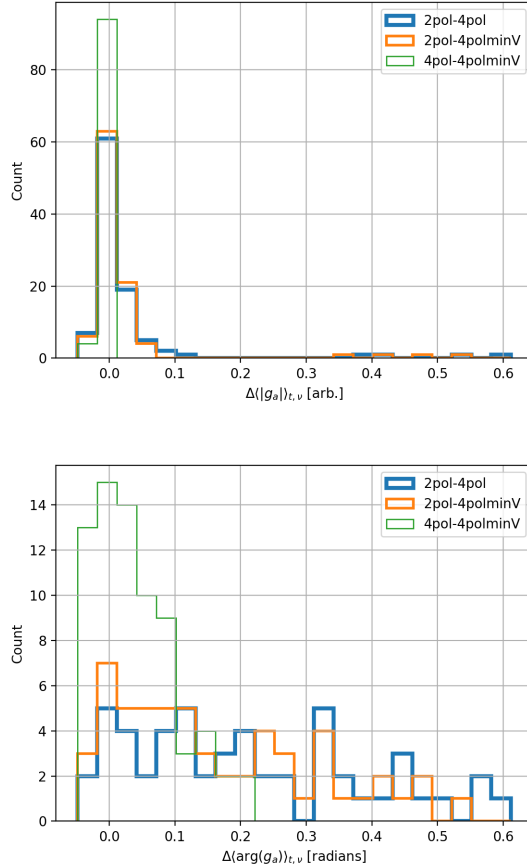


Figure 7.4: Histograms of differences in the ‘x’ gain calibrations per antenna between calibration schemes. Above: difference in absolute value. Below: difference in phase. For most antennae, absolute value of the gain does not change by large amounts between calibration schemes; most of the change takes place in the phase. The difference between *4pol* and *4pol+minV* is consistently smaller than the difference of either of these with the *2pol* scheme. This is likely a sign of different realizations of phase degeneracies between calibration schemes.

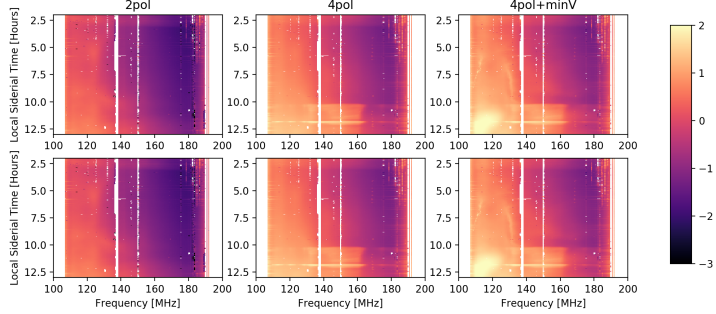


Figure 7.5:  $w^2$  values, summed across the array, for the  $x$  (above) and  $y$  (below) feeds in different calibration schemes. From left to right: *2pol*, *4pol* and *4pol+minV*. The color axis is logarithmic, in arbitrary data units. The white gaps are due to RFI flagging.

I power was dominant given any calibration scheme used. This was expected, since the linear polarizations had much higher signal-to-noise than the cross polarizations that form  $V_U$  and  $V_V$ . We saw that the amplitude of pseudo-Stokes Q was reduced across the band in the *4pol* and *4pol+minV* schemes. This was also expected, given that these calibration schemes allowed information in  $xx$ -polarized visibilities to influence the calibration of  $yy$ -polarized ones, and vice-versa. In the regime of a single night's observation, we did not expect to observe substantial power from the Stokes Q sky (Kohn et al., 2016; Lenc et al., 2016; Moore et al., 2017). Although we set no specification on the Stokes Q sky during calibration, we observe our gain solutions tending towards lower Stokes Q power during polarized redundant calibration.

A similar but less-substantial difference was seen in the pseudo-Stokes U visibility amplitudes, but an interesting interplay between pseudo-Stokes U and V was more clearly seen in the delay-transformed visibilities in Figure 7.7. First, we must observe that the *4pol+minV* calibration scheme worked as expected, reducing the amplitude of pseudo-Stokes V across most of the band. In Figure 7.7, we show that the difference between the foreground signal for pseudo-Stokes U and V in the *4pol* case, compared to the *4pol+minV* case, was the increase in U signal and the decrease of V. This effect was observed in Kohn et al. (2016) when minimizing pseudo-Stokes V using an array-wide

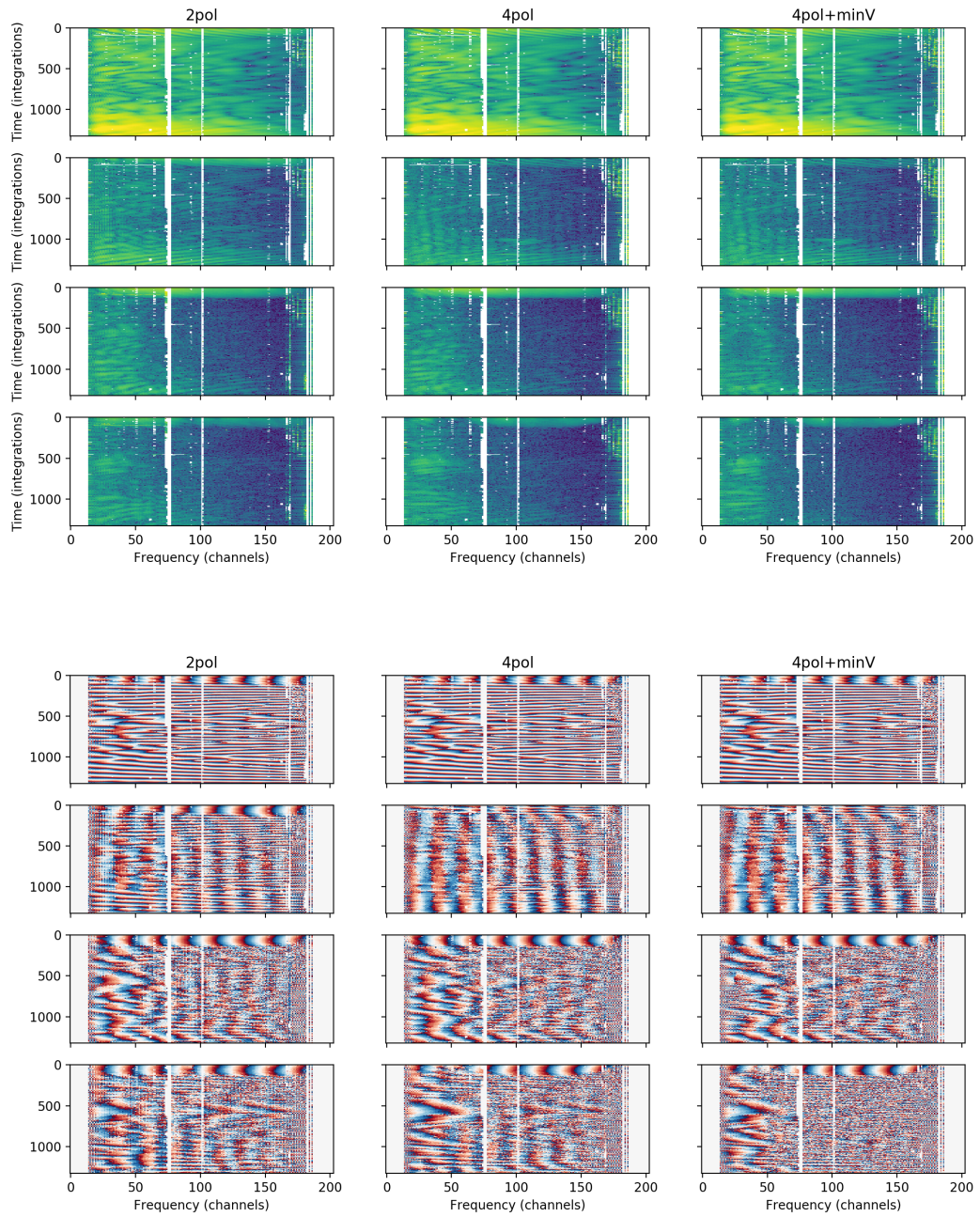


Figure 7.6: Pseudo-Stokes visibility amplitudes (*top*) and phases (*bottom*). Amplitudes are plotted on a logarithmic color scale that spans 3 orders of magnitude (without absolute calibration, this scale is in arbitrary units). Phases are on a linear scale of  $-\pi$  to  $\pi$ . The three columns correspond to the three different calibration schemes. Rows are from top to bottom:  $V_I$ ,  $V_Q$ ,  $V_U$ , and  $V_V$ .

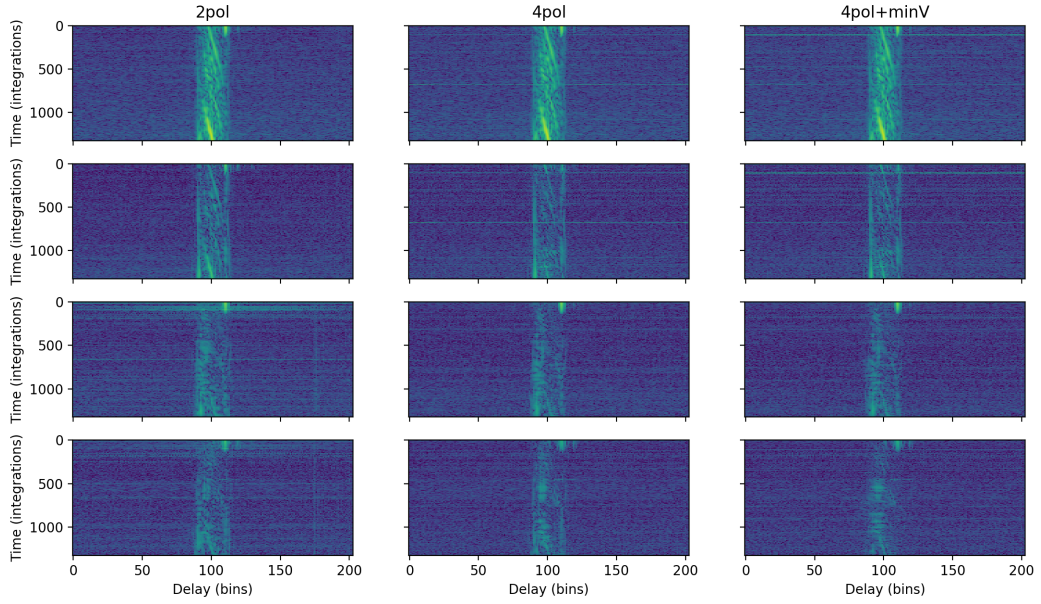


Figure 7.7: Delay-transformed pseudo-Stokes visibilities. Plotted on a logarithmic color scale that spans 4 orders of magnitude (without absolute calibration, this scale is in arbitrary units). The three columns correspond to the three different calibration schemes. Rows are from top to bottom:  $V_I$ ,  $V_Q$ ,  $V_U$ , and  $V_V$ .

constant, as opposed to the per-sample basis implemented in this work. It is mathematically consistent with partially accounting for uncalibrated  $D$ -terms on each feed.

We also note that the lowest frequencies in the band (below channel 70) are consistently poorly behaved. This is a property seen in many PAPER measurements (e.g. Jacobs et al., 2015; Moore et al., 2017) and is due to brighter foregrounds at low-frequencies, a larger solid angle of the beam, and higher receiver temperatures at lower frequencies.

A comparison of the simulations presented in Figure 7.1 is best made using the phase panels of Figure 7.6. Comparison of phase structure in frequency and time showed that the  $4pol+minV$  scheme gave the best match with simulation. The  $2pol$  scheme did not allow pseudo-Stokes Q visibilities to be constructed in a way that replicates the constant-in-time striping seen in the simulations. Instead, we see an imprint of the fringing as seen in

pseudo-Stokes I. This was most likely direction-independent leakage from this parameter. The *4pol* and *4pol+minV* schemes contained most of this fringing to the pseudo-Stokes I visibilities. The *4pol+minV* scheme achieves a noise-like pseudo-Stokes V, whereas the *4pol* scheme shows V at a higher signal-to-noise than expected from PAPER system temperature measurements.

### 7.1.4 Discussion & Conclusions

The OMNICAL software package was optimized to calculate diagonal gains as efficiently as possible (Zheng et al., 2014). Of course, this meant that it is impossible to fully address the *D*-terms in the instrumental Jones matrix (e.g. Thompson et al., 2017) within the OMNICAL framework. This incomplete modelling of the instrument will result in biased gain solutions (e.g. Barry et al., 2016; Dillon et al., 2017).

Dillon et al. (2017) showed that the relative gain error incurred through redundantly calibrating in the presence of 1% *D*-terms was  $\sim 0.3\%$  in the *2pol* scheme, and systematically higher in the *4pol* scheme by an additional  $\sim 0.2\%$ . Additional work is required to understand how the *4pol+minV* calibration scheme interacts with *D*-terms.

In this Section we have demonstrated the capacity for polarized redundant calibration of radio interferometric data from the PAPER-128 array. The three redundant calibration schemes we investigate have different strengths. Neglecting the polarized component of the measurements in the *2pol* scheme grants lower values of  $w^2$  than the other schemes. Imposing that the Stokes V sky be empty in the *4pol+minV* gives the best agreement with simulation. Conservatively, this points to using the *2pol* scheme to give the most precise gain calibrations. However, given that *2pol* matches full-polarization simulations the least well, the calibrations it produces may be inaccurate, even if they are precise.

Unlike PAPER, HERA is designed to be both highly-redundant and a capable imaging array, since outrigger antennae, although physically separated from the redundant core, are arranged on their own redundant sub-grid, and the redundant core itself is fragmented into three redundantly-calibrate-able sub-grids (see Dillon & Parsons 2016 for

full details). The utility of redundant and imaging calibration routines will allow for more thorough tests of the nature of the polarized sky at low frequencies.

## 7.2 Imaging Calibration

The PAPER-32 imaging array sampled a large region of the *uv*-plane at relatively low signal-to-noise (see Chapters 4, 9 and Kohn et al. (2016)). The extreme wide field of view of the PAPER feeds provided an interesting opportunity to test polarized imaging calibration. In this Section we provide an initial exploration of PAPER-32 data using the CASA software package (McMullin et al., 2007).

### 7.2.1 Converting historical PAPER data into Measurement Sets

As described in Chapter 4, PAPER-32 was arranged in an imaging configuration for three nights in September 2011. In order to interact with these data using modern software packages, including the conversion into “Measurement Set” format used by CASA, several changes to the MIRIAD files had to be implemented.

1. After the first night of integration, it was discovered that antenna number 24 was malfunctioning, and it was replaced with antenna number 63. This presents complications for conversion into Measurement Sets, since this format requires a constantly-incremented antenna axis – no numbers may be “skipped”. A simple work-around is to relabel the data from antenna 63 to that of antenna 24.
2. The PAPER-32 imaging configuration was really a subset of the PAPER-64 imaging configuration. The existing correlator had only 64 inputs, so the 64-element imaging configuration could be run in single-polarization mode, or half of it could be used in full-polarization mode. However, within the MIRIAD files, 64 antennas are listed, with only half of them containing data. These must be specifically down-selected upon.

3. PAPER correlators incorrectly labelled the  $uv$  coordinates of all baselines. This was by design, since PAPER build outs were purposefully reconfigurable and therefore the antenna positions were not built-in to hardware. However, correct  $uv$  information is essential for imaging algorithms. These coordinates must be placed inside the MIRIAD file, instead of supplied externally.
4. CASA cannot convert MIRIAD files to Measurement Sets on its own, but it can do so for UVFITS files. Seamless MIRIAD to UVFITS conversions are implemented by the `pyuvdata` Python package (Hazelton et al., 2017). During conversion, antenna diameters and physical antenna positions must be supplied as metadata.
5. CASA’s `importfits` function can then be used for the UVFITS to Measurement Set conversion.

After a successful conversion, an additional step needs to take place within the CASA Measurement Set. The MIRIAD files could have their antenna indices out of order, such that a baseline could be referenced as  $i, j$  where  $i > j$ . This can be easily corrected within the CASA console.

### 7.2.2 Imaging PAPER-32 data with CASA

To calibrate the complex gains, we had to provide CASA with a *model image*, from which it will create model visibilities by convolving with a model beam (assumed to be Gaussian, with Full-Width Half Max based on the antenna diameter) and sampling the  $uv$ -plane according to the antenna positions provided. Images of the primary beam model and point spread function of the PAPER-32 array are shown in Figure 7.8. The model visibilities were compared to the observed ones, and CASA’s internal fitting algorithms determined complex gains to bring the ratio close to unity.

The times observed by the PAPER-32 imaging array contained the transits of Pictor A and Fornax A. Pictor A is one of the brightest sources in the low frequency sky, is an unresolved point source, and has a simple spectrum (Jacobs et al., 2013):

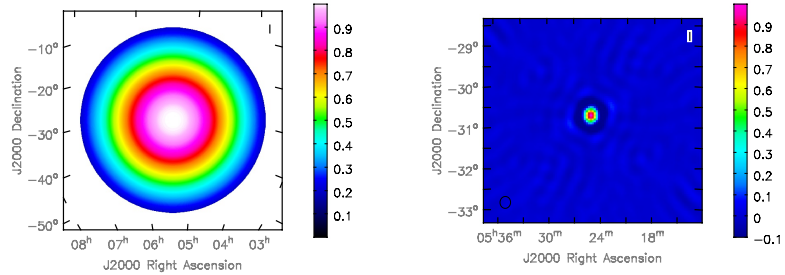


Figure 7.8: The beam model and point spread function of the PAPER-32 array, calculated by CASA. In reality, the beam is far less symmetric (e.g. Parsons et al., 2010). The PSF is likely more accurate. Note the difference in axis scales between the two panels.

$$S_{\text{PicA}}(\nu) = 382 \pm 5.4 \text{Jy} \times (\nu/150\text{MHz})^{-0.76 \pm 0.01}, \quad (7.13)$$

making it an ideal flux-calibrator. While it is highly polarized at optical wavelengths ( $\sim 50\%$  Thomson et al., 1995), it has a low polarization fraction at radio frequencies ( $< 5\%$ ; Perley et al. (1997); Huffenberger et al. (2015)). Little-to-no expected polarization is useful for obtaining diagonal gains, but a polarized point source is more useful for precisely calculating the off-diagonal  $D$ -terms (see, for example, Chapter 3 or Thompson et al. (2017)). There is a dearth of low-frequency polarized point sources in the low frequency sky (Bernardi et al., 2013; Asad et al., 2016; Lenc et al., 2016), and only one that is bright enough to be detected by PAPER-32 – PMN J0351-2744 – and this we were not able to detect.

To increase the precision of our calibration model, we included a model of Fornax A as well as Pictor A. Fornax A is a bright, resolved radio galaxy which we modelled using three spherical components for its East lobe, West lobe and central core according to MWA observations (McKinley et al., 2015):

$$S_{\text{East}}(v) = 260 \text{Jy} \times (v/154\text{MHz})^{-0.77}, \quad (7.14)$$

$$S_{\text{West}}(v) = 480 \text{Jy} \times (v/154\text{MHz})^{-0.77}, \quad (7.15)$$

$$S_{\text{Core}}(v) = 12 \text{Jy} \times (v/154\text{MHz})^{-1.00}. \quad (7.16)$$

$$(7.17)$$

Fornax A has been found to have a low polarized fraction at higher frequencies (20 GHz López-Caniego et al., 2009), and a  $\sim 20\%$  polarized fraction at 1.51 GHz (Fomalont et al., 1989). Bernardi et al. (2013) found no evidence for polarized emission at 151 MHz using the MWA-32, which may have been partially due to beam depolarization (an effect that would only increase with PAPER-32).

Using this two-source (but with four points) sky model, we used the CASA `gaintcal` and `bandpass` routines to calibrate a 10 minute snapshot of the transit of Pictor A. We were able to specify a “Stokes Vector” for each source, and we used  $S = (1, 0, 0, 0)$ : that is, all components were strictly unpolarized. Applying the calibration solutions and gridding to the *uv*-plane and CLEANing granted the pseudo-Stokes images shown in Figure 7.9. As expected, Pictor A dominated the sky in pseudo-Stokes I. However, an excess at its position in the pseudo-Stokes Q image suggested a mis-calibration in the diagonal gains at the  $\sim 10\%$  level. No sources are visible above the noise in pseudo-Stokes U and V. However, these parameters (as well as pseudo-Stokes Q) exhibited a high fringe-rate oscillation in the North-West to South-East direction, which suggested that a long baseline of that orientation was poorly calibrated, or the antenna was malfunctioning. A similar effect was seen with a low fringe-rate from North-East to South-West, suggesting a problem on a short baseline with that orientation. Indeed, Kohn et al. (2016) found three malfunctioning antennas during their study using the PAPER-32 imaging array, which match the orientation and lengths indicated by the fringing (see Chapter 9, Figure 9.1). Removing those antennas resulted in cleaner images with lower noise-floors, as shown in Figure 7.10. New fringing is seen at various angles, the source of which would be more

difficult to identify. Excesses at the position of Pictor A in pseudo-Stokes U and V are likely the result of uncalibrated D-terms, which will be addressed in Section 7.2.3. The morphology of point sources in pseudo-Stokes I matched the PSF shown in Figure 7.8, showing that the CLEAN algorithm converged when during imaging.

We were able to test the stability of the instrument by applying the calibration solutions derived from the Pictor A transit to a completely different field. The imaging results of such a test at  $LST \approx 0.5$  hours are shown in Figure 7.11. The pseudo-Stokes I image showed a point-source dominated field, as expected for this LST, and pseudo-Stokes Q, U and V were dominated by noise. These results were proof of instrument stability in time at the  $\sim 6$  hour level.

### 7.2.3 D-term calibration

Calibration of the off-diagonal terms of the instrumental Jones matrix can be partially calculated using a Stokes I-only sky model. If there were a visible source of known polarization fraction, an absolute phasing could be derived based on its polarization angle. Using the source model described in the section above, we were able to calculate the magnitude of the off-diagonal,  $D$ -terms.

CASA supplies routines for linear-basis feeds that iteratively solve for ‘x’ and ‘y’ gains by, in our case, maximizing pseudo-Stokes I and minimizing pseudo-Stokes Q (if the polarization fraction was known, it would regress on that fraction for pseudo-Stokes Q). The `polcal` routine uses a built-in regressor to find the best fit for the  $D$ -terms, given previous calibrations. That is, one must have supplied an initial gain calibration and a guess of the parallactic angle of the polarized source.

Using `polcal` on the Pictor A field described in the previous section granted  $D$ -term estimates of  $\sim 5\%$ ; comparable to other low-frequency instruments (MWA-32 was found to have  $\sim 2\%$   $D$ -terms [G. Bernardi, private communication]). Correcting for these granted identical pseudo-Stokes I and Q images and lower-amplitude pseudo-Stokes U and V – as expected for a regime where pseudo-Stokes I leakage dominates over actual

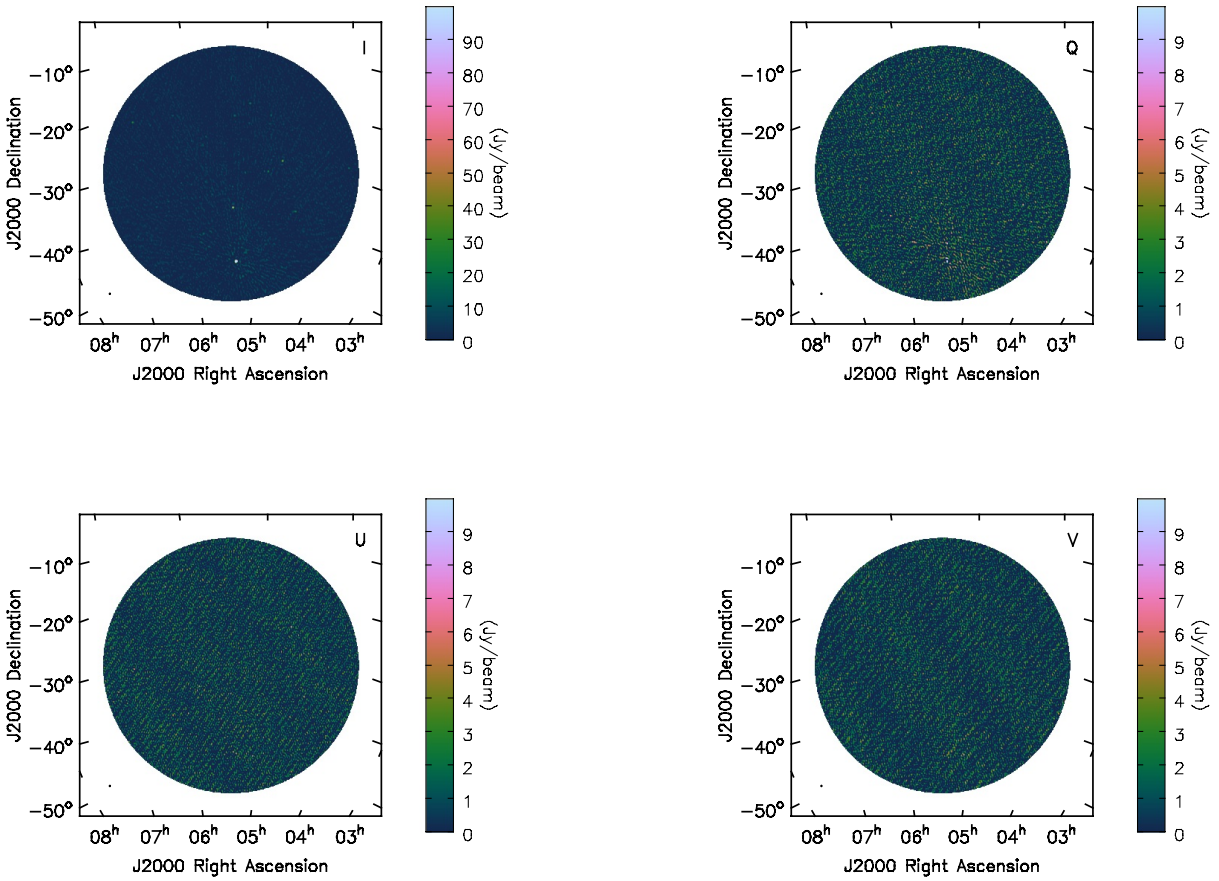


Figure 7.9: Full-polarization imaging results from a four-component, Stokes I-only sky model. Images are multi-frequency syntheses from 110 to 180 MHz. Pictor A, the brightest unresolved source in the Southern Sky at our frequencies, is in transit and dominates the sky in pseudo-Stokes I. An excess in pseudo-Stokes Q at the  $\sim 10\%$  level indicates inaccuracies in the gain calibration. Pseudo-Stokes U and V are noise-like, save for a fringe that rises above the noise – indicating a poor calibration of a single baseline of that orientation.

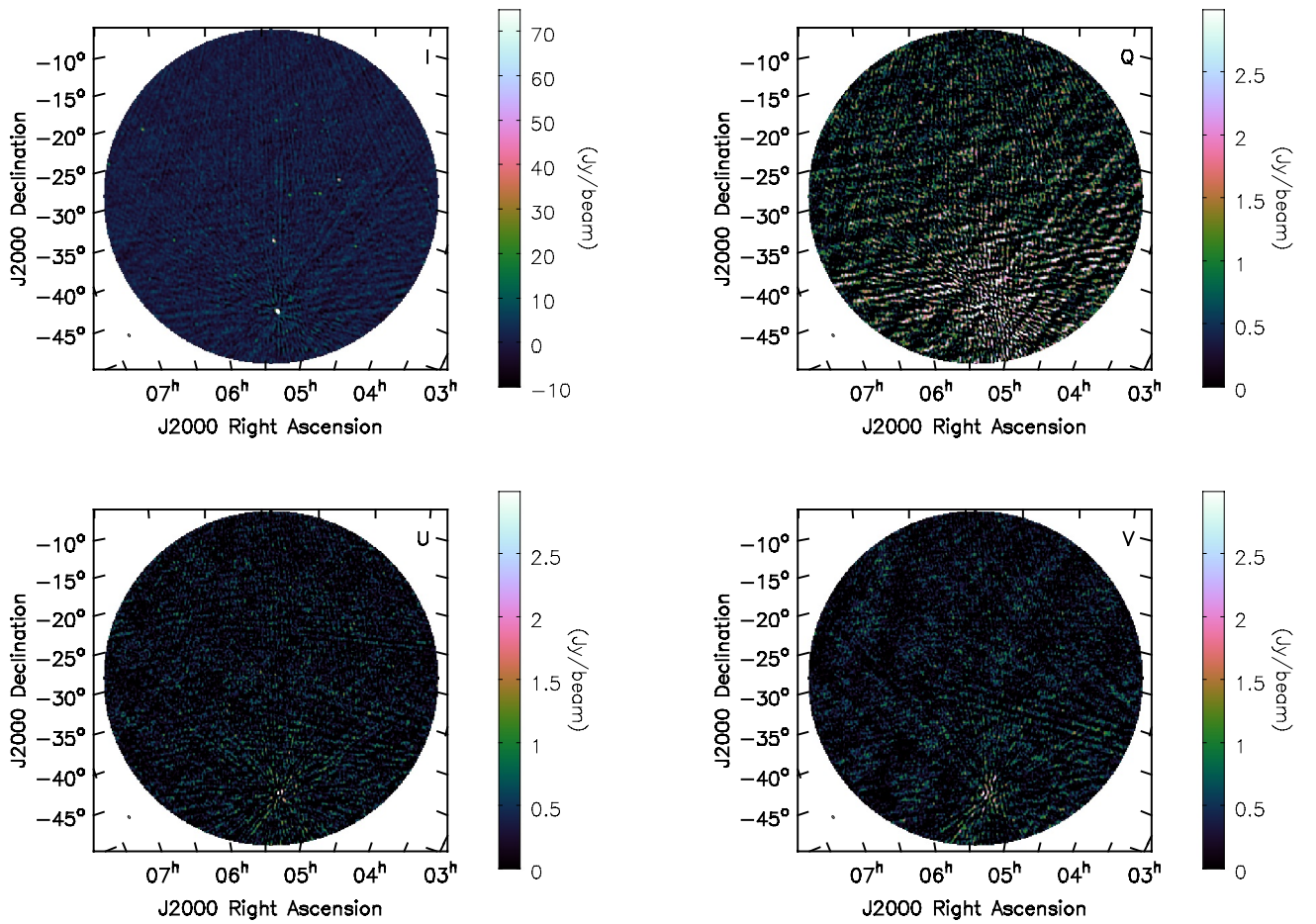


Figure 7.10: The same field as shown in Figure 7.9, but with the removal of malfunctioning antennas identified by Kohn et al. (2016). The noise level drops and much of the fringing in pseudo-Stokes Q, U and V disappears (note the change in color scales and zoom level).

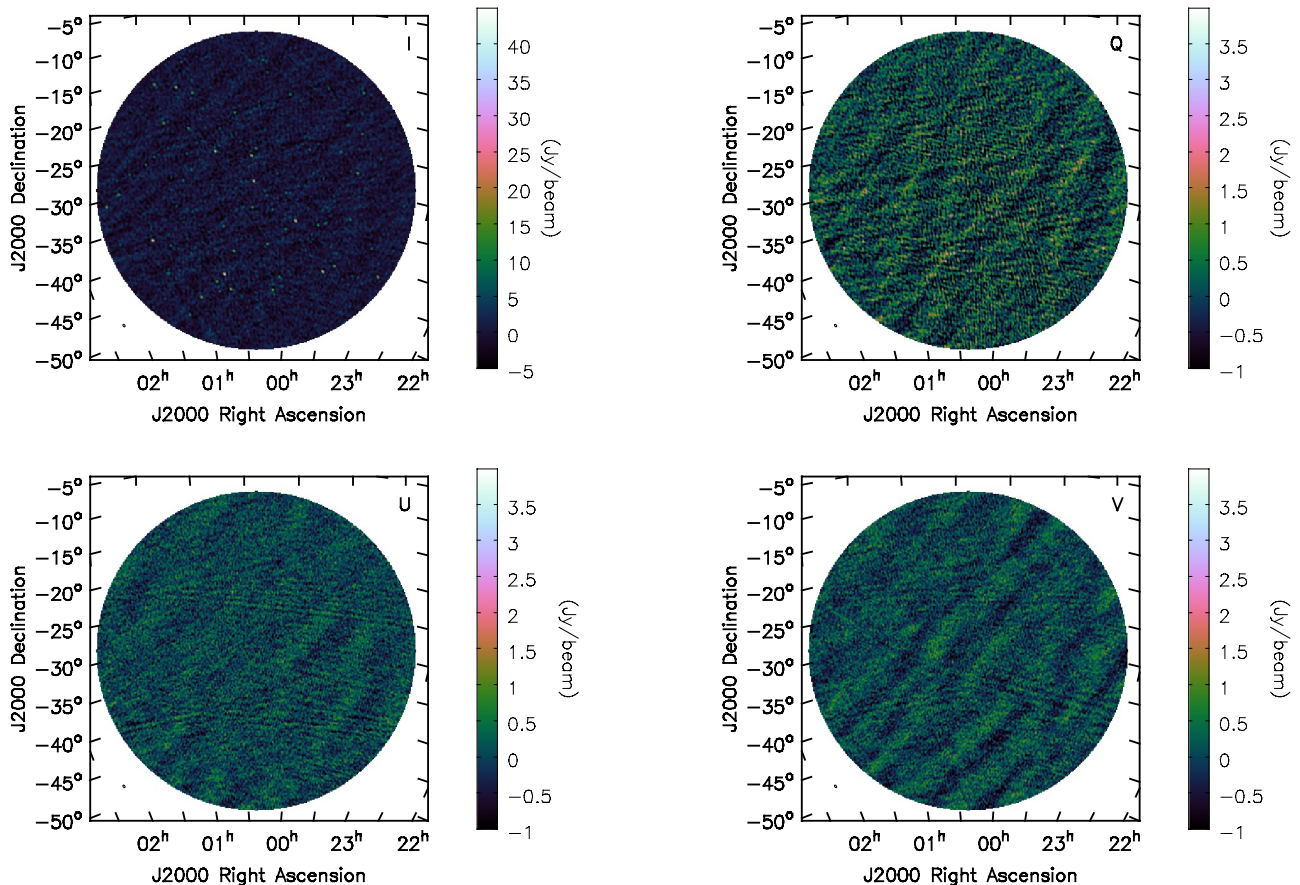


Figure 7.11: Imaging results from a file calibrated with gain values derived from the Pictor A transit, which occurred  $\sim$ 6 hours after these data were acquired. The realistic images suggest that the instrument is stable on such time scales.

polarized power. The improved U and V maps are shown in Figure 7.12.

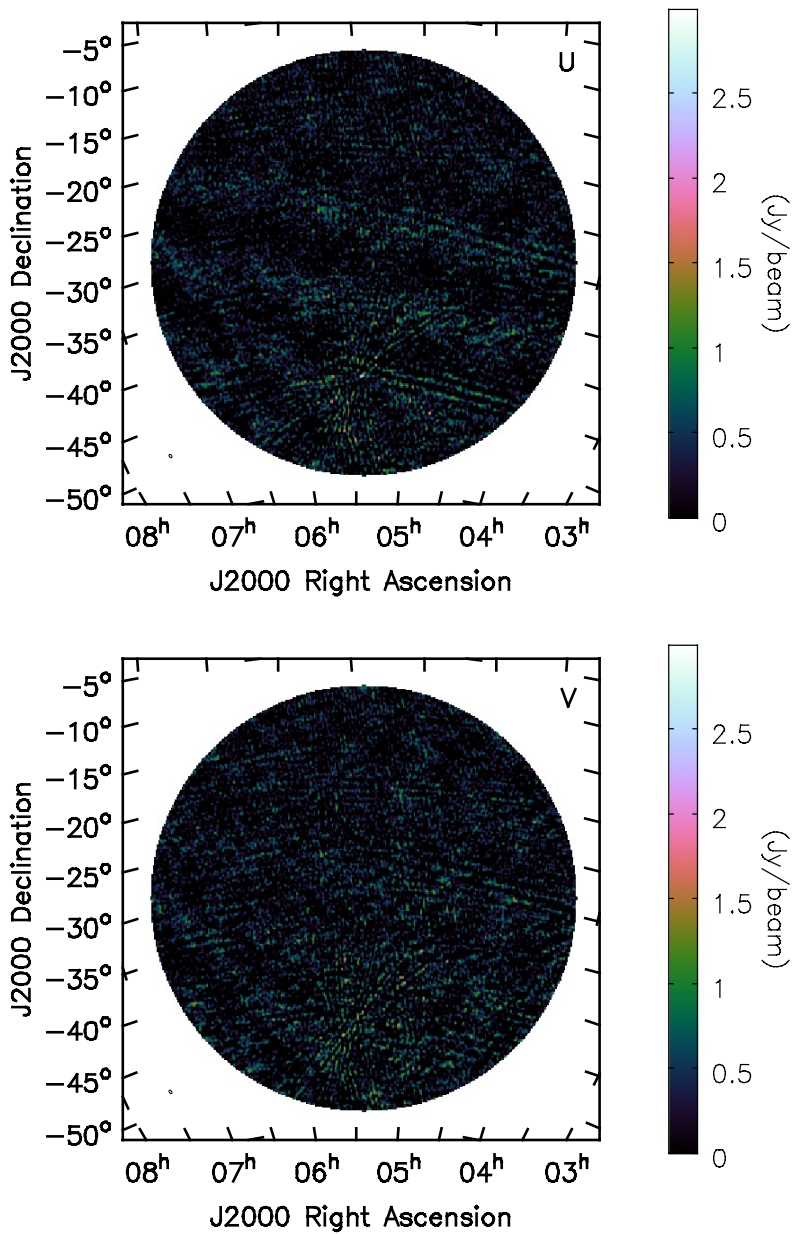


Figure 7.12: The same field as shown in Figure 7.10, but for pseudo Stokes U and V only, with  $D$ -terms partially calibrated. Comparing to Figure 7.10, the amplitude at the position of Pictor A has decreased. Pseudo-Stokes I and Q maps are not shown, since they are qualitatively identical to the images in Figure 7.10 – as expected for a regime in which pseudo-Stokes I leakage dominates over actual polarized power.

# Chapter 8

## The Ionosphere

The ionosphere is a section of Earth's atmosphere composed of several layers, between 60 and 1000 km in altitude. It overlaps the Troposphere, Stratosphere, Mesosphere, Thermosphere and Exosphere. The ionosphere is an ionized plasma, composed of ions from molecules in the atmospheric layers it overlaps that are ionized by solar radiation. The ionization state of the ionosphere can be quantified by the Total Electron Content (TEC) – an integral of electron count in a given direction – among other metrics.

Spatiotemporal variations of the TEC are tied to solar activity, and therefore largely both diurnal and seasonal. More ionization, and therefore a larger TEC, is to be expected in the day time and closer to the summer solstice. The Solar Cycle also influences TEC, with more sunspots proportional with a higher TEC; at solar maximum, this effect dominates the seasonal variation (Sotomayor-Beltran et al., 2013). Ionospheric variations are typically described as Kolmogorov turbulence (i.e. small scale motions are isotropic in their direction and scale with wavenumber; Zolesi & Cander 2014), however, LOFAR observations report deviations from isotropy in their observations (Intema et al., 2009; Mevius et al., 2016). Regions of the ionosphere that can be assumed to be constant in density and shape at a given time are referred to as "isoplanatic patches". At 74 MHz, these patches are observed to be  $1^\circ - 2^\circ$  in radius (Cotton & Condon, 2002).

The ionosphere is composed of three main layers: D, E and F, which vary according to

Table 8.1. Ionospheric Layers

Layer	Time	Altitude km	Components	Electron Density $e^- m^{-3}$
D	Day	60–90	$\text{NO}^+$ , $\text{N}_2$ , $\text{Ar}$ , $\text{O}_2^-$	$10^8 - 10^9$
E	Day/Night	90–150	$\text{NO}^+$ , $\text{O}_2^+$ , $\text{O}^+$ , $\text{N}_2^+$	$10^{11}$
$F_1$	Day	140–600	$\text{NO}^+$ , $\text{O}_2^+$ , $\text{O}^+$ , $\text{N}^+$	$10^{11}$
$F_2$	Day/Night	220–800	$\text{O}^+$ , $\text{H}^+$ , $\text{He}^+$	$10^{10} - 10^{13}$

the day-night cycle. These are summarized in Section 8 (which summarizes Chapter 2 of Zolesi & Cander 2014). At night, there are not enough high-energy electrons to penetrate to lower altitudes, causing the D layer to recombine. The E layer increases in altitude at night due to a similar effect. The E and F layers persist at all times, but during daylight the F layer is divided into two sub-layers,  $F_1$  and  $F_2$ .

The diurnal nature of the ionosphere is important to radio propagation. During the day, the D layer reflects radio transmissions much closer to the Earth than during the night, when the E and F layers reflect. This leads to longer-range transmissions being possible after sunset<sup>1</sup>.

The relevance of the ionosphere to this work is its coupling with Earth's magnetic field. Recall that, as mentioned in previous chapters, a linearly polarized electromagnetic wave, propagating through an ionized plasma which has an incident magnetic field, will experience Faraday Rotation of its original polarization angle  $\chi$ :

$$\chi_{\text{obs}} = \chi + \phi \lambda^2 \quad (8.1)$$

where  $\lambda$  is the wavelength, and

$$\phi(\hat{s}) \approx 0.81 \int_{\text{source}}^{\text{obs}} n_e(\hat{s}) \vec{B}(\hat{s}) \cdot d\vec{s} \quad (8.2)$$

---

<sup>1</sup>This effect was first observed by E. V. Appleton (Appleton, 1946), confirming the ionosphere's existence, for which he was awarded the 1947 Nobel Prize in Physics.

where the source of the electromagnetic wave is in direction  $\hat{s}$  on the sphere,  $n_e$  is the electron density scalar field and  $\vec{B}$  is the magnetic vector field. The Rotation Measure (RM)  $\phi$  is the integral of the product along the line of sight, and has units of rad m<sup>-2</sup>. Since the ionosphere is capable of imparting an additional RM to polarized radio waves, inducing spectral structure to interferometric visibilities, understanding it is crucial to quantifying the effect of polarization on EoR measurements.

In this chapter, I review historical measurements of the ionospheric TEC and RM distributions in Section 8.1 and modern observations in Section 8.2. In Section 8.3 I present our work on the role of the ionosphere in PAPER and HERA measurements, and software we developed to quantify those effects.

## 8.1 Historical measurements of TEC and RMs

The existence and layered nature of the ionosphere was confirmed between the 1920s and the 1940s. Measurements of the TEC and RM distributions came later, once radio-communications satellites were put in orbit, and are closely tied to the Global Positioning System (GPS) launched in the late 1970s (called the NAVSTAR system). NAVSTAR GPS satellites transmit at two narrow frequency bands, centered about 1.2276 GHz (“L<sub>2</sub>”) and 1.57542 GHz (“L<sub>1</sub>”). Encoded in these transmissions are the local clock times per satellite (precisely calibrated with one another and with ground clocks) and their positions. With four satellites in view of a receiver, one is capable of computing their three-dimensional position and their local clock relative deviation from the satellite clock time.

MacDoran & Spitzmesser (1989) showed that one could use a frequency-dependent time delay induced by the ionospheric plasma (Klobuchar, 1983; Brunner & Welsch, 1993):

$$\Delta t_{\text{iono}} = \frac{40.3}{cv^2} \text{TEC} \quad (8.3)$$

to calculate an estimate of the TEC in the direction of a GPS satellite. Their approach

has been continuously refined. Using an estimate of the polarization angle of the emitted L<sub>1,2</sub> transmissions, Titheridge (1972) and Royden et al. (1984) presented measurements of TEC by measuring the Faraday Rotation induced and worked towards an estimate of the TEC based on the RM. Lanyi & Roth (1988) showed that the more accurate method was calculation of the TEC using  $\Delta t_{\text{iono}}$  from Equation 8.3. Mannucci et al. (1998) introduced the Ionosphere Map Exchange Format (IONEX): a method and file format for storing TEC measurements using GPS beacons across the globe, allowing the first global TEC maps to be calculated. IONEX files contain global TEC measurements with a 2 hour cadence and generally 5° by 2.5° resolution in longitude and latitude respectively. They neglect the layered nature the ionosphere, modelling it as a thin sheet. Iijima et al. (1999) provided a server that automatically pushed IONEX files to the World Wide Web as soon as they could be constructed. Komjathy et al. (2005) presented the first measurements with over 1000 GPS stations. Recently, Erdogan et al. (2016) presented a method for time-series forward modelling of the TEC distribution using IONEX files.

Meanwhile, many generations of the International Geomagnetic Reference Field (IGRF Finlay et al., 2010) have continually improved the model of the Earth's magnetic field. This model is composed by spatial interpolation of magnetic field measurements (in up to 13th-order spherical harmonic coefficients) reported by institutions around the world.

Combining these two measurements – IONEX and IGRF data – can provide a map of RM distribution above any given position on Earth to moderate precision (better in the Northern Hemisphere than the Southern one, based on the number of GPS beacons in each). Afraimovich et al. (2008) offered the first such software implementation, with the objective of using it to track Solar Activity<sup>2</sup>. Sotomayor-Beltran et al. (2013) introduced the `ionFR` package, which calculated ionospheric RMs towards a given position on the sky. We generalized their approach for the wide-field measurements in our `radionopy` software package, which we present in Section 8.3.

---

<sup>2</sup>Erickson et al. (2001) were the first to present software capable of calculating ionospheric RMs using the IGRF, but they used local GPS beacons instead of IONEX files

## 8.2 Low frequency observations: discoveries and challenges

Low frequency interferometric observations are effected in two main ways by ionospheric turbulence: scintillation in Stokes I observations, and Faraday Rotation in Stokes Q and U observations.

TEC variations introduce a variable index of refraction across a field of view. Stokes I signal from a point source will scintillate, change position, by an amount (e.g. Thompson et al., 2017):

$$\Delta\theta = -\frac{1}{8\pi^2} \frac{e^2}{\varepsilon_0 m_e} \frac{1}{v^2} \nabla_{\perp}(\text{TEC}) \quad (8.4)$$

at the observed frequency  $v$ , where  $\nabla_{\perp}$  is the transverse gradient in TEC towards the direction of the source. The time, space and frequency dependence of this effect causes difficulty for long integrations, since the scintillation will cause averaging of point sources with empty space, spreading-out their signal over a  $\sim \Delta^2\theta$  area. This can be interpreted as an additional source of noise in a Stokes I map. Vedantham & Koopmans (2015) showed that this scintillation noise can be much larger than image noise for baselines longer than  $\sim 200$  m. Vedantham & Koopmans (2016), extending the previous analysis to the Fourier domain, showed that this noise does not pose large issues to HERA or SKA-Low EoR efforts, since realistic amounts scintillation were not sufficient to wash-out EoR signals on large scales (their dense cores of relatively short baselines also help). However, it could pose large issues for point-source calibration and subtraction methods – as emphasized in a public SKA memo by Cornwell (2016).

Loi et al. (2015) used MWA observation snapshots to map the scintillation as a function of space and time, resulting in the discovery of “tubes” of plasma density waves across the Southern Hemisphere in lines of roughly constant latitude. Comparing the sources in their snapshot images to source positions in the NRAO VLA Sky Survey (NVSS Condon et al., 1998) they were able to calculate displacement vectors, and showed

that they were strongly aligned to Earth’s magnetic field.

The literature surrounding ionospheric Faraday Rotation is less extensive than work focussing on the unpolarized component. Lenc et al. (2016) showed that MWA measurements of diffuse foregrounds could provide a map of ionospheric spatiotemporal variance as their RM changed throughout a series of observations. Lenc et al. (2017) showed that point source power could be seen “twinkling” in and out of polarized intensity maps due to ionospheric activity.

### 8.3 Relevance for PAPER and HERA EoR measurements

Within the PAPER and HERA power spectrum pipelines, many tens to hundreds of days of visibilities are averaged over during binning in LST. The ionosphere-induced spatial and temporal fluctuations in RM could produce sufficient phase scrambling of the celestial Faraday-rotated, polarized signal to suppress a fraction of any polarized signal leaked by some mechanism into Stokes I measurements. The fringe size of the 30 m baselines used in power spectrum analyses is large enough that scintillation effects are negligible.

This effect was first investigated in Moore et al. (2017). Using the `ionFR` package (Sotomayor-Beltran et al., 2013) we calculated the RM distribution at a single zenithal pointing throughout the PAPER-32 observation season. This was a vast simplification given the PAPER primary beam was much larger than a typical isoplanatic patch. Shown in Figure 8.1, there was a large spread of ionospheric RMs for each LST. There was a decrease in the average magnitude of the RM as LST increased. This was expected, given the strong correlation between the day/night cycle and TEC values (e.g. Tariku, 2015), and given that for this observing season, LST=4 hr corresponded to observations taken shortly after sunset, while LST=8 hr was always well into the night.

Treating the single pointing as constant over the sky, we calculated the expected attenuation of polarized signal, leaked into pseudo-Stokes I visibilities, that would be averaged over varying ionospheric conditions during LST binning. These attenuation factors were

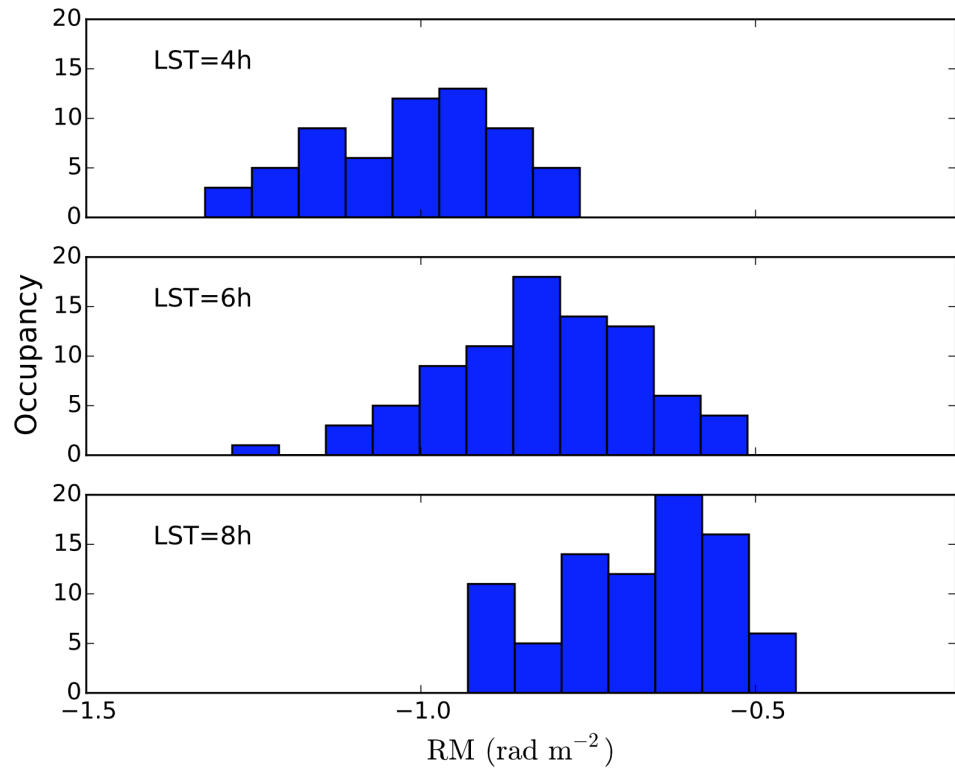


Figure 8.1: Distribution of zenithal ionospheric RMs for 3 LSTs in the PAPER-32 observing season. From top to bottom: a histogram of the zenith ionospheric RMs over the season, for the transit of LSTs 4, 6, and 8 hr. Taken from Moore et al. (2017).

$43 \pm 6\%$  at 165 MHz and  $7 \pm 5\%$  at 126 MHz.

To build on this result, we required more sophisticated simulations of the interaction of the polarized sky with the instrument and whole-sky maps of the ionosphere. To accomplish the latter, we developed the open-source Python package `radionopy`<sup>3</sup>. Like `ionFR`, `radionopy` uses GPS-derived TEC maps from IONEX files and the IGRF to estimate the value of ionospheric RM at a given latitude, longitude and date. Unlike its predecessor, `radionopy` does not necessarily calculate an RM at a given pointing, but instead is capable of calculating the ionospheric RM over a HEALPix grid of the sky (Górski et al., 2005). Such an expression of ionospheric variation is natural to wide-field, drift-scanning EoR arrays, and reflects the format of the IONEX input measurements, which are given in their spherical harmonic decompositions. `radionopy` is vectorized, leading to efficient generation of full-sky ionospheric maps, and object-oriented, allowing for easier collaborative development. Additionally we implemented the interpolation scheme recommended in the IONEX documentation to obtain “best-guess” full-sky maps for arbitrary times between the 2-hour time resolution of IONEX data.

An example output from `radionopy` is shown in Figure 8.2 as a HEALPIX grid of the hemisphere observable from the PAPER site in the Karoo. In Figure 8.3 we show `radionopy` and `ionFR` output for a single pointing towards Cassiopeia A (Cas A; RA= $23^{\text{h}}23^{\text{m}}27.9^{\text{s}}$ , Dec= $+58^{\circ}48'42.4''$ ) from the LOFAR Core site in the Netherlands. The two codes gave qualitative agreement. Slight offsets at the highest RM values that day could be attributed to differences in our interpolation schemes.

[Martinot et al. \(in prep.\)](#) investigated the full interaction of the polarized sky with the ionosphere, using realistic polarized sky models and fully-polarized HERA beam models (see Chapter 10 for an example). Their work revealed that the Moore et al. (2017) analysis overestimated the ionospheric attenuation due to their single-pointing and simple beam models. Realistic levels of attenuation for a 100 day HERA integration can be expected to reach a factor of  $\leq 0.1$ . If polarization leakage occurs close to the EoR level, this is

---

<sup>3</sup><https://github.com/UPennEoR/radionopy>

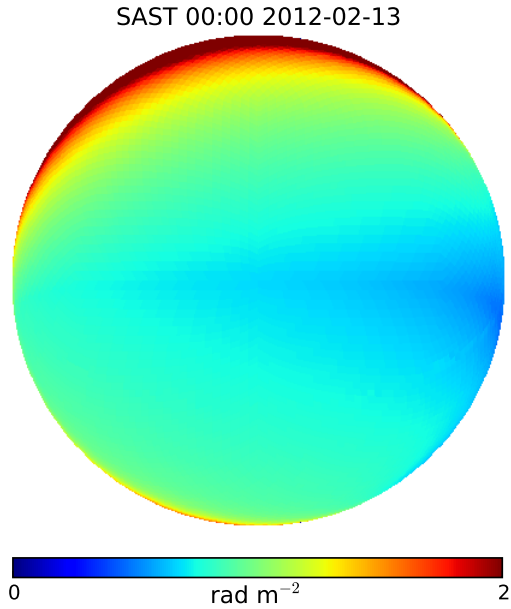


Figure 8.2: An example of widefield ionospheric RMs calculated by radionopy.

sufficient to recover the EoR power spectrum. However, if it is above the EoR level (as expected by Nunhokee et al. 2017), the ionosphere alone will not be sufficient to rule out polarization leakage being detected before the EoR can be recovered.

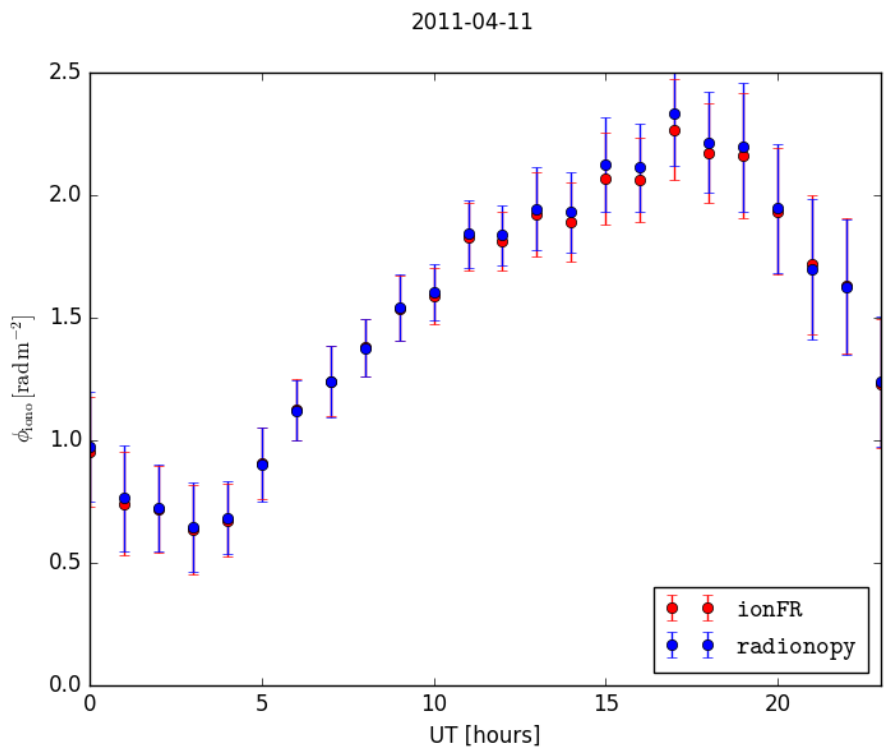


Figure 8.3: The RM of Cas A as viewed from the LOFAR Core site in the Netherlands on April 11th, 2011, according to `ionFR` and `radionropy`. The two codes show quantitative agreement, demonstrating that `radionropy` can be used for single-pointing as well as full-sky RM measurements.

# Chapter 9

## A view of the EoR window from the PAPER-32 imaging array

In this Section, we present 2D power spectra created from data taken by the PAPER-32 imaging array in Stokes I, Q, U and V.

The PAPER 32-antenna array relied on its highly redundant configuration in order to take the measurements resulting in the strong upper limits on the 21 cm power spectrum (Parsons et al., 2014; Jacobs et al., 2015; Moore et al., 2017). However, for three nights in 2011 September, the 32 elements were reconfigured into an polarized imaging configuration. Creating power spectra allowed us to observe and diagnose systematic effects in our calibration at high signal-to-noise within the Fourier space most relevant to EoR experiments. We observed well-defined windows in the Stokes visibilities, with Stokes Q, U and V power spectra sharing a similar wedge shape to that seen in Stokes I. With modest polarization calibration, we saw no evidence that polarization calibration errors moved power outside the wedge in any Stokes visibility, to the noise levels attained. Deeper integrations will be required to confirm that this behavior persists to the depth required for EoR detection.

The layout of this Chapter is as follows. In Section 9.1 we provide a brief description of the PAPER array in its imaging configuration, the data from which this paper is based,

and describe its calibration and reduction. We also describe the method used to create 2D power spectra in this section. We analyze the power spectra in Section 9.2, and discuss the implications of our findings and conclude in Section 9.3.

## 9.1 Observations & Reduction

We present measurements taken overnight on 2011 September 14–15 over local sidereal times (LSTs) 0–5 hr.

Antennae were arranged in a pseudo-random scatter within a 300 m-diameter circle, the layout of which is shown in Figure 9.1. This allowed us to obtain resolutions between 15' and 25' across the bandwidth (100–200 MHz nominally, although in reality this extends 110–185 MHz due to band edge effects and VHF TV). Drift-scan visibilities were measured every 10.7 s, and divided into datasets about 10 minutes in length. We express an interferometric visibility  $V_{ij}^{pq}$  between antennae  $i$  (with dipole arm  $p$ , which can be  $x$  (East-West) or  $y$  (North-South) for PAPER dipoles), and  $j$  (with dipole arm  $q$ ), in directional cosines  $l$  and  $m$  for frequency  $\nu$  at time  $t$ , as:

$$V_{ij}^{pq}(\nu, t) = g_i^p g_j^{q*} \exp(-2\pi i \nu \tau_{pq}) \times \int d\Omega A^{pq}(\Omega, \nu) S(\Omega, \nu) \exp\left(\frac{-i\nu}{c} \vec{b}(t) \cdot \hat{s}(\Omega)\right) \quad (9.1)$$

where the  $g$  terms represent the complex gains for each antenna and dipole arm,  $A^{pq}$  is the polarized beam and  $S$  is the sky. The product  $\vec{b}(t) \cdot \hat{s}(\Omega)$  represents the projection of the baseline between  $i$  and  $j$  with respect to an arbitrary location on the sky. The motivation for including the term for the delay between dipole arms  $p$  and  $q$ ,  $\tau_{pq}$ , is given in Section 9.1.1.3. This delay is clearly zero if  $p = q$ .

Visibilities were obtained from correlating both  $x$  and  $y$  dipoles, forming  $V^{xx}$ ,  $V^{xy}$ ,  $V^{yx}$  and  $V^{yy}$ . Frequencies from 100 to 200 MHz were sampled into 2048 channels. Data were delay-filtered to 203 frequency channels (see the Appendix of Parsons et al., 2014) and Chapter 6. Cross-talk was modelled and removed by subtracting the average power over

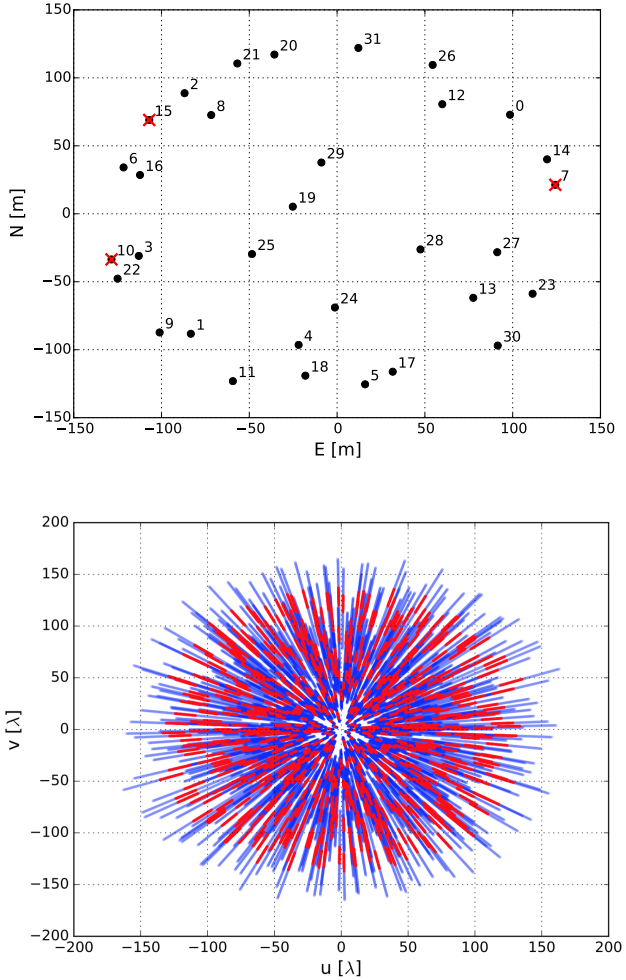


Figure 9.1: The PAPER-32, dual-pol antenna imaging configuration (top). They were arranged in a pseudo-random scatter within in a  $\sim 300$  m diameter circle to maximize instantaneous  $uv$  coverage (bottom).  $uv$  coverage is shown for 100–200 MHz over 203 channels in blue, and 146–166 MHz over 20 channels in red (the latter being the frequencies used in our power spectrum analysis). Malfunctioning antennae identified during calibration are overlaid with red crosses (and are excluded from the  $uv$  coverage map).

the 5 hours of observation, which extended across LST=0h–5h. An initial RFI-flagging removed any outliers more than  $6\sigma$  from a spectrally smooth profile.

### 9.1.1 Calibration

Calibration took place in three stages, detailed below: a first-order delay-space calibration for the initial gains and phases with respect to Pictor A, an absolute calibration using imaging with respect to Pictor A and Fornax A, and a polarimetric correction for the  $\tau_{xy}$  phase term in the  $V^{xy}$  and  $V^{yx}$  visibilities. Traditional polarimetric calibration proceeds by observing a source with a known polarization angle, and solving for up to seven direction-independent terms in the Jones matrix (e.g. Thompson et al., 2017; Hamaker et al., 1996), as well correcting for the effects of the primary beam. Given the dearth of suitable calibrators at our observing frequencies, especially at the relatively low resolution and sensitivity of the array, we proceeded with polarized calibration using different techniques, as described in Section 9.1.1.3 below.

#### 9.1.1.1 Initial calibration

A first-order gain and phase calibration was performed by a similar approach to Jacobs et al. (2013). Each 10 minute drift-scan dataset was phased to the known position of Pictor A using aipy routines.

The gain term in Equation 9.1 was approximated as

$$g_i^p = G_i^p \exp(-2\pi i v \tau_{ip}) \quad (9.2)$$

and the required delay  $\tau_{ip}$  offset of the uncalibrated delay tracks to the real position on the sky solved for to obtain a phase calibration; the absolute flux calibration  $G_i^p$  was found by isolating the tracks of Pictor A in delay space, and applying the required flux scale across the band (for a discussion of delay-space calibration, see Parsons et al., 2012b, and Figure 9.4).

#### 9.1.1.2 Absolute Calibration

Visibilities were converted to CASA Measurement Sets to be further calibrated using a custom pipeline developed around CASA libraries. Snapshot images were generated for

each 10 minute observation by Fourier transforming the visibilities. We used uniform weights and the multi-frequency synthesis algorithm to further improve the *uv* coverage. Dirty images were deconvolved down to a 5 Jy threshold using the Cotton-Schwab algorithm. The sky model generated by the CLEAN components was used to self-calibrate each snapshot over the full bandwidth, using a frequency-independent sky-model and averaging over the 10 minute observation. We corrected for residual cable length errors by computing antenna-based phase solutions for each frequency channel for each snapshot observation. After self-calibration, snapshot visibilities were again Fourier transformed into images and deconvolved down to a 2 Jy threshold to form the final sky models. These final sky models were used to solve for a frequency independent, diagonal, complex Jones matrix (Hamaker et al., 1996; Smirnov, 2011a) for each antenna in order to calibrate gain variations from snapshot to snapshot. We make no attempt to correct sky models for polarized primary beams and, therefore, our gain solutions incorporate both the direction independent and the direction dependent responses of the two gain polarizations. This is a reasonable approximation for the scope of the paper, as, eventually, wide-field polarization corrections cannot be implemented directly in the per-baseline power spectrum estimation (see Section 9.2).

The average correction in magnitude through this second-order calibration was a  $\pm 6\%$  change for *x* gains and  $\pm 7\%$  for *y* gains from those derived in the initial delay-space calibration. If the gain on an antenna deviated by more than 30% from image-to-image during this analysis, it was discarded from future processing stages, since it was likely malfunctioning. This was true for 3 antennae (see the top panel of Figure 9.1).

The final gain amplitude calibration was carried out similarly to Ali et al. (2015). We generated single channel images between 120 and 174 MHz for each snapshot and deconvolved each of them down to 10 Jy. For each snapshot, a source spectrum is derived for Pictor A by fitting a two dimensional Gaussian the source using the PyBDSM<sup>1</sup> source extractor (Mohan & Rafferty, 2015). Spectra were optimally averaged together

---

<sup>1</sup><http://www.lofar.org/wiki/doku.php?id=public:usersoftware:pybdsm>

by weighting them with the primary beam model evaluated in the direction of Pictor A. To fit the absolute calibration, we divided the model spectrum (Jacobs et al., 2013) by the measured one and fit a 6th order polynomial over the 120-174 MHz frequency range. This procedure was repeated using Fornax A with the only difference that a taper was applied to the visibilities (120 m) in order to reduce Fornax A to a point-like source and use the model spectrum from Bernardi et al. (2013). The best fit coefficients for Pictor A and Fornax A were averaged together to obtain the final absolute flux density calibration. Snapshots of fully CASA-calibrated data are shown in Figure 9.2.

### 9.1.1.3 Polarimetric factors

Standard full polarization calibration involves correcting for leakage of Stokes  $I$  into the  $V_{ij}^{xy}$  and  $V_{ij}^{yx}$  visibilities and leakage of polarized signal into total intensity (the so called Jones  $D$  matrices or  $D$ -terms; e.g. Thompson et al. (2017); Hamaker et al. (1996)), and an unknown phase difference between the  $x$  and  $y$  feeds (e.g. Sault et al., 1996).

We attempt no  $D$  matrix calibration in this paper, as there is not a dominant source to be used for such calibration: the limited sensitivity of our observations does not offer good signal-to-noise ratio on PMN J0351-2744, the only polarized source at low frequencies known so far in our survey area. In addition,  $D$ -term calibration would require determination of the primary beam Mueller matrices beyond our current accuracy. The consequences of this limitation are discussed in the analysis of our power spectra in Section 9.2.

As an intermediate measure compatible with these limitations, we therefore adopted a minimization of the phase difference between the  $V_{ij}^{xy}$  and  $V_{ij}^{yx}$  visibilities, minimizing a sum of squared weighted residuals  $w$ :

$$w(v, t, \tau_{xy}) = \sum_{ij} |V_{ij}^{xy} - V_{ij}^{yx} \exp(-2\pi i v \tau_{xy})|^2 \quad (9.3)$$

to find an estimated value of  $\tau_{xy}$  for the array at each  $(v, t)$  sample. This is equivalent to assuming that the sky is intrinsically not circularly polarized at the frequencies observed

by PAPER.

We choose not to correct for ionospheric Faraday rotation in our calibration. Not only is this difficult to do for widefield instruments, but also the ionosphere was relatively stable during the observations, so we expect little incoherent averaging during the power spectrum stage below. We calculated the stability of ionospheric RM ( $\phi_{\text{iono}}$ ) using the IONFR software (Sotomayor-Beltran et al., 2013), which calculates the  $\phi_{\text{iono}}$  for a given longitude, latitude and time by interpolating values of GPS-derived total electron content maps and the International Geomagnetic Reference Field (Finlay et al., 2010). The values of  $\phi_{\text{iono}}$  for different lines of sight are shown in Figure 9.3. Fluctuations of  $\phi_{\text{iono}}$  will cause incoherent time-averaging and subsequent loss of polarized signal. Using the formalism of Moore et al. (2017) to calculate the attenuation factor, we found that none of the lines of sight (except for the 21h,0° one which goes beneath the horizon) shown are responsible for attenuating signal by > 20% in power-spectrum space (see Section 9.1.2).

We form linear combinations of the instrument visibilities, the so-called pseudo-Stokes visibilities (see e.g. Moore et al., 2013)  $V^I$ ,  $V^Q$ ,  $V^U$  and  $V^V$  as:

$$\begin{pmatrix} V^I \\ V^Q \\ V^U \\ V^V \end{pmatrix} = \begin{pmatrix} 1 & 0 & 0 & 1 \\ 1 & 0 & 0 & -1 \\ 0 & 1 & 1 & 0 \\ 0 & -i & i & 0 \end{pmatrix} \begin{pmatrix} V^{xx} \\ V^{xy} \\ V^{yx} \\ V^{yy} \end{pmatrix} \quad (9.4)$$

Data that were reduced, calibrated, and formed into Stokes visibilities were separated into delay spectra inside and outside of the horizon for each baseline. We used a 50 ns margin for what was considered ‘inside’ the horizon, in order to confine all supra-horizon emission (e.g. Parsons et al., 2012b; Pober et al., 2013) to the foreground component of the data. We implemented a one-dimensional CLEAN (Parsons & Backer, 2009; Parsons et al., 2012a) with a Blackman-Harris window to a tolerance of  $10^{-9}$ . RFI is more easily identified in foreground-removed data, so we RFI-flagged again on the background data deviations greater than  $3\sigma$ . We then added the inside- and outside-horizon visibilities back together; RFI flags were preserved in the process.

The effect of our calibration is shown in the delay-transformed visibilities in Fig-

ure 9.4. As is apparent in Figure 9.2, after improved calibration there are fewer delay tracks (i.e. sources) in the Stokes Q visibilities, while there is little overall change in Stokes U. The minimization of Stokes V, performed after the imaging calibration stage, moves power from Stokes V into Stokes U, effectively accounting for part of a  $D$ -term correction. But without an accurate  $D$ -term calibrator, Stokes U exhibits additional (and dominant)  $D$ -term leakage from Stokes I, in this case due to Pictor A. Pictor A is the brightest source in Stokes I in our observed field, and thus dominates the visibility shown. There is no reason to suppose that Pictor A is pure Stokes U (compare also Figure 9.2), and thus the bulk of this emission must be leakage.

### 9.1.2 Creating power spectra

Expressing the visibility  $V_{ij}^{pq}(v, t)$  observed at time  $t$  (see Equation 9.1) in terms of the geometrical delay  $\tau_g = \vec{b}(t) \cdot \hat{s}(l, m)/c$  for the baseline  $ij$ , Parsons et al. (2012b) define the delay transform as the Fourier transform of the visibility along the frequency axis:

$$\tilde{V}_{ij}^{pq}(\tau, t) = \int d\nu V_{ij}^{pq}(\nu, t) e^{2\pi i v \tau} \quad (9.5)$$

We can represent the power at each frequency and baseline in an array as a power spectrum in terms of their respective Fourier components  $k_{\parallel}$  and  $k_{\perp}$  as:

$$P(k_{\parallel}, k_{\perp}) \approx |\tilde{V}_{ij}^{pq}(\tau, t)|^2 \frac{X^2 Y}{\Omega B} \left( \frac{c^2}{2k_B v^2} \right)^2 \quad (9.6)$$

where  $B$  is the bandwidth,  $\Omega$  is the angular area (i.e. proportional to the beam area), and X and Y are redshift-dependent scalars calculated in Parsons et al. (2012a).

To form  $|\tilde{V}_{ij}^{pq}(\tau, t)|^2$ , consecutive integrations were cross-multiplied, phasing the zenith of latter to the former i.e.:

$$|\tilde{V}_{ij}^{pq}(\tau, t)|^2 \approx |V_{ij}^{pq}(\tau, t) \times V_{ij}^{pq}(\tau, t + \Delta t) e^{i\theta_{ij,zen}(\Delta t)}|^2 \quad (9.7)$$

where  $\Delta t = 10.7$  seconds and  $\theta_{ij,zen}(\Delta t)$  is the appropriate zenith rephasing factor. This method should avoid noise-biased power spectra except on very long baselines, which

the PAPER configuration does not contain, while sampling essentially identical  $k$ -modes. Note that this is the same method used by Pober et al. (2013) in their investigation of the unpolarized wedge.

## 9.2 Results

Combining visibilities using Equation 9.4, we formed power spectra over frequencies 146–166 MHz according to Equation 9.6 using consecutive integrations for each Stokes visibility over time, and gridded our results into  $k$ -space, averaging in time. The  $k_{\perp}$ -axis is binned with a resolution of  $4.65 \times 10^{-4} h \text{ Mpc}^{-1}$  to slightly reduce gaps in  $k$ -space due to missing baselines. This gave an average bin occupancy of  $1.7 \pm 0.9$ . The resolution in  $k_{\parallel}$  ( $5.06 \times 10^{-4} h \text{ Mpc}^{-1}$ ) is set by the 20 MHz bandwidth with 500 kHz resolution that we use in this analysis. Note that the Blackman-Harris window used in the delay-filtering stage after forming Stokes visibilities correlates adjacent frequency bins, and hence  $k_{\parallel}$  bins. Each  $(k_{\perp}, k_{\parallel})$  bin was normalized by its occupancy.

Two-dimensional power spectra have been proven as powerful tools for large dipole array experiments, not only for assessing cosmology but also in order to constrain instrumental and analytical systematics (e.g. Morales et al., 2012). Polarization axes are a useful addition for such analyses, since we expect Stokes I to be approximately 3 orders of magnitude stronger than the other polarization products at the low radio frequencies and tens-of-arcminute scales native to PAPER observations (e.g. Pen et al., 2009; Moore et al., 2013) and when observing far from the Galactic Plane. This alone allows us to assume that much of the structure in the power spectra with power comparable to Stokes I is leakage. As we explore below, these leakage terms can come from direction-dependent effects (e.g. wide-field beam leakage; Carozzi & Woan, 2009) or direction independent ones (e.g. Mueller matrix mixing via gain errors and  $D$ -terms; Thompson et al., 2017) and appear with high signal-to-noise in power spectra.

Figure 9.5 shows power spectra in ‘pitchfork’ form (Thyagarajan et al., 2015b,a), with

$k_{\parallel}$  in negative and positive directions (according to the East and West horizons, marked in white (horizon) and orange (horizon+50 ns delay, respectively). Each Stokes parameter pitchfork has its own interesting characteristics, which allow us to analyze different sky and instrument behaviors. The ‘wedges’ described in the literature that define the EoR window are simply the average of negative and positive values of  $k_{\parallel}$ . While we focus on the pitchfork expression of the power spectra in our results, we also show them in wedge form in Figure 9.6<sup>2</sup>.

Simplifying the results of Thyagarajan et al. (2015b,a, see their papers for a full discussion), we expect power from diffuse emission to appear at low values of  $k_{\perp}$  and high values of  $k_{\parallel}$ , while point sources lie at all  $k_{\parallel}$  (all over the sky) but are down-weighted by the primary beam, which is broad, leaving a concentration of the power close to the  $k_{\parallel} = 0$  line.

In Stokes I, we see the strongest power on most baselines arising at values  $k_{\parallel} \approx 0$ . This is expected in a situation of point sources that are relatively bright compared to any diffuse emission. Indeed, at the LSTs we observed at, several unresolved bright point sources transit the field (e.g. Figure 9.2), while the dominant source of diffuse emission at these frequencies, the Galactic plane, was below the horizon. However, we do see strong super-horizon emission at  $0.02 \leq k_{\perp} \leq 0.03$ , biased towards negative  $k_{\parallel}$  values. There is also a decrease in power with increasing  $k_{\perp}$  – both of these effects are consistent with the Thyagarajan et al. (2015a) simulations of faint diffuse structure transiting zenith.

The Stokes Q wedge shows a concentration of power close to  $k_{\parallel} \approx 0$ , similar to Stokes I. The inherent low polarization fraction at our frequencies works in our favor in detecting gain errors, since Stokes Q is largely expected to be faint, and thus the gain errors causing leakage from I appear at high signal-to-noise there. Indeed, this power decreases noticeably with more accurate gain amplitude calibration, but bright streaks at specific values

---

<sup>2</sup>Note the difference in the power distribution within the horizon differs from that shown in the Pober et al. (2013)  $V^{yy}$  wedge. That study used the PAPER 64-element, single-polarization imaging array to create power spectra in a ‘loud’ field containing point sources and Galactic signal, causing their wedge to be ‘fuller’ than the ones presented in this study.

of  $k_{\perp}$  remain, suggesting lower-level residual gain calibration errors on select baselines. Another possible source of power in Stokes Q stems from wide-field direction-dependent gain errors causing a non-smooth evolution of the sources on the edges of the beam. However, we would expect this effect to be biased towards horizon values of  $k_{\parallel}$ .

Power appears distributed in ‘pockets’ in the Stokes U power spectrum, not strongly correlated with the distribution of power in I. Stokes I is able to leak into Stokes U via  $D$ -term leakage (Thompson et al., 2017; Geil et al., 2011), which could occur at any post-amplification stage of observations, such as in cables or receivers. These leakages would be direction independent, and therefore uncorrelated in  $k$ -space. Such a mechanism could explain the behavior within Stokes U wedge. Before absolute calibration, similar structure is seen in the Stokes V power spectrum.

At these frequencies, Stokes V is thought to be intrinsically zero, with few exceptions. However, Hamaker et al. (1996) show that antennae rotated with respect to one another can produce erroneous Stokes V power via  $I \rightarrow V$  leakage.<sup>3</sup> This effect may explain some of the small pockets of power that remain in the Stokes V power spectrum after absolute calibration, although such an effect is also consistent with  $D$ -term leakage. The fact that power within the horizon was greater than the noise level may also have been due to  $I \rightarrow V$  leakage through the primary beam.

The relationship between polarizations is highlighted in Figure 9.7. We show a slice of the wedges over  $0.097 < k_{\perp} < 0.098 h\text{Mpc}^{-1}$  ( $\sim 175$  m) for Stokes I, Q, U and V (right panels) and the average power over these slices as a function of  $k_{\parallel}$  (left panel). The standard deviations for each Stokes parameter are shown as dotted lines. Dashed vertical lines show the horizon at  $k_{\perp}=0.097$  (left) and super-horizon at  $k_{\perp}=0.098$  (right).

A heartening aspect of Figure 9.7, and indeed all of the power spectra in this work, is that the power in Stokes Q, U and V proves to be just as confined within the horizon

---

<sup>3</sup>It should be noted that while such an error could plausibly have been made in the antenna placement for this imaging array, it is extremely unlikely that it would be made in the redundant PAPER configuration for EoR seasons. In these cases, the antennae were positioned to sub-cm accuracy.

as Stokes I. Whether the polarized Stokes parameters are due to real polarization or mis-calibration, not enough spectral structure is being introduced to move emission into the EoR window. Outside of the horizon, Stokes I, Q and U are consistent with the noise level expected for this range of  $k$ -modes ( $P_{\text{noise}} \sim 10^9 \text{ mK}^2(h^{-1}\text{Mpc})^3$ ), according to the formalism Parsons et al. (2012a) and assuming a system temperature  $T_{\text{sys}} = 450 \text{ K}$  (e.g. Moore et al., 2017).

### 9.3 Discussion and Conclusions

We have presented measurements of instrumental polarization leakage in PAPER-32 using 2D power spectra. These have allowed us to quantify some of the possible instrumental effects that could limit a statistical detection of the EoR within the wedge, diagnosed in the Fourier space most relevant EoR statistical detection experiments. To our knowledge, this is the first study of Q, U and V 2D power spectra at these  $k$ -modes. We have shown that power from Stokes Q, U and V is as confined to the wedge as Stokes I. Any calibration errors do not appear to spread power outside the horizon.

In their study of 2D power spectra, Asad et al. (2015) reported evidence of polarized leakage into the EoR window at the sub-percent level, considering a  $4^\circ$  degree field of view. Their study differs from this work not only over the field of view ( $4^\circ$  versus almost whole-sky), but also in the observing mode (tracked versus drift scan) and in the different  $k$ -space probes by LOFAR’s longer baselines. In this work the power spectrum is calculated on a per-baseline basis, whereas their study calculates power spectra for gridded data which are more prone to mode mixing effects (Hazelton et al., 2013).

Our results are expected, in principle, to be more prone to leakage contamination due to the intrinsic extremely wide field of view of the PAPER primary beams, however, we see no evidence of leakage in the EoR window down to our sensitivity limits even without correction for polarized beams that is instead included in Asad et al. (2015). Our analysis indicates therefore that neither intrinsic polarized emission nor the PAPER primary

beam are leaking power in the EoR window, although longer integrations are required to demonstrate that this is true down to the sensitivities required for EoR detection.

We showed that systematics can be probed with high signal-to-noise using 2D polarized power spectra, using the inherently low polarization fraction at the frequencies PAPER observes at to our advantage. We found that gain errors on specific baselines were easily probed using Stokes Q power spectra. Gain errors appear as continuous streaks within the horizon at specific values of  $k_{\perp}$ , allowing us to diagnose the precision of the gain calibration on a per-baseline basis. This is much more difficult to do with only Stokes I power spectra in a non-redundant array, and can be accomplished quickly without imaging. While the features in the Stokes U power spectra are more difficult to attribute to specific baselines, they appear to be consistent with direction-independent leakage. Stokes V power is slightly higher than noise-level within the horizon, suggesting a small but unaccounted-for leakage term from Stokes I, an effect which was explored Nunhokee et al. (2017) – and found to be consistent with beam-leaked signal from Stokes I.

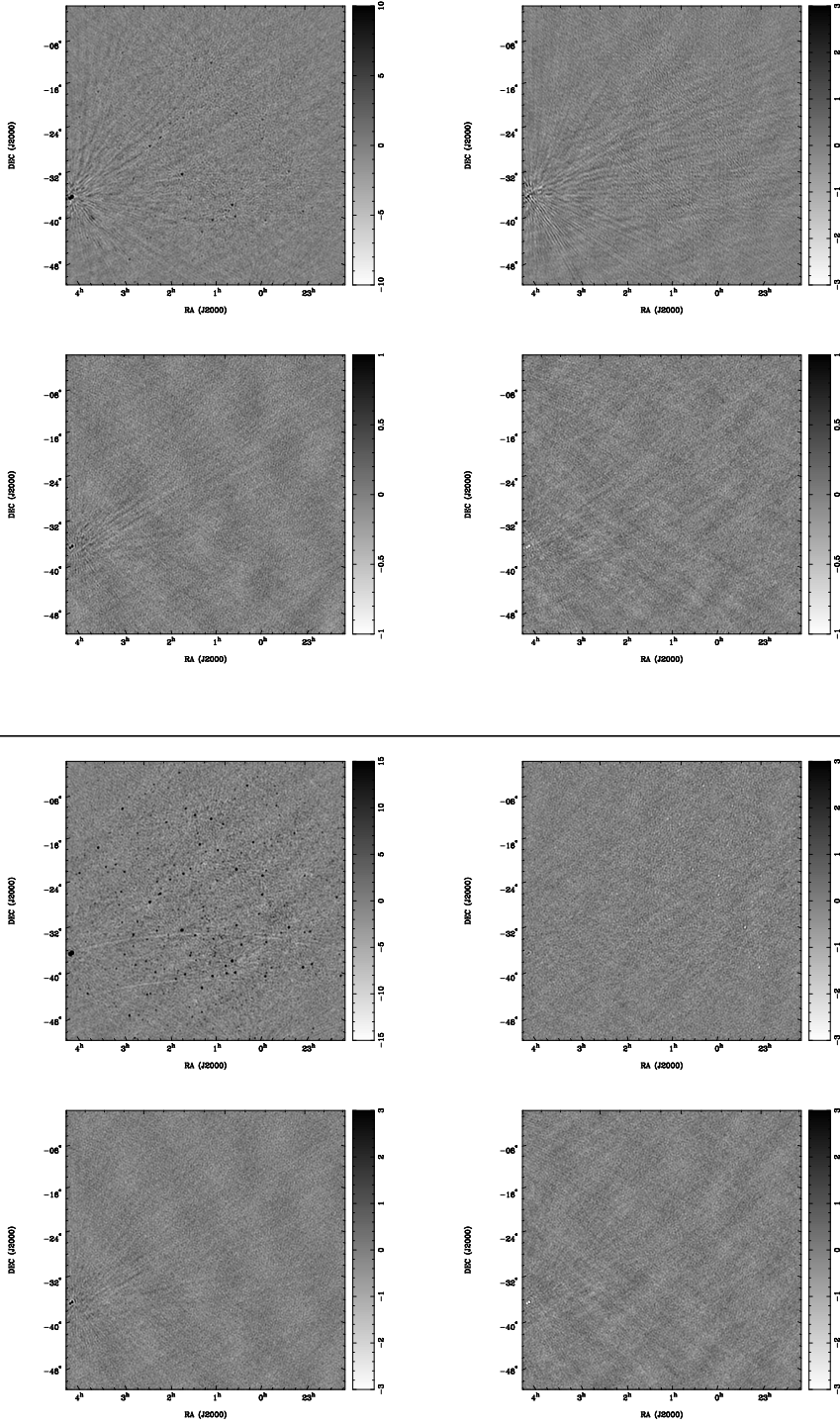


Figure 9.2: *Above:* Example of a Stokes I snapshot image (top left) with corresponding Stokes Q (top right), Stokes U (bottom left) and Stokes V (bottom right) images before absolute calibration. *Below:* The same organization as above, after absolute calibration. No primary beam correction was applied. The Stokes I image was deconvolved down to  $5 \text{ Jy beam}^{-1}$  whereas the other images were not deconvolved. Units are  $\text{Jy beam}^{-1}$ ; note the change in scale between polarizations and calibration stages.

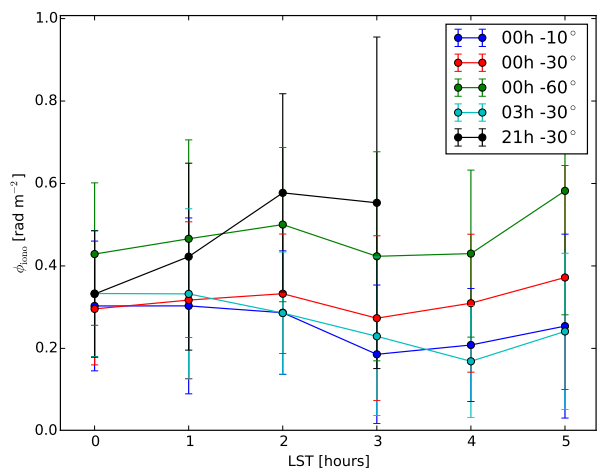


Figure 9.3: The values of ionospheric RM for different lines of sight the range of LSTs in this analysis, as calculated by IONFR (Sotomayor-Beltran et al., 2013). The 21h,0° line of sight goes beneath the horizon after LST=3h, and therefore has fewer data points.

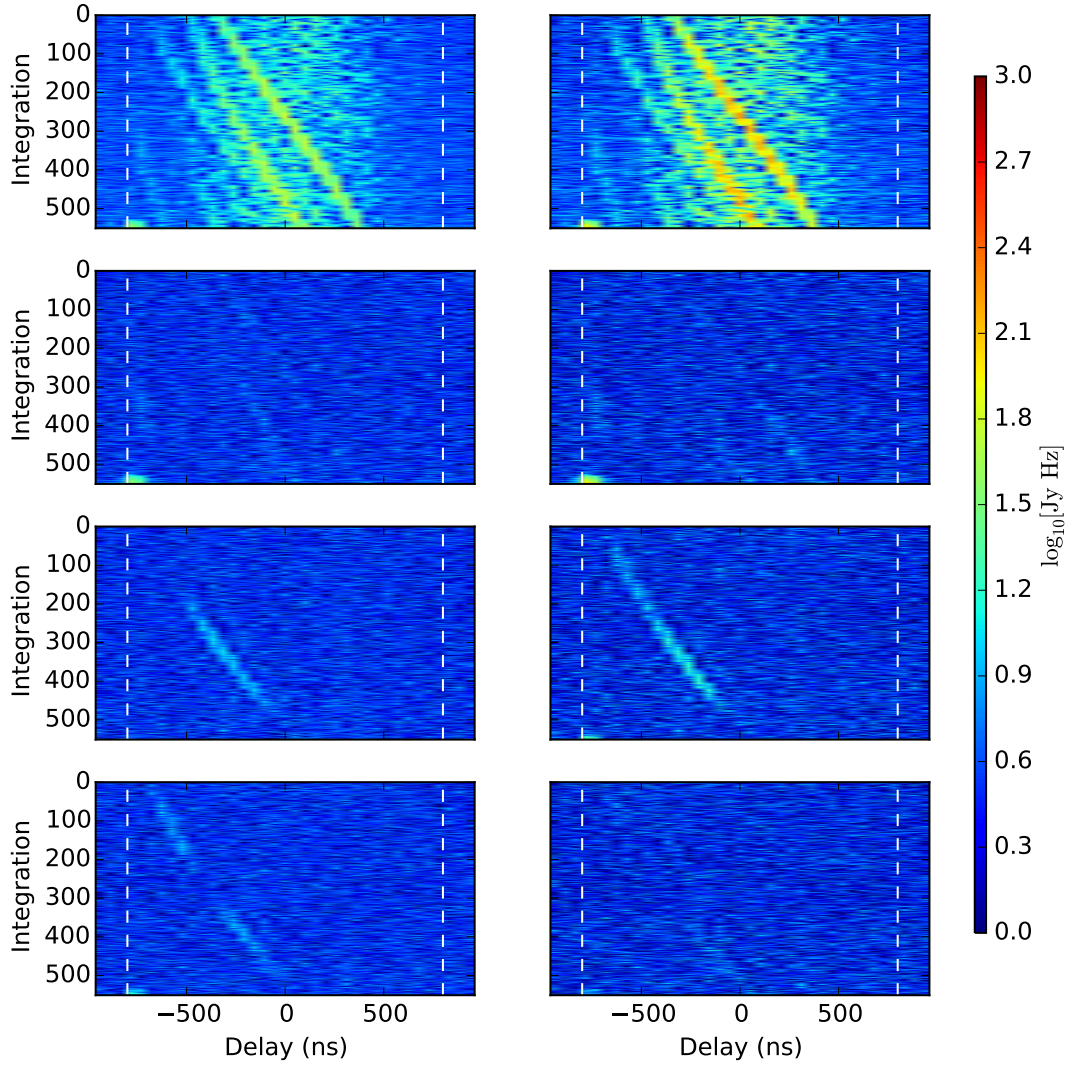


Figure 9.4: The absolute value of delay-transformed visibilities over the bandwidth (146–166 MHz) used to create the power spectra shown in this Chapter. The left and right columns show the visibilities before and after absolute calibration (and for Stokes U and V, the application of the  $\tau_{xy}$  parameter), respectively, for baseline formed by antennae 6 and 14 ( $\sim 250$  m in length, approximately East-West). The flux scale in the left column as been boosted for a more fair comparison to the absolute-calibrated data. From top to bottom, the rows correspond to Stokes I, Q, U and V. The horizon limit is marked by white dashed lines.

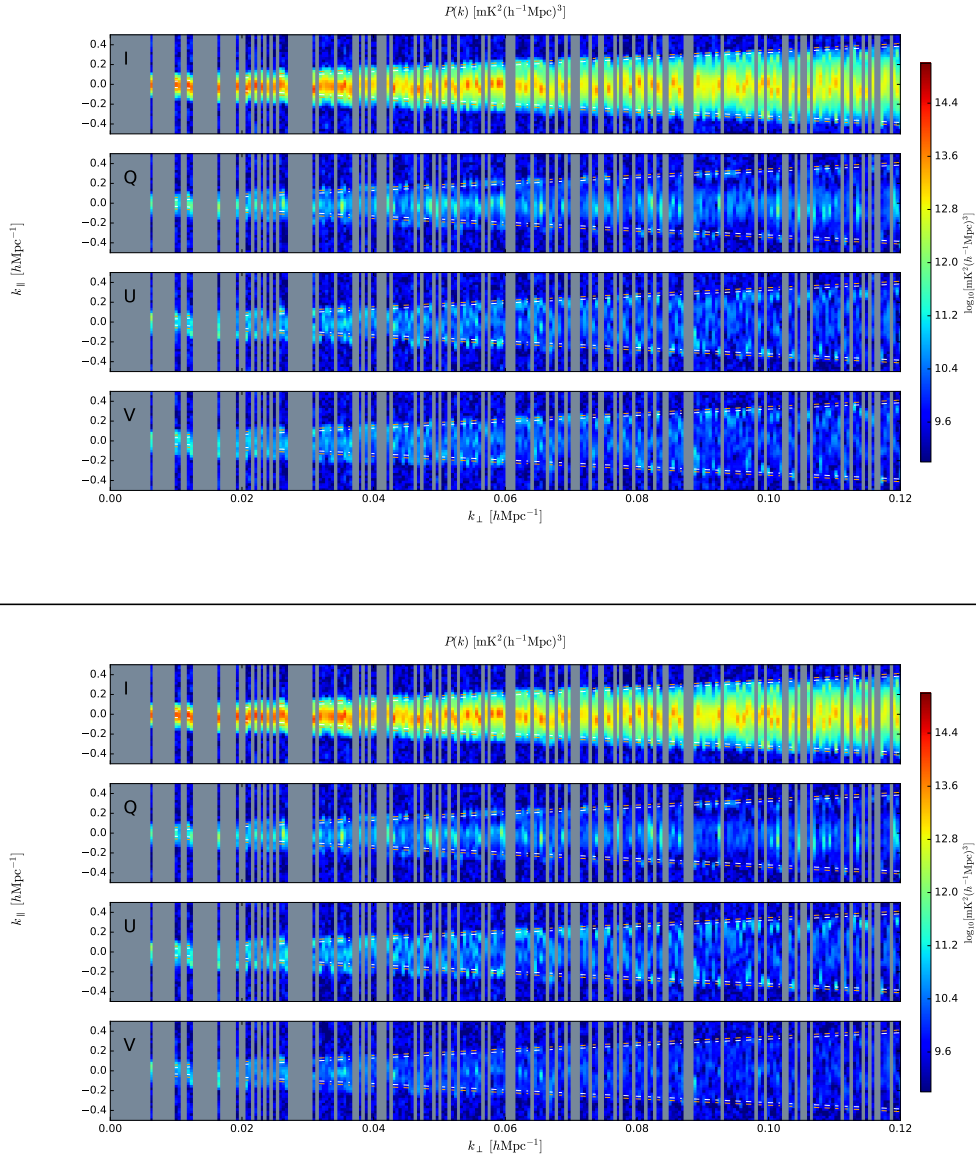


Figure 9.5: *Above:* Log-scaled 2D power spectra formed from (*top to bottom*): I, Q, U and V visibilities after before absolute calibration. Blank regions indicate the incomplete  $uv$  coverage for a given  $k_{\perp}(u)$ . The colorbar spans  $10^9$  to  $10^{15}$   $\text{mK}^2(h^{-1}\text{Mpc})^3$ . The flux scale has been boosted for a more fair comparison to the absolute-calibrated data. *Below:* The same organization as above, but after absolute calibration. Briefly, the structure in Stokes I is consistent with a point-source-dominated field with a weak diffuse component. The other Stokes parameters are consistent with calibration errors and systematics: Stokes Q shows gain errors on specific antennae, Stokes U gives an estimate of possible D-term leakage, and any structure in V shows unaccounted-for systematics, due to D-terms or mis-oriented antennae.

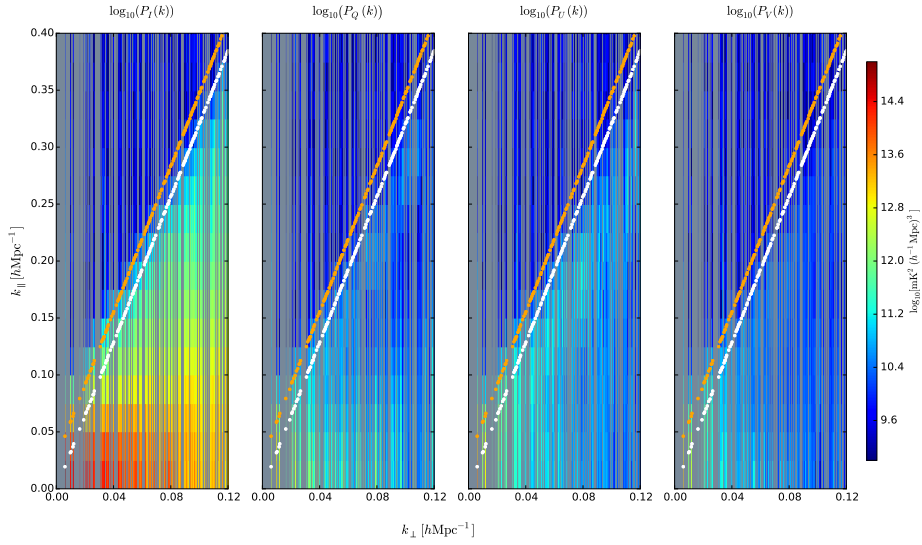


Figure 9.6: Log-scaled 2D power spectra formed from (*left to right*): I, Q, U and V absolute-calibrated visibilities. Blank regions indicate the incomplete *uv* coverage for a given  $k_\perp(u)$ . White and orange lines indicate the horizon and horizon plus a 50 ns boundary for super-horizon emission.

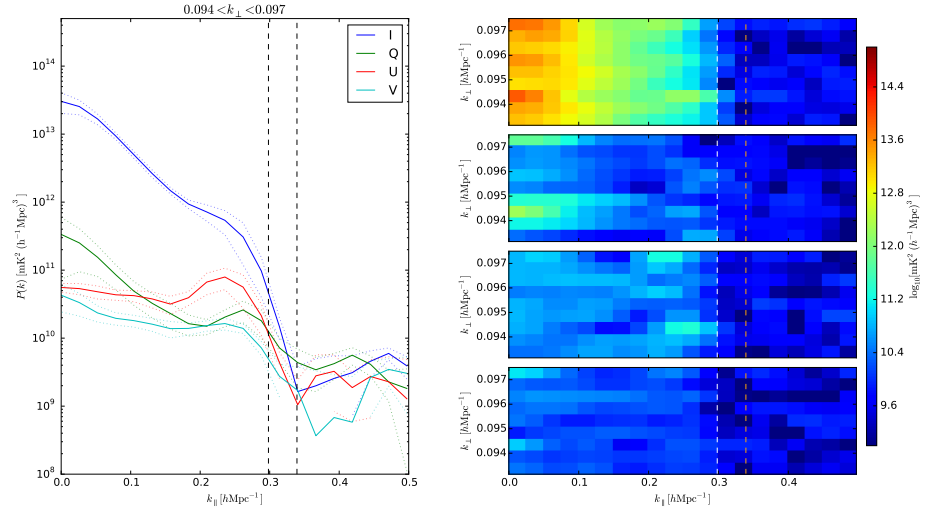


Figure 9.7: *Left:* The average power in  $0.093 < k_{\perp} < 0.098 h\text{Mpc}^{-1}$  as a function of  $k_{\parallel}$  for each polarization. In the horizon–super-horizon range that we see the sharp fall-off in power indicative of the edge of the EoR window. Outside of the wedge, Stokes I, Q and U are at noise level, while Stokes V is below noise level, most likely due to the  $\tau_{xy}$  calibration scheme removing a degree of freedom from this Stokes parameter. *Right:* the region of k-space that was averaged over to create the lines in the left panel. From top to bottom, the panels correspond to Stokes I, Q U and V.

# **Chapter 10**

## **A view of the EoR window from the HERA-19 commissioning array**

As emphasized in Chapter 9, it is important to constrain intrinsic and leaked polarized signal for any HI EoR experiment. The objective of this Chapter was an exploration of eight nights of data from the Hydrogen Epoch of Reionization Array (HERA) 19-element commissioning array, coupled with simulations of the instrument, in order to forecast how much of a problem polarization would pose for this interferometer. This work also represents the first power spectral analysis from HERA. While not in the realm of an EoR-level integration, we were able to offer some initial expectations for this new instrument’s performance in the Fourier domain.

This work is organized as follows: in Section 10.1 we review the theory behind polarization leakage into unpolarized signal and simulate the effect for a model of HERA. In Section 10.2 we describe the HERA data that we used, its calibration and reduction to power spectra. We present our results, and discuss the implications for HERA’s EoR measurements, in Section 10.3, and conclude in Section 10.4. We assume the cosmological parameters reported by Planck Collaboration et al. (2016) throughout.

## 10.1 Polarization Leakage Simulations

In Chapter 3, we presented direction dependent and independent ways for polarized power to “leak” between visibilities. Direction dependent leakage arises because dipole arm ‘n’ is sensitive to electromagnetic radiation with polarization axis aligned with perpendicular dipole arm ‘e’. Forming pseudo-Stokes visibilities from those in the instrumental basis,

$$\begin{pmatrix} V^I \\ V^Q \\ V^U \\ V^V \end{pmatrix} = \frac{1}{2} \begin{pmatrix} 1 & 0 & 0 & 1 \\ 1 & 0 & 0 & -1 \\ 0 & 1 & 1 & 0 \\ 0 & -i & i & 0 \end{pmatrix} \begin{pmatrix} V^{nn} \\ V^{ne} \\ V^{en} \\ V^{ee} \end{pmatrix}. \quad (10.1)$$

results in each pseudo-Stokes visibility containing a direction-dependent mix of the “true” Stokes parameters on the sky. Using simulations of the HERA feed, faceted parabolic dish and analog signal chain (Fagnoni & de Lera Acedo, 2016), we proceeded to simulate pseudo-Stokes visibilities using the polarized formalism in Chapter 3 (Figure 3.4 shows the direction-dependent leakage matrices used here). We simulated visibilities for the HERA-19 commissioning array, described below, using an *unpolarized* model of the low frequency sky from the Global Sky Model (de Oliveira-Costa et al., 2008; Price, 2016a; Zheng et al., 2017, GSM;) at the appropriate R.A. range to match our observations. Forming power spectra and images from these visibilities allowed for a comparison of our data to a ‘leakage from Stokes I only’ regime. At the low frequencies and large scales probed by HERA, Stokes I is extremely bright compared to the other Stokes parameters (e.g. Chapter 2, Kohn et al. (2016)), so this regime is realistic for the measurements in question.

In Chapter 3, we also presented a formalism for propagating direction-independent calibration errors into polarization leakage. We did not include calibration errors in our simulations, allowing us to build intuition around power spectrum estimates for a “perfectly behaving” instrument.

## 10.2 Observations & Reduction

In this work we used eight nights of observations from the HERA-19 commissioning array. HERA is a low-frequency interferometer composed of 14 m-diameter dishes arranged in a close-packed hexagonal array of 14.7 m spacing. The commissioning array consists of nineteen dishes (see Figure 10.1); HERA is being constructed in staged build-outs, and upon completion will consist of 350 dishes in a fractured hexagon configuration (see Dillon & Parsons, 2016; DeBoer et al., 2017). A feed cage containing two dipole feeds (recycled from the PAPER array, see Parsons et al. 2010), oriented in North-South and East-West directions, is suspended above each dish (Neben et al., 2016; Ewall-Wice et al., 2016a; Thyagarajan et al., 2016).

HERA only observes in drift-scan mode. The observations we used were eight nights, from Julian Date (JD) 2457548 to 2457555; LSTs 10.5 – 23 hr. Drift-scan visibilities were recorded every 10.7 seconds for 1024 evenly-spaced channels across the 100-200 MHz bandwidth. These data were divided into MIRIAD data sets roughly 10 minutes long. A night’s observation lasted 12 hours in total (6pm to 6am South African Standard Time; SAST); of these we used the central 10 hours, to avoid the thermal effects of the Sun.

To identify samples contaminated by radio frequency interference (RFI), a two-dimensional median filter in time and frequency was applied to the visibility data to smooth out high pixel-to-pixel variations, and remove significant outliers that were likely unphysical. The variance of the resulting data was computed, and points with a  $z$ -score greater than 6 (i.e., points where the value is more than  $6\sigma$  away from the mean) were flagged as initial seeds for RFI extraction. A two-dimensional watershed algorithm was applied using these seeds as starting points, enlarging the regions of RFI-contamination to neighboring pixels with  $z$ -scores greater than 2, until all such pixels were flagged. Figure 10.2 shows the fractional RFI flag occupancy per time (displayed in LST) and frequency across the 8 days of observations. The majority of the band is relatively clear of RFI. Some clear features are: the FM radio band (below 110 MHz), ORBCOMM satellite communications (137 MHz), an

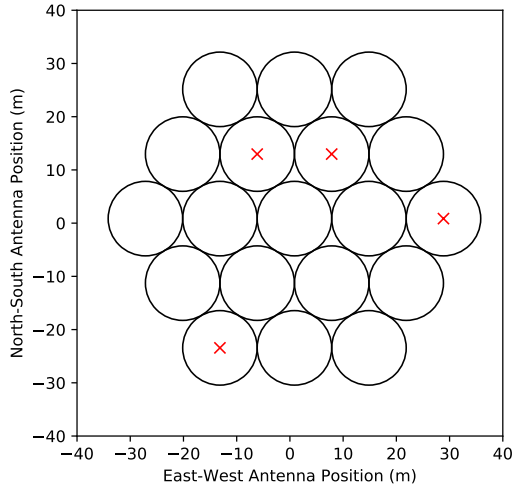


Figure 10.1: The perimeter of each dish in the HERA-19 array. A red "X" marks antennae that were identified during preprocessing and calibration as malfunctioning and were excluded from further analysis.

ISS downlink (150 MHz) and VHF TV channels (above 170 MHz)<sup>1</sup>. The Galaxy, when transiting zenith at  $LST \approx 17.75$  hours, is so bright that it appears to degrade our ability to flag RFI.

### 10.2.1 Calibration

HERA is designed to be calibrated using redundant calibration techniques (Dillon & Parsons, 2016), but for this preliminary view of HERA commissioning data, we used image-based calibration. Future studies with deeper integrations targeting EoR detections will take advantage of redundancy to obtain more precise calibration solutions (DeBoer et al., 2017). We used the CASA (McMullin et al., 2007) package for calibration, taking advantage of its CLEAN, gaincal and bandpass functions.

To enable the use of CASA, we first converted from native MIRIAD to a UVFITS file format which could be ingested by CASA using PYUVDATA (Hazelton et al., 2017).

---

<sup>1</sup>For an extended discussion of RFI as seen by HERA, see the public HERA Memo # 19

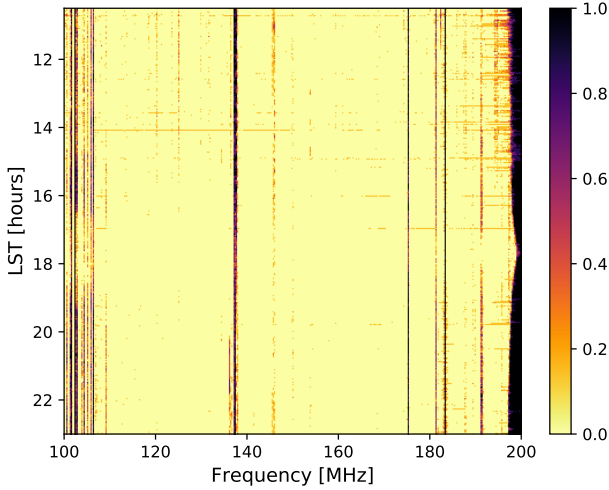


Figure 10.2: Fractional RFI flag occupancy per time and frequency over the eight days of observations.

Using LSTs in which the Galactic center (GC;  $\alpha, \delta = 17h\ 45m\ 40.04s, -29d\ 0m\ 28.12s$ ) was transiting, we built a CLEAN model which modeled the GC as an unpolarized point source of strength 1 Jy and flat spectrum, which could be scaled appropriately later (see Equation 10.2). Clearly, this is an incomplete calibration model. However, as the objective of this work is to explore the response of the instrument in power spectrum space without combining baselines of different lengths, most of the purpose of the calibration is correcting an initial large cable delay per antenna. Treating the GC as unpolarized is adequate for this study. The large optical depth towards the GC (Oppermann et al., 2012) results in large amounts depolarization in the plane of the Galaxy (Wolleben et al., 2006). Moreover, we expected non-negligible amounts of beam depolarization due to the large solid angle of the synthesized beam.

For each night of observations, we used the CASA `gaincal` and `bandpass` functions to obtain frequency-dependent phase and amplitude solutions for each antenna and dipole arm. Four antennae had very deviant solutions, and their inclusion resulted in low-quality images. These were omitted from further analysis (and are marked with red "X"s in

Figure 10.1). Before calibration, we manually flagged the edges of the band (below 110 MHz and above 190 MHz), where spectral behavior is dominated by the high and low pass filtering in the HERA signal chain (DeBoer et al., 2017).

In Figure 10.3, we show images formed from the simulated pseudo-Stokes visibilities (top panels) and our observations (bottom panels). These are multi-frequency synthesis images, where we used all unflagged frequencies on either side of the band edges; 115 MHz to 188 MHz. We do not specify a beam model during imaging. At HERA’s position ((latitude, longitude) = (-30:43:17.5, 21:25:41.9)) the Galactic Center transits  $2^{\circ}$  from zenith, while the HERA primary beam has a FWHM of  $\sim 5^{\circ}$  at 150 MHz (Neben et al., 2016). For the simulated visibilities, we flagged the same antennae as in the data. As expected for a compact array, the Stokes I images capture only a low-resolution view of the Galactic Center. The simulated and observed visibilities form remarkably similar images in Stokes I, Q and U, but the simulation under-predicts pseudo-Stokes V power. We defer further discussion to Section 10.3.

Example bandpass solutions from JD 2457548 are shown in Figure 10.4. Although some residual RFI remains obvious, the derived bandpasses were smooth. Thus, even though the gains were imprecise, we expected that using them should not add additional spectral structure.

The complex gain solutions were subsequently applied to the MIRIAD files. Figure 10.5 shows the effect of calibration on the visibilities of three nominally redundantly-spaced baselines. Shown in that figure are the phases of three  $V^{mn}$  visibilities from 14.7 m baselines before and after calibration. There were no shared antennae between the visibilities shown. The qualitative agreement is obvious, providing a consistency check on the solutions.

We did not attempt to calibrate  $D$ -terms in this work.

We down-selected to two relatively RFI-free 20 MHz sub-bands (Figure 10.2); 115 to 135 MHz and 152 to 172 MHz, henceforth referred to the “low band” and the “high band”. As we discuss in Section 10.2.2, these bands were multiplied by a Blackman-

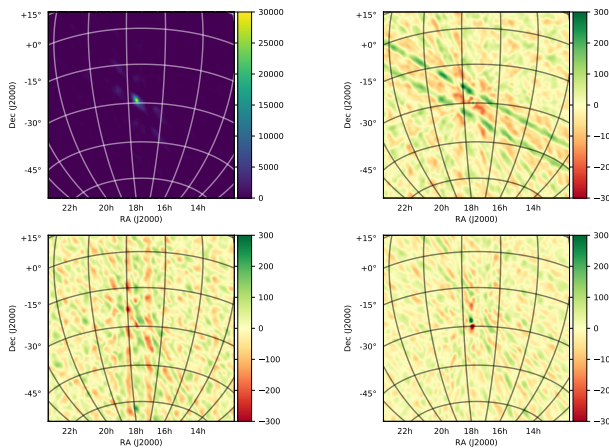
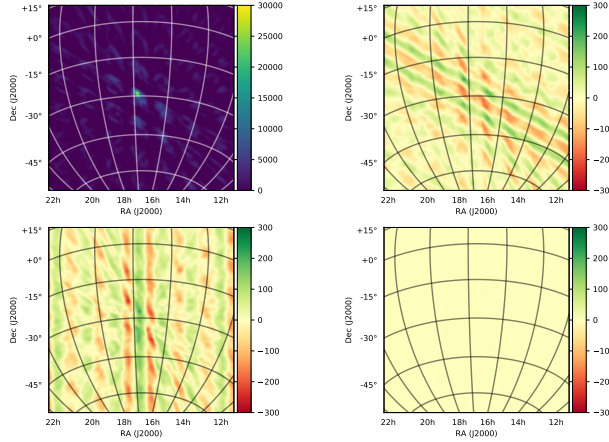


Figure 10.3: *Above:* Multi-frequency synthesis pseudo-Stokes images formed from simulation, where only a Stokes I sky was used; any polarized power is due to direction-dependent polarization leakage (see Section 10.1). *Below:* Multi-frequency synthesis pseudo-Stokes images formed from observed visibilities on JD 2457548. Both sets of panels show the Galactic Center (our calibrator source) close to transit in pseudo-Stokes I, Q, U and V visibilities (*top left, top right, lower left, lower right*). A Briggs-weighting with robustness 0 was used when gridding into the image plane. No deconvolution was performed. The colorbar is in units of Jy/Beam. A separate color scale is used for Stokes I for suitable dynamic range. An R.A., Dec. grid is shown, illustrating the wide-field nature of HERA observations.

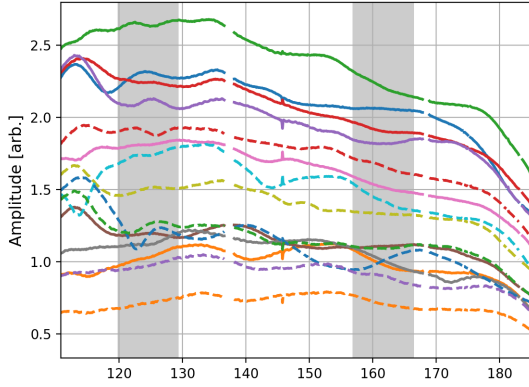


Figure 10.4: Bandpass solutions for the North-South dipole orientation obtained for the functioning antennae in the array on JD 2457548. Differences in line color and style is merely to distinguish different antennae. Shaded regions indicate the effective sub-bands used for power spectrum analysis.

Harris window, centered on their central frequencies, before Fourier transforming in order to minimize side-lobes. This windowing lead to an noise-effective bandwidth of 10 MHz, appropriate for EoR analyses since the HI signal is to a reasonable approximation coeval over the corresponding redshift range (Furlanetto et al., 2006).

Pseudo-Stokes visibilities were formed from the instrumental polarizations. These visibilities were then scaled to the appropriate amplitude using a model for the GC spectrum

$$S_{\text{SgrA}^*}(v) \approx 3709 \text{ Jy} \times (v/408 \text{ MHz})^{-0.5} \quad (10.2)$$

drawn from the Global Sky Model (GSM; de Oliveira-Costa et al., 2008; Price, 2016a; Zheng et al., 2017). Note that the GSM is inherently  $\sim 5\%$  uncertain at these frequencies. We note that this scaling is heavily resolution dependent; we are treating the Galactic Center as a point source when it is extended in reality. However, in Section 10.3 we show that we obtain sensible power levels for the foregrounds and noise, lending confidence to our overall scaling.

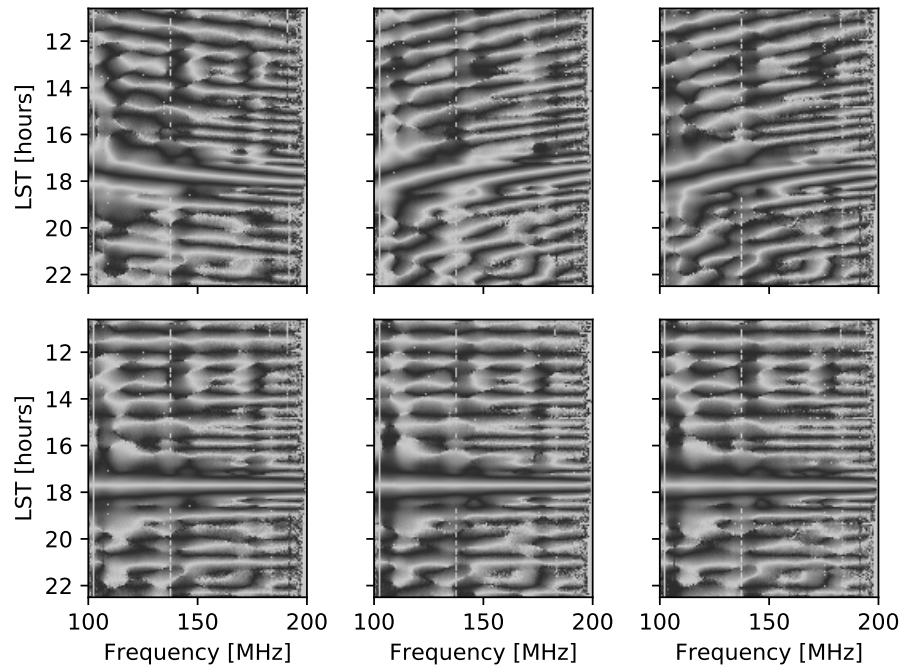


Figure 10.5: The effect of calibration on the phases of visibilities from three redundantly-spaced 14.7 m baselines;  $nn$  polarization. The color scale is cyclic; black is  $\pm\pi/2$  and white is 0 and  $\pm\pi$ . *Above:* before calibration; *below:* after calibration. A simple sky model was sufficient to enforce redundancy for redundant baselines.

### 10.2.2 Forming power spectra

Power spectra were formed according to the method used in Pober et al. (2013) and Kohn et al. (2016), which we briefly review here. All Fourier transforms were windowed using a Blackman-Harris window at the center of the sub-band, which minimized sidelobes. Parsons et al. (2012b) define the *delay transform* as the Fourier transform of a visibility for baseline  $ij$  and pseudo-Stokes parameter  $P$  along the frequency axis

$$\tilde{V}_{ij}^P(\tau, t) = \int dv \tilde{V}_{ij}^P(v, t) e^{2\pi i v \tau}. \quad (10.3)$$

We note that using a Blackman-Harris window will induce a correlation between consecutive  $\tau$  modes. The Fourier transform of the window function in frequency will be sharply peaked in the delay space, and can be ignored to some extent. Hence the self-correlation of  $V_{ij}^P(\tau, t)$  can be used to define the power spectrum, although the small correlation of different  $\tau$  modes could effect the variance of the power spectrum (Parsons et al., 2014).

The power at each delay-mode and baseline can be represented in terms of their respective Fourier components  $k_{\parallel}$  and  $k_{\perp}$  (Parsons et al., 2012b; Thyagarajan et al., 2015a):

$$P(k_{\parallel}, k_{\perp}) \approx |\tilde{V}_{ij}^P(\tau)|^2 \frac{X^2 Y}{\Omega B} \left( \frac{c^2}{2k_B v^2} \right)^2,$$

$$k_{\parallel} = \frac{2\pi v_{21\text{cm}} H(z)}{c(1+z)^2} \tau,$$

$$k_{\perp} = \frac{2\pi}{D(z)\lambda} b$$

for: bandwidth  $B$ , angular area of the beam  $\Omega$ ,  $v_{21\text{cm}} \approx 1420$  MHz, baseline length  $b$ , wavelength of observation  $\lambda$ , Hubble parameter  $H(z)$ , transverse comoving distance  $D(z)$  and redshift-dependent scalars  $X$  and  $Y$  (Parsons et al., 2012a). Note that the angular

area of the beam refers to the diagonal components of the Mueller matrices shown in Figure XXX. For further discussion of forming polarized power spectra in  $k$ -space, refer to Nunhokee et al. (2017).

To avoid a noise-bias when forming the  $|\tilde{V}_{ij}^P(\tau, t)|^2$  term, we cross-multiplied consecutive integrations, rephasing the zenith angle of the latter to the former:

$$|\tilde{V}_{ij}^P(\tau, t)|^2 \approx |\tilde{V}_{ij}^P(\tau, t) \times \tilde{V}_{ij}^P(\tau, t + \Delta t) e^{i\theta_{ij,\text{zen}}(\Delta t)}| \quad (10.4)$$

where  $\theta_{ij,\text{zen}}(\Delta t)$  was the appropriate phasing for baseline  $ij$  and  $\Delta t = 10.7$  seconds.

Pseudo-stokes power spectra were formed for each pair of integrations, for every baseline. After forming power spectra, baselines of identical lengths were averaged together. Appealing to cosmological isotropy, baselines of the same length but different orientation should be sampling the same cosmological structure. These 2D power spectra were averaged over our 8 days of observations. Note that all averaging was performed after forming power spectra; this incoherent averaging was non-optimal from a signal-to-noise perspective outside the wedge, slightly reducing our sensitivity in the EoR window. However, the intention of this investigation was not a deep integration on noise; we were more interested in the polarized response of the instrument. As such, the power spectra presented in the Section below should be interpreted as approximate.

## 10.3 Results & Discussion

Power spectra are shown for the high and low bands in Figure 10.6 and Figure 10.7, respectively, where white dotted lines mark the boundary of the EoR window on the 2D plots. The same data are presented in middle and lower panels, with the latter overlaid as lines to emphasize common features of the power spectra with respect to baseline length.

Theoretical noise levels for the high and low bands were between  $P_{\text{noise}}(k) \approx 1.7 \times 10^8$  mK $^2$ Mpc $^3$ h $^{-3}$  and  $3.4 \times 10^9$  mK $^2$ Mpc $^3$ h $^{-3}$  in the high band, and between  $2.3 \times 10^8$  mK $^2$ Mpc $^3$ h $^{-3}$  and  $6.1 \times 10^9$  mK $^2$ Mpc $^3$ h $^{-3}$  in the low band. These estimates used using a temperature

model of the sky

$$T_{\text{sky}} = 180 \text{ K} \left( \frac{\nu}{180 \text{ MHz}} \right)^{-2.55}, \quad (10.5)$$

assume receiver temperatures of 300 K and 600 K for the high band and low band, respectively (DeBoer et al., 2017, also see the public HERA Memo # 16), and were calculated according to the formalism for noise power spectra in Parsons et al. (2012b), with the inclusion of a baseline-number dependence (to account for different occupancies in each  $k_{\perp}$  bin). These noise power estimates were roughly corroborated by our observations (see Figure 10.8). We observe excess noise on the shortest baselines (also obvious in the lower panels of Figures 10.6 and 10.7).

### 10.3.1 General features of the power spectra

The most striking feature of these power spectra is the degree of foreground isolation achieved in all pseudo-Stokes parameters. In similar studies of 2D polarized power spectra, both PAPER (Kohn et al., 2016) and LOFAR (Asad et al., 2017) measurements found “filled” regions of Fourier space out to the edge of the EoR window (in the delay-spectrum paradigm, this corresponds to the horizon; zenith angle  $\pm 90^\circ$ ), with some supra-horizon leakage (Pober et al., 2013) into the EoR window itself. The power spectra in Figures 10.6 and 10.7 show no such behavior; all foreground emission appears to be contained within a narrow region around  $k_{\parallel} = 0 \text{ h/Mpc}$ . This behavior was predicted for an array of HERA-like dishes by Thyagarajan et al. 2015a (although that study only concentrated on the Stokes I component).

Power at horizon delays, as predicted by Thyagarajan et al. (2015a) and Neben et al. (2016), was not observed. This was likely a resolution effect. To resolve horizon-delay power, one would need to sample many periods of  $\tau_h = b/c$ , where  $b$  is the magnitude of the baseline vector. The maximum length baseline in the HERA-19 array was 58.4 m, corresponding to a  $\sim 5 \text{ MHz}$  period: barely sampled by the 10 MHz windows we use in this study. The lack of horizon power is corroborated by the simulations of the HERA delay

response in Ewall-Wice et al. (2016a) and Thyagarajan et al. (2016), although those studies used a different windowing function for the delay transform. Their simulations also predict a high degree of foreground isolation: the presence of noise in our data of course meant that we do not realize the 11 dex of isolation that can be achieved in simulation, but the  $\sim$ 8 dex we do see, without any foreground subtraction and a simple calibration, speaks to the power of HERA’s future capabilities.

Visible in the observational data, but not in the simulation, is an excess of power at  $k_{\parallel} = 0.04 \text{ h/Mpc}$ , corresponding to a delay of 100 ns, which is independent of baseline length. This suggests that its origins are in the HERA signal chain. There are 15 m coaxial cables at one stage of the signal chain from the HERA dishes to the correlator<sup>2</sup>. In the limit of little delay induced by the cable and our limited delay resolution, a reflection along this stage of the signal chain would produce an alias of the foreground signal at a  $\tau \approx 100 \text{ ns}$  (Beardsley et al., 2016; Ewall-Wice et al., 2016b).

### 10.3.2 Day-to-day variability

The foreground and EoR window power levels appeared to be relatively stable between days, with variation most likely due to the incomplete sky model used for gain calibration. Figure 10.8 shows power as a function of baseline length for  $k_{\parallel} = 0 \text{ h/Mpc}$  (solid lines) and  $k_{\parallel} = 0.2 \text{ h/Mpc}$  (dot-dashed lines). Deviations from the mean at  $k_{\parallel} = 0 \text{ h/Mpc}$  may be a limitation imposed by our simplistic sky model. Since the noise levels in the EoR window region remained noise-like throughout our observations, the uncertainty in the absolute gain scale did not have a large impact on our largely-diagnostic investigation.

### 10.3.3 Polarimetric results

Figures 10.6 and 10.7 qualitatively illustrate that the simulations described in Section 10.1 reproduced the main features of the observed power spectra. The simulations were run

---

<sup>2</sup>This stage of the signal chain is only present in the commissioning array. Future HERA build-outs will transition to a different architecture (DeBoer et al., 2017).

only with a Stokes I sky component and no simulated calibration errors, so the only signal in the polarized power spectra was from wide-field beam leakage (Figure XXX). An example comparison between simulation and observation in the image plane is shown in Figure 10.3.

In Figure 10.9 we show the power levels observed on the shortest baseline (14.7 m) compared to our simulations for each band. The simulations used an unpolarized diffuse sky model (the most recent version of the GSM; Zheng et al., 2017), which should be accurate at the scales probed by a 14.7 m baseline. Inset panels zoom-in on the region around  $k_{\parallel} = 0 \text{ h/Mpc}$ , where most of the foreground power was concentrated. We saw that the simulations reproduced  $\sim 75\%$  of the foreground power observed in pseudo-Stokes I in the high band, and over-predicted foreground power by  $\sim 35\%$  in the low band. This could have been due to unrealistic frequency scaling of the diffuse foregrounds in the GSM.

For pseudo-Stokes Q and U, the simulations accounted for  $\sim 60 - 75\%$  of power seen within the pitchfork region, suggesting that most of the power seen in these power spectra, at least for the shortest baselines, can be mostly attributed to direction-dependent leakage effects. As noted in Section 10.1, residual gain and phase errors are able to leak a fraction of pseudo-Stokes I into Q and U, but some fraction of the observed power ( $\leq 25\%$ ) may have been due to linearly polarized foregrounds. This is corroborated by residual power close to the location of the Galactic Center, and increased power over the sky, in the observed pseudo-Stokes Q and U skies compared to the simulated ones in Figure 10.3. As the Galactic Center is the highest-amplitude source of power, we expect residual gain errors to be most obvious in the same position as it is in the pseudo-Stokes I image. Such an excess is present in the observed pseudo-Stokes Q and U images, but absent in the simulated ones – pointing to direction-independent gain errors being present. However, the simulated pseudo-Stokes Q and U images contain only direction-dependent leakage from Stokes I. Since they reproduce most of the features seen in the observed data, pseudo-Stokes Q and U are clearly dominated by direction dependent leakage.

Lenc et al. (2016) observed linearly polarized emission from diffuse structure with  $\sim 1.6 - 4.5\%$  fractional polarization at 150 MHz, corresponding to power levels of  $\sim 10^5 \text{ mK}^2 \text{Mpc}^3 \text{h}^{-3}$ . This power level is similar to expected EoR power levels (e.g. Lidz et al., 2007; Moore et al., 2013; Nunhokee et al., 2017); a detection of a power spectrum of polarized galactic synchrotron will require much deeper integrations.

The observed pseudo-Stokes V power spectrum was more poorly modelled by our simulation. In both bands we observed  $\sim 20$  dB more power in pseudo-Stokes V at  $k_{\parallel} = 0 \text{ h/Mpc}$  than predicted by our simulations. The peak power observed in pseudo-Stokes V was roughly 0.1% of the peak power observed in pseudo-Stokes I. Likewise in the sky images shown in Figure 10.3, there is little pseudo-Stokes V power in the simulated images, compared to observation. This suggests that most or all of the power in pseudo-Stokes V is due to direction independent leakage. While the leakage appears localized in Figure 10.3, we see in Figure 10.9 that it is statistically similar to pseudo-Stokes Q and U in power. Since  $D$ -terms cause direction-independent leakage from pseudo-Stokes I to pseudo-Stokes V, the excess power we observed could be interpreted as an approximate  $D$ -term level of  $\sim 1\%$  (Thompson et al., 2017). This is similar to  $D$ -term levels from other low frequency instruments such as MWA-32, which was found to have  $\sim 2\%$   $D$ -terms (G. Bernardi, private communication). The under-prediction of pseudo-Stokes V from the simulation could, of course, also be due to some unmodelled direction-dependent instrumental effect.

To understand which effect, if either, is dominant, a precise  $D$ -term calibration of HERA is required. This effort is underway with data taken with bright polarized point sources in transit, and will be presented in future work. Another potential cause of the discrepancy could have been that our simulations under-predicted Stokes V power, due to lack of accounting for some variety of instrumental circular polarization.

In Section 10.3.1 we noted the presence of excess power at  $k_{\parallel} = \pm 0.04 \text{ h/Mpc}$  ( $\pm 100 \text{ ns}$ ) that was independent of baseline length, suggesting that it was due to a reflection along 15 m cables. Figure 10.9 shows that power at this delay is not consistent between polar-

izations. Stokes U and V power only exhibited excess signal at -100 ns in the high band, and in the low band, it was only Stokes U that did not exhibit that excess at +100 ns. This may be a clue about the polarization state of cable reflections, perhaps as a function of frequency, but we defer this to future work – noting it as a point of interest here.

## 10.4 Conclusions

In this work we have presented polarized power spectra from the HERA-19 commissioning array. With modest calibration, HERA is able isolate total intensity and polarized foregrounds to within the “pitchfork” region of  $k$ -space, as predicted by Thyagarajan et al. (2015a), lending confidence to its future performance as an instrument capable of both detecting and characterizing the EoR power spectrum. Of course, the array used in this study had just 19 antennae, 15 of which were used for analysis – future build-outs of HERA with up to 350 antennae will require strong quality-assurance efforts.

Simulations of the polarized response of the instrument, mapped into the same Fourier space as the data, suggest that most or all of the polarized power observed in pseudo-Stokes Q and U power spectra is due to direction-dependent beam leakage from pseudo-Stokes I. Residual gain and phase errors could account for the rest of the power, but some fraction of the total ( $\leq 25\%$ ) may be due to linearly polarized foregrounds. Excess power in pseudo-Stokes V may be due to  $D$ -terms at the 1% level, but a full image-based calibration with a polarized point source is required to confirm this. The general accuracy of our simulations suggests current modelling of the complex HERA beam is accurate.

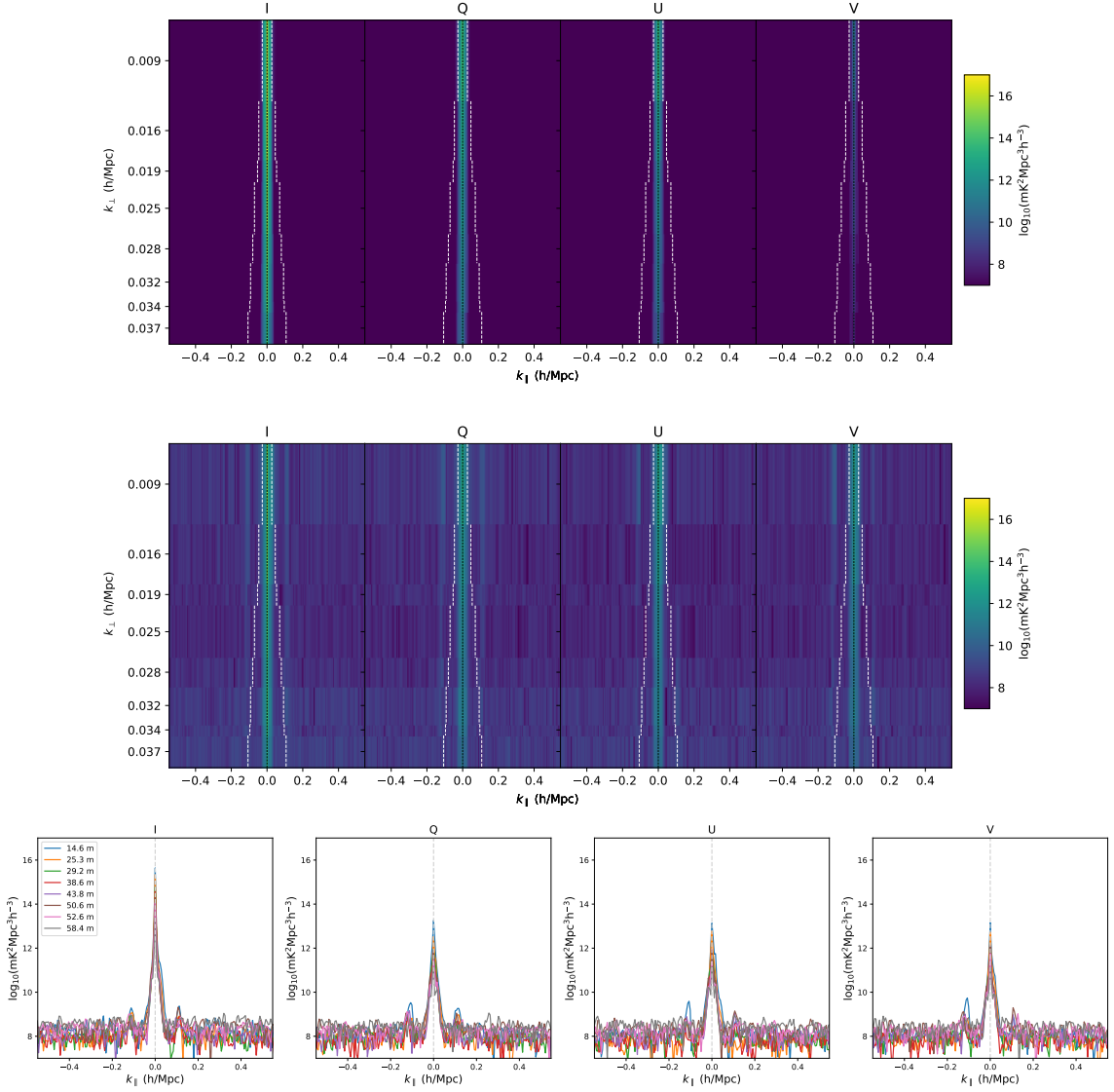


Figure 10.6: Results from the high-band (157–167 MHz). White dotted lines indicate the boundary of the pitchfork and the EoR window. A black dotted line indicates the  $k_{\parallel} = 0$  h/Mpc line. *Top:* Simulated power spectra in Stokes I, Q, U and V, following the formalism in Section 10.1 – no polarized sky model was used, so power in Stokes Q, U and V was only due to direction-dependent leakage from Stokes I. No instrumental noise was included in the simulation. *Middle:* Eight-day average power spectra from data. *Bottom:* The same data as shown in the middle panel, but with each baseline length overlaid on one another to allow shared features to be more easily identified.

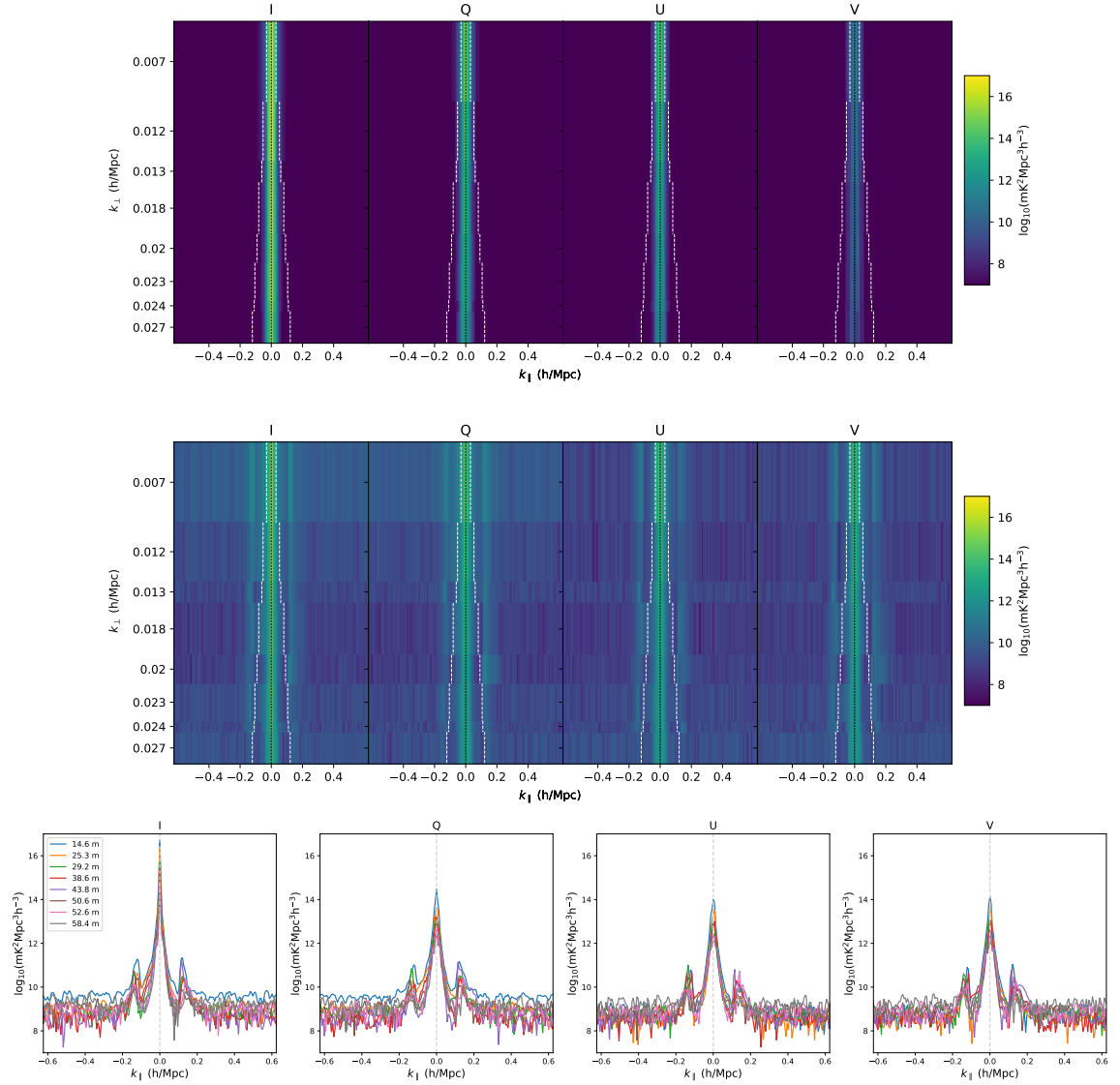


Figure 10.7: Results from the low-band (120–130 MHz), arranged in the same format as Figure 10.6.

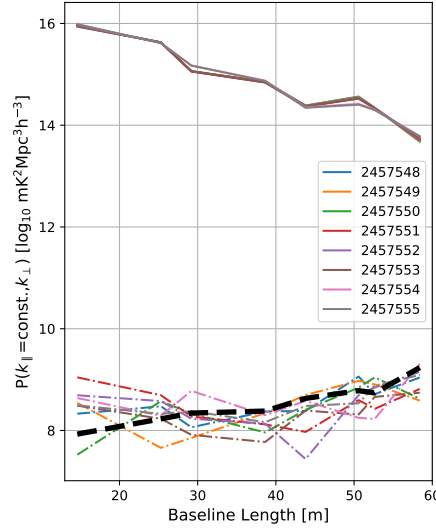


Figure 10.8: High band power as a function of baseline length for the center of the pitch-fork ( $k_{\parallel} = 0$  h/Mpc; solid lines) and in the EoR window ( $k_{\parallel} = 0.2$  h/Mpc; dot-dashed lines) for each JD of observation. The black dashed line represents the approximate noise power assuming a receiver temperature of 300 K. A very similar relationship is shown in the low band, but with a higher noise floor, which is consistent with system temperature as a function of frequency. The noise level climbs with baseline length as the compact nature of the array gives more short baselines to average-over in a given  $(k_{\parallel}, k_{\perp})$  bin than longer ones.

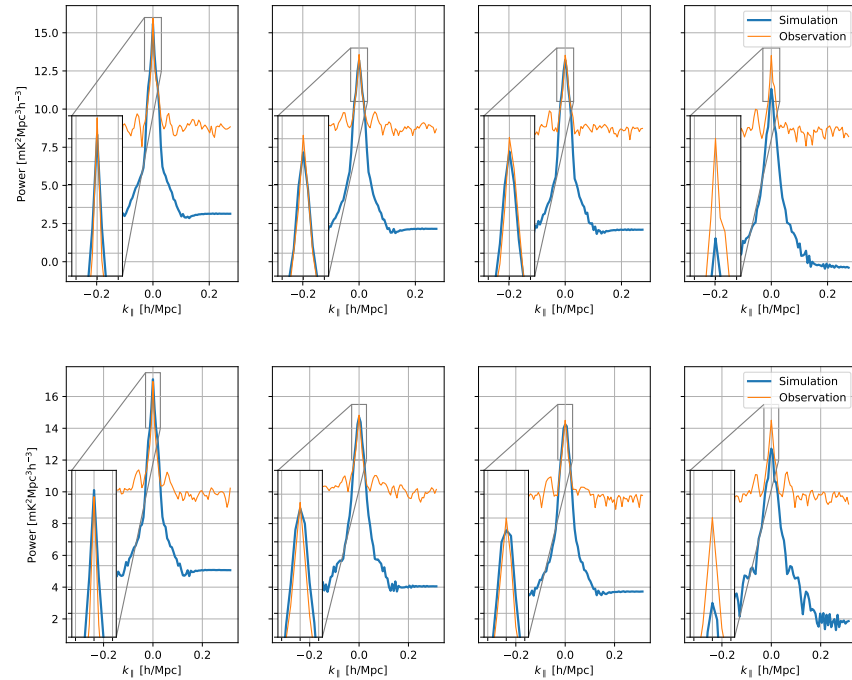


Figure 10.9: Simulated and observed power as a function of  $k_{\parallel}$  for the shortest baseline (14.7 m). *Right to left*: pseudo-Stokes I, Q, U and V; *above*: the high band; *below*: the low band. The simulations were noiseless and used an unpolarized sky model. Inset panels zoom-in on the peak region. They capture the foreground power levels in pseudo-Stokes I, Q and U, suggesting all power in Q and U is due to leakage from Stokes I. The power level in V is highly discrepant, however, suggesting some sort of beam-independent instrumental leakage.

# Chapter 11

## Deep integrations on polarization with PAPER-128

In Chapter 9, I presented polarized power spectra from a short integration – a few hours of one night – over a wide range of  $k_{\perp}$ -modes probed by the PAPER-32 polarized imaging array (Kohn et al., 2016). Chapter 10 presented the first power spectral results from HERA. The HERA-19 commissioning array was small and dense, meaning that only a few  $k_{\perp}$ -modes were accessible. For that study, we averaged over 10 hours per night, for 8 consecutive nights (Kohn et al., 2018). This Chapter presents results from the PAPER-128 array. In this Chapter I present roughly one quarter of the total number of observations recorded by this interferometer (Section 11.1). I show results of a deep integration on a very narrow range of  $k_{\perp}$ -modes (corresponding to  $\sim 30$  m spacings of the redundant grid; Section 11.2) and discuss the implications for deep, fully-polarized integrations with large interferometers (Section 11.3).

### 11.1 Observations & Reduction

PAPER-128 was the largest build-out of the PAPER experiment. As described in Chapter 4, PAPER-128 consisted of 128 antennas, 112 of which were arranged in a redundant

Table 11.1. PAPER-128 Observing Seasons & Epochs

Season	Epoch	Julian Dates	Calendar Dates	Notes
1	1	2456617 - 2456673	Nov 20, 2013 - Jan 15, 2014	1/8 F-Engine failure
	2	2456678 - 2456724	Jan 20, 2014 - Mar 7, 2014	Good
2	1	2456625 - 2456732	Mar 8, 2014 - Mar 7, 2014	Too few data
	2	2456843 - 2456873	Jul 4, 2014 - Aug 3, 2014	Uninteresting LST range
	3	2456881 - 2456928	Aug 11, 2014 - Sep 27, 2014	Many malfunctioning antennas
	4	2456942 - 2457008	Oct 11, 2014 - Dec 11, 2014	Good
	5	2457030 - 2457050	Jan 7, 2015 - Jan 27, 2015	Many malfunctioning antennas

grid. An annotated photograph of the array is shown in Figure 11.1. In this section, I review the PAPER-128 campaign (Section 11.1.1) and the subsequent reduction of roughly one quarter of the total number of observations (Section 11.1.2).

### 11.1.1 Overview of PAPER-128 observations

Observations were recorded for two years, with first light on November 20th 2013 and final readings on January 27th 2015. However, these observations were not always contiguous. Human errors, experimentation and malfunctioning electronics required the correlator and connected electronics to be turned off and restarted, altering the characteristic phasing and gain scale of the array. Each of these restarts constituted the beginning of a new “Epoch” of the array which required different quality assurance steps and initial calibration stages. Table 11.1.1 summarizes the length and nature of these Epochs.

Figure 11.2 illustrates the challenge imposed by the correlator restarts. Epoch changes were characterized by large shifts in the overall phase of visibilities, of course leading to changed magnitudes of the real and imaginary parts of the visibilities recorded. The quality assurance metrics described in Chapter 6 were sensitive to these changes. Of course, absolute calibration – that is phasing to the correct point on the sky and scaling the visibilities from arbitrary to physical flux density units – had to be run separately on

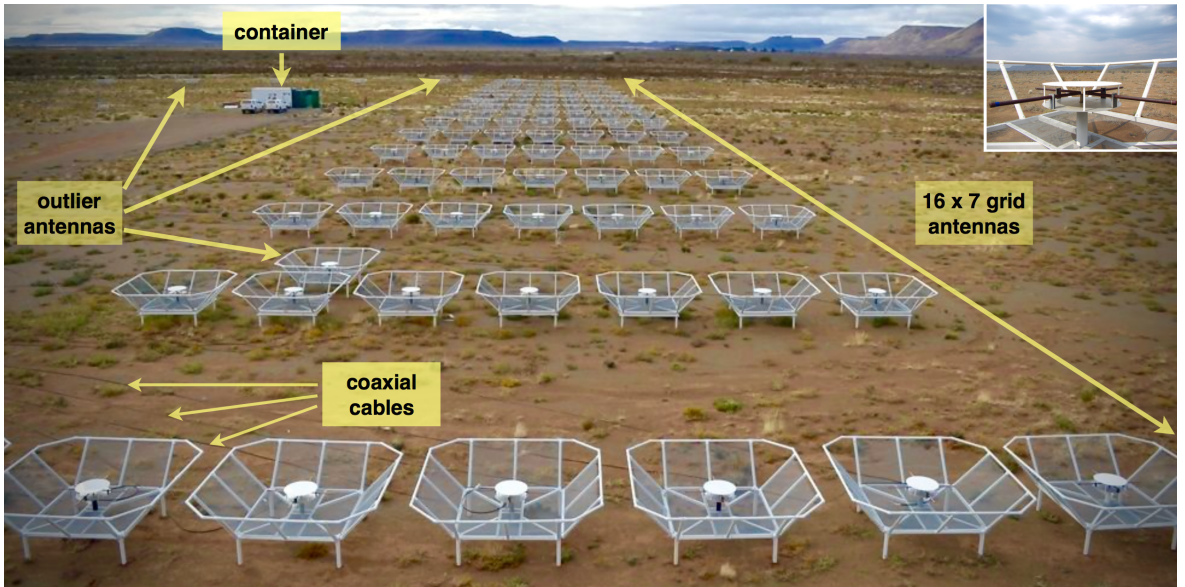


Figure 11.1: An annotated photograph of the PAPER-128 array, looking to the East. Highlighted are the 112 antenna redundant grid, with 15 m East-West spacings between each row; outlier antennas from the main grid used to increase *uv*-coverage; coaxial cables running to the receiverators and correlator (see Chapter 4). An inset panel shows a PAPER sleeved dipole. Photo credit: J. E. Aguirre. Figure credit: C. D. Nunhokee; (Nunhokee, 2018).

individual Epochs.

As shown in Table 11.1.1, Season 2 had a larger number of observed nights than Season 1. However, the analysis of Season 2 was especially challenging due to large numbers of malfunctioning antennas. This may have been due to the antennas ageing past a critical point. Nothing in the array was replaced during build-outs except for the correlator; 32 of the antennas had been out in the desert for 4–5 years (PAPER-32) and another 32 for 3–4 years (PAPER-64). Most of the time, these were the antennas that were identified as malfunctioning.

Season 2 Epoch 4 was relatively well-behaved, and may be analyzed in the future. For this work, we concentrated our analysis on Season 1. Season 1 Epoch 2 was ten days shorter than Season 1 Epoch 1, but Epoch 1 had two major challenges associated with it: a data loss event, and an F-engine failure. Due to human error, Epoch 1 data was deleted and had to be restored and recompressed (see Chapter 6). This was almost entirely successful, at the loss of one week’s worth of observations. The F-engine failure was more critical. We discovered during our analysis that exactly one eighth of the antennas in the array produced noise-like visibilities with the rest of the array, but normal correlations between one another. These antennas had “seceded” from the array. They shared the characteristic of all being attached to the same F-engine (of which there were eight; see Figure 4.2). This suggested that there was a clock-offset on that F-engine, resulting in no correlation between the signal from those antennas and those running through the other in-sync F-engines.

This left Season 1 Epoch 2 as the most well-characterized and well-behaved Epoch of PAPER-128 observations, and we focused on this Epoch alone from now on. Cross-polarization metrics identified seven incorrectly-rotated antennas, which were corrected during initial processing. Eight antennas were identified as malfunctioning by mean visibility amplitude metrics, including one of those that was incorrectly-rotated. The state of the array for Season 1 Epoch 2 is summarized in Figure 11.3.

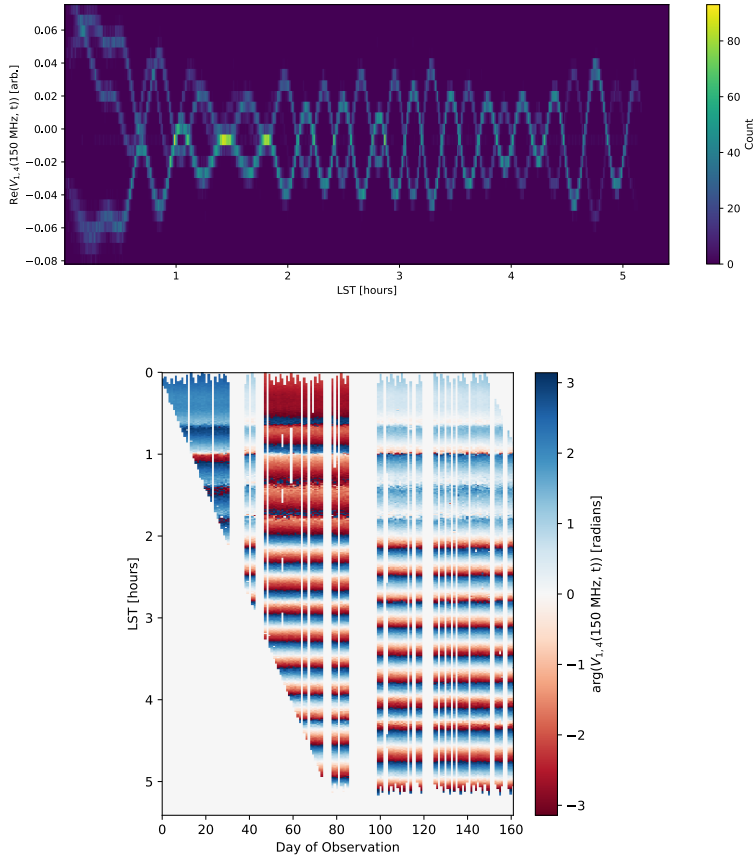


Figure 11.2: The challenge of Epoch changes. Shown are all of the Season 2 time samples of the visibilities recorded by the 30 m baseline between antennas 1 and 4, LSTs 0–5, for only the 150 MHz frequency bin. The above panel shows a histogram of the real part of the visibilities as a function of LST – there is a dramatic change in magnitude with respect to LST. Likewise, the lower panel shows the phase of each visibility sample (color axis) as a function of LST (vertical axis) and day of observation (x axis). There are obvious large shifts in phase, which require separate calibration stages.

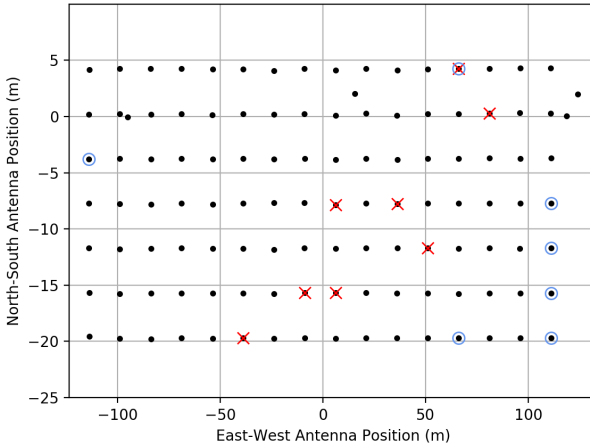


Figure 11.3: Good, bad (red crosses) and rotated (blue circles) antennas in Season 1 Epoch 2, as identified by the cross-polarization and visibility amplitude metrics defined in Chapter 6.

### 11.1.2 Reduction of Season 1 Epoch 2 data

After correcting for cross-polarized and malfunctioning antennas, we were able to begin processing the data using the redundant calibration techniques described in Chapter 7. We used the phase-flattening algorithm described in Section 7.1.2 to solve for phase slopes for each antenna. This was performed for the North-South and East-West feed arms separately using the linear instrumental polarizations ('nn' and 'ee'), as this method is sensitive to signal-to-noise. We performed a single calculation of these overall delays at the start of the Epoch, and applied those to the rest of the days observed. These overall delays are largely due to electrical delays along the cables leading to the receiverators and the correlator, so we did not expect them to vary a by large amount.

#### 11.1.2.1 Redundant calibration

After phase-wraps were flattened, the OMNICAL algorithm could be invoked safely. For this study, we implemented the *4pol+minV* calibration method. For a full exploration of

OMNICALibration methods, see Chapter 7. Briefly, the *4pol+minV* calibration scheme redundantly solves for diagonal gains for the North-South and East-West feed arms at the same time, *and* imposes that the ‘ne’ and ‘en’ visibilities are equal. That is, it produces a redundant calibration which minimizes pseudo-Stokes V. Figures 11.4 and 11.5 show the successful results of the *4pol+minV* OMNICALibration, where visibilities from 30 m East-West baselines showed a high degree of redundancy in all pseudo-Stokes polarizations, and pseudo-Stokes V is almost complete noise-like.

After calibration, we down-selected to only the baselines we sought to analyze for our power spectrum studies. This was partly a utilitarian step: reducing the entire data set would represent a large feat of data processing, since Season 1 Epoch 2 was  $\sim 2.5$  TB in size if all baselines were retained, and several processing stages that would duplicate the data were still required. The baselines kept were the 30 m East-West type and their closest diagonals – that is, 30 m East-West &  $\pm 4$  m North-South baselines (e.g. [Kolopanis et al. \(2018\)](#)).

### 11.1.2.2 Foreground removal

To remove foreground signal from the data, we implemented a variation of the 1D-CLEAN (Parsons & Backer, 2009) used by past PAPER studies (Parsons et al., 2014; Ali et al., 2015; Jacobs et al., 2015; Moore et al., 2017; Kerrigan et al., 2018, ; [Kolopanis et al. 2018](#)). Instead of performing an iterative CLEAN we used a linear least-squares approach which we termed linCLEAN.

Using linCLEAN, we endeavoured to model the foreground component of the visibilities using the finite number of Fourier modes that exist within the foreground wedge of the EoR window paradigm. The number of these modes was set by the frequency resolution of the instrument, and the baseline length (see Chapter 5). The Fourier conjugate of the frequency axis, known as the delay axis, is specified through the delay transform of a visibility, which for short baselines may be written as (Parsons et al., 2012a):

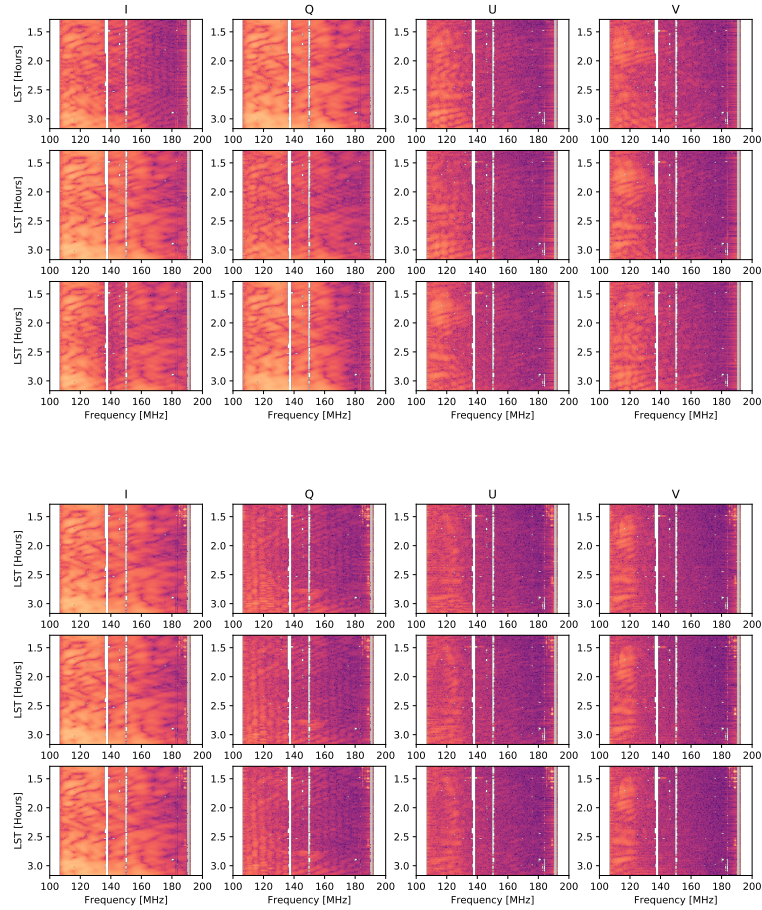


Figure 11.4: Amplitudes of three redundant visibilities before (above) and after (below) OMNICALibration using the *4pol+minV* scheme. All four pseudo-Stokes polarizations attained a high degree of redundancy in magnitude after calibration. The color axis is logarithmic and spans 5 orders of magnitude in arbitrary data units.

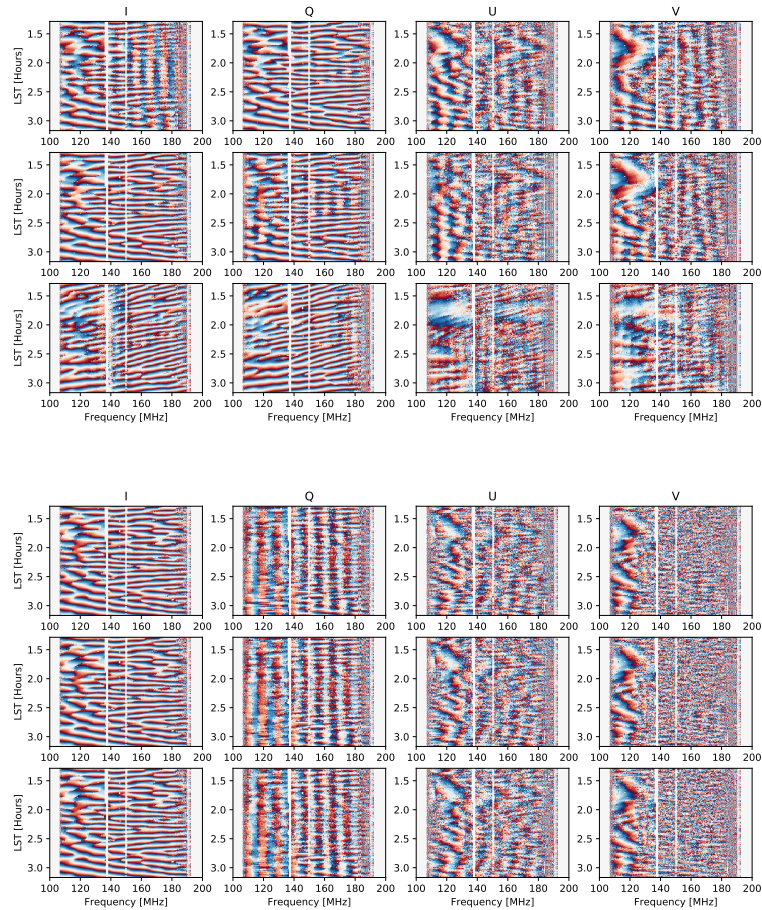


Figure 11.5: The same visibilities as shown in Figure 11.4, but showing their phases instead of their amplitudes. Again, a high degree of redundancy is obtained between baselines for all polarizations. The color axis is linear and spans  $\pi$  (red) to  $-\pi$  (blue) radians.

$$\tilde{V}(\tau) = \int_{v_{\min}}^{v_{\max}} V(v) \exp(2\pi i \tau v) dv \quad (11.1)$$

for visibility  $V(v)$  and delay mode  $\tau$ . Delay modes become estimators for the Fourier-transformed brightness temperature field.

We constructed a visibility  $\vec{m}(v)$  as a model, per time integration, of an individual visibility  $\vec{d}(v)$  (which we represent as a vector along the frequency axis), seeking to minimize the chi-square

$$\chi^2(v) = (\vec{d}(v) - \mathbf{A}(v', \tau)\vec{m}(v))^T \mathbf{W}(v', v) (\vec{d}(v) - \mathbf{A}(v, \tau)\vec{m}(v)). \quad (11.2)$$

In the above equation, the matrix  $\mathbf{A}$  had dimensions “number of frequency channels” by “number of allowed delay modes”. An allowed delay mode  $\tau$  was within the interval  $[0, \frac{|\vec{b}|}{c} + t_{SH}]$ , for baseline vector  $\vec{b}$ , speed of light  $c$  and an allowed “supra-horizon leakage” term  $t_{SH}$  (Pober et al., 2013), which we set to 15ns.

The contents of  $\mathbf{A}$  were the concatenation of matrices  $\mathbf{C}$  and  $\mathbf{S}$ :

$$\mathbf{C}_{ij} = \cos(2\pi v_i \tau_j) \quad (11.3)$$

$$\mathbf{S}_{ij} = \sin(2\pi v_i \tau_j) \quad (11.4)$$

$$(11.5)$$

for frequency channel  $i$  and delay bin  $j$ . The matrix  $\mathbf{W}$  was diagonal, and assigned weighting per frequency channel. With an estimated system temperature one could implement an inverse variance weighting per frequency channel, but we pursued a simpler scheme where the entries were zero for RFI-flagged channels, and unity otherwise.

This system was least-squares solvable for the delay modes, and granted a foreground model

$$\vec{m}(v) = (\mathbf{A}^T \mathbf{W} \mathbf{A})^{-1} \mathbf{A}^T \mathbf{W} \vec{d}(v) \quad (11.6)$$

which could subsequently be subtracted from the  $\vec{d}(v)$ , leaving only the noise-like backgrounds.

We ran linCLEAN on the Epoch of OMNICALibrated data, using the entire unflagged part of the band (for details on flagging of PAPER-128 data, see Chapter 6) to obtain an estimate of  $\mathbf{A}$ . After this, we implemented a round of RFI flagging that clipped any samples that represented  $> 4\sigma$  fluctuations above the average, where averages were performed along the time and frequency axes.

### 11.1.2.3 Binning in LST

We could then average-down on the noise by binning visibilities according to the LST they were observed at. The LST bin size used was 41s long, and we split the Epoch into even and odd days, constructing two separate LST-binned data sets. Cross-multiplying these allowed us to construct an unbiased power spectrum estimate (e.g. Parsons et al., 2014, ; Cheng et al. 2018). Unflagged RFI events would dominate any other signal in a given LST bin. To avoid binning RFI with sky signal, before averaging we computed the median of all observations in a given LST bin and flagged any observations with amplitude  $> 3\sigma$  above the median. This clipping narrowed the distribution of visibilities about the median, altering the thermal noise variance, but leaving the expectation value unchanged, so we expect little loss of signal due to this step.

For this analysis, we created two LST-binned data sets (each split into even and odd days): a set constructed from the foreground subtracted visibilities, and another set with the foregrounds included. We used the latter to calculate an absolute calibration of both data sets.

### 11.1.2.4 Absolute calibration & fringe-rate filtering

We formed images of the Pictor A transit in order to derive an absolute calibration for the ‘n’ and ‘e’ feed arms in the fashion described in Chapter 7. We converted the MIRIAD files of the LST-binned foreground data into CASA (McMullin et al., 2007) Measurement Sets at  $LST \approx 5.3$  hours (the relevant LST for the transit of Pictor A). Our sky model consisted only of Pictor A as a unpolarized point source. Because we had already down-selected to

the power spectrum baselines, Pictor A completely dominated the signal. The images of the four pseudo-Stokes parameters we obtained are shown in Figure 11.6. In that image, pseudo-Stokes I is on a color scale with double the dynamic range of Q, U and V – that is, pseudo-Stokes Q, U and V were almost completely noise-like. In pseudo-Stokes I, Pictor A dominated the field. These images were low quality because only the power spectrum baselines were used to produce the image, leading to large grating lobes and an elongated point-spread function; shown in Figure 11.7.

We used the CASA bandpass routine to derive an overall frequency-dependent scaling that brought the North-South and East-West dipole arms to a physical scale that minimized pseudo-Stokes Q in Pictor A, and converted the data units to a physical level in Janskies. For the Jansky scaling we used the spectrum from Jacobs et al. (2013). CASA provided separate scalings for all antennas used in the analysis. We plot the average scaling for the North-South and East-West dipole arms in Figure 11.8, shading-in the standard deviation between antennas. We implemented aggressive RFI flags, leading to large gaps in the spectrum. The higher frequency portion of the band had a very low variance its bandpass solutions, as expected given that they were OMNICALibrated and that the low band was historically poorly-behaved and characterized (e.g. Chapter 7).

As discussed in Chapter 6, every baseline not only samples characteristic delay modes based on its length, but also characteristic modes in time, per frequency, known as ‘fringe rates’ (if frequency dependence is ignored, they are referred to as “delay rates”; e.g. Parsons & Backer, 2009). For drift-scan telescopes such as PAPER, the sky, beam and fringe terms are locked to one another and can be thought of as an enveloped fringe pattern which varies in time as the Earth rotates. The rate of change of this pattern – the fringe rate – depends only on the baseline length (which gives the fringe width) and the position of the drift-scanning telescope on Earth. By Fourier-transforming along the time axis of recorded visibilities, one can identify a “window” of physical Fourier modes that represent fringe rates reflective of the Earth’s rotation. Such a window is shown for a 30 m single baseline in Figure 11.9. By convolving an appropriate filter, one could extract

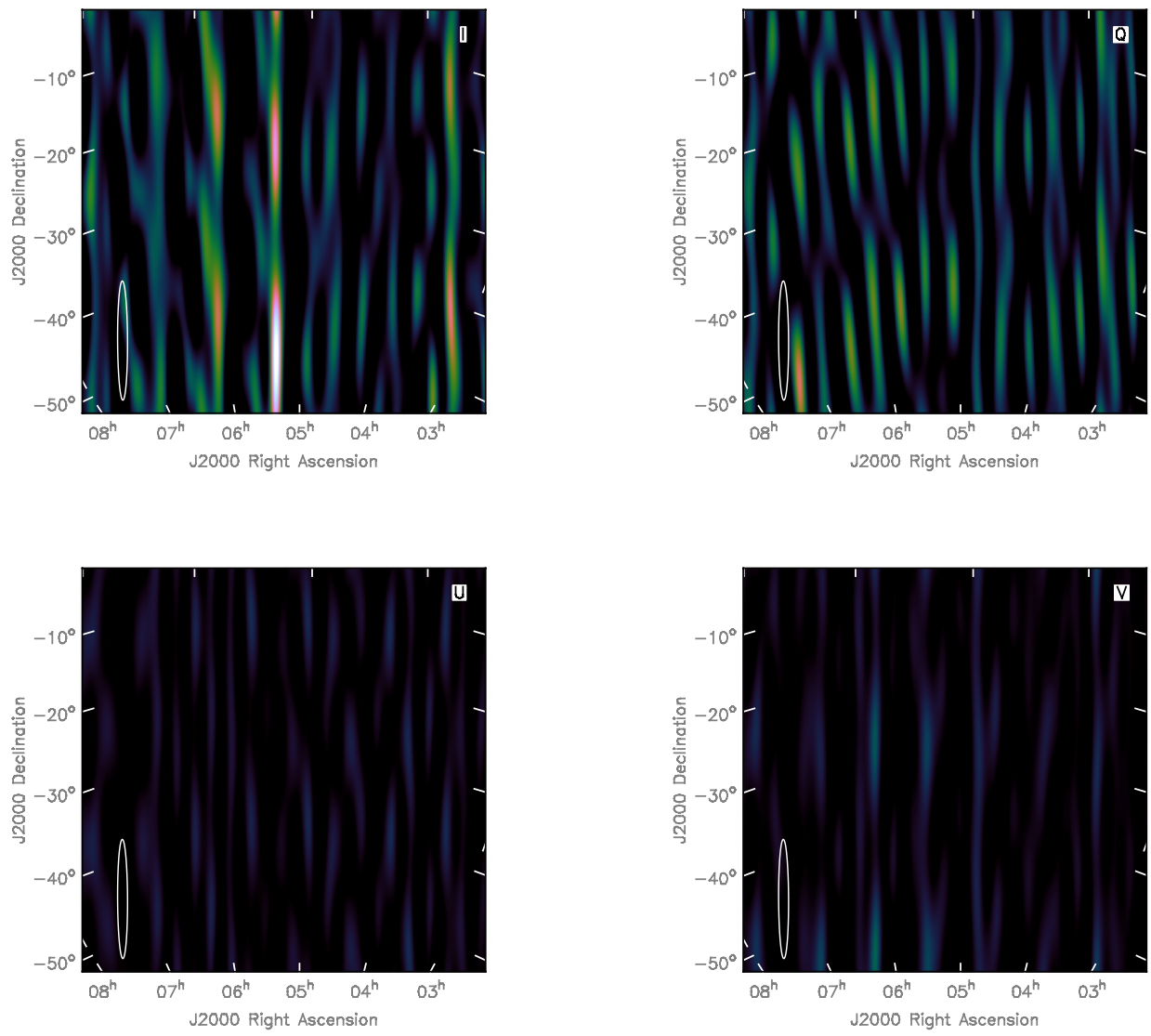


Figure 11.6: Images of Pictor A, used to calibrate the absolute scaling to physical units. These images are multi-frequency syntheses, but we used per-channel information for the final calibration (see Figure 11.8). Pseudo-Stokes I is on a linear scale of twice the dynamic range of pseudo-Stokes Q, U and V. A beam ellipse is shown in the South-West corner of the images. The poor quality of the images is a result of using only the baselines that go into the power spectrum estimates. Pictor A dominates the field in pseudo-Stokes I, and is of the morphology expected given the PSF shown in Figure 11.7.

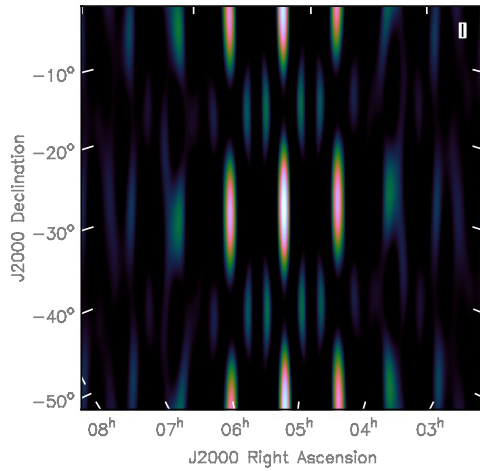


Figure 11.7: The point-spread function of an array consisting only of the  $\sim 30\text{ m}$  power spectrum baselines. The sparseness and asymmetry of the array lead to an elongated PSF with large grating lobes.

these physical fringe rates and filter-out noise. This is equivalent to changing the shape of the primary beam of an antenna after observation, and was explored in Parsons et al. (2016), and implemented in Ali et al. (2015). However, because the range of physical fringe rates for a short baseline is narrow, this amounts to correlating a large number of visibility measurements in time, which must be accounted for in signal-to-noise estimates (Ali et al., 2015, [Cheng et al. \(2018\)](#)).

We implemented such a filter on the LST-binned and absolute-calibrated background data, and proceeded to form power spectra.

### 11.1.3 Forming power spectra

As shown in Figures 11.4 and 11.8, the 150–180 MHz section of the band had lower noise and a more precise calibration. Within this, we down-selected to the 10 MHz-wide 155–165 MHz sub-band to form power spectra. This bandwidth was appropriate for an

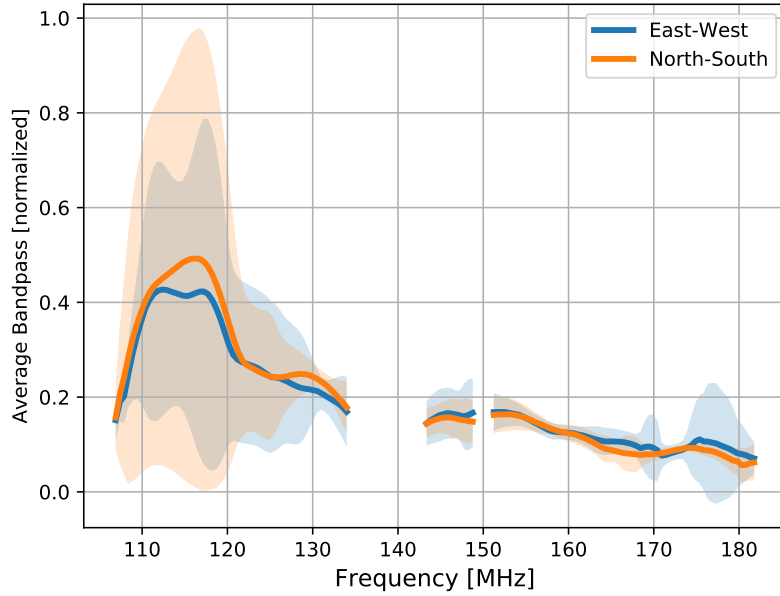


Figure 11.8: The average bandpass scaling used for absolute calibration, with shading indicating the  $1\sigma$  deviation about the average across antennas.

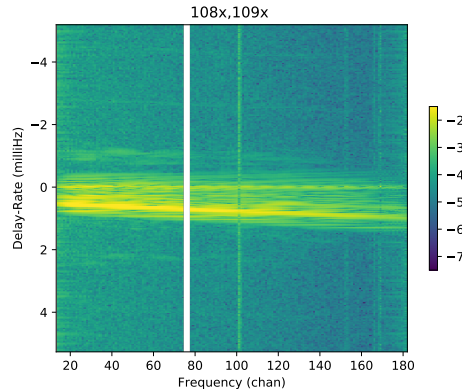


Figure 11.9: Delay-rate vs. frequency for a 30 m baseline in the ‘xx’ (East-East) polarization. The color axis is logarithmic, in arbitrary data units – there is a clear “window” of delay-rate modes of high amplitude. These correspond to physical modes to do with the Earth’s rotation. The rest of the delay-rates are simply noise-modes and can be filtered-out.

EoR analysis, since the HI signal is to a reasonable approximation coeval over the corresponding redshift range (Furlanetto et al., 2006). The central redshift our frequencies corresponded to was  $z = 8.07$  (we assumed the Planck Collaboration et al. (2016) cosmological parameters throughout this Chapter).

Power spectrum estimators per baseline and time were formed by cross-multiplying delay-transformed visibilities between even and odd days, at identical  $\tau$  modes and LSTs:

$$\hat{P}_{ij}(\tau, t) = \left( \frac{\lambda^2}{2k_B} \right)^2 \frac{X^2 Y}{\Omega_{PP} \Delta v} \left\langle \tilde{V}_{ij}^{*, P, \text{even}}(\tau, t) \tilde{V}_{ij}^{P, \text{odd}}(\tau, t) \right\rangle. \quad (11.7)$$

Above,  $\hat{P}_{ij}(\tau, t)$  is an estimate of the power spectrum for baseline  $ij$ , for delay mode  $\tau$  at LST  $t$ . The  $\lambda^2/2k_B$  term is the conversion from Jansky to Kelvin,  $\Omega_{PP}$  is the solid angle of the squared primary beam,  $\Delta v$  is the 10 MHz bandwidth and  $X^2 Y$  is the conversion from observed volume  $\Omega_{PP} \Delta v$  to cosmological volume in  $h^{-3} \text{Mpc}^3$  (Parsons et al., 2012a).  $\tilde{V}_{ij}^{*, P, \text{even}}$  indicates the delay-transformed visibility for baseline  $ij$ , conjugated, for pseudo-Stokes polarization  $P$  within the “even days” LST-binned data set.

Delay modes could be converted to  $k_{\parallel}$  line-of-sight modes measured in  $h/\text{Mpc}$  following

$$k_{\parallel} = \frac{2\pi v_{21\text{cm}} H(z)}{c(1+z)^2} \tau, \quad (11.8)$$

where  $v_{21\text{cm}} \approx 1420.1$  MHz, and  $H(z)$  is the Hubble parameter at redshift  $z$ . The angular cosmological distance surveyed was proportional to the magnitude of the baseline length  $b$ , represented in Fourier space by  $k_{\perp}$ :

$$k_{\perp} = \frac{2\pi}{D(z)\lambda} b \quad (11.9)$$

where  $D(z)$  is the transverse comoving distance at redshift  $z$ . For the  $\sim 30$  m baselines used in this study,  $k_{\parallel} \gg k_{\perp}$ .

The spherically-averaged power spectrum estimate  $\hat{P}(k)$  could be formed by averaging over LSTs and redundant baselines, where  $k^2 = k_{\parallel}^2 + k_{\perp}^2$ . These estimates in turn were averaged over the three separation types described in Section 11.1.2.1. Uncertainties were estimated by bootstrapping over groups of redundant baselines and LST samples. Obtain-

ing the correct uncertainties when bootstrapping from the data used to form the estimate is not a trivial process, and we defer the reader to [Cheng et al. \(2018\)](#) for full details of this important step.

Past PAPER power spectrum results have used inverse covariance-weighting and optimal quadratic estimators to improve the accuracy of the final power spectrum estimate (e.g. Parsons et al., 2014, ; [Cheng et al. 2018](#)). We do not implement any weighting in our power spectrum estimates. This avoided risk of signal-loss effects, but more generally avoided making any assumptions about the nature of the polarized sky. Down-weighting polarized foregrounds using optimal quadratic estimation is a contemporary analysis challenge that has not yet been implemented on data.

## 11.2 Results

Figure 11.10 shows the spherically-averaged power spectra for pseudo-Stokes I, Q, U and V with 95% confidence intervals. Green curves show analytical thermal noise estimates drawn from a 21CMSENSE model of the array (Pober et al., 2014; Pober, 2016) and given our observing time and bandwidth. The analytical thermal noise estimates used a simplistic model of the polarized beam, leading to different, but valid, noise levels per Stokes parameter. An equivalent series of power spectra based on Gaussian noise of the same variance as our data are shown in Figure 11.11, as a consistency-check on our method.

All of the power spectra in Figure 11.10 showed an excess at low  $k$  values, consistent with spectral structure of the PAPER beam and signal chain leaking power outside of the foreground wedge (Pober et al., 2013; Kerrigan et al., 2018). Excesses at  $k \approx 0.3\text{h/Mpc}$  in these power spectra were also seen in PAPER-32 (Moore et al., 2017) and PAPER-64 ([Kolopanis et al. 2018](#)), suggesting an artefact from the PAPER signal chain was the cause.

Neglecting these artefacts, pseudo-Stokes I power spectra were broadly consistent with the analytical noise estimate, with a slight bias compared to the pure-noise power

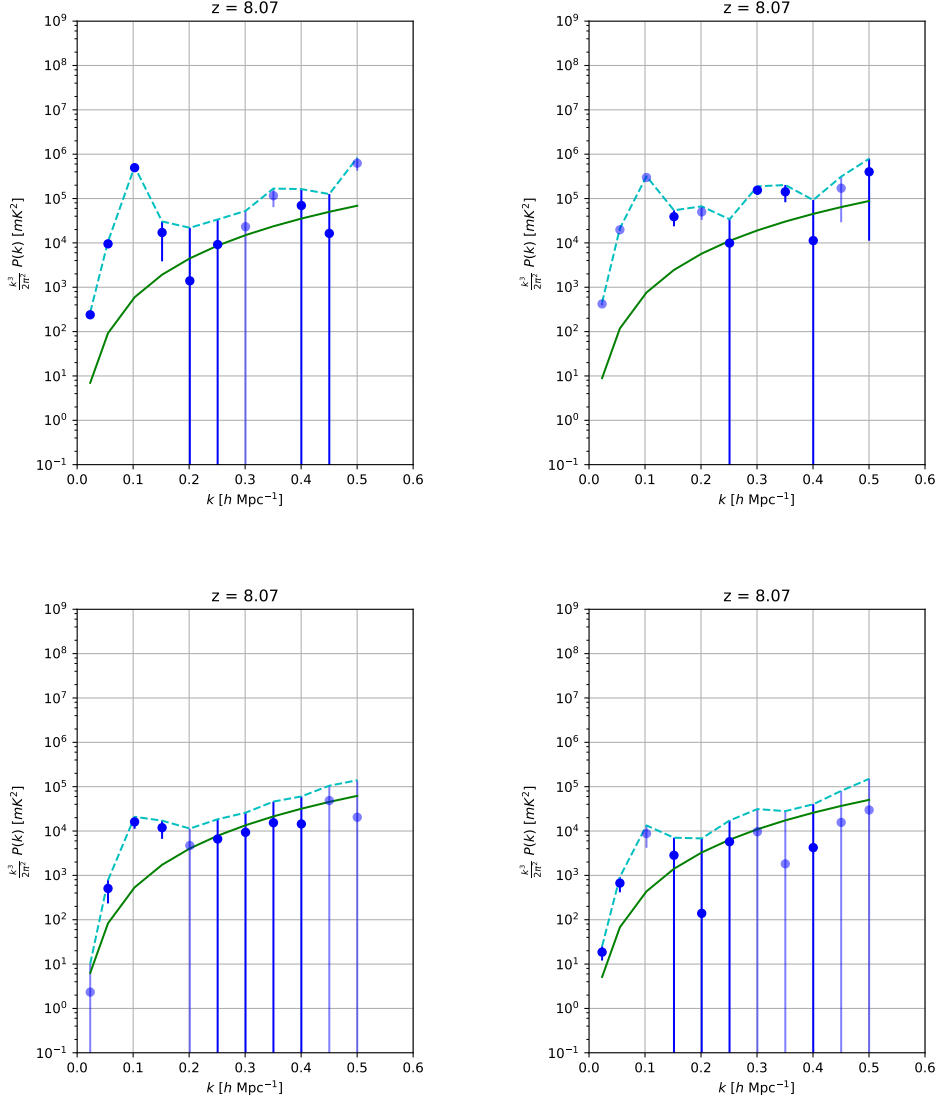


Figure 11.10: Spherically-averaged power spectra in pseudo Stokes I, Q (top left, top right) U and V (bottom left, bottom right). Pale points indicate negative values. Error bars show 95% confidence intervals, and the cyan dashed line indicates the  $1\sigma$  upper-limit given by each power spectrum. The green curve is the analytical thermal noise estimate, drawn from 21CMSENSE.

spectra of Figure 11.11. This represented an upper limit of  $\Delta_{21\text{cm}}^2(k) \lesssim (140\text{mK})^2$  at  $k = 0.2 \text{ h/Mpc}$ , which is competitive with contemporary limits (e.g. Kolopanis et al. 2018).

The pseudo-Stokes Q power spectrum was largely inconsistent with noise, with excesses at  $0.15 \text{ h/Mpc} \leq k \leq 0.2 \text{ h/Mpc}$  and  $0.3 \text{ h/Mpc} \leq k \leq 0.35 \text{ h/Mpc}$ . For this power to be due to Faraday-rotated emission from the diffuse foregrounds probed by a 30 m baseline would require rotation measures of  $\sim 30 \text{ rad m}^{-2}$  and  $\sim 60 \text{ rad m}^{-2}$ , respectively (Moore et al., 2013). Such high rotation measures have not been observed on diffuse scales (e.g. Oppermann et al., 2012; Bernardi et al., 2013; Lenc et al., 2016). Neither Asad et al. (2016) nor Lenc et al. (2016) found polarized point sources of such high rotation measure in their surveys of the LOFAR and MWA EoR fields, respectively. Kohn et al. (2016) showed that the PAPER beam was not expected to scatter power to such high  $k_{\parallel}$  values. These factors pointed to the excess of pseudo-Stokes Q power as an indicator of calibration errors and instrument systematics leaking pseudo-Stokes I into Q. The effect is also likely larger than observed in the power spectra, as some attenuation will have occurred during LST binning due to ionospheric effects (Moore et al., 2017, ; Martinot et al. (2018)).

Simulations by Nunhokee et al. (2017) showed that Stokes Q and U power may exist at  $\Delta_{Q,U}^2(k) \approx 2 \times 10^4 \text{ mK}^2$  levels as the ensemble average of Faraday-rotated polarized point sources (for a particularly pessimistic sky model). However, it is doubtful that we detected such power, since the pseudo-Stokes U power spectrum is so different from Q.

At  $k > 0.15 \text{ h/Mpc}$ , pseudo-Stokes U and V power spectra showed excellent consistency with noise, both in comparison the analytical noise estimate and the pure-noise power spectra shown in Figure 11.11. This suggests that the excess in pseudo-Stokes Q, if due to calibration errors, was due to the diagonal gains being mis-matched. Uncalibrated off-diagonal gains,  $D$ -terms, leak pseudo-Stokes I into U and V (Thompson et al., 2017). We saw little evidence for such leakage.

Treating power at  $k = 0.2 \text{ h/Mpc}$  as a limit (valid for U and V, but less realistic for Q),

our  $1\sigma$  upper limits on polarized power were:  $\Delta_Q^2(k) \lesssim (245\text{ mK})^2$ ,  $\Delta_U^2(k) \lesssim (100\text{ mK})^2$  and  $\Delta_V^2(k) \lesssim (83\text{ mK})^2$ . These are the deepest limits to date on polarized power in the EoR window.

## 11.3 Discussion & Conclusions

This analysis represented the first power spectrum results from PAPER-128. The processing and reduction of the two Season and seven Epochs taught us many lessons about the challenges associated with long integrations of large low-frequency arrays. These lessons were invaluable for the construction and activation of HERA, and the quality assurance techniques developed (see Chapter 6) for such an analysis continue to be essential components of the HERA real-time system (Ali et al. 2018).

Nunhokee et al. (2017) and Asad et al. (2015) predicted that the power spectrum of diffuse polarized foregrounds should exist outside of the foreground wedge at  $\Delta^2(k) \approx 10^3 \text{ mK}^2$ . This is roughly two orders of magnitude above predicted EoR power (Lidz et al., 2007), and will therefore need to be extremely well characterized, since just 1% of leakage into Stokes I could prevent an EoR detection. This study advanced that effort, setting the most stringent upper limits on pseudo-Stokes Q, U and V power to date. However, any deeper integrations with PAPER-128 may be limited by systematics due to calibration errors.

It is unlikely that the “detection” of power in much of the pseudo-Stokes Q power spectrum is real. However, this could be tested in the future by collecting a Epoch’s-worth of ionospheric data and calculating the attenuation coefficient for different fractions of the Epoch being LST-binned together. If real pseudo-Stokes Q power is present in the power spectrum, the noise level should decrease with increasing numbers of observations in the LST bin at a rate faster than a coherent average. This variety of “jackknifing on the ionosphere” will be investigated in future work.

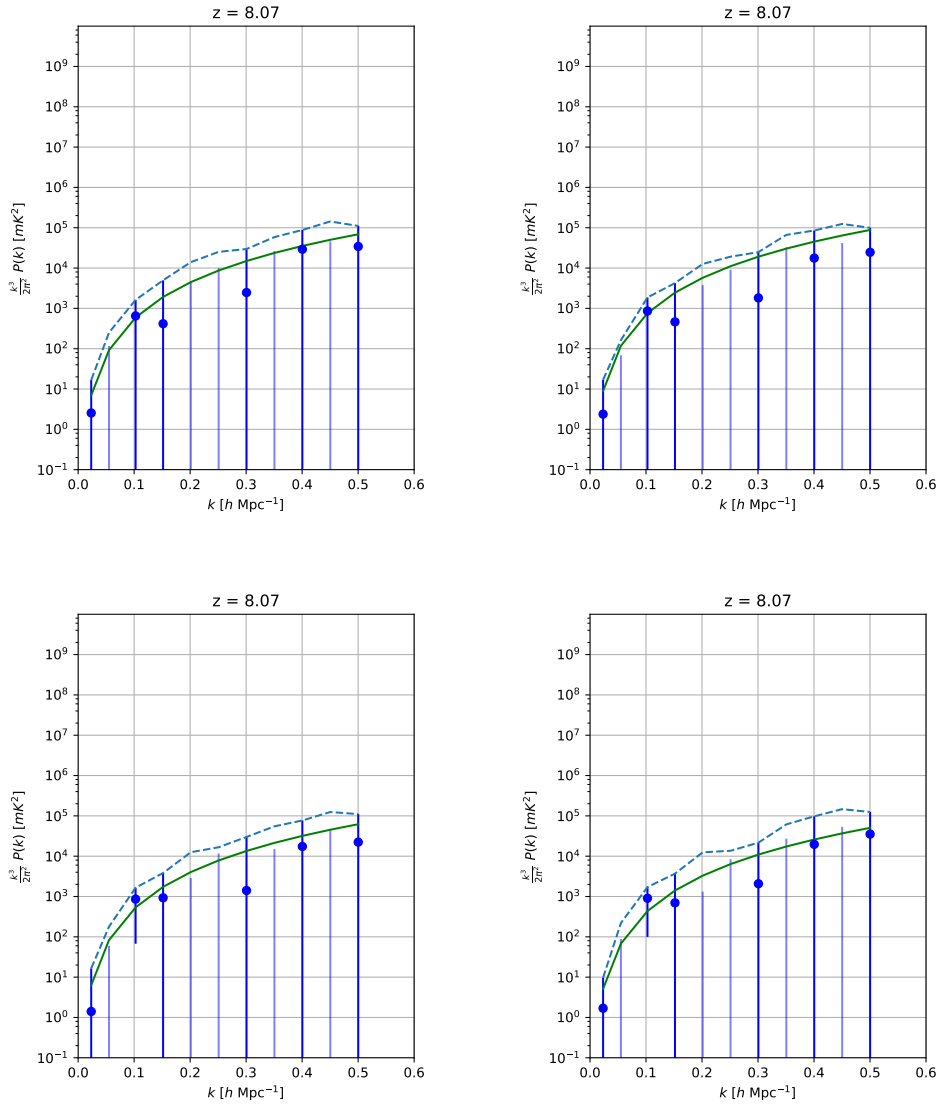


Figure 11.11: Spherically-averaged power spectra of noise based on the variance of the data in our power-spectrum band. Pale points indicate negative values, error bars show 95% confidence intervals, and the dashed line indicates the  $1\sigma$  upper-limit. All power spectrum values are consistent with the analytical noise estimate, showing the accuracy of our methods.

# **Part III**

## **Expanding the potential of EoR**

### **measurements**

There is one glory of the sun, and another glory of the moon, and another  
glory of the stars; for star differs from star in glory.

*1 Corinthians (15:41)*

# **Chapter 12**

## **Interferometric sensitivity to the monopole moment**



# **Chapter 13**

## **Higher-order correlation functions between kSZ and 21cm observations**

### **13.1 The kSZ-21cm connection**

#### **13.1.1 Foregrounds**

#### **13.1.2 Noises**

### **13.2 kSZ<sup>2</sup>-21cm squeezed-triangle bispectra**

#### **13.2.1 Semi-analytic approximation**

#### **13.2.2 Counting triangles**

#### **13.2.3 Signal-to-noise estimates**

### **13.3 kSZ<sup>2</sup>-21cm<sup>2</sup> squeezed-rectangle trispectra**

#### **13.3.1 Semi-analytic approximation**

#### **13.3.2 kSZ<sup>2</sup>-21cm bispectra cross-power spectrum**

# Chapter 14

## Deep Learning for 21cm Observations

Modern cosmological theory is capable of predicting the statistical features of many aspects of the observable Universe, using either theoretical calculations (e.g. Bond et al., 1991; Sheth & Tormen, 1999) or sophisticated numerical simulations (e.g. Lewis et al., 2000; Vogelsberger et al., 2014). These theories may be tested by making observations of various large-scale fields, in surveys spanning large cosmological volumes in space and time. The ultimate goal of measurements is extract from the data some parameters which are believed to describe the underlying processes, and to relate these parameters to a theoretical understanding of the physics at work. In some cases – most conspicuously the primordial CMB – the statistics of the fields are Gaussian, and are completely described by the two-point correlation function, or its Fourier conjugate, the power spectrum (e.g. Liddle & Lyth, 2000, for a review).

A field described only by Gaussian statistics practically does not exist in cosmology beyond the CMB. For nearly every other scenario involving the non-linear interactions of gravity, radiation, and fluid mechanics, the resultant fields are non-Gaussian. Within the non-Gaussianity of these fields is encoded additional valuable information about the astrophysical processes at work, and can also serve as a cross-validation of two-point statistics of the same field (Alvarez, 2016; Majumdar et al., 2017). The specific details of the non-Gaussianity are not usually straightforwardly obtained from the theory, and thus

devising appropriate higher-order statistics to efficiently probe the non-Gaussian information is in general a difficult problem.

By analyzing a field using power spectra, one explicitly neglects all non-Gaussian information. In Chapter 13, we presented higher-order correlation functions that are sensitive to non-Gaussian information in Fourier space. In the case of 21 cm emission, working in Fourier space provides a natural and relatively simple way to avoid foreground contamination. Another solution could be to search for non-Gaussian information in image space, assuming some future development that could overcome the foreground challenge (e.g. Shaw et al., 2014, 2015; Zhu et al., 2016; Patil et al., 2017), or that we may operate on wedge-filtered image fields in a physically meaningful way (Beardsley et al., 2015). Staying in image space allows us to retain the non-Gaussian information in our data.

## 14.1 Neural Networks

A potential solution for parameter extraction is available due to advances in computation, allowing us to generate large numbers of numerical simulations which are realizations that capture the relevant physics of an astrophysical process (e.g. Mesinger et al., 2011), and the development of deep learning algorithms which can be “trained” to recognize patterns in data (e.g. Hinton & Salakhutdinov, 2006; Hinton et al., 2012).

Convolutional Neural Networks (CNNs; e.g. LeCun et al., 1995) have proven exceptionally useful for extracting non-Gaussian information from images in order to classify or extract information from their contents to a very high accuracy (e.g. Krizhevsky et al., 2012). There are many, many explanations of the inner calculus of neural networks, and the intention of this chapter is not a comprehensive review of that field. For the purposes of this chapter, a few concepts must be mentioned:

- Convolutional Neural Networks are systems of 1, 2 or 3-dimensional matrices that are used as convolutional kernels on an input image. An image is propagated forward through the network via consecutive convolutions by these kernels. Each

kernel entry (i.e. pixel) is known as a ‘weight’  $w$ .

- The desired output of a ‘training set’, for example, the contents of an image, is given as a vector which the total of all the convolutions must reproduce.
- Inevitably, if the convolutional kernels are initially randomly generated, the output vector will not contain the desired quantities. A ‘cost function’ is a metric that specifies how ‘wrong’ an output is. This could be the mean squared error, for example.
- Neural networks ‘learn’ through a process called ‘backpropagation’. Based on the cost function, a chain rule can be applied backwards along the network for each input, updating the values of the weights by some fraction of the user-specified ‘learning rate’ (Rumelhart et al., 1986).
- Associated with each weight is an ‘activation function’,  $a(x)$ . The value of  $a(w * x)$  (the output of the activation function given the convolved input) is actually what is handed to the next convolutional kernel along the network. Activation functions can be non-linear, allowing neural networks to learn complex decision boundaries.
- In order to down-sample the data to a more manageable size, ‘pooling layers’ are often implemented. These extract a moving statistic such as the moving average or maximum in a given region of the image.
- CNNs often end with a ‘fully connected’ or ‘dense’ layer. These are multi-layer perceptrons (e.g. Rosenblatt, 1961) that propagate the value  $s$  of  $a(wx)$  – that is, no convolution is applied, and each layer is 1-dimensional.
- After training on some subset of the total data (which may be done several times over), a neural network can be ‘tested’ by forward-propagating new images, not used in training, and not backpropagating. Testing can also be implemented after some subsample of the training data has been propagated – i.e., as the network is in the middle of training – often called ‘validation’.

With this primer in mind, we will present two uses of CNNs for understanding simulated realizations of reionization: classifying the main causes (galaxies or active galactic nuclei) of reionization (Hassan et al., 2018), and regressing upon a physical parameter of interest.

## 14.2 Classifying reionization models

The 21 cm power spectrum is a powerful tool for quantifying the relative clustering of large and small scaled ionized regions (Hassan et al., 2017). However, the topology of the regions themselves can provide information on the dominant mechanism of their formation. We considered two scenarios: one in which only galaxies, and the other in which only active galactic nuclei (AGN), provided ionizing photons.

We used SIMFAST21 (Santos et al., 2010; Hassan et al., 2017) to generate a dark matter density field, evolve it into the non-linear regime using the Zel'dovich approximation. Dark matter halos were generated using the excursion set formalism (Bond et al., 1991). Either galaxies or AGN were placed in halos, with populations following the parametrization of Hassan et al. (2016). Ionized regions are “painted on top of” the dark matter halos according to parametrizations from high-resolution radiative transfer simulations and large-volume hydrodynamic simulations (see Hassan et al. (2016); Hassan et al. (2018)). An example of a galaxy-dominated and AGN-dominated reionization field is shown in Figure 14.1. For this study, we focused on the field at redshift  $z = 8$ . Galaxies produce more, small, ionized regions, whereas AGN produce larger more spherical ones. This is due to the strong clustering AGN and their harder X-ray spectrum.

We used Tensorflow (Abadi et al., 2016) to build a classifying CNN with 2 layers of 2-dimensional convolutional kernels interleaved with two maximum-pooling layers, a single dense layer, and an output layer. The convolutional and dense layers used the ReLU activation function, which is defined as

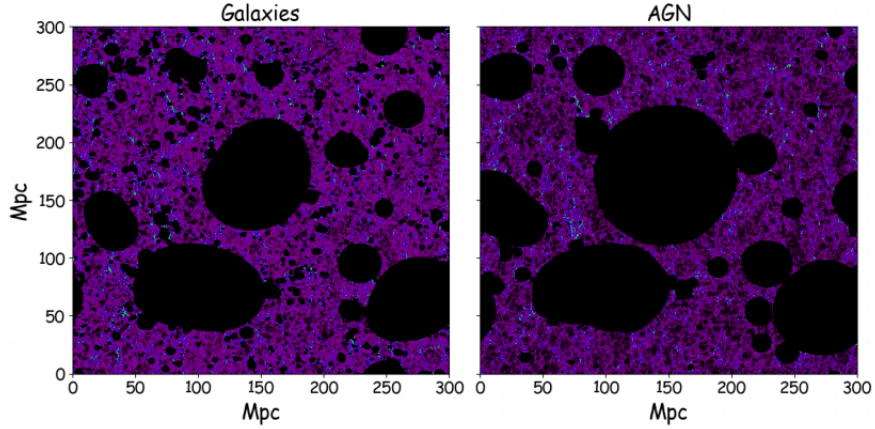


Figure 14.1: 21 cm brightness temperature fields (in arbitrary units) for Galaxy-Only (left) and AGN-only (right) models. Figure from Hassan et al. (2018).

$$\text{ReLU}(x) = \begin{cases} 0 & x < 0 \\ x & x > 0 \end{cases} \quad (14.1)$$

The network is shown in Figure 14.2. To train it, we used  $\sim 1000$  images of  $z = 8$  realizations. Each image was a  $140 \times 140$  greyscale image of 21 cm brightness temperature, with a simulation box size of 75 Mpc. Each image came from a separate simulation, which varied the photon escape fraction, X-ray spectrum of the ionizing sources and the ionizing efficiency of those sources. The testing set was  $\sim 100$  additional images. To prevent over-fitting, only a random set of 75% of neurons were used during each forward propagation (a method known as ‘dropout’). The logistic cross-entropy function was used as the cost function.

Using the 21CMSENSE package (Pober et al., 2014), we could simulate the expected thermal noise of a foreground-decontaminated image cube for LOFAR, HERA-331 and SKA-Low (see Chapter 4). Adding this noise to each image allowed us to make predictions of the accuracy of such a tool for predicting ionization models for actual data.

The results of training and validation are shown in Figure 14.3. During training, the HERA and SKA fields quickly become  $> 99\%$  accurately classified. Systematic gaps

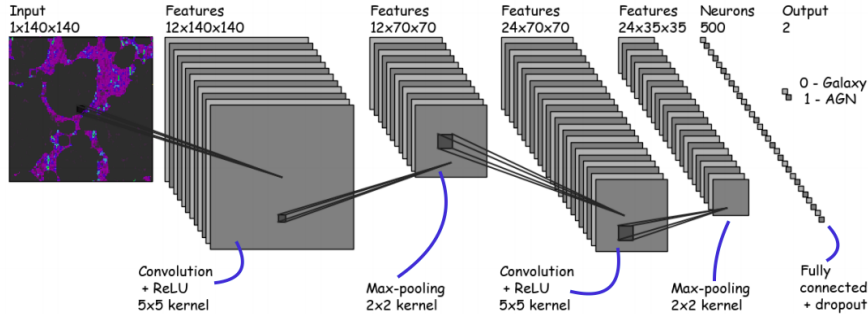


Figure 14.2: The classification CNN used in this study. Figure taken from Hassan et al. (2018).

between training and validation data for HERA suggests that an additional linear bias parameter may be useful for future networks. While the LOFAR classification eventually reaches high accuracy during training, validation shows that the network is strongly overfitting in this case – suggesting that LOFAR will not be able to produce data in which the galaxy and AGN contributions to reionization. This result is substantiated by power spectrum studies by Hassan et al. (2017).

We can inspect the effect that kernels of a given layer have on an input image to gain some interpretation of what the network regards as ‘important’ for the classification. An example of such an inspection is shown in Figure 14.4, which shows a single (galaxy-dominated) training image propagated through the trained kernels of the first convolutional layer. Some form of edge detection emphasizing the small, high-temperature regions of the map has been learned by the kernels. A comprehensive understanding of the relationship between the physical processes and the kernels required to identify them will be the subject of future work.

### 14.3 Regressing upon reionization parameters

Cosmological studies often want to go beyond binary classifications, instead seeking to understand the value of some collection of variables that describe physical processes in

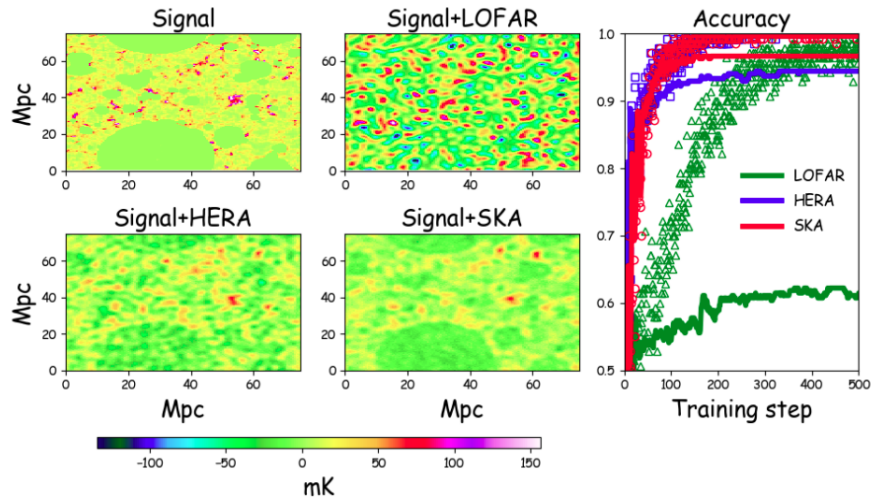


Figure 14.3: Training data and results of the classifier. On the left, an example 21 cm brightness temperature field from the training set, with different thermal noise instances according to instrument designs. On the right, the accuracy of training (open symbols) and testing (solid lines) for the three different instruments considered. Figure taken from Hassan et al. (2018).

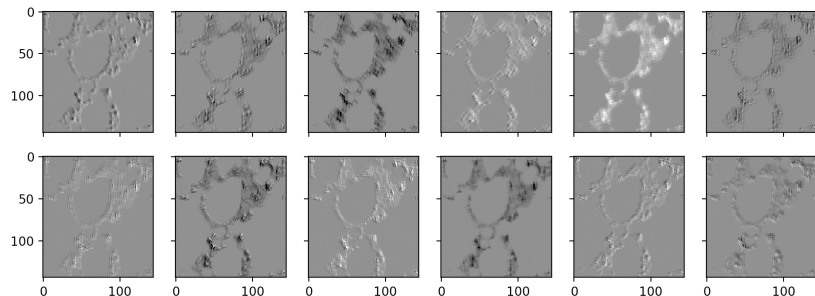


Figure 14.4: An input image propagated through the trained kernels of the first layer of the classifier. In this case, the color scale is arbitrary – contrasts within an image are more important. The axes are labelled by pixel index. Small, high-temperature regions are frequently emphasized.

the Universe. The 21CMFAST (Mesinger et al., 2011) and 21CMMC (Greig & Mesinger, 2015) software packages, widely used for realizations of the 21 cm brightness temperature field, parametrize reionization according to a few variables: the mean free path of ionizing photons ( $R_{\text{mfp}}$ ) the minimum virial temperature of star-forming haloes ( $T_{\text{vir}}$ ) and the ionizing efficiency of high-redshift galaxies ( $\zeta$ ).

We investigated the effectiveness of using CNNs to regress upon  $\zeta$ , holding all other parameters constant.  $\zeta$  is defined as:

$$\zeta = \frac{f_{\text{esc}} f_* N_\gamma}{1 + n_{\text{rec}}}, \quad (14.2)$$

where  $f_{\text{esc}}$  is the fraction of ionizing photons that escape into the IGM,  $f_*$  is the fraction of galactic gas in stars,  $N_\gamma$  is the number if ionizing photons produced per baryon in stars, and  $n_{\text{rec}}$  is the expected number of recombinations per hydrogen atom. The theoretical values of  $f_{\text{esc}}$  and  $f_*$  are highly uncertain at high redshifts (e.g. Paardekooper et al., 2015; Meiksin et al., 2017). For the Population II stars at the redshift range of the EoR,  $N_\gamma \approx 4000$  (Barkana & Loeb, 2005). During the EoR, it is expected that  $n_{\text{rec}} \sim 1$  (e.g. McQuinn et al., 2011; Sobacchi & Mesinger, 2014). In 21CMFAST,  $\zeta$  is typically varied between 5 and 100, corresponding to  $f_{\text{esc}}$  values between 5% and 100%.

The  $\zeta$  is an attractive parameter for an initial analysis, as it has a large effect on the topology of the temperature field and a relatively intuitive interpretation. We generated 2000 21 cm brightness temperature fields with values of  $\zeta$  between 10 and 50, all at redshift  $z = 10$ , in a 150 Mpc box with 200 pixels on a side. Figure 14.5 shows two of these fields on the same mK color scale – one with  $\zeta = 30$ , the other with  $\zeta = 50$ . The effect of increased efficiency is extreme.

We built a CNN using keras (Chollet et al., 2015) to learn to regress on the value of  $\zeta$  for a training set of 1400 images (70% of the data). We used 3 convolutional layers interleaved with 3 average pooling layers and two dense layers with 10% dropout. Every kernel and dense-layer weight had an additive linear bias term which could also be learned by the network. We used ReLU activation functions throughout, and a mean squared error

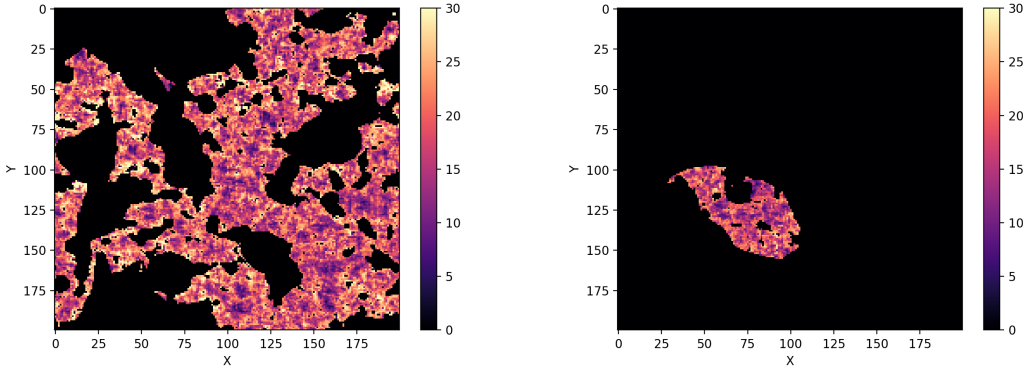


Figure 14.5: The effect of changing  $\zeta$  on the 21 cm brightness temperature field. The left panel shows a realization of reionization at  $z = 10$  with  $\zeta = 30$ . On the right, with all other parameters fixed and at the same redshift, is a realization with  $\zeta = 50$ . In the latter, almost the entire region has been reionized. The color scale is in mK.

cost function. A diagram of the CNN is shown in Figure 14.6.

The results of training are shown in Figure 14.7. For each step of training, we computed the cost function and the coefficient of determination ( $R^2$ ), which measured what fraction of the variance of the overall distribution of  $\zeta$  values the model, represented by forward propagation through the CNN, is capturing (e.g. Glantz & Slinker, 1990). The CNN quickly learns to regress to a mean squared error of  $\sim 5$ , which explains  $\sim 80\%$  of the variance of the  $\zeta$  distribution. Note that the number of steps is far fewer than the number of images in the training set. This is because, for computational efficiency, we only implemented backpropagation after a batch of training images had propagated forward through the network (this is known as ‘batch learning’). Batches were chosen randomly from the training set.

Figure 14.8 shows the predicted and true values of  $\zeta$  from the test set. The CNN was able to predict values to an accuracy suggested by the training results shown in Figure 14.7, but with a systematic bias towards lower  $\zeta$ . Agreement is better at the lowest values of  $\zeta$ . This is most likely due to the fact that the ReLU function is only extracting positive-valued information. In higher  $\zeta$  regimes, as shown in Figure 14.5,

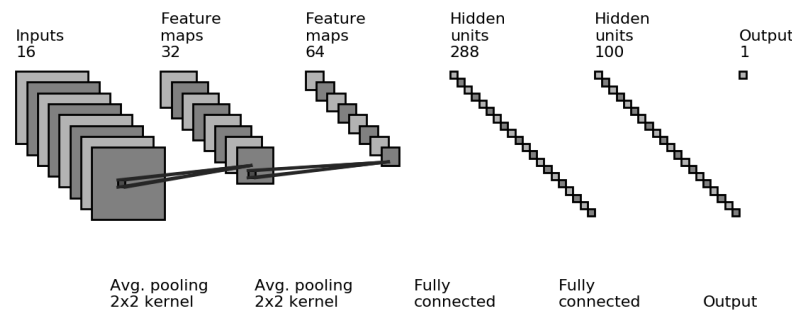


Figure 14.6: The CNN used for regression.

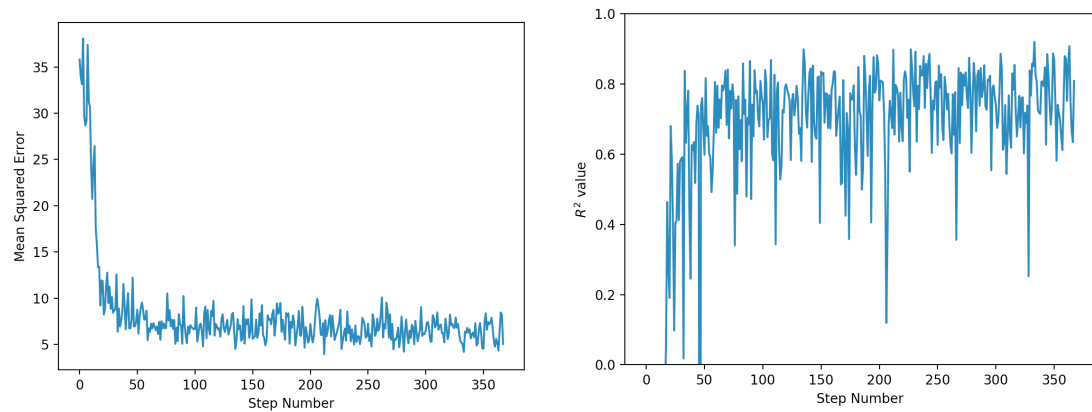


Figure 14.7: The results of training the CNN regressor. The left panel shows the value of the cost function at each step of training, which quickly reduces to a value of  $\sim 5$ . At each training step we also calculate the  $R^2$  value. Its value suggests that the CNN is capturing about 80% of the variance of the  $\zeta$  distribution.

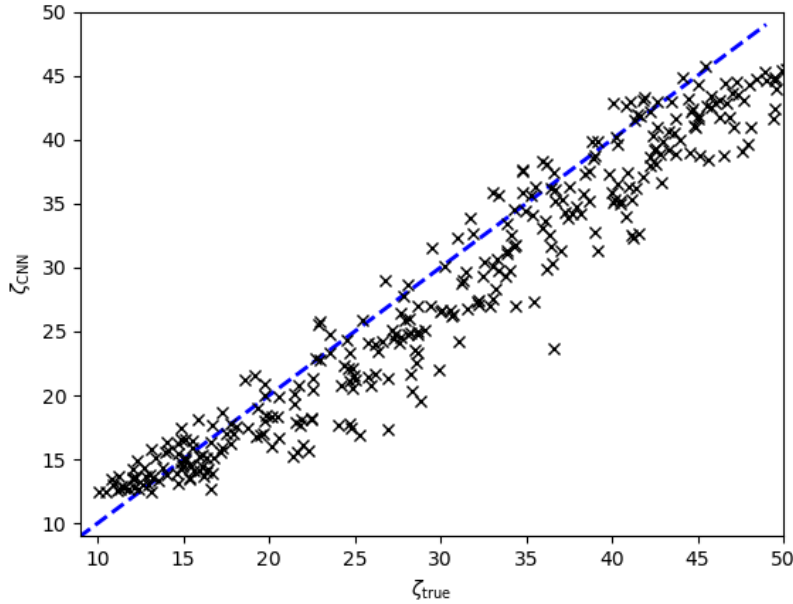


Figure 14.8: True vs. predicted values of  $\zeta$  from the test set. A 1:1 line is overplotted in blue.

reionization occurs very quickly, leaving much of the map reionized and blank – as far as the CNN can tell, featureless – so the examples it is able to learn had a lower-valued  $\zeta$  than they should. Moving to a ‘Leaky ReLU’ activation function in future attempts would go a ways toward rectifying this issue.

## 14.4 Future directions

We have presented some basic test that showed that deep learning techniques may be worth developing to analyze 21 cm measurements. There are a host of directions to pursue in the future, as the field of deep learning is ripe for exploration. An immediate step to take is the development of a formalism for analyzing the trained convolutional kernels. These may contain useful data about what features in a 21 cm map are the most important for extracting physical parameters.

By moving to 3-dimensional cosmological maps and kernels, rather than reducing the information to a power spectrum, CNNs should be sensitive to the particular kinds of non-Gaussianity present in the data, without a priori knowledge. The result should be both more precise parameter estimates, due to extracting more information than the traditional methods. We hope to pursue the extraction of the bispectrum of the 21 cm field, or some proxy for it, in future work. Related to Chapter 13, one could also build a correlational neural network (Chandar et al., 2015) capable of calculating the optimal combination of two fields (for example, the HI and dark matter density fields, or the HI and kSZ fields) to extract the maximum amount of information (Feng et al., 2004). This may be the most useful avenue to pursue, to build the best tools for combining future survey data. However, it may be difficult to form a training set for such a network.

Finally, Chapter 6 presented large amounts of work building metrics to understand how to assure the quality of visibility data. The result of that work could be configured into a very large training set of ‘how and where interferometric visibilities can be corrupted’. The major challenge of using visibility data is its complex nature. Backpropagation of complex-valued input is a contemporary challenge (Guberman, 2016; Popa, 2017; Zhang et al., 2017) that is not fully-supported by any mainstream deep learning software packages. However, the volume of data generated by an interferometer such as HERA and the automatic flagging algorithms we have created could prove to be a powerful combination for future deep learning studies.

# **Chapter 15**

## **Conclusions**

# **Appendices**

# Appendix A

## Software

Software engineering and maintenance of existing codebases has been, generally speaking, historically undervalued and unappreciated by the astronomy community (Muna et al., 2016). In this Appendix I would like to provide a brief description of the major software packages used in this work – without which, the work would not exist.

### A.1 Astronomical Interferometry in Python (aipy)

The aipy software package (Parsons, 2016) was developed by a team based largely at the University of California, Berkeley and led by Aaron Parsons. Developed under NSF funding for the PAPER experiment, it provides a Python API to interact with interferometric visibilities stored in the MIRIAD file format (Sault et al., 2011). It is able to efficiently query large MIRIAD files due the APIs closeness to the underlying C code. It also contains calibration, deconvolution, imaging and phasing code in Python, and interfaces with HEALPix (see Section A.5, below) as well as other astronomical Python packages.

aipy is maintained by the HERA software team, and can be found at: <https://github.com/HERA-Team/aipy>.

## A.2 Astronomy in Python (astropy)

astropy is an open-source and community-developed core Python package for Astronomy, containing a host of extremely useful utility functions and objects (Astropy Collaboration et al., 2013).

## A.3 Common Astronomy Software Applications (CASA)

CASA is under active development, with the primary goal of supporting the data post-processing needs of the next generation of radio telescopes. It is developed by an international consortium of scientists based at the National Radio Astronomical Observatory (NRAO), the European Southern Observatory (ESO), the National Astronomical Observatory of Japan (NAOJ), the CSIRO Australia Telescope National Facility (CSIRO/ATNF), and the Netherlands Institute for Radio Astronomy (ASTRON), under the guidance of NRAO (McMullin et al., 2007).

## A.4 Deep Learning packages

Experimentation with deep learning analyses of 21 cm simulated observations took place in Keras (Chollet et al., 2015), PyTorch (Paszke et al., 2017) and Tensorflow (Abadi et al., 2016).

## A.5 Hierarchical Equal Area isoLatitude Pixelization of the sphere (HEALPix)

The HEALPix software, and its Python wrapper healpy, provide a pixelization which subdivides a spherical surface into pixels which each cover the same surface area as every other pixel. Pixel centers occur on a discrete number of rings of constant latitude. This

scheme makes natively spherical measurements, such as angular power spectra and wide-field images, simple and efficient to interact with (Górski et al., 2005).

## A.6 pyuvdata

pyuvdata provides a Python interface to interferometric data. It can read and write MIRIAD and UVFITS file formats, as well as read CASA measurement sets and FHD (Sullivan et al., 2012b) visibility save files (Hazelton et al., 2017).

pyuvdata is maintained by the HERA software team, and can be found at: <https://github.com/HERA-Team/pyuvdata>.

## A.7 The Scientific Python Ecosystem (scipy)

Many of the above tools require at least one of the many packages under the `scipy` ecosystem. It is truly foundational to almost any scientific analysis that takes place in Python (Jones et al., 2001).

# Bibliography

Abadi, M. et al. 2016, ArXiv e-prints

Afraimovich, E. L., Astafyeva, E. I., Oinats, A. V., Yasukevich, Y. V., & Zhivetiev, I. V. 2008, *Annales Geophysicae*, 26, 335

Ali, Z. S. et al. 2015, ArXiv e-prints

Alvarez, M. A. 2016, *ApJ*, 824, 118

Appleton, E. V. 1946, *Nature*, 157, 691

Asad, K. M. B., Koopmans, L. V. E., Jelić, V., de Bruyn, A. G., Pandey, V. N., & Gehlot, B. K. 2017, ArXiv e-prints

Asad, K. M. B. et al. 2016, *MNRAS*, 462, 4482

—. 2015, *MNRAS*, 451, 3709

Astropy Collaboration et al. 2013, *A&A*, 558, A33

Backer, D. C. et al. 2010, HERA âĂŞ Hydrogen Epoch of Reionization Arrays, Submitted for consideration by the Astro2010 Decadal Survey Program Panel

Barkana, R. & Loeb, A. 2005, *The Astrophysical Journal*, 626, 1

Barry, N., Hazelton, B., Sullivan, I., Morales, M. F., & Pober, J. C. 2016, *MNRAS*, 461, 3135

- Beardsley, A. P. et al. 2016, ApJ, 833, 102
- Beardsley, A. P., Morales, M. F., Lidz, A., Malloy, M., & Sutter, P. M. 2015, ApJ, 800, 128
- Bernardi, G. et al. 2013, ApJ, 771, 105
- Bond, J. R., Cole, S., Efstathiou, G., & Kaiser, N. 1991, ApJ, 379, 440
- Bowman, J. D. & Rogers, A. E. E. 2010, Nature, 468, 796
- Brunner, F. K. & Welsch, W. M. 1993, GPS World, 4, 42
- Carilli, C. L. & Rawlings, S. 2004, NewAR, 48, 979
- Carozzi, T. D. & Woan, G. 2009, MNRAS, 395
- Chandar, S., Khapra, M. M., Larochelle, H., & Ravindran, B. 2015, ArXiv e-prints
- Chollet, F. et al. 2015, Keras, <https://github.com/fchollet/keras>
- Civil Aviation Authority. 2016, <http://wwwcaa.co.za/>, website
- Condon, J. J., Cotton, W. D., Greisen, E. W., Yin, Q. F., Perley, R. A., Taylor, G. B., & Broderick, J. J. 1998, AJ, 115, 1693
- Cornwell, T. 2016
- Cornwell, T. J. 1983, A&A, 121, 281
- Cotton, W. & Condon, J. 2002, in Proceedings of the URSI General Assembly
- de Oliveira-Costa, A., Tegmark, M., Gaensler, B. M., Jonas, J., Landecker, T. L., & Reich, P. 2008, MNRAS, 388, 247
- DeBoer, D. R. et al. 2017, PASP, 129, 045001

- Dewdney, P. E., Hall, P. J., Schilizzi, R. T., & Lazio, T. J. L. 2009, Proceedings of the IEEE, 97, 1482
- Dillon, J. S. et al. 2017, ArXiv e-prints
- . 2014, Phys. Rev. D, 89, 023002
- . 2015, Phys. Rev. D, 91, 123011
- Dillon, J. S. & Parsons, A. R. 2016, ApJ, 826, 181
- Erdogan, E. et al. 2016, in EGU General Assembly Conference Abstracts, Vol. 18, EGU General Assembly Conference Abstracts, 12685
- Erickson, W. C., Perley, R. A., Flatters, C., & Kassim, N. E. 2001, A&A, 366, 1071
- Ewall-Wice, A. et al. 2016a, ApJ, 831, 196
- . 2016b, MNRAS, 460, 4320
- Fagnoni, N. & de Lera Acedo, E. 2016, ArXiv e-prints
- Feng, D.-Z., Zhang, X.-D., & Bao, Z. 2004, IEEE Transactions on Neural Networks, 15, 1541
- Finlay, C. C. et al. 2010, Geophysical Journal International, 183, 1216
- Fomalont, E. B., Ebnetter, K. A., van Breugel, W. J. M., & Ekers, R. D. 1989, ApJL, 346, L17
- Furlanetto, S. R., Oh, S. P., & Briggs, F. H. 2006, Physics Review, 433, 181
- Geil, P. M., Gaensler, B. M., & Wyithe, J. S. B. 2011, MNRAS, 418, 516
- Glantz, S. A. & Slinker, B. K. 1990, Primer of applied regression and analysis of variance  
No. Sirsi) i9780070234079

- Górski, K. M., Hivon, E., Banday, A. J., Wandelt, B. D., Hansen, F. K., Reinecke, M., & Bartelmann, M. 2005, ApJ, 622, 759
- Greig, B. & Mesinger, A. 2015, MNRAS, 449, 4246
- Guberman, N. 2016, ArXiv e-prints
- Hamaker, J. P. & Bregman, J. D. 1996, A&AS, 117, 161
- Hamaker, J. P., Bregman, J. D., & Sault, R. J. 1996, A&AS, 117, 137
- Hassan, S., Davé, R., Finlator, K., & Santos, M. G. 2016, Monthly Notices of the Royal Astronomical Society, 457, 1550
- Hassan, S., Davé, R., Finlator, K., & Santos, M. G. 2017, MNRAS, 468, 122
- Hassan, S., Davé, R., Mitra, S., Finlator, K., Ciardi, B., & Santos, M. G. 2017, Monthly Notices of the Royal Astronomical Society, 473, 227
- Hassan, S., Liu, A., Kohn, S., Aguirre, J. E., La Plante, P., & Lidz, A. 2018
- Hazelton, B., Beardsley, A., Pober, J., Jacobs, D., Ali, Z., & Lanman, A. 2017, HERA-Team/pyuvdata: Version 1.1
- Hazelton, B. J., Morales, M. F., & Sullivan, I. S. 2013, ApJ, 770, 156
- Hinton, G. E. & Salakhutdinov, R. R. 2006, Science, 313, 504
- Hinton, G. E., Srivastava, N., Krizhevsky, A., Sutskever, I., & Salakhutdinov, R. R. 2012, ArXiv e-prints
- Högbom, J. A. 1974, A&AS, 15, 417
- Huffenberger, K. M. et al. 2015, ApJ, 806, 112
- Hurley-Walker, N. et al. 2017, MNRAS, 464, 1146

- Iglewicz, B. & Hoaglin, D. 2010, Engineering Statistical Handbook, 1
- Iijima, B. et al. 1999, Journal of Atmospheric and Solar-Terrestrial Physics, 61, 1205
- Intema, H., Van der Tol, S., Cotton, W., Cohen, A., Van Bemmel, I., & Röttgering, H. 2009, Astronomy & Astrophysics, 501, 1185
- Jacobs, D. C. et al. 2016, ApJ, 825, 114
- . 2013, ApJ, 776, 108
- . 2015, ApJ, 801, 51
- Jelić, V. et al. 2014, A&A, 568, A101
- . 2015, A&A, 583, A137
- Jones, E., Oliphant, T., Peterson, P., et al. 2001, SciPy: Open source scientific tools for Python, [Online; accessed <today>]
- Jones, R. C. 1941, Journal of the Optical Society of America (1917-1983), 31, 488
- Kerrigan, J. et al. 2018, ArXiv e-prints
- Klobuchar, J. A. 1983, Ionospheric Effects on Earth-Space Propagation
- Kohn, S. et al. 2018, ArXiv e-prints
- Kohn, S. A. et al. 2016, ApJ, 823, 88
- Komjathy, A., Sparks, L., Wilson, B. D., & Mannucci, A. J. 2005, Radio Science, 40
- Krizhevsky, A., Sutskever, I., & Hinton, G. E. 2012, in Advances in neural information processing systems, 1097–1105
- Lanyi, G. E. & Roth, T. 1988, Radio Science, 23, 483

- LeCun, Y., Bengio, Y., et al. 1995, The Handbook of Brain Theory and Neural Networks, 3361, 1995
- Lenc, E. et al. 2017, PA&A, 34, e040
- . 2016, ApJ, 830, 38
- Lewis, A., Challinor, A., & Lasenby, A. 2000, ApJ, 538, 473
- Liddle, A. R. & Lyth, D. H. 2000, Cosmological inflation and large-scale structure (Cambridge University Press)
- Lidz, A., Zahn, O., McQuinn, M., Zaldarriaga, M., Dutta, S., & Hernquist, L. 2007, ApJ, 659, 865
- Liu, A., Tegmark, M., Morrison, S., Lutomirski, A., & Zaldarriaga, M. 2010, MNRAS, 408, 1029
- Loeb, A. & Furlanetto, S. R. 2012, The First Galaxies in the Universe (Princeton, NJ: Princeton University Press)
- Loi, S. T. et al. 2015, Geophys. Res. Lett., 42, 3707
- López-Caniego, M., Massardi, M., González-Nuevo, J., Lanz, L., Herranz, D., De Zotti, G., Sanz, J. L., & Argüeso, F. 2009, ApJ, 705, 868
- MacDoran, P. & Spitzmesser, D. 1989, Method and apparatus for deriving pseudo range from earth-orbiting satellites, uS Patent 4,797,677
- Majumdar, S., Pritchard, J. R., Mondal, R., Watkinson, C. A., Bharadwaj, S., & Mellema, G. 2017, ArXiv e-prints
- Mannucci, A., Wilson, B., Yuan, D., Ho, C., Lindqwister, U., & Runge, T. 1998, Radio science, 33, 565
- McKinley, B. et al. 2015, MNRAS, 446, 3478

- McMullin, J. P., Waters, B., Schiebel, D., Young, W., & Golap, K. 2007, in Astronomical Data Analysis Software and Systems XVI, ed. R. A. Shaw, F. Hill, & D. J. Bell, 376, ASP, San Francisco, CA, 127
- McQuinn, M., Lidz, A., Zahn, O., Dutta, S., Hernquist, L., & Zaldarriaga, M. 2007, MNRAS, 377, 1043
- McQuinn, M., Oh, S. P., & Faucher-Giguère, C.-A. 2011, ApJ, 743, 82
- Meiksin, A., Khochfar, S., Paardekooper, J.-P., Dalla Vecchia, C., & Kohn, S. 2017, MNRAS, 471, 3632
- Mesinger, A., Furlanetto, S., & Cen, R. 2011, MNRAS, 411, 955
- Mevius, M. et al. 2016, Radio Science, 51, 927
- Mohan, N. & Rafferty, D. 2015, PyBDSM: Python Blob Detection and Source Measurement, Astrophysics Source Code Library, record 1502.007
- Moore, D. F. 2014, PhD thesis, University of Pennsylvania
- Moore, D. F. et al. 2017, ApJ, 836, 154
- Moore, D. F., Aguirre, J. E., Parsons, A. R., Jacobs, D. C., & Pober, J. C. 2013, ApJ, 769, 154
- Morales, M. F., Hazelton, B., Sullivan, I., & Beardsley, A. 2012, ApJ, 752, 137
- Mueller, H. 1948, The foundation of optics, Vol. 38, 661
- Muna, D. et al. 2016, ArXiv e-prints
- Neben, A. R. et al. 2016, ApJ, 826, 199
- Nhan, B. D., Bradley, R. F., & Burns, J. O. 2016, ArXiv e-prints

- NRC, N. R. C. 2010, New Worlds, New Horizons in Astronomy and Astrophysics (Washington, DC: The National Academies Press)
- Nunhokee, C. D. 2018, PhD thesis, Rhodes University
- Nunhokee, C. D. et al. 2017, ApJ, 848, 47
- Offringa, A. R., van de Gronde, J. J., & Roerdink, J. B. T. M. 2012, A&A, 539, A95
- Oppermann, N. et al. 2012, A& A, 542, A93
- Paardekooper, J.-P., Khochfar, S., & Dalla Vecchia, C. 2015, MNRAS, 451, 2544
- Parashare, C. R. & Bradley, R. F. 2006, 120-205 MHz Receiver for PAPER: Precision Array to Probe the Epoch of Reionization, Dynamic Spectroscopy Laboratory Report Series 4, NRAO NTC-DSL Laboratory Report
- Parsons, A. 2016, AIPY: Astronomical Interferometry in PYthon, Astrophysics Source Code Library
- Parsons, A. et al. 2008, PASA, 120, 1207
- Parsons, A., Pober, J., McQuinn, M., Jacobs, D., & Aguirre, J. 2012a, ApJ, 753, 81
- Parsons, A. R. & Backer, D. C. 2009, AJ, 138, 219
- Parsons, A. R. et al. 2010, AJ, 139, 1468
- . 2014, ApJ, 788, 106
- Parsons, A. R., Liu, A., Ali, Z. S., & Cheng, C. 2016, ApJ, 820, 51
- Parsons, A. R., Pober, J. C., Aguirre, J. E., Carilli, C. L., Jacobs, D. C., & Moore, D. F. 2012b, ApJ, 756, 165
- Paszke, A. et al. 2017

- Patil, A. H. et al. 2017, ApJ, 838, 65
- Pen, U.-L., Chang, T.-C., Hirata, C. M., Peterson, J. B., Roy, J., Gupta, Y., Odegova, J., & Sigurdson, K. 2009, MNRAS, 399, 181
- Perley, R. A., Roser, H.-J., & Meisenheimer, K. 1997, A& A, 328, 12
- Planck Collaboration et al. 2016, A& A, 594, A13
- Pober, J. 2015, Updated 21cm Experiment Sensitivities, Tech. Rep. 4, Brown University
- . 2016, 21cmSense: Calculating the sensitivity of 21cm experiments to the EoR power spectrum, Astrophysics Source Code Library
- Pober, J. C. et al. 2015, ApJ, 809, 62
- . 2014, ApJ, 782, 66
- . 2013, ApJL, 768, L36
- . 2012, AJ, 143, 53
- Popa, C.-A. 2017, in Neural Networks (IJCNN), 2017 International Joint Conference on, IEEE, 816–822
- Price, D. C. 2016a, PyGSM: Python interface to the Global Sky Model, Astrophysics Source Code Library
- . 2016b, ArXiv e-prints
- Pritchard, J. R. & Loeb, A. 2010, PRD, 82, 023006
- Rosenblatt, F. 1961, Principles of neurodynamics. perceptrons and the theory of brain mechanisms, Tech. rep., CORNELL AERONAUTICAL LAB INC BUFFALO NY
- Royden, H., Miller, R., & Buennagel, L. 1984, Radio science, 19, 798

- Rumelhart, D. E., Hinton, G. E., & Williams, R. J. 1986, *nature*, 323, 533
- Santos, M. G., Ferramacho, L., Silva, M. B., Amblard, A., & Cooray, A. 2010, *MNRAS*, 406, 2421
- Sault, R. J., Hamaker, J. P., & Bregman, J. D. 1996, *A&AS*, 117, 149
- Sault, R. J., Teuben, P., & Wright, M. C. H. 2011, MIRIAD: Multi-channel Image Reconstruction, Image Analysis, and Display, Astrophysics Source Code Library
- Schilizzi, R. et al. 2007, SKA Memorandum, 100
- Shaw, J. R., Sigurdson, K., Pen, U.-L., Stebbins, A., & Sitwell, M. 2014, *ApJ*, 781, 57
- Shaw, J. R., Sigurdson, K., Sitwell, M., Stebbins, A., & Pen, U.-L. 2015, *Phys. Rev. D*, 91, 083514
- Sheth, R. K. & Tormen, G. 1999, *MNRAS*, 308, 119
- SKA Panel. 2012, Expert Panel on Radio Quiet Zone and RFI Regulation Report, Tech. rep., Square Kilometer Array, [https://www.skatelescope.org/wp-content/uploads/2012/06/79\\_Report\\_of\\_The\\_Expert\\_Panel\\_on\\_Radio\\_Quiet\\_Zone\\_and\\_RFI\\_Regulation.pdf](https://www.skatelescope.org/wp-content/uploads/2012/06/79_Report_of_The_Expert_Panel_on_Radio_Quiet_Zone_and_RFI_Regulation.pdf)
- Smirnov, O. M. 2011a, *A&A*, 527, A106
- . 2011b, *A&A*, 527, A107
- . 2011c, *A&A*, 527, A108
- . 2011d, *A&A*, 531, A159
- Sobacchi, E. & Mesinger, A. 2014, *Monthly Notices of the Royal Astronomical Society*, 440, 1662
- Sotomayor-Beltran, C. et al. 2013, *A&A*, 552, A58

- South African Civil Aviation Authority. 2008, FLIGHT CALIBRATION DATES OF VOR's IN THE REPUBLIC OF SOUTH AFRICA, Tech. Rep. 25.6, Aeronautical Information Circular, <http://209.203.9.244/resource%20center/AIC'S/25.6.pdf>
- Staatskoerant. 2008, South African Table of Frequency Allocations, Tech. Rep. 31264, ICASA, [http://thornton.co.za/resources/31264\\_890\\_complete-1.pdf](http://thornton.co.za/resources/31264_890_complete-1.pdf)
- Stefan, I. I. et al. 2013, MNRAS, 432, 1285
- Sullivan, I. S. et al. 2012a, ApJ, 759, 17
- . 2012b, ApJ, 759, 17
- Tariku, Y. A. 2015, Earth, Planets, and Space, 67, 35
- Thompson, A. R., Moran, J. M., & Swenson, Jr., G. W. 2017, Interferometry and Synthesis in Radio Astronomy, 3rd Edition
- Thomson, R. C., Crane, P., & Mackay, C. D. 1995, ApJL, 446, L93
- Thyagarajan, N. et al. 2015a, ApJ, 804, 14
- . 2015b, ApJ, 807, L28
- Thyagarajan, N., Parsons, A. R., DeBoer, D. R., Bowman, J. D., Ewall-Wice, A. M., Neben, A. R., & Patra, N. 2016, ApJ, 825, 9
- Tingay, S. J. et al. 2013, PASA, 30, 7
- Titheridge, J. E. 1972, P& SS, 20, 353
- Trott, C. M. et al. 2016, ApJ, 818, 139
- Van Eck, C. L. et al. 2018, ArXiv e-prints
- van Haarlem, M. P. et al. 2013, A&A, 556, A2

- Vedantham, H. K. & Koopmans, L. V. E. 2015, MNRAS, 453, 925
- . 2016, MNRAS, 458, 3099
- Vogelsberger, M. et al. 2014, MNRAS, 444, 1518
- Voytek, T. C., Natarajan, A., Jáuregui García, J. M., Peterson, J. B., & López-Cruz, O. 2014, ApJ, 782, L9
- Wieringa, M. H. 1992, Experimental Astronomy, 2, 203
- Wolleben, M., Landecker, T. L., Reich, W., & Wielebinski, R. 2006, A&A, 448, 411
- World Aero Data. 2016, <http://worldaerodata.com/>, website
- Yatawatta, S. et al. 2013, A&A, 550, A136
- Zhang, Z., Wang, H., Xu, F., & Jin, Y.-Q. 2017, IEEE Transactions on Geoscience and Remote Sensing, 55, 7177
- Zheng, H. et al. 2014, MNRAS, 445, 1084
- Zheng, H. et al. 2017, MNRAS, 464, 3486
- Zhu, H.-M., Pen, U.-L., Yu, Y., Er, X., & Chen, X. 2016, Physical Review D, 93, 103504
- Zolesi, B. & Cander, L. R. 2014, Ionospheric prediction and forecasting (Springer)